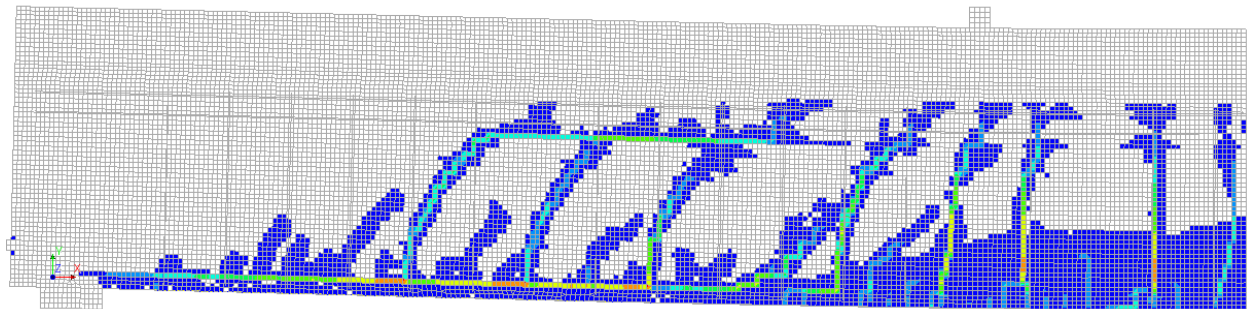




**CHALMERS**  
UNIVERSITY OF TECHNOLOGY

---



# **An Innovative Application of FRP Composites in Bridge Strengthening and Repair**

FE Analysis of FRP Strengthened Beams for Bridge Refurbishment

Master's Thesis in Master Program Structural Engineering and Building Technology

Sarah Gratwick & Mohammad Raihan Abir



MASTER'S THESIS ACEX30-19-88

# **An Innovative Application of FRP Composites in Bridge Strengthening and Repair**

FE Analysis of FRP Strengthened Beams for Bridge Refurbishment

Sarah Gratwick & Mohammad Raihan Abir



**CHALMERS**  
UNIVERSITY OF TECHNOLOGY

Department of Architecture and Civil Engineering  
*Division of Structural Engineering*  
Structural Engineering Group  
CHALMERS UNIVERSITY OF TECHNOLOGY  
Gothenburg, Sweden 2019

An Innovative Application of FRP Composites in Bridge Strengthening and Repair  
FE Analysis of FRP Strengthened Beams for Bridge Refurbishment

Sarah Gratwick & Mohammad Raihan Abir

© Sarah Gratwick & Mohammad Raihan Abir, 2019.

Supervisors: Johan Söderman (Engineer at ÅF Consult) and Jincheng Yang (Phd Student at Chalmers University of Technology)

Examiner: Associate Professor Reza Haghani Dogaheh, Department of Architecture and Civil Engineering

Master's Thesis 2019:**ACEX30-19-88**

Department of Architecture and Civil Engineering

Division of Structural Engineering

Structural Engineering Group

Chalmers University of Technology

SE-412 96 Gothenburg

Telephone +46 31 772 1000

Cover: Cracking Pattern for a FRP Strengthened RC Beam

Department of Architecture and Civil Engineering

Gothenburg, Sweden 2019

An Innovative Application of FRP Composites in Bridge Strengthening and Repair  
FE Analysis of FRP Strengthened Beams for Bridge Refurbishment  
Sarah Gratwick & Mohammad Raihan Abir  
Department of Architecture and Civil Engineering  
Chalmers University of Technology

## Abstract

With the gradual increase of vehicle loads in recent years, growing numbers of the existing bridge stock are becoming structurally obsolete. To tackle this issue, a bridge strengthening project, named SUREBridge, was initiated in 2015 at Chalmers University of Technology, with the support of several other partners. This project proposed an innovative strengthening method; the utilization of pretensioned carbon fiber reinforced polymer (CFRP) laminates on the base of bridge girders, in combination with glass fiber reinforced polymer (GFRP) sandwich panels on the top, to increase the yield and ultimate capacities of existing bridge decks. From experimental tests, 90 and 160% increases in the bending stiffness and ultimate bending capacity were found.

This master thesis aims to replicate the experimental results from the four SURE-Bridge beams which were tested in the laboratory, through the finite element software ABAQUS and DIANA. Verification is made through comparisons of the load-deflection curves, maximum crack width sizes and crack patterns. A secondary purpose is to document all approaches and modelling techniques when developing the finite element models.

To achieve the objective, an extensive literature study was performed to determine appropriate approaches to include bond-slip between the steel reinforcement and the concrete beam, as well as the CFRP and the concrete beam. Several sensitivity analyses were also performed to determine the most appropriate model and material parameters, to find the best fit to the experimental results.

From the analyses, it was concluded that the inclusion of the full bond-slip curves between both the concrete and steel, and concrete and CFRP are vital to obtain accurate results. However, the delamination load can accurately be predicted with a deviation of less than 2.5% by modelling the steel reinforcement as embedded. Hence it is concluded that in design, embedded steel can be utilized without significant losses in accuracy, and with considerable savings in the amount of time spent modelling and analyzing.

Keywords: Reinforced Concrete beam, CFRP, GFRP, Delamination, Crack Width, Bond-slip, Smear Length



# Acknowledgements

The master thesis was carried out from January 2019 to June 2019, in collaboration between Chalmers University of Technology and Åf Infrastructure AB.

The work presented in this thesis is based on the work performed by Jincheng Yang, PhD student at the division of Structural Engineering, who is also involved in SUREBridge project. We would like to express our gratitude to Jincheng Yang, our supervisor from Chalmers, Johan Söderman, our supervisor from Åf, and Associate Professor Reza Haghani, our examiner from Chalmers, for their continuous support and constructive critique throughout the duration of our thesis.

We would also like to thank our parents, our beloved ones and our friends, for being there beside us, making it possible to finish the work. We want to dedicate this work to them.

Sarah Gratwick and Mohammad Raihan Abir, Gothenburg, Sweden, June 2019



# Contents

<b>List of Figures</b>	<b>xv</b>
<b>List of Tables</b>	<b>xxi</b>
<b>1 Introduction</b>	<b>1</b>
1.1 Background . . . . .	1
1.2 Purpose . . . . .	3
1.3 Objectives . . . . .	3
1.4 Methodology . . . . .	4
1.5 Scope & Limitations . . . . .	5
1.6 Outline of the Report . . . . .	5
<b>2 Review of the SUREBridge Solution</b>	<b>7</b>
2.1 General Overview . . . . .	7
2.2 Life Cycle Cost Analysis: San Miniato Bridge . . . . .	8
2.3 Pretensioning of CFRP . . . . .	9
2.4 Experimental Verification . . . . .	10
2.4.1 Material Properties . . . . .	11
2.4.2 Loading . . . . .	12
2.4.3 Results . . . . .	12
2.4.3.1 Failure Mechanisms . . . . .	12
2.5 Earlier Finite Element Models . . . . .	14
2.5.1 Recommendations . . . . .	14
<b>3 Mechanical Properties of Materials</b>	<b>15</b>
3.1 Concrete Behaviour . . . . .	15
3.1.1 General Properties . . . . .	15
3.1.1.1 Factors Affecting Strength and Ductility . . . . .	16
3.1.2 Compressive Response . . . . .	17
3.1.3 Tensile Response . . . . .	18
3.1.3.1 Pre-crack Behaviour . . . . .	18
3.1.3.2 Post-crack behaviour . . . . .	19
3.1.3.3 Fracture Energy . . . . .	20
3.2 Steel Behaviour . . . . .	21
3.3 CFRP Behaviour . . . . .	24
3.3.1 Elastic Response . . . . .	24
3.3.2 Failure Mechanisms . . . . .	25

3.4	GFRP Behaviour . . . . .	26
3.4.1	Elastic Behaviour . . . . .	27
3.4.1.1	Component Based . . . . .	28
3.4.1.2	Equivalent Web Core . . . . .	29
3.4.1.3	Equivalent Properties . . . . .	30
3.4.2	Failure Mechanisms . . . . .	31
3.5	Mortar . . . . .	32
3.6	Epoxy . . . . .	32
<b>4</b>	<b>Material Modelling</b>	<b>33</b>
4.1	Concrete Material Models . . . . .	33
4.1.1	Linear Elastic Model . . . . .	34
4.1.2	Fracture Mechanics . . . . .	34
4.1.3	Cracking Approaches . . . . .	35
4.1.3.1	Discrete Crack Approach . . . . .	35
4.1.3.2	Smearred Crack Approach . . . . .	36
4.1.3.3	Embedded Crack Approach . . . . .	38
4.1.4	Concrete Damaged Plasticity Model (ABAQUS) . . . . .	39
4.1.4.1	Compressive Response . . . . .	39
4.1.4.2	Tensile Response . . . . .	41
4.1.4.3	Damage Factors . . . . .	43
4.1.4.4	Plasticity Parameters . . . . .	47
4.1.5	Total Strain Crack Model (DIANA) . . . . .	48
4.1.5.1	Rotating vs Fixed Cracks . . . . .	48
4.1.5.2	Compressive Response . . . . .	49
4.1.5.3	Tensile Response . . . . .	49
4.1.5.4	Shear Retention . . . . .	52
4.2	Steel Material Model . . . . .	53
4.2.1	Elastic Behaviour . . . . .	53
4.2.2	Plastic Behaviour . . . . .	54
4.2.3	Bond-slip Relationship . . . . .	54
4.3	CFRP Material Model . . . . .	56
4.3.1	Elastic Response . . . . .	56
4.4	Epoxy Material Models (CFRP to Concrete) . . . . .	57
4.4.1	Epoxy . . . . .	57
4.4.2	Bond-Slip Model . . . . .	57
4.5	GFRP Material Model . . . . .	59
4.5.1	Elastic Behaviour . . . . .	59
4.6	Epoxy Material Model (GFRP to Concrete) . . . . .	60
4.7	Mortar Material Model . . . . .	60
<b>5</b>	<b>Finite Element Models</b>	<b>61</b>
5.1	Geometry . . . . .	62
5.2	Boundary Conditions . . . . .	65
5.3	Loading Conditions . . . . .	66
5.3.1	Pretensioning the CFRP Laminates . . . . .	66
5.3.2	Self-weight . . . . .	67

5.3.3	Four-point bending . . . . .	67
5.4	Bond between the Steel Reinforcement and Concrete Beam . . . . .	68
5.4.1	Perfect Bond . . . . .	68
5.4.2	Bond-slip Modelling in ABAQUS . . . . .	68
5.4.2.1	Springs . . . . .	69
5.4.2.2	Connector Elements (translator) . . . . .	70
5.4.2.3	Adhesive Elements . . . . .	74
5.4.2.4	Bond Zone Models . . . . .	74
5.4.3	Bond-slip Modelling in DIANA . . . . .	76
5.4.3.1	fib 2010 Bond-slip Model . . . . .	76
5.4.4	Smearred Length . . . . .	77
5.5	Bond between the CFRP laminates and the Concrete Beam . . . . .	78
5.5.1	Modelling the Epoxy in 2D . . . . .	78
5.5.2	Bond-slip . . . . .	78
5.5.2.1	In ABAQUS . . . . .	78
5.5.2.2	In DIANA . . . . .	79
5.6	Analysis Procedure . . . . .	80
5.7	Mesh . . . . .	81
5.7.1	Elements in ABAQUS . . . . .	81
5.7.2	Elements in DIANA . . . . .	82
5.7.3	Mesh Density . . . . .	83
5.8	Iteration Method . . . . .	84
5.9	Convergence of Solutions . . . . .	85
5.9.1	Elastic Analysis . . . . .	85
5.9.2	Step size . . . . .	85
5.9.3	Viscosity Parameter (ABAQUS) . . . . .	85
5.9.4	Alternative Solution Methods . . . . .	86
<b>6</b>	<b>Sensitivity Analyses</b> . . . . .	<b>87</b>
6.1	Perfect Bond . . . . .	87
6.1.1	Effect of Mesh Density . . . . .	88
6.1.1.1	Results . . . . .	88
6.1.1.2	Discussion of Results . . . . .	89
6.1.2	Effect of the Smearred Length . . . . .	90
6.1.2.1	Results . . . . .	90
6.1.2.2	Discussion of Results . . . . .	92
6.1.3	Effect of the Damage Model (ABAQUS) . . . . .	93
6.1.3.1	Results . . . . .	93
6.1.3.2	Discussion of Results . . . . .	93
6.1.4	Effect of the Dilation Angle (ABAQUS) . . . . .	95
6.1.4.1	Results . . . . .	95
6.1.4.2	Discussion of Results . . . . .	96
6.1.5	Effect of the Viscosity Parameter (ABAQUS) . . . . .	97
6.1.5.1	Results . . . . .	97
6.1.5.2	Discussion of Results . . . . .	98
6.2	Bond-Slip Included . . . . .	99

6.2.1	Effect of the Mesh Density . . . . .	99
6.2.1.1	Results . . . . .	99
6.2.1.2	Discussion of Results . . . . .	101
6.2.2	Effect of the Smear Length (DIANA) . . . . .	104
6.2.2.1	Results . . . . .	104
6.2.2.2	Discussion of Results . . . . .	105
6.2.3	Effect of the Smear Length (ABAQUS) . . . . .	107
6.2.3.1	Results . . . . .	107
6.2.3.2	Discussion of Results . . . . .	108
6.2.4	Effect of the Tension Model (DIANA) . . . . .	110
6.2.4.1	Results . . . . .	110
6.2.4.2	Discussion of Results . . . . .	111
6.2.5	Effect of the Damage Model (ABAQUS) . . . . .	113
6.2.5.1	Results . . . . .	113
6.2.5.2	Discussion of Results . . . . .	114
<b>7</b>	<b>Finite Element Results &amp; Discussion</b>	<b>115</b>
7.1	Beam 1 . . . . .	116
7.1.1	Perfect Bond . . . . .	116
7.1.1.1	Load-Deflection Results . . . . .	116
7.1.1.2	Discussion of Results . . . . .	117
7.1.2	Bond-Slip Included . . . . .	118
7.1.2.1	Load-Deflection Results . . . . .	118
7.1.2.2	Maximum Crack Width Results . . . . .	119
7.1.2.3	Crack Patterns . . . . .	119
7.1.2.4	Discussion of Results . . . . .	122
7.2	Beam 2 . . . . .	125
7.2.1	Perfect Bond . . . . .	125
7.2.1.1	Load-Deflection Results . . . . .	125
7.2.1.2	Discussion of Results . . . . .	128
7.2.2	Bond-Slip Included . . . . .	130
7.2.2.1	Load-Deflection Results . . . . .	130
7.2.2.2	Maximum Crack Width Results . . . . .	132
7.2.2.3	Crack Patterns . . . . .	132
7.2.2.4	Discussion of Results . . . . .	135
7.3	Beam 3 . . . . .	138
7.3.1	Perfect Bond . . . . .	138
7.3.1.1	Load-Deflection Results . . . . .	138
7.3.1.2	Discussion of Results . . . . .	141
7.3.2	Bond-Slip Included . . . . .	143
7.3.2.1	Load-Deflection Results . . . . .	143
7.3.2.2	Maximum Crack Width Results . . . . .	146
7.3.2.3	Crack Patterns . . . . .	146
7.3.2.4	Discussion of Results . . . . .	149
7.4	Beam 4 . . . . .	152
7.4.1	Perfect Bond . . . . .	152

7.4.1.1	Load-Deflection Results . . . . .	152
7.4.1.2	Discussion of Results . . . . .	155
7.4.2	Bond-Slip Included . . . . .	157
7.4.2.1	Load-Deflection Results . . . . .	157
7.4.2.2	Maximum Crack Width Results . . . . .	160
7.4.2.3	Crack Patterns . . . . .	160
7.4.2.4	Discussion of Results . . . . .	163
<b>8</b>	<b>Conclusions</b>	<b>165</b>
<b>9</b>	<b>Future Studies</b>	<b>167</b>
	<b>Bibliography</b>	<b>169</b>
<b>A</b>	<b>Appendix 1</b>	<b>I</b>
A.1	Beam 1 Results . . . . .	I
A.1.1	Crack Patterns According to Mesh Density . . . . .	I
A.1.1.1	ABAQUS, Crack Patterns at 30 kN . . . . .	II
A.1.1.2	ABAQUS, Crack Patterns at 60 kN . . . . .	III
A.1.1.3	ABAQUS, Crack Patterns at 90 kN . . . . .	IV
A.1.1.4	ABAQUS, Crack Patterns at 120 kN . . . . .	V
A.1.1.5	DIANA, Crack Patterns at 30 kN . . . . .	VI
A.1.1.6	DIANA, Crack Patterns at 60 kN . . . . .	VII
A.1.1.7	DIANA, Crack Patterns at 90 kN . . . . .	VIII
A.1.1.8	DIANA, Crack Patterns at 120 kN . . . . .	IX
A.1.2	Crack Patterns According to Smear Length (DIANA) . . . . .	X
A.1.2.1	DIANA, Crack Patterns at 30 kN . . . . .	X
A.1.2.2	DIANA, Crack Patterns at 60 kN . . . . .	XI
A.1.2.3	DIANA, Crack Patterns at 90 kN . . . . .	XII
A.1.2.4	DIANA, Crack Patterns at 120 kN . . . . .	XIII
A.1.3	Crack Patterns According to Smear Length (ABAQUS) . . . . .	XIV
A.1.3.1	ABAQUS, Crack Patterns at 30 kN . . . . .	XIV
A.1.3.2	ABAQUS, Crack Patterns at 60 kN . . . . .	XV
A.1.3.3	ABAQUS, Crack Patterns at 90 kN . . . . .	XVI
A.1.3.4	ABAQUS, Crack Patterns at 120 kN . . . . .	XVII
A.1.4	Crack Patterns According to Tension Curves (DIANA) . . . . .	XVIII
A.1.4.1	DIANA, Crack Patterns at 30 kN . . . . .	XVIII
A.1.4.2	DIANA, Crack Patterns at 60 kN . . . . .	XIX
A.1.4.3	DIANA, Crack Patterns at 90 kN . . . . .	XX
A.1.4.4	DIANA, Crack Patterns at 120 kN . . . . .	XXI
A.1.5	Crack Patterns According to Damage Models (ABAQUS) . . . . .	XXII
A.1.5.1	ABAQUS, Crack Patterns at 30 kN . . . . .	XXII
A.1.5.2	ABAQUS, Crack Patterns at 60 kN . . . . .	XXIII
A.1.5.3	ABAQUS, Crack Pattern at 90 kN . . . . .	XXIV
A.1.5.4	ABAQUS, Crack Pattern at 120 kN . . . . .	XXV



# List of Figures

1.1	Overview of the SUREBridge Proposal . . . . .	2
2.1	Cross Sectional View of the SUREBridge Solution . . . . .	7
2.2	Axial and Shear stresses in (a) traditional pretensioning methods and (b) using the step-wise pretensioning tool, Jincheng Yang 2019 . . . . .	9
2.3	Location of the Load application . . . . .	12
2.4	CFRP Failure in the Laboratory . . . . .	13
3.1	Stress Strain relationship for concrete under compression . . . . .	17
3.2	Stress Strain relationship for concrete under tension . . . . .	18
3.3	Stress ( $\sigma_t$ ) - crack opening ( $\omega$ ) relationship for concrete under tension	19
3.4	Stress-Strain relationship for 8 and 16mm diameter rebar . . . . .	21
3.5	Stress strain curve of 16 mm rebar (True vs Nominal) . . . . .	23
3.6	Stress-Strain relationship for CFRP . . . . .	24
3.7	GFRP Cross Section, with main components labelled . . . . .	26
3.8	Fiber direction in GFRP deck panel . . . . .	27
3.9	GFRP cross section with an equivalent web core . . . . .	29
3.10	Load-deflection relationship from 3-point bending test . . . . .	30
4.1	Different Concrete Cracking Approaches . . . . .	35
4.2	Concrete Compressive Response, with the effect of the damage factor on elasticity . . . . .	39
4.3	Concrete Tensile Response, with the effect of the damage factor on elasticity . . . . .	41
4.4	Comparison of Compressive Damaged Plasticity Values . . . . .	45
4.5	Comparison of Tensile Damaged Plasticity Values . . . . .	45
4.6	Concrete Tensile Softening Relations in DIANA . . . . .	51
4.7	Elastic-Plastic Material Model for Steel . . . . .	53
4.8	Bond-slip relationship between Steel and Concrete . . . . .	54
4.9	Bond-slip relationship between CFRP and Concrete . . . . .	58
5.1	Beam Geometry for beams 2 - 4 . . . . .	62
5.2	Cross Section of the Reinforced Concrete Beam . . . . .	63
5.3	Boundary Conditions in the FE Models. From left to right; support, loading and symmetry conditions . . . . .	65
5.4	Pretensioning Loads and Positions [mm] . . . . .	67
5.5	Overview of the translator behaviour in ABAQUS . . . . .	71

5.6	Translator element in ABAQUS . . . . .	72
5.7	Partitions for defining bond-slip in ABAQUS . . . . .	73
5.8	Location of T6MEM elements in a mesh from DIANA (highlighted in red) . . . . .	82
6.1	B1: Effect of different mesh densities on the load-deflection curves in ABAQUS, Perfect Bond . . . . .	88
6.2	B1: Effect of different mesh densities on the load-deflection curves in DIANA, Perfect Bond . . . . .	89
6.3	B1: Effect of different smeared lengths on the load-deflection curves in ABAQUS, Perfect Bond . . . . .	90
6.4	B1: Effect of different smeared lengths on the load-deflection curves in DIANA, Perfect Bond, for smeared lengths 25 - 50 mm . . . . .	91
6.5	B1: Effect of different smeared lengths on the load-deflection curves in DIANA, Perfect Bond, for smeared lengths 50 - 150 mm . . . . .	91
6.6	B1: Effect of different damage models on the load-deflection results in ABAQUS, Perfect Bond, Mesh 25 x 25 mm . . . . .	93
6.7	B1: Effect of different dilation angles on the load-deflection curves in ABAQUS, Perfect Bond (zoomed in) . . . . .	95
6.8	B1: Effect of different dilation angles on the load-deflection curves in ABAQUS, Perfect Bond (zoomed out) . . . . .	96
6.9	B1: Effect of different viscosity parameters on the load-deflection curves in ABAQUS, Perfect Bond . . . . .	97
6.10	B1: Effect of different mesh densities on the load-deflection curves in ABAQUS, with Bond-Slip . . . . .	100
6.11	B1: Effect of different mesh densities on the load-deflection curves in DIANA, with Bond-Slip . . . . .	100
6.12	B1: Effect of different smeared lengths on the load-deflection curves in DIANA, with Bond-Slip . . . . .	104
6.13	B1: Effect of different smeared lengths on the load-deflection curves in ABAQUS, with Bond-Slip . . . . .	107
6.14	B1: Effect of different tension models on the load-deflection curves in DIANA, with Bond-Slip . . . . .	110
6.15	B1: Effect of different damage models on the load-deflection curves in ABAQUS, with Bond-Slip . . . . .	113
7.1	B1: Load-deflection of beam 1, Perfect bond . . . . .	116
7.2	B1: Final Curves in ABAQUS and DIANA, with Bond-Slip . . . . .	118
7.3	B1: Crack Patterns at 90 kN. From top to bottom: ABAQUS, DIANA, Lab (LHS) and Lab (RHS) . . . . .	120
7.4	B1: Crack Patterns at 120 kN. From top to bottom: ABAQUS, DIANA, Lab (LHS) and Lab (RHS) . . . . .	121
7.5	B2: Load-deflection of beam 2, Perfect bond . . . . .	125
7.6	B2: Load-deflection of Beam 2.1 and 2.2 in DIANA, Perfect Bond . . . . .	126
7.7	B2: Crack Pattern in beam 2.1 in DIANA, just prior to failure, Perfect . . . . .	127
7.8	B2: Slip in the interface in beam 2.1 in DIANA, just prior to failure, Perfect . . . . .	127

7.9	B2: Slip in the interface in beam 2.1 in DIANA, just following failure, Perfect . . . . .	127
7.10	B2: Final Curves in ABAQUS and DIANA, with Bond-Slip . . . . .	130
7.11	B2: Crack Pattern just prior to Failure point of DIANA Model, with Bond-Slip . . . . .	131
7.12	B2: Interface Slip just prior to Failure point of DIANA Model, with Bond-Slip . . . . .	131
7.13	B2: Crack Pattern just following Failure point of DIANA Model, with Bond-Slip . . . . .	132
7.14	B2: Interface Slip just following Failure point of DIANA Model, with Bond-Slip . . . . .	132
7.15	B2: Crack Patterns at 150 kN. From top to bottom: ABAQUS, DIANA, Lab (LHS) and Lab (RHS) . . . . .	133
7.16	B2: Crack Patterns at 180 kN. From top to bottom: ABAQUS, DIANA, Lab (LHS) and Lab (RHS) . . . . .	134
7.17	B3: Load-deflection of beam 3, Perfect Bond . . . . .	138
7.18	B3: Load-deflection of beam 3.1 in DIANA, Perfect Bond . . . . .	139
7.19	B3: Crack Pattern in beam 3.1 in DIANA, just prior to failure, Perfect	140
7.20	B3: Slip in the interface in beam 3.1 in DIANA, just prior to failure, Perfect . . . . .	140
7.21	B3: Slip in the interface in beam 3.1 in DIANA, just following failure, Perfect . . . . .	140
7.22	B3: Load-deflection of Beam 3, with Bond-Slip . . . . .	143
7.23	B3: Beam 3.1 and 3.2 results from DIANA, with Bond-Slip . . . . .	144
7.24	B3: Crack Pattern just prior to Failure Point of DIANA model, with Bond-Slip . . . . .	145
7.25	B3: Slip just prior to Failure Point of DIANA model, with Bond-Slip	145
7.26	B3: Crack Pattern just prior to Failure Point of DIANA model, with Bond-Slip . . . . .	145
7.27	B3: Slip at Failure Point of DIANA model, with Bond-Slip . . . . .	145
7.28	B3: Crack Patterns at 150 kN. From top to bottom: ABAQUS, DIANA, Lab (LHS) and Lab (RHS) . . . . .	147
7.29	B3: Crack Patterns at 180 kN. From top to bottom: ABAQUS, DIANA, Lab (LHS) and Lab (RHS) . . . . .	148
7.30	B4: Load-deflection of beam 4, Perfect Bond . . . . .	152
7.31	B4: Load-deflection of beams 4.1 and 4.2 in DIANA, Perfect Bond . .	153
7.32	B4: Crack Pattern in beam 4.1 in DIANA, just prior to failure, Perfect	154
7.33	B4: Slip in the interface in beam 4.1 in DIANA, just prior to failure, Perfect . . . . .	154
7.34	B4: Slip in the interface in beam 4.1 in DIANA, just following failure, Perfect . . . . .	154
7.35	B4: Final Curves in ABAQUS and DIANA, with Bond-Slip . . . . .	157
7.36	B4: Failure point of the DIANA model, with Bond-Slip . . . . .	158
7.37	B4: Crack Pattern just prior to failure, with Bond-slip . . . . .	159
7.38	B4: Slip in the interface just prior to failure, with Bond-slip . . . . .	159
7.39	B4: Crack Pattern just following failure, with Bond-slip . . . . .	159

7.40	B4: Slip in the interface just following failure, with Bond-slip . . . . .	159
7.41	B4: Crack Patterns at 150 kN. From top to bottom: ABAQUS, DI- ANA, Lab (LHS) and Lab (RHS) . . . . .	161
7.42	B4: Crack Patterns at 180 kN. From top to bottom: ABAQUS, DI- ANA, Lab (LHS) and Lab (RHS) . . . . .	162
A.1	B1: Crack Patterns at 30 kN in ABAQUS. From top to bottom: Mesh 92x92, 46x46, 23x23, 11x11 and from Lab . . . . .	II
A.2	B1: Crack Patterns at 60 kN in ABAQUS. From top to bottom: Mesh 92x92, 46x46, 23x23, 11x11 and from Lab . . . . .	III
A.3	B1: Crack Patterns at 90 kN in ABAQUS. From top to bottom: Mesh 92x92, 46x46, 23x23, 11x11 and from Lab . . . . .	IV
A.4	B1: Crack Patterns at 120 kN in ABAQUS. From top to bottom: Mesh 92x92, 46x46, 23x23, 11x11 and from Lab . . . . .	V
A.5	B1: Crack Patterns at 30 kN in DIANA. From top to bottom: Mesh 92x92, 46x46, 23x23, 11x11 and from Lab . . . . .	VI
A.6	B1: Crack Patterns at 60 kN in DIANA. From top to bottom: Mesh 92x92, 46x46, 23x23, 11x11 and from Lab . . . . .	VII
A.7	B1: Crack Patterns at 90 kN in DIANA. From top to bottom: Mesh 92x92, 46x46, 23x23, 11x11 and from Lab . . . . .	VIII
A.8	B1: Crack Patterns at 120 kN in DIANA. From top to bottom: Mesh 92x92, 46x46, 23x23, 11x11 and from Lab . . . . .	IX
A.9	B1: Crack Patterns at 30 kN in DIANA. From top to bottom: Smear- ed Length 23 mm, 32 mm and result from Lab . . . . .	X
A.10	B1: Crack Patterns at 60 kN in DIANA. From top to bottom: Smear- ed Length 23 mm, 32 mm and result from Lab . . . . .	XI
A.11	B1: Crack Patterns at 90 kN in DIANA. From top to bottom: Smear- ed Length 23 mm, 32 mm and result from Lab . . . . .	XII
A.12	B1: Crack Patterns at 120 kN in DIANA. From top to bottom: Smear- ed Length 23 mm, 32 mm and result from Lab . . . . .	XIII
A.13	B1: Crack Patterns at 30 kN in ABAQUS. From top to bottom: Smear- ed Length 11 mm, 46 mm and result from Lab . . . . .	XIV
A.14	B1: Crack Patterns at 60 kN in ABAQUS. From top to bottom: Smear- ed Length 11 mm, 46 mm and result from Lab . . . . .	XV
A.15	B1: Crack Patterns at 90 kN in ABAQUS. From top to bottom: Smear- ed Length 11 mm, 46 mm and result from Lab . . . . .	XVI
A.16	B1: Crack Patterns at 120 kN in ABAQUS. From top to bottom: Smear- ed Length 11 mm, 46 mm and result from Lab . . . . .	XVII
A.17	B1: Crack Patterns at 30 kN in DIANA. From top to bottom: Tension model Hordijk, Exponential and fib, and result from Lab . . . . .	XVIII
A.18	B1: Crack Patterns at 60 kN in DIANA. From top to bottom: Tension model Hordijk, Exponential and fib, and result from Lab . . . . .	XIX
A.19	B1: Crack Patterns at 90 kN in DIANA. From top to bottom: Tension model Hordijk, Exponential and fib, and result from Lab . . . . .	XX
A.20	B1: Crack Patterns at 120 kN in DIANA. From top to bottom: Ten- sion model Hordijk, Exponential and fib, and result from Lab . . . . .	XXI

A.21 B1: Crack Patterns at 30 kN in ABAQUS. From top to bottom:  
     Damage model 1 and 2, and result from Lab . . . . . XXII

A.22 B1: Crack Patterns at 60 kN in ABAQUS. From top to bottom:  
     Damage model 1 and 2, and result from Lab . . . . . XXIII

A.23 B1: Crack Patterns at 90 kN in ABAQUS. From top to bottom:  
     Damage model 1 and 2, and result from Lab . . . . . XXIV

A.24 B1: Crack Patterns at 120 kN in ABAQUS. From top to bottom:  
     Damage model 1 and 2, and result from Lab . . . . . XXV



# List of Tables

2.1	Material Properties from the experimental tests . . . . .	11
2.2	Delamination Strain in CFRP from the laboratory . . . . .	13
3.1	Material Properties for 28 day Concrete, grade C35/45 . . . . .	16
3.2	Material Properties for B500B Steel; 16mm and 8mm diameter . . . . .	21
3.3	Material Properties of CFRP, determined from testing . . . . .	24
3.4	Material Properties for GFRP panel per component . . . . .	28
3.5	Material Properties for GFRP panel with an equivalent core . . . . .	29
3.6	Material Properties for GFRP, with equivalent properties . . . . .	30
3.7	Material Properties for weber EXM 702 Mortar . . . . .	32
3.8	Material Properties for StoPox SK 41 Epoxy . . . . .	32
4.1	Steel Bond-slip values for good and all other bond conditions . . . . .	55
5.1	Dimensions of each component in the four beam models, excl. GFRP . . . . .	64
5.2	Dimensions of the GFRP Panels . . . . .	64
5.3	Pretensioning Loads used in FE . . . . .	66
6.1	B1: Maximum crack width size, according to mesh size . . . . .	101
6.2	B1: Maximum crack width size, according to smeared length (DIANA) . . . . .	105
6.3	B1: Maximum crack width size, according to smeared length (ABAQUS) . . . . .	108
6.4	B1: Maximum crack width size, according to tension model (DIANA) . . . . .	111
6.5	B1: Maximum crack width size, according to damage model (ABAQUS) . . . . .	114
7.1	B1: Maximum crack width size . . . . .	119
7.2	B2: Maximum crack width size . . . . .	132
7.3	B3: Maximum crack width size . . . . .	146
7.4	B4: Maximum crack width size . . . . .	160



# 1

## Introduction

### 1.1 Background

In 2018, Sweden introduced a new load-bearing class whereby longer, heavier vehicles with a gross weight of up to 74 tonnes were able to operate on selected roads. Sweden however, was not the first country to increase capacities; Finland made a similar increase in 2013, to ensure their forestry sector remained competitive in the global market (Palander & Kärhä 2017). Whilst most of the EU is still limited to 40-tonne vehicles, similar increases could also be expected in coming years (Forsberg 2017).

As increased loads are allowed on road networks, updates to bridge capacities and expansion of the deck area will need to be made to cope with these increased demands. In the first roll out of the new load-bearing class in Sweden, 66 bridges needed strengthening, and it is anticipated that a further 1000 bridges will need similar strengthening measures to cope with the new load-bearing class (Forsberg 2017).

The EU-funded project *Sustainable Refurbishment of Existing Bridges* (SUREBridge), which was started in October 2015, proposed a method of bridge strengthening which would increase both the load capacity and the deck area.

Their proposal is to utilize pretensioned carbon fibre reinforced polymer (CFRP) laminates on the tension side of bridge girders, in combination with glass fibre reinforced polymer (GFRP) sandwich panels on the compressive side. At this stage, it has only been explored as a strengthening option for T-sectioned beams. This design is displayed in figure 1.1.

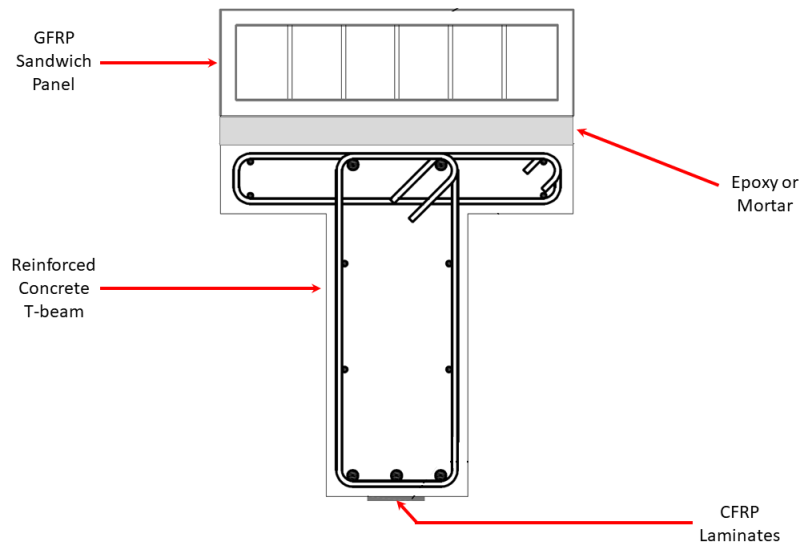


**Figure 1.1:** Overview of the SUREBridge Proposal

In developing this design, the SUREBridge group aimed to find a holistic and sustainable alternative to the traditional solution, which meant a full replacement of the bridge. This would usually result in large financial costs related to the demolition and construction, as well as large time delays to the public due to rerouting, and sizable amounts of noise pollution, which it would seek to reduce.

As the GFRP panels are able to be prefabricated off-site, their rapid installation on the bridge deck would reduce the assembly time compared to other materials. This would allow for the strengthening period to be shorter than other refurbishment options, as well as providing a quick method of replacement of sections if required in its service life.

This proposed strengthening solution would also theoretically reduce some of the costs related to life cycle maintenance. Most bridges are constructed from reinforced concrete, which is susceptible to degradation due to the repeated freeze-thaw cycles, as well from the extensive use of de-icing salts. FRP is resistant to damage by these sources, so its placement on the deck surface would assist in providing a layer of corrosion protection to the existing reinforced concrete deck below.

Laboratory testing of the SUREBridge proposal determined that it could dramatically increase the load-bearing capacity of the bridge; leading to a 90% and 160% increase in the bending stiffness and ultimate bending capacity respectively.

## 1.2 Purpose

This master thesis seeks to fulfill one primary purpose;

- To replicate the experimental results from the four SUREBridge beams, with the use of two finite element programs; ABAQUS and DIANA.

Linked to this primary purpose, a secondary purpose is also defined:

- To provide clear documentation of the modelling process, as to act as a guide for other researches who may be attempting to replicate similar model behaviour.

As the structural benefits of the SUREBridge solution have already been determined through experimental testing, no further results can be determined from performing a finite element analysis. However, if such a model is developed which is able to capture the same response as the experiments, it can be used as a base from which other models can be built upon. For example, if the capacity of a beam using the SUREBridge solution needed to be calculated, but its dimensions differed from the original lab tested beams, an FE model can be used to calculate this capacity, rather than further experimental testing. By already having a verified FE model in which to base the modelling around, the accuracy of further modelling can be increased. This negates the need for experimental testing every time a change is made to the original, tested solution; saving time and money.

Furthermore, by ensuring high quality documentation and description of the modelling process at all levels, it assists other researchers who seek to model similar behaviours. From a literature review of the different modelling processes for different bond-slip relationships, it is apparent that there exists no clear definition of the modelling process, making it challenging for beginners to replicate the model. It is the secondary aim of this thesis to provide clarity in this area.

## 1.3 Objectives

In order to fulfill the primary purpose of the thesis, the following objectives need to be completed:

1. Investigation of different modelling techniques to:
  - Replicate the material response of CFRP and GFRP;
  - Include bond-slip between the steel and the concrete;
  - Include bond-slip between the CFRP and the concrete.
2. Modelling of the four SUREBridge beams where;
  - Beam 1: Reinforced Concrete
  - Beam 2: Reinforced Concrete beam with GFRP panel with longitudinal webs attached via an epoxy, with pretensioned CFRP laminates
  - Beam 3: Reinforced Concrete beam with GFRP panel with longitudinal webs attached via a mortar, with pretensioned CFRP laminates
  - Beam 4: Reinforced Concrete beam with GFRP panel with tangential webs attached via a mortar, with pretensioned CFRP laminates

3. Analyze the effect on the structural response and cracking behaviour of each beam when;
  - Either perfect bond or bond-slip is included between the steel reinforcement and the concrete beam
  - The partial or full bond-slip curve is defined between the CFRP and the concrete

## 1.4 Methodology

To satisfy the aims and objectives of this thesis, the following methodology will be followed.

To provide some background for the thesis, a literature review will first be performed. This will seek to review the work of the SUREBridge project team, and provide some orientation as to which materials and cross-sectional design was used in the laboratory testing, as well as any recommendations for the development of the FE model.

Following this, an investigation into the appropriate material behaviour, model inputs and modelling techniques will then be performed, in order to provide an adequate background of knowledge in which to commence modelling.

Two finite element programs will be used to model the SUREBridge solution; ABAQUS and DIANA. ABAQUS was used in modelling the earlier iteration of the SUREBridge project; where the cross-sections were rectangular, and only CFRP laminates were applied. It was the recommendation of our examiner that we continue working with ABAQUS as the models were available to us, and would provide a good base in which to build upon. However, the option to model in DIANA was also presented. It is well known in its ability to model concrete cracking, in addition to having several built-in functions which would allow for the bond-slip relationship between steel and concrete to be modelled with ease. The decision was made to utilize both software and model the same beam simultaneously in both programs, to compare the behaviour captured and determine whether one might prove to generate more accurate results.

To measure the success of each software in capturing the response of the SUREBridge solution, the load-displacement curves, crack pattern and maximum crack width size will be compared.

## 1.5 Scope & Limitations

The scope of this thesis is to determine what level of complexity is required in finite element models, to capture the same response from the experimental tests. This includes different variations in the level of modelling complexity originating from the bond-slip interactions between the steel rebar and the CFRP laminates.

The following limitations were made to narrow the scope of the thesis:

- Only the strengthening of a reinforced concrete, t-section beam will be investigated. The strengthening of any other bridge element is not considered, including columns and cross beams.
- Only non-linear static implicit analyses will be used to analyze the beams in the finite element software
- The concrete beam is assumed to be uncracked and undamaged
- The effect of creep and fatigue is ignored
- Cracking from other sources such as shrinkage are also ignored

## 1.6 Outline of the Report

In *Chapter 2*, the work performed by the SUREBridge group will be reviewed, to greater understand the behaviour which should be captured in the FE models in later sections.

*Chapter 3* will investigate the properties related to each material used in the SUREBridge beams, whilst *Chapter 4* will discuss how they translate into the finite element models. The bond-slip relationships will also be discussed in this section.

*Chapter 5* will detail the finite element models which were built in both ABAQUS and DIANA, and how some of the more complex interactions (bond-slip) were included in each of the models.

*Chapter 6* provides the results from the sensitivity analyses, as well as a discussion of the findings and which values were adopted for the final results.

*Chapter 7* provides the results from all four SUREBridge beams, as well as a detailed discussion of them.

*Chapter 8* concludes the report, summarizing the main findings, whilst *Chapter 9* provides some recommendations for future research.



# 2

## Review of the SUREBridge Solution

### 2.1 General Overview

The Sustainable Refurbishment of Existing Bridges (SUREBridge) project proposed a method of strengthening existing concrete bridge decks utilizing pretensioned carbon fibre reinforced polymer (CFRP) laminates and glass fibre reinforced polymer (GFRP) sandwich panels, with the orientation as shown in figure 2.1.

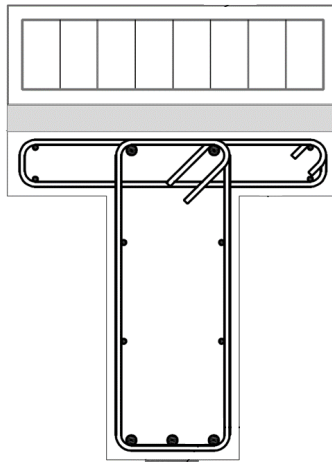


**Figure 2.1:** Cross Sectional View of the SUREBridge Solution

The GFRP panels are attached to the concrete beam via a mortar or epoxy layer, whilst the CFRP are attached with a thin layer of epoxy. A piece-wise pretensioning system was developed by the SUREBridge group to pretension the CFRP laminates in such a way to reduce the risk of failure due to delamination. This system is explained in detail in section 2.3.

## 2.2 Life Cycle Cost Analysis: San Miniato Bridge

Ricci & Valvo (2018) completed a comparative life cycle cost analysis of the SURE-Bridge solution, for use on a bridge near Tuscany, Italy. The San Miniato bridge is a 60 metre-long reinforced concrete, single-lane bridge, composed of four spans of roughly 15 metres long (Ricci & Valvo 2018). It was originally constructed in 1969, however given recent upgrades in regulations, requires an upgrade in its load-bearing capacity, as well as deck area (Ricci & Valvo 2018).

The life cycle costing analysis which was performed on the bridge, was carried out to determine the economical advantages of adopting the SUREBridge solution, over the traditional method of replacement. The costs related to the construction, operation and maintenance and end of life was considered in their analysis.

The different life cycle costs were categorized into three areas:

1. Agency Cost
2. User Cost
3. Society Cost

The *agency cost* includes all costs related to the owner of the bridge, such as pre-contract costs, construction, operation and maintenance, and disposal.

The *user cost* relates to those costs to the road users, and hence considers any traffic delays caused by the refurbishment/replacement, and any additional vehicle operation costs (from detours ect).

In terms of the *society cost*, this is related to the environmental impact (of the construction methods and materials etc) and any cultural and aesthetic values of the community. This cost was not considered in the analysis.

When performing the life cycle cost analysis, it was assumed the typical lifespan of a bridge with the SUREBridge solution would be 50 years, however a parametric study was also performed to determine the effect how variability in the traffic count, discount rate, life span of the bridge and length of detour would affect the results.

It was found that in all cases, except one, where the lifespan of the refurbishment fell under 20 years and user costs were ignored, the SUREBridge solution was always the most cost effective option (Ricci & Valvo 2018).

## 2.3 Pretensioning of CFRP

A piece-wise pretensioning system was developed by the SUREBridge group for pretensioning the CFRP laminates. In traditional pretensioned CFRP, failure is most commonly due to debonding of the laminate from the beam. With proper anchorage this risk is reduced, however it usually requires quite sizable anchorage systems to be installed which are unattractive and protrude from the silhouette of the bridge structure. With the development of the piece-wise pretensioning system, the need for anchorage is negated.

In traditional pretensioning measures, a force is applied to the end of the CFRP laminates, before it is attached via an epoxy to the base of the concrete beam. This method results in a constant axial force throughout the length of the CFRP, decreasing to zero near the ends of the lamina over a length  $L_{0.conventional}$ . The shear force between the epoxy and the CFRP however increases substantially over this length, causing the failure due to delamination which is commonly seen in reality. Figure 2.2 (a) graphically shows the development of shear and axial force along the length of the CFRP when utilizing the traditional pretensioning method.

The advantage of pretensioning the laminates piece-wise is that the axial force is slowly increased along their length, resulting in much longer transmission length  $L_{0.stepwise}$ . This reduces the amount of shear force along the laminar substantially, removing the risk of delamination failure. Figure 2.2 (b) graphically shows the progression of the axial and shear force when using the step-wise method.

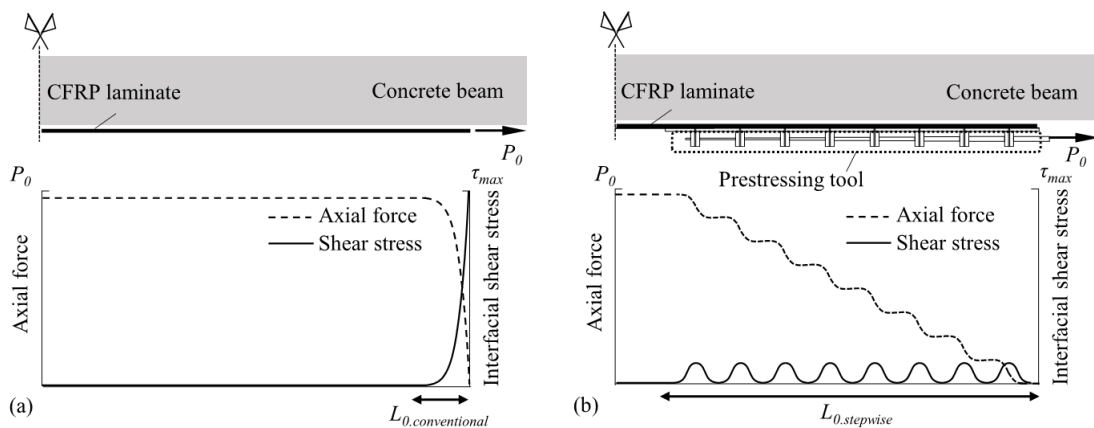
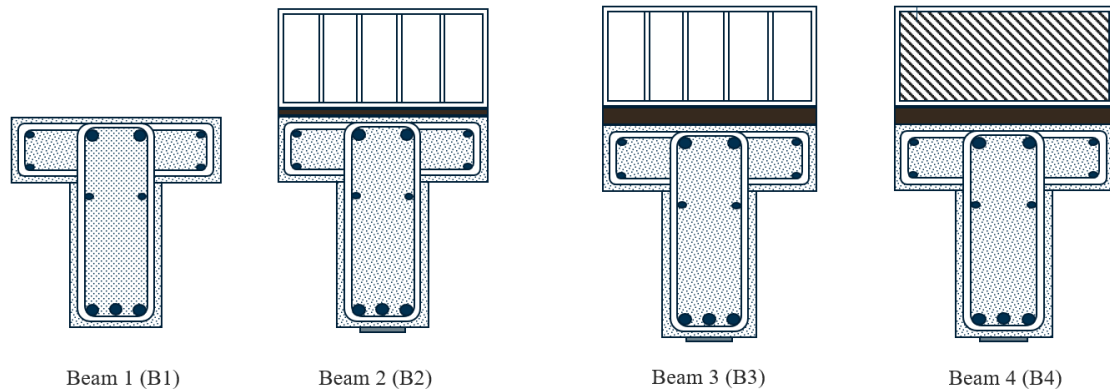


**Figure 2.2:** Axial and Shear stresses in (a) traditional pretensioning methods and (b) using the step-wise pretensioning tool, Jincheng Yang 2019

To obtain the step-wise pretensioning in the CFRP, a special device was developed by the SUREBridge group. It consists of a series of aluminum tabs and steel bars of varying cross sections. The aluminum tabs act as nodes, and between them the steel bars act as springs. Depending on the stiffness of the spring (i.e. the diameter of the bars), the force through the section will change. Therefore, different axial forces are able to be applied to different lengths of the CFRP lamina.

## 2.4 Experimental Verification

Four 6-meter long beams were tested under four-point bending conditions. The first beam was a control beam, whereby no CFRP laminates or GFRP panels were attached. The other three beams tested the full SUREBridge solution, with variations in both the material used to attach the GFRP, and in the orientation of the GFRP panels. A summary of the beams and their variations is detailed below:



- B1 Control beam of reinforced concrete
- B2 SUREBridge Solution, GFRP orientation 1\*, Epoxy\*\*
- B3 SUREBridge Solution, GFRP orientation 1\*, Mortar\*\*
- B4 SUREBridge Solution, GFRP orientation 2\*, Mortar\*\*

Notes:

\*GFRP orientation 1 refers to GFRP panels with webs aligned to the longitudinal axis of the beam (hence loading in the strong direction), whilst GFRP orientation 2 refers to GFRP panels with webs aligned to the transverse axis of the beam (hence loading in the weak direction).

\*\*Two attachment materials were tested between the GFRP and concrete beam; a 10mm thick layer of an epoxy-based adhesive (StoPox SK 41) and a 30 mm thick layer of a low-shrinkage mortar (weber EXM 702).

For all SUREBridge solutions, the CFRP was pretensioned with a force of 100 kN using the step-wise pretensioning method described in section 2.3. Some relaxation of the pretensioning force was observed after the release of the pretensioning system.

Some small cracks were also observed in the concrete beams prior to the application of the SUREBridge solution, which were likely caused by concrete shrinkage.

The exact reinforcement amount is unknown in all beams. From the initial finite element analyses, it became clear that there were notable differences between the experimental results and the results obtained from the FE analyses. From some hand-calculations, it became clear that one of the layers of longitudinal reinforcement bars was not present in the beams. Without breaking apart the beams (which are no longer at the university), it is impossible to confirm the exact reinforcement amount.

### 2.4.1 Material Properties

Table 2.1 summarizes the material properties and geometries of the concrete beam, CFRP, mortar and epoxy used in testing. The properties of the GFRP can be specified in several ways (per component, globally, or equivalent section), hence the properties related to the GFRP tested in the laboratory will be specified in each of these ways in section 3.4. The dimensions of the GFRP panels also vary, both between the laboratory tests, but according to the method of specification of the properties. Therefore, the dimensions of the GFRP panels are detailed in section 5.1.

<b>Concrete C35/45</b>			
Age on the testing day		148	days
Compressive Strength on testing day	$\sigma_{cm}$	49.5	[MPa]
Tensile Strength on testing day	$\sigma_{tm}$	3.5	[MPa]
Modulus of Elasticity on testing day	$E$	36.5	[GPa]
Poisson's ratio	$\nu$	0.2	[-]
<b>Steel Rebar <math>\phi 8</math> B500B</b>			
Diameter of reinforcement bars	d	8	[mm]
Elastic Modulus (mean)	E	202	[GPa]
Yield Stress (mean)	$\sigma_{s.y}$	541	[MPa]
Ultimate Tensile stress (mean)	$\sigma_{s.u.t}$	668	[MPa]
Ultimate Tensile strain (mean)	$\epsilon_{s.u.t}$	0.0668	[-]
Poisson's ratio	$\nu$	0.3	[-]
<b>Steel Rebar <math>\phi 16</math> B500B</b>			
Diameter of reinforcement bars	d	16	[mm]
Elastic Modulus (mean)	E	197.6	[GPa]
Yield Stress (mean)	$\sigma_{s.y}$	580	[MPa]
Ultimate Tensile stress (mean)	$\sigma_{s.u.t}$	673.8	[MPa]
Ultimate Tensile strain (mean)	$\epsilon_{s.u.t}$	0.0706	[-]
Poisson's ratio	$\nu$	0.3	[-]
<b>CFRP</b>			
Dimension	b x t	81.98 x 1.45	[mm x mm]
Tensile Elastic Modulus	E	214	[GPa]
Ultimate Tensile Strain	$\epsilon_u$	0.0127	[-]
<b>Epoxy Sto SK 41</b>			
Thickness of layer (CFRP)	t	1.45	[mm]
Thickness of layer (GFRP)	t	10	[mm]
Elastic Modulus	E	7.1	[GPa]
Tensile Strength	$\sigma_{e.u.t}$	34	[MPa]
Poisson's Ratio	$\nu$	0.3	[-]
<b>Mortar Weber 702</b>			
Thickness of layer	t	30	[mm]

**Table 2.1:** Material Properties from the experimental tests

## 2.4.2 Loading

The beams were tested under the four-point bending configuration shown in figure 2.3. Two loading jacks were used with displacement control.

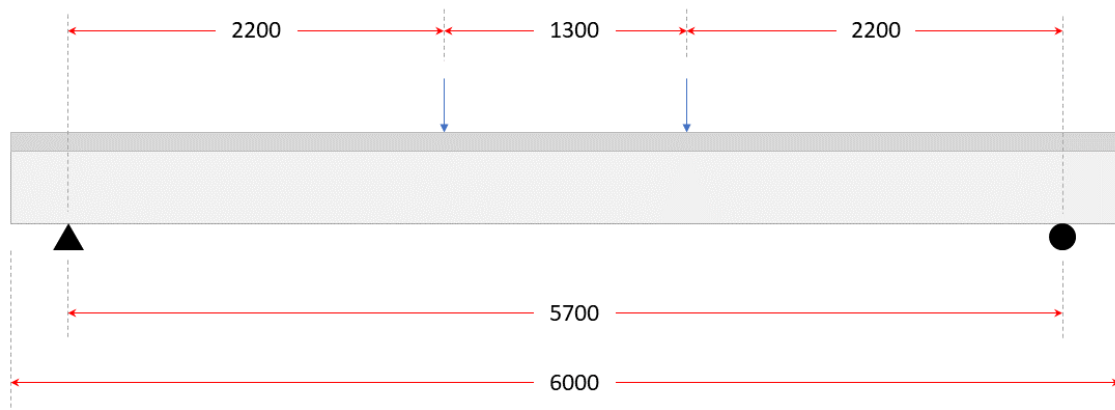


**Figure 2.3:** Location of the Load application

## 2.4.3 Results

Through four-point bending tests of a number of t-section beams, it was found that with their proposed strengthening solution, the ultimate load bearing capacity could be increased by up to 160%. Furthermore, the cracking loads were increased compared to an unstrengthened beam, as was the flexural strength. Following the failure of the CFRP laminar, but before ultimate failure of the beam ductile behaviour was observed. They determined that due to the addition of the GFRP panels, the neutral axis of the beam had moved, hence some of the steel reinforcement which was originally in compression was now under tension. This provided additional capacity to the bridge deck.

### 2.4.3.1 Failure Mechanisms

It should be emphasized that none of the four beams tested in the laboratory failed. It was deemed that further testing of the beams would be unsafe.

For beams 2 - 4, failure occurred for the CFRP laminates at approximately half-way through loading. The laminates themselves did not fail, rather a layer of concrete was peeled off of the beams with the CFRP still attached. This can be seen in figure 2.4. Loading did continue after this failure.



**Figure 2.4:** CFRP Failure in the Laboratory

Capturing this failure behaviour will be difficult to achieve through FE modelling, and hence it is proposed that the analysis of beams 2 - 4 is broken down into two models. The first of the models will replicate the entire beam with the attached pretensioned CFRP, whilst the second will model the beam with no CFRP.

As strain gauges were attached to the surface of the CFRP in the laboratory, it is known at what strain the CFRP failed, and hence when the first beam model will reach "failure". These levels of strain are displayed in table 2.2.

	<b>Beam 2</b>	<b>Beam 3</b>	<b>Beam 4</b>
$\epsilon_{f.mean}[\%]$	1.087	1.094	1.036

**Table 2.2:** Delamination Strain in CFRP from the laboratory

Load-deflection results, maximum crack sizes and crack patterns were all recorded from all four beams in the laboratory. These will be used to validate the finite element models.

## 2.5 Earlier Finite Element Models

An earlier set of laboratory experiments performed by the SUREBridge group tested the strengthening effect which the application of step-wise pretensioned CFRP laminates would have on rectangular reinforced concrete beams. For this set of experiments, a matching numerical model was developed in the finite element software ABAQUS. It was able to capture the load-deflection results well, however the crack pattern and maximum crack size was unable to be determined with accuracy. This is likely due to the assumption of perfect bond between the concrete and steel, which was made.

Due to the similarity of the experiments, a summary of the recommendations resulting from this model is provided.

### 2.5.1 Recommendations

From this finite element analysis, there are a number of recommendations made by Jincheng Yang which may be of assistance in the finite analysis which will be performed in this thesis. Namely;

- Smear length: recommended value 100mm for embedded reinforcement
- Mesh size: 25 x 25 mm
- Viscosity parameter for concrete:  $10^{-4}$
- Dilation angle for concrete:  $30^\circ$

Additionally, the finite element models were provided by Jincheng Yang, for reference in developing the models for this thesis.

# 3

## Mechanical Properties of Materials

### 3.1 Concrete Behaviour

Concrete is a non-homogeneous material which is made from a mix of cement, water and aggregates. In modern design, admixtures and additions are often added to the mix as well. Each of these components can influence the properties of the concrete at different stages of its life cycle, from curing to its behaviour under loading. Depending on which components are included, and what proportions, the properties of concrete can change.

#### 3.1.1 General Properties

Due to large variations in composition, different concrete samples can possess distinctly individual properties. However, with the introduction of the concrete compressive classes, it is possible to identify the properties associated with a given concrete if the density and compressive strength is known.

Different concrete compressive classes exist for different density concretes, therefore it is important to first determine the density of the sample. There are three classifications of density which a concrete can fall under (Fib 2013):

- Light weight; with density between 800 to 2000  $\text{kg}/\text{m}^3$ ,
- Normal weight; density between 2000 to 2600  $\text{kg}/\text{m}^3$ ,
- Heavy weight, density over 2600  $\text{kg}/\text{m}^3$ .

Once the density of the concrete is known, the compressive strength of a cylindrical or cube sample can be determined through testing according to ISO 1920-3.

This procedure was performed for the SUREBridge concrete samples, and the concrete used in the testing was determined to be a normal weight concrete, compressive strength class C35/45. The properties for this class is shown in table 3.1, according to Eurocode 2, for 28-day old concrete.

Density ( $\rho$ )	2330 $kg/m^3$
Poisson's ratio ( $\nu$ )	0.20
Young's Modulus ( $E_{ci.28d}$ )	34 GPa
Characteristic Compressive Strength ( $f_{ck.28d}$ )	35 MPa
Mean Compressive Strength ( $f_{cm.28d}$ )	43 MPa
Mean Tensile Strength ( $f_{ctm.28d}$ )	3.2 MPa

**Table 3.1:** Material Properties for 28 day Concrete, grade C35/45

#### 3.1.1.1 Factors Affecting Strength and Ductility

There are several factors which affect the properties of concrete, including age, creep and shrinkage, temperature and the type of loading (cyclic or non-static), among others (Fib 2013). As stated in section 1.5, only the effect of age on the beam will be considered in the analysis.

Age will affect both the tensile and compressive strength of the concrete, as well as the Young's modulus. This is due to the continuous reaction (hydration) between the cement and water in the concrete, at a decreasing rate in time. The properties listed in table 3.1 refer to the 28 day properties of C35/45 concrete. Multiplying the strength and elasticity by an age factor ( $\beta_{cc}(t)$ ) will take into account the changing properties in time, enabling for an accurate estimation of the properties associated with the 148 day old concrete used in the SUREBridge project. The age factor is calculated according to equation 3.1 (Fib 2013), as a function of time.

$$\beta_{cc}(t) = \exp\left(s \cdot \left[1 - \left(\frac{28}{t}\right)^{0.5}\right]\right) \quad (3.1)$$

Where:  $s = 0.25$  for 42.5 N concrete

At 148 days, the age factor is calculated to be 1.152.

### 3.1.2 Compressive Response

According to Fib (2013), concrete loaded under short-term, uniaxial compression exhibits the stress-strain relationship which is displayed in figure 3.1.

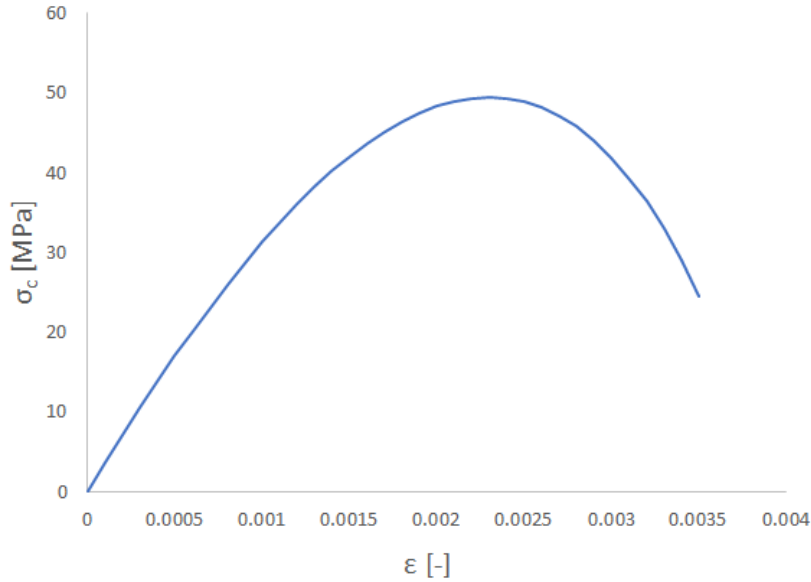


**Figure 3.1:** Stress Strain relationship for concrete under compression

Equation 3.2 defines this curve mathematically (Fib 2013).

$$\sigma_c = -f_{cm} \cdot \left( \frac{k \cdot \eta - \eta^2}{1 + (k - 2) \cdot \eta} \right) \quad \text{for } |\epsilon_c| < |\epsilon_{c.lim}| \quad (3.2)$$

Where:

$$k = E_{ci} / E_{c1};$$

$$\eta = \epsilon_c / \epsilon_{c1};$$

$$E_{c1} = f_{cm} / \epsilon_{c1}$$

For concrete C35/45, the yield ( $\epsilon_{c1}$ ) and ultimate ( $\epsilon_{c.lim}$ ) strains are as follows (Fib 2013);

$$\epsilon_{c1} = 0.0023;$$

$$\epsilon_{c.lim} = 0.0035;$$

which allows for the full concrete response curve to be defined.

### 3.1.3 Tensile Response

As a brittle material, concrete fails at low tensile stresses. The tensile response is easiest to understand by separating the reaction into two phases; pre-cracking, and post-cracking behaviour. Pre-cracking behaviour can be described by a bi-linear relationship, between stress and strain. Post-cracking response is best described as a relationship between stress and crack width size.

#### 3.1.3.1 Pre-crack Behaviour

The stress-strain relationship of concrete under tension, pre-cracking, is displayed in figure 3.2 (Fib 2013).

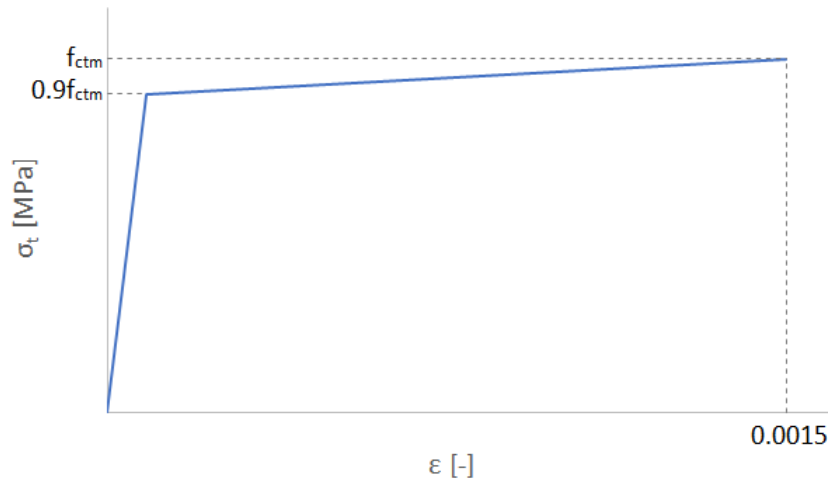


**Figure 3.2:** Stress Strain relationship for concrete under tension

Equations 3.3 and 3.4 describe this bi-linear behaviour (Fib 2013).

$$\sigma_{ct} = E_{ci} \cdot \epsilon_{ct} \quad \text{for} \quad \sigma_{ct} \leq 0.9 \cdot f_{ctm} \quad (3.3)$$

$$\sigma_{ct} = f_{ctm} \cdot \left( 1 - 0.1 \cdot \frac{0.00015 - \epsilon_{ct}}{0.00015 - 0.9 \cdot f_{ctm}/E_{ci}} \right) \quad \text{for} \quad 0.9 \cdot f_{ctm} < \sigma_{ct} \leq f_{ctm} \quad (3.4)$$

At 90% of the tensile strength, small micro cracks begin to form at the fracture zone, reducing the elasticity of the material, resulting in the bi-linear behaviour described above. The fracture zone is the location whereby a crack will eventually form from the growth of the micro cracks.

This relationship is sometimes simplified to a linear relationship, ignoring the slight change in elasticity for this small zone which eventually forms a crack. This linear relationship is described by equation 3.5.

$$\epsilon_{ct,max} = \frac{f_{ctm}}{E_{ci}} \quad (3.5)$$

However, for the fracture zone, a yield strain of 0.00015 should be assumed (Fib 2013).

### 3.1.3.2 Post-crack behaviour

Once a crack exists, the post-cracking behaviour in the fracture zone can be described by a relationship between stress and crack width size. This relationship is shown in figure 3.3, whilst equations 3.6 and 3.7 describe this relationship mathematically (Fib 2013).

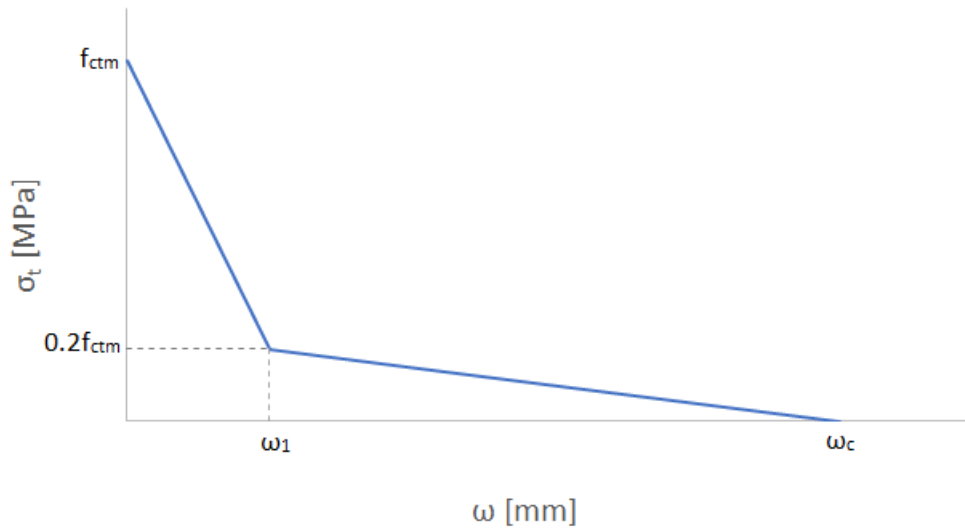


**Figure 3.3:** Stress ( $\sigma_t$ ) - crack opening ( $\omega$ ) relationship for concrete under tension

$$\sigma_{ct} = f_{ctm} \cdot \left(1.0 - 0.8 \cdot \frac{\omega}{\omega_1}\right) \quad \text{for } \omega \leq \omega_1 \quad (3.6)$$

$$\sigma_{ct} = f_{ctm} \cdot \left(0.25 - 0.05 \cdot \frac{\omega}{\omega_1}\right) \quad \text{for } \omega_1 < \omega \leq \omega_c \quad (3.7)$$

Where:

- $\omega$  is the crack opening [mm]
- $\omega_1$  is the crack size when  $\sigma_{ct} = 0.2 \cdot f_{ctm}$ ; calculated according to eqn 3.8
- $\omega_c$  is the crack size when  $\omega_{ct} = 0$ ; calculated according to eqn 3.9
- $f_{ctm}$  is the mean tensile strength [MPa]
- $G_F$  is the fracture energy, discussed in 3.1.3.3

$$\omega_1 = \frac{G_F}{f_{ctm}} \quad (3.8)$$

$$\omega_c = 5 \cdot \frac{G_F}{f_{ctm}} \quad (3.9)$$

#### 3.1.3.3 Fracture Energy

The fracture energy can be calculated according to equation 3.10 (Fib 2013). It describes the amount of energy needed to propagate a tensile crack of unit area.

$$G_F = 73 \cdot f_{cm}^{0.18} \quad (3.10)$$

Where:

$f_{cm}$  = Mean compressive strength [MPa]

## 3.2 Steel Behaviour

Due to the low tensile strength of concrete, steel reinforcement bars are commonly placed in the tensile zone of concrete beams, to increase the overall load bearing capacity. They have a higher tensile strength than concrete, and it is this feature, paired with their ductility, which makes them well suited to this placement.

In the SUREBridge project, B500B steel reinforcement bars are utilized for both the longitudinal reinforcement and the stirrups, with a diameter of either 8 or 16mm. The properties related to these bars was determined according to the testing procedure of ISO 15630 Part 1, and is displayed in table 3.2.

Properties (mean)	$\phi 16mm$	$\phi 8mm$
Poisson's ratio ( $\nu$ )	0.3	0.3
Young's Modulus ( $E_{mean}$ )	197.6 GPa	202 GPa
Yield Strength ( $\sigma_y$ )	580 MPa	541 MPa
Ultimate strength ( $\sigma_u$ )	673.8 MPa	668 MPa
Ultimate strain ( $\epsilon_u$ )	7.06%	6.68%

**Table 3.2:** Material Properties for B500B Steel; 16mm and 8mm diameter

Figure 3.4 compares the stress-strain relationships for the 8 and 16mm bars, which was obtained from testing.

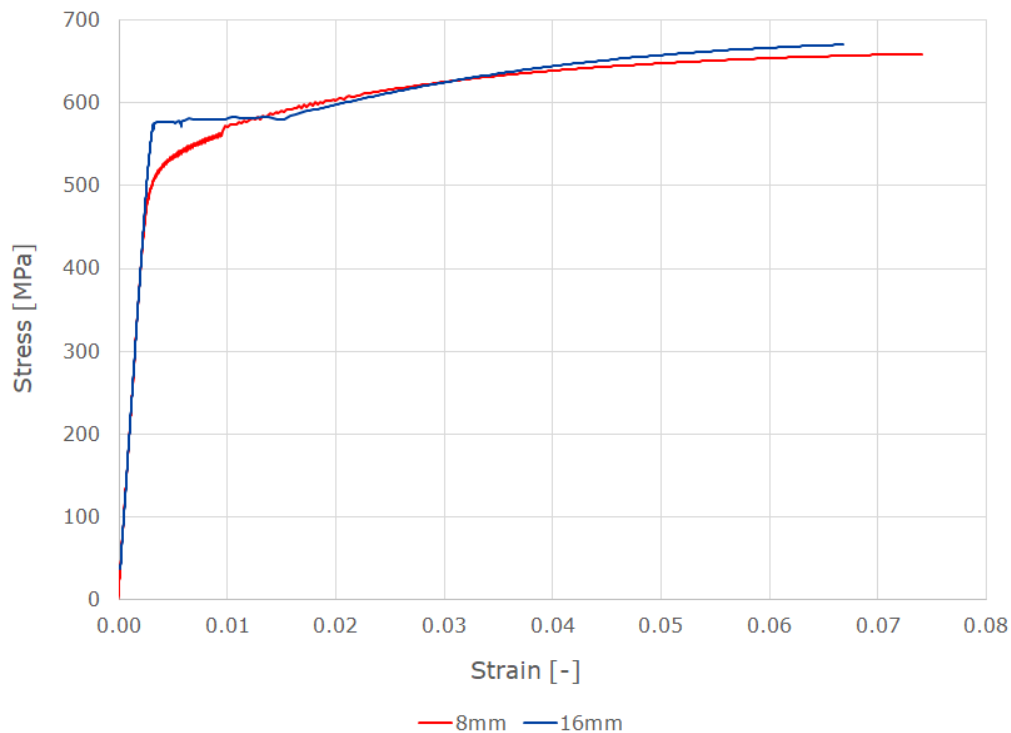


**Figure 3.4:** Stress-Strain relationship for 8 and 16mm diameter rebar

The stress-strain relationship of reinforcing steel can be decomposed into three sections; linear elastic (prior to yielding), yield plateau (at yield stress) and strain hardening (after yield stress). For both the 8mm and 16mm bars, the linear elastic response prior to yielding is approximately the same. The 8mm bars yield at a lower stress than the 16mm bars and display no yield plateau, rather they immediately progress to strain hardening behaviour. The 16mm bars however have a very pronounced yield plateau, whereby the strain increases with little change to the stress. Following this, strain hardening is also observed. Strain hardening is characterized as increasing levels of strain, at increasing levels of stress, at a decreasing rate, until failure.

It is important to note that the stress-strain relationships in figure 3.4 show the nominal stress-strain relationships for the 16 and 8mm bars respectively, not the true stress. The true stress in the section is always higher than the nominal, as it takes into account the decreasing cross-section throughout loading (i.e.  $A < A_0$ ).

The nominal stress is calculated according to equation 3.11, whilst the true stress is calculated according to equation 3.12.

$$\sigma_{nominal} = \frac{F}{A_0} \quad (3.11)$$

$$\sigma_{true} = \frac{F}{A} < \sigma_{nominal} \quad (3.12)$$

To find the true stress and strain values, equations 3.13 and 3.14 can be used.

$$\sigma_{true} = \sigma_{nominal} * (1 + \epsilon_{nominal}) \quad (3.13)$$

$$\epsilon_{true} = \ln(1 + \epsilon_{nominal}) \quad (3.14)$$

Figure 3.5 shows how the stress-strain curves can change depending on whether the true or nominal stress-strains are utilized, for the 16mm diameter bar.

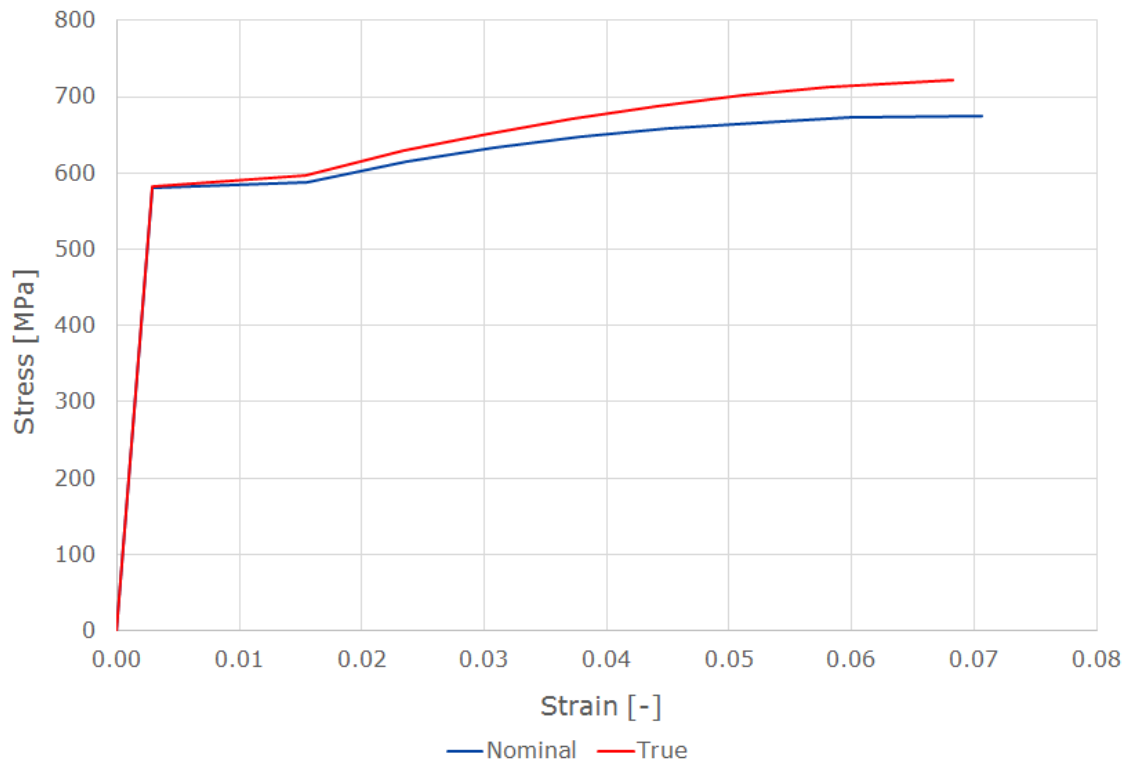


**Figure 3.5:** Stress strain curve of 16 mm rebar (True vs Nominal)

For the finite element analyses, only the nominal stress is input.

### 3.3 CFRP Behaviour

Carbon fibre reinforced polymer (CFRP) is a relatively new reinforcing material, which has a high strength and stiffness compared with its weight. It is most prominently used in strengthening structures, however, unlike steel and concrete, it has yet to be included in the Eurocode (Täljsten, B., Blanksvärd, T. and Sas 2016).

CFRP is a composite material composed of carbon fibres surrounded by a matrix. The fibres provide the greatest contribution to axial stiffness and strength, and hence govern the behaviour depending on their arrangement and orientation (Zoghi 2013). As such, CFRP is considered an anisotropic material, which behaves linear elastically until brittle failure (Täljsten, B., Blanksvärd, T. and Sas 2016)

#### 3.3.1 Elastic Response

The CFRP utilized in the SUREBridge beams is StoFRP Plate IM 80 C. The material properties related to the CFRP was determined through coupon testing, according to the testing standard of ASTM D 3039. They are displayed in table 3.3.

Properties (mean)	
Young's Modulus ( $E$ )	214 GPa
Ultimate Tensile Strength ( $f_u$ )	2718 MPa
Ultimate strain ( $\epsilon_u$ )	1.27%

**Table 3.3:** Material Properties of CFRP, determined from testing

Figure 3.6 shows the stress-strain relationship of the CFRP when loaded tension in the main fibre direction.

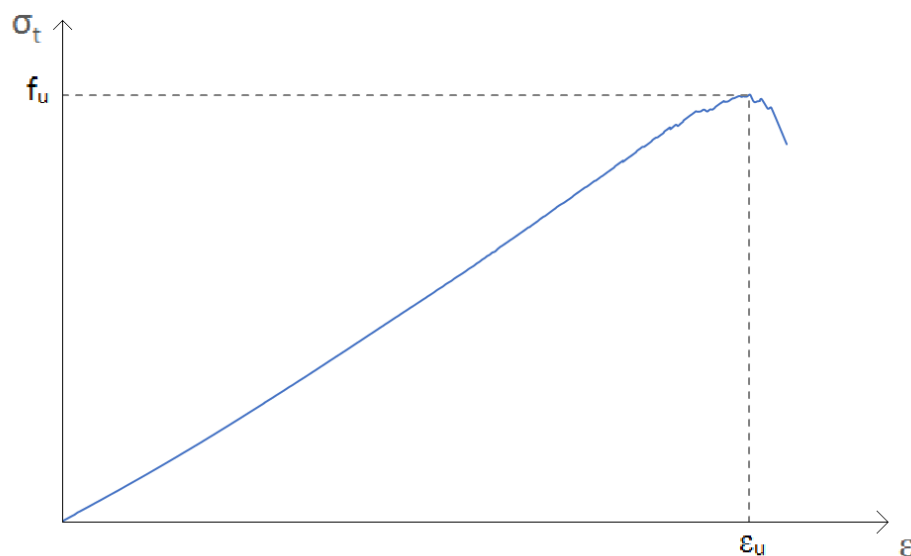


**Figure 3.6:** Stress-Strain relationship for CFRP

As observed in figure 3.6, CFRP behaves linear elastically until fibre failure occurs. This failure is characterized as brittle, due to the immediate loss of strength. It should be noted that the slight non-linearity of the response near ultimate strength is due to the progressive failure of different lamina (Ditcher & Webber 1981), not due to yielding.

#### 3.3.2 Failure Mechanisms

There are six failure modes associated with externally bonded CFRP (Chen & Teng (2001)). They are:

- Concrete failure;
- Tensile failure (fibre rupture);
- Adhesive failure (between the CFRP and Concrete beam);
- Delamination (for FRP-to-concrete joints);
- Concrete-adhesive interface failure; and
- FRP-adhesive interface failure.

From a review of 55 single and double shear tests, Chen & Teng (2001) found that concrete failure, at the level just a few millimeters above the concrete-adhesive interface, was the most common failure mode. Failure in the concrete-adhesive or FRP-adhesive interfaces was not found in their review, nor failure in the adhesive (Chen & Teng 2001). They concluded that these three failure mechanisms are rarely observed due to the availability of strong adhesives (Chen & Teng 2001).

In the SUREBridge beams, the failure method which was observed is concrete failure. As this is related to the stress in the concrete at this level, and not a failure related to the CFRP material properties, no input of the ultimate strain is needed.

### 3.4 GFRP Behaviour

Glass fibre reinforced polymer (GFRP) is a relatively new reinforcement material, which boasts a high strength to weight ratio. Among all types of glass fibers, electrical grade (E) glass, strength grade (S) glass and alkali resistant (AR) glass are used heavily in the industry for structural reinforcement. Out of the three, E-glass is more predominant due to its lower cost (Wallenberger, F.T and Bingham, P.A. 2010). Coincidentally, this was the class of fibre utilized in the GFRP panels for the SUREBridge solution.

Similarly to CFRP, GFRP is also a composite material. The deck panels which were used in lab test were composed of E-glass fibres surrounded by a polyester matrix. The strength and elasticity of the material depends greatly on the orientation and arrangement of the fibres. Hence, it is considered to be anisotropic in nature.

In the SUREBridge project, sandwich panels made from GFRP were used to strengthen reinforced concrete beams. The sandwich panels were produced by the company FiberCore Europe, and were designed to be resistant to skin-core debonding failure. A typical panel is displayed in figure 3.7 , with the main components labelled.

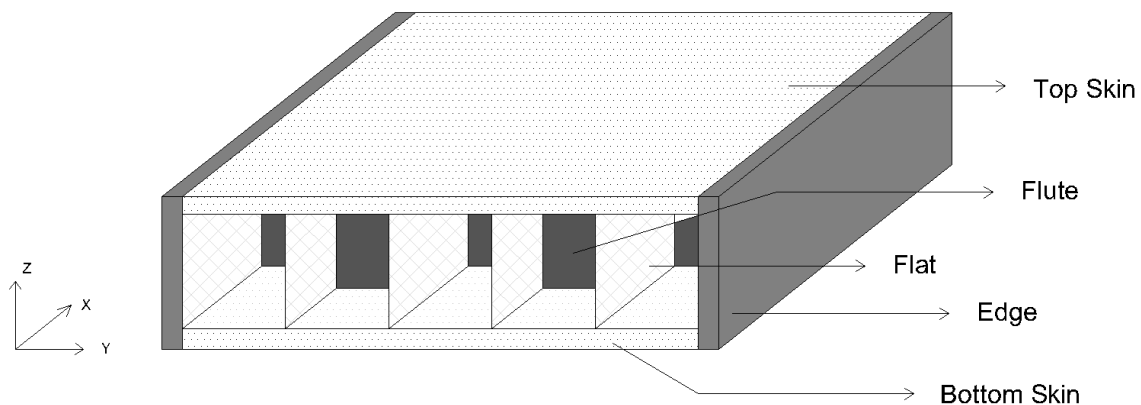


**Figure 3.7:** GFRP Cross Section, with main components labelled

Whilst not shown in figure 3.7, the voids between the different components are filled with polyurethane foam, which is a non-structural component. The main fibre direction of the edges, top and bottom skins is displayed in figure 3.8.

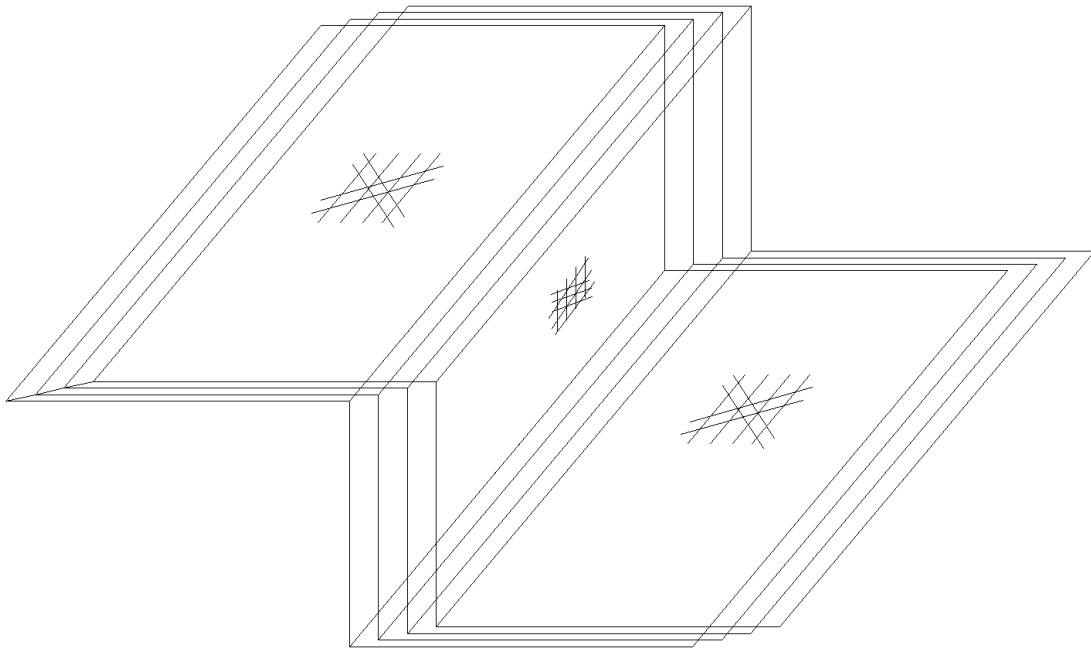


**Figure 3.8:** Fiber direction in GFRP deck panel

### 3.4.1 Elastic Behaviour

Similarly to CFRP, GFRP exhibits linear elastic behaviour until brittle failure. However, compared to CFRP, it displays a more ductile response and has a much lower tensile strength.

There currently is no Eurocode standard governing its use, and no standardized test to determine its axial compressive strength (Zhou et al. 2018).

There are three possible ways to define the mechanical properties of GFRP:

1. According to each component;
2. Assuming an equivalent section of a web and two flanges; or
3. Assuming equivalent properties.

#### 3.4.1.1 Component Based

The first approach decomposes the sandwich deck into its various components (which were detailed in figure 3.7) and measures the mechanical properties of each. The supplier has provided these properties, which are listed in table 3.4.

Properties	Skin	Edge	Flat	Flute
Young's Modulus along x ( $E_x$ )	32 GPa	21 GPa	12 GPa	9.12 GPa
Young's Modulus along y ( $E_y$ )	17 GPa	21 GPa	12 GPa	9.12 GPa
Young's Modulus along z ( $E_z$ )	10 GPa	10 GPa	6 GPa	5.69 GPa
Shear Modulus along xy plane ( $G_{xy}$ )	6 GPa	9 GPa	5 GPa	6.08 GPa
Shear Modulus along yz or xz plane ( $G_{yz} = G_{xz}$ )	7 GPa	8 GPa	4.5 GPa	3.5 GPa
Poisson's ratio along xy plane	0.22	0.29	0.31	0.45
Poisson's ratio along yz or xz plane	0.27	0.27	0.31	0.31

**Table 3.4:** Material Properties for GFRP panel per component

It is important to note that the axis definition provided in table 3.4 are according to the coordinate system provided in figure 3.7.

Whilst these properties are a direct representation of reality, they are unable to be used in the modelling of the sandwich deck in 2D. This is because some assumptions need to be made to reduce the 3D model into a 2D model.

### 3.4.1.2 Equivalent Web Core

The second approach smears the properties of the edges, flutes and flats into an equivalent web core, as displayed in figure 3.9.

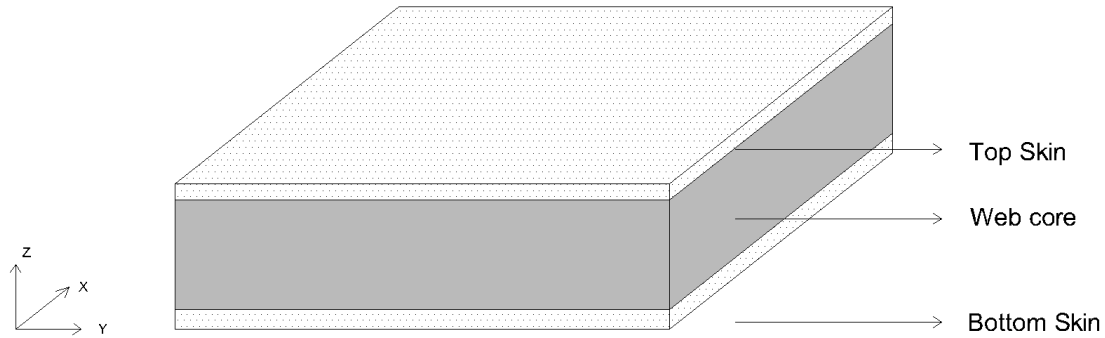


**Figure 3.9:** GFRP cross section with an equivalent web core

The properties of this equivalent section have been provided by the supplier and are listed in table 3.5.

Properties	Skin	Web core
Young's Modulus along x ( $E_x$ )	32 GPa	0.7 GPa
Young's Modulus along y ( $E_y$ )	17 GPa	0.15 GPa
Young's Modulus along z ( $E_z$ )	10 GPa	0.85 GPa
Shear Modulus along xy plane ( $G_{xy}$ )	6 GPa	0.1 GPa
Shear Modulus along yz plane ( $G_{yz}$ )	7 GPa	0.1 GPa
Shear Modulus along xz plane ( $G_{xz}$ )	7 GPa	0.29 GPa
Poisson's ratio along xy plane	0.22	0.22
Poisson's ratio along yx plane	0.12	0.12
Poisson's ratio along xz or yz plane	0.27	0.27

**Table 3.5:** Material Properties for GFRP panel with an equivalent core

This approach is more feasible to integrate in a 2D model than the first approach, whilst still keeping some definition of the changing elasticity across the section.

### 3.4.1.3 Equivalent Properties

The third approach considers only the flats (webs) and the top and bottom skins in the cross section. The material properties of these sections is considered to be constant, and hence global stiffness values are calculated for the two orientations.

Four 3-meter long, 0.5m wide GFRP panels were tested through three-point bending tests, to determine the load-displacement responses of the cross section in the two orientations (webs aligned to the longitudinal direction, and webs aligned to the transverse direction). The results are displayed in 3.10.

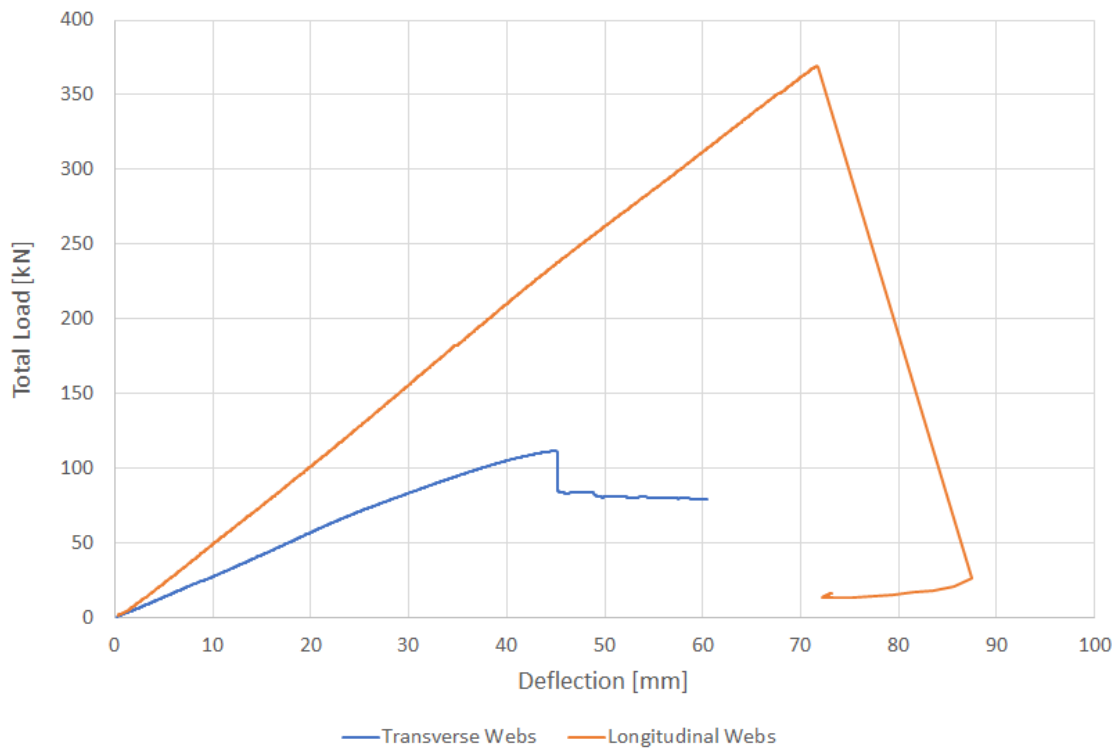


**Figure 3.10:** Load-deflection relationship from 3-point bending test

From these results, the global properties of the section was calculated, with the results displayed in table 3.6.

Properties	
Young's Modulus in longitudinal direction ( $E_{11}$ )	29 GPa
Young's Modulus in transverse direction ( $E_{22}$ )	15 GPa
Deformation stiffness in longitudinal direction	5.3 kN/mm
Deformation stiffness in transverse direction	2.8 kN/mm

**Table 3.6:** Material Properties for GFRP, with equivalent properties

### 3.4.2 Failure Mechanisms

There are several failure mechanisms possible for GFRP sandwich panels (de Almeida & M. 2009), such as:

- Tensile failure of the skin
- Buckling failure
- Inter-cellular buckling failure
- Wrinkling failure
- Core shear failure
- Crushing failure of the skin and core
- Failure in the epoxy joining the core and skins

In the SUREBridge beams which were tested in the laboratory, loading was stopped prior to any failure mechanism developing in the GFRP sandwich decks. Therefore, no failure mechanism needs to be accounted for in the modelling of the GFRP panels.

### 3.5 Mortar

Connecting the GFRP sandwich panels to the concrete beams for beams 3 and 4 in the laboratory tests, is a 30mm thick layer of mortar. This mortar is weber EXM 702.

The material properties for this mortar were provided by the supplier, and are listed in table 3.7.

Properties	
Young's Modulus ( $E_{mean}$ )*	36500 MPa
Compressive strength, 1 day (according to SS-EN 196-1)	>30 MPa
Compressive strength, 28 day (according to SS-EN 196-1)	>60 MPa
Poisson's ratio ( $\nu$ )	0.2

**Table 3.7:** Material Properties for weber EXM 702 Mortar

\*Note: The elasticity of the mortar was not provided by the supplier. The elasticity is assumed to be approximately the same as the concrete used in the beam.

### 3.6 Epoxy

Connecting the GFRP sandwich panels to the concrete beam for beam 1 in the laboratory testing, is a 10mm thick layer of epoxy. This epoxy was also used for beams 2 - 4 to connect the CFRP laminates to the beam. The epoxy is StoPox SK 41.

As per the supplier, the epoxy meets the conditions of EN 1504-4, and is intended for the adhesion of either FRP or steel to concrete (Sto Scandinavia AB 2019).

The material properties for this material were provided by the supplier, and are listed in table 3.8

Properties	
Young's Modulus ( $E_{mean}$ )	7100 MPa
Tensile Strength ( $f_{mean}$ )	1.5 MPa
Poisson's ratio ( $\nu$ )	0.3

**Table 3.8:** Material Properties for StoPox SK 41 Epoxy

# 4

## Material Modelling

There are several approaches which can be used to model the behaviour of different materials in finite element programs. Depending on the response the user intends to capture and the limitations within the software, different models may be more or less appropriate for use under certain circumstances.

Two commercial finite element analysis programs will be used to model the SURE-Bridge solution; DIANA and ABAQUS. For both, there exists several models which capture different material responses, and hence require different input data. A review of the available literature on these models is presented in this chapter, with a focus on the theory behind each approach, the recommended model inputs and a discussion into whether it would capture the desired response for this situation. For some of the inputs, there is no clearly defined value which should be selected, so in these cases a sensitivity analysis will be performed in section 6 to find the most appropriate value to use in order to match the experimental results.

### 4.1 Concrete Material Models

As discussed in section 3, concrete behaviour changes once cracked. Prior to cracking, the relationship between stress and strain is purely linear-elastic, however after cracking, the response becomes non-linear and plastic. When replicating this response in finite element software, the two states are handled separately. The pre-cracked beam is modelled solely using the elastic model, whilst the cracked beam is modelled using one of several plastic models available.

This section will first briefly discuss the elastic response and how it can be included in the software, before touching on the plastic response. To provide some orientation for how the cracked behaviour is modelled by the different plastic material models, some background information on the different crack approaches will first be provided. Then two material models, one from DIANA and one from ABAQUS will be presented, with a discussion on the behaviour they seek to replicate and the appropriate material inputs required.

From ABAQUS, the concrete damaged plasticity model is used, as it simulates the cracking behaviour of concrete well. From DIANA, the total strain crack model is selected.

### 4.1.1 Linear Elastic Model

One of the simplest material models to define is the linear elastic model, where the stiffness of the beam is assumed to be constant throughout loading. The concrete is assumed to be isotropic, that is, the stiffness is the same in all directions. Therefore, only one stiffness property needs to be defined in the finite element software; the Young's Modulus ( $E$ ).

Whilst it is possible to only define the elastic response and ignore the plastic, this assumes that no cracking will take place in the concrete and hence inaccurate results will be obtained past the point the beam would have cracked. As the cracking behaviour and response throughout loading is desired, the elastic response will not solely be specified.

DIANA Input:	Material Module:	Material Editor:	Linear material properties
ABAQUS Input:	Property Module:	Material Editor:	Mechanical: Elasticity: Elastic

### 4.1.2 Fracture Mechanics

When considering the fracture mechanics of brittle materials such as concrete, there are three modes of cracking possible. Mode I cracking describes the opening of a crack due to tensile loading. Mode II describes a sliding crack, due to in-plane shear stresses, and Mode III describes a tearing crack, due to out-of-plane shear stresses.

In both ABAQUS and DIANA, the Rankine criterion is used to detect the presence of cracks based on mode I fracture mechanics. A crack is detected when the maximum principle tensile stress is greater than the tensile stress of the concrete. The formation of this crack will be normal to the direction of the maximum tensile stress detected.

Following the formation of a crack, mode I, II and III fracture mechanics can affect the post-cracking behaviour of the concrete.

Once a crack is detected at a point in the analysis, it remains there. However, it can open and close throughout the analysis.

### 4.1.3 Cracking Approaches

There are three approaches which can be adopted to model the cracking behaviour of concrete; discrete, smeared and embedded. They are shown in figure 4.1.

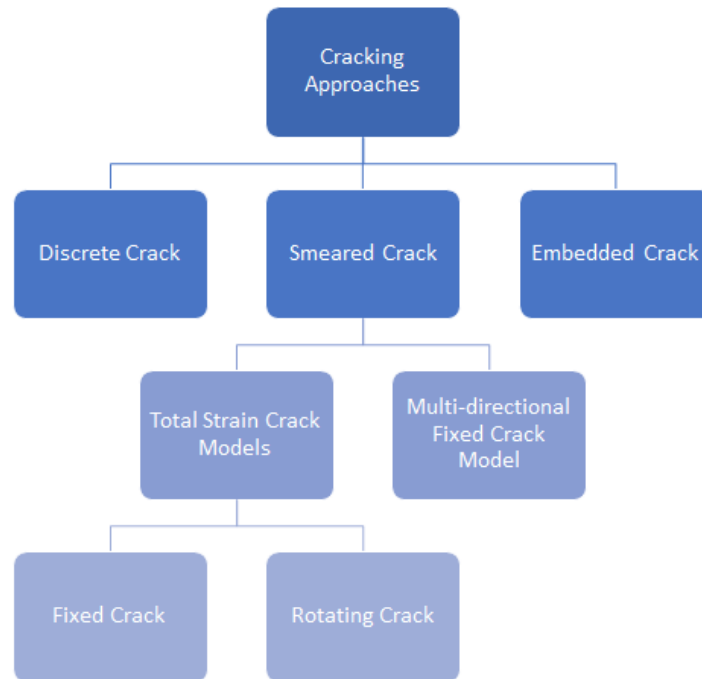


**Figure 4.1:** Different Concrete Cracking Approaches

#### 4.1.3.1 Discrete Crack Approach

The discrete crack approach incorporates discontinuities into the model through the use of separate spring or interface elements, between particular, predetermined concrete elements. The problem with using this method is that the location of the cracks must be known beforehand, to selectively choose where to place these additional elements. However, it does enable the concrete material behaviour to be directly input without any manipulation or adjustments, ensuring the response is preserved. Additionally, by modelling the cracks using these elements it maintains the concept that cracks are discontinuities in the beam, which is exactly the situation in real life.

This method was popular in early modelling approaches (Rots 1989), however as it cannot predict cracking behaviour, it is usually less favoured today than the smeared crack approach. This approach will not be used.

### 4.1.3.2 Smearred Crack Approach

The smeared crack approach is the most common model used for capturing concrete cracking behaviour in finite element software today. Unlike the discrete method which models the cracks as discontinuities, this approach models the cracked concrete as a continuum. This means that rather than including additional elements to model the cracks, adjustments can be made to the concrete material behaviour to reflect both the pre-cracked and post-cracked stages. These adjustments take into consideration the changes in stiffness and stress at cracked locations when analyzing the model.

There are several models which exist under the umbrella term *smeared crack approach*. Such as the standard fixed crack approach, the fixed smeared crack with strain decomposition, the multi-dimensional fixed crack model and the rotating smeared crack approach (Rots 1989). Depending on the software, some or all of these models are available for use. Only the standard fixed and rotating crack models will be explored in depth in this thesis.

#### Fixed Smeared Crack Model

The stress-strain relationship for the fixed smeared crack approach is defined relative to the fixed principle axes of n, s, and t, which are defined as normal to the crack surface (mode I), tangential, in-plane (mode II) and tangential, out-of-plane (mode III) respectively. The relationship in full is as follows (in the 3D plane) (Rots 1989):

$$\begin{bmatrix} \sigma_{nn} \\ \sigma_{ss} \\ \sigma_{tt} \\ \sigma_{ns} \\ \sigma_{st} \\ \sigma_{tn} \end{bmatrix} = \begin{bmatrix} E_{nn} & E_{ns} & E_{nt} & 0 & 0 & 0 \\ E_{ns} & E_{ss} & E_{st} & 0 & 0 & 0 \\ E_{nt} & E_{st} & E_{tt} & 0 & 0 & 0 \\ 0 & 0 & 0 & G_{ns} & 0 & 0 \\ 0 & 0 & 0 & 0 & G_{st} & 0 \\ 0 & 0 & 0 & 0 & 0 & G_{nt} \end{bmatrix} \cdot \begin{bmatrix} \epsilon_{nn} \\ \epsilon_{ss} \\ \epsilon_{tt} \\ \gamma_{ns} \\ \gamma_{st} \\ \gamma_{tn} \end{bmatrix} \quad (4.1)$$

In early formations of this approach,  $E_{nn}$ ,  $E_{ns}$ ,  $E_{nt}$ ,  $G_{ns}$  and  $G_{nt}$  were set to zero, thus causing  $\sigma_{nn}$ ,  $\sigma_{ns}$  and  $\sigma_{tn}$  to be equal to zero once a crack was formed (Rots 1989). In reality, this is not the case - some strength still remains in the material due to interlock of aggregates and gradual debonding at the site of the crack.

Additionally, this approach would result in numerical difficulties in practice. This is because of the sudden change of material definition, from isotropic to an orthotropic once cracking is detected, as well as large discontinuities due to the zero value of  $\sigma_{nn}$ ,  $\sigma_{ns}$  and  $\sigma_{tn}$  (Rots 1989).

Therefore, a new formation was proposed which dealt with both of these issues. An isotropic elasticity was adopted, and the stresses were merely reduced, rather than set to zero. In the 2D plane, the following stress-strain relationship was proposed (Rots 1989):

$$\begin{bmatrix} \Delta\sigma_{nn} \\ \Delta\sigma_{tt} \\ \Delta\sigma_{nt} \end{bmatrix} = \begin{bmatrix} \frac{\mu \cdot E}{1-\nu^2 \cdot \mu} & \frac{\nu \cdot \mu \cdot E}{1-\nu^2 \cdot \mu} & 0 \\ \frac{\nu \cdot \mu \cdot E}{1-\nu^2 \cdot \mu} & \frac{E}{1-\nu^2 \cdot \mu} & 0 \\ 0 & 0 & \frac{\beta \cdot E}{2(1+\nu)} \end{bmatrix} \cdot \begin{bmatrix} \Delta\epsilon_{nn} \\ \Delta\epsilon_{tt} \\ \Delta\gamma_{nt} \end{bmatrix} \quad (4.2)$$

Where:

- $\mu$  is the the reduction factor for the mode I stiffness (negative value)
- $\nu$  is Poisson's Ratio
- $\beta$  is the shear retention factor

### Rotating Smeared Crack Model

Unlike the fixed smeared crack model where the n,s,t axes are aligned to the initial crack formation, the axes of the rotating crack model continually rotate to align to the axes of the principle strain (Rots 1989).

For the fixed crack model, the direction of the cracks is saved in the model, and unless the threshold angle is reached, no new crack will form in that location (Rots 1989). However, for the rotating crack model, their direction is not saved, and hence the crack will rotate through the loading progression, aligned to the principle strain axes. In reality, cracking behaviour exists somewhere between these two approaches.

### Smeared Crack Length

The key concept behind the smeared crack approach is the continuum modelling of the crack within the concrete. The relationship between the stress and crack opening, discussed in section 3.1.3, needs to be converted into a relationship between stress and strain in order to model this relationship in finite element software. To do this, the crack width size is divided by a variable  $l_s$ . This variable is called the smeared crack length, or the crack band width, which is the length at which the cracks are *smeared* along the beam. It assumes the micro-cracks created are smeared over this length, usually the length of an element, so that the whole element will fracture.

Depending on whether a perfect bond is assumed between the concrete and the reinforcement, or whether bond-slip is included, it will have some influence on the value which is recommended to take as the smeared crack length.

For concrete with embedded reinforcement, some authors will recommend taking a value which is related to the size of the mesh, whilst others follow the idea that it is a material property in this case (mesh independent). One of the members of the SUREBridge project, Jincheng Yang, modelled the CFRP strengthened beams discussed in section 2. In his FE analysis in ABAQUS, he found that for a mesh size of 25 x 25 mm, the smeared length of 100mm provided the closest fit to the experimental data, when assuming perfect bond behaviour. Given the similarity in the experiments and the same consistent concrete class, this value should be used

as a starting point when modelling perfect bond. A value similar to the mesh size will also be tested, to determine whether there is any mesh sensitivity involved for this case.

When bond-slip is included in the model, the smeared length which should be taken is related to the size of the elements. In DIANA, the user has the option to call an inbuilt approach called Rots. Depending on whether linear or higher order two-dimensional elements are used, they recommend utilizing either equation 4.3 or 4.4 respectively (Rots 1988).

$$l_s = \sqrt{2 \cdot A} \quad (4.3)$$

$$l_s = \sqrt{A} = l_{el} \quad (4.4)$$

In section 6, a sensitivity analysis will be performed to determine which smeared length is most appropriate to take, to fit the results from the experimental tests.

### 4.1.3.3 Embedded Crack Approach

The last cracking approach, the embedded crack model is a combination of the smeared and discrete crack approaches, where the discontinuity is modelled within the concrete elements themselves. It has the benefits of both of the models, however it is very challenging to model and hence is not available in any commercial FE program. It will not be used for this reason.

#### 4.1.4 Concrete Damaged Plasticity Model (ABAQUS)

The concrete damaged plasticity model is available in ABAQUS and is based on a smeared, rotating crack approach. The core principle behind this approach is that once cracked the elasticity of concrete is forever altered, affecting the slope of the unloading curve (i.e. the elastic stiffness). This degradation is controlled by two damage factors  $d_c$  and  $d_t$ , for concrete crushing (compression) or cracking (tension) respectively. The value of these factors start at zero (for undamaged concrete), to one (full strength loss).

In order to use the concrete damaged plasticity model in ABAQUS, the concrete compressive and tensile curves must be input, as well as the plasticity parameters. Whilst the damage factors are not strictly necessary, they have been included in the analysis in order to provide more control over the concrete behaviour.

##### 4.1.4.1 Compressive Response

The stress-strain relationship for concrete under compression is shown in figure 4.2, along with two unloading paths. The first path ignores any change to the concrete elasticity (gradient of  $E_0$ ), whilst the second represents the response from the damaged plasticity model (gradient of  $(1 - d_c)E_0$ ).

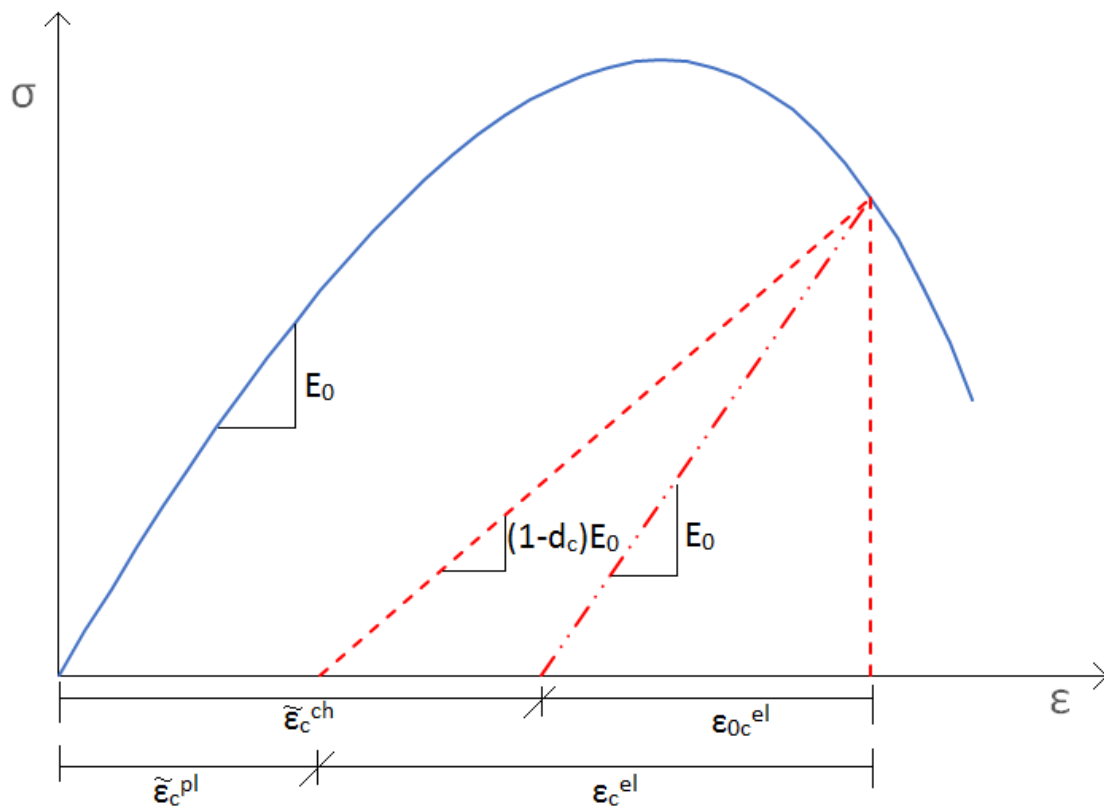


**Figure 4.2:** Concrete Compressive Response, with the effect of the damage factor on elasticity

Up until the point of yielding, concrete under compression will follow an unloading path as defined by the elastic modulus ( $E_0$ ). However, once it reaches this point and begins to deform plastically, the gradient of the unloading path begins to change, becoming  $(1 - d_c)E_0$ . It is important to note that the damage factor is not a set parameter, it changes through the course of the loading, beginning from zero at the point of yield stress.

The stress at each point of the unloading path can be determined with equation 4.5, which relates the stress to the damage factor and the compressive equivalent plastic strain ( $\tilde{\epsilon}_c^{pl}$ ).

$$\sigma_c = (1 - d_c) \cdot E_0 \cdot (\epsilon_c - \tilde{\epsilon}_c^{pl}) \quad (4.5)$$

The effective cohesion stress is given in equation 4.6, which is the stress which determines the size of the yield surface (Abaqus 2010).

$$\bar{\sigma}_c = \frac{\sigma_c}{(1 - d_c)} = E_0 \cdot (\epsilon_c - \tilde{\epsilon}_c^{pl}) \quad (4.6)$$

Inputting this material behaviour in ABAQUS requires for the relationship between compressive stress and inelastic strain to be known, as well as the damage plasticity factors at different levels of inelastic strain ( $\tilde{\epsilon}_c^{in}$ ). The stress-strain relationship defined in section 3.1.2 can be altered to become a stress-plastic strain relationship by removing the elastic portion of the strain from the total strain, as shown in equation 4.7.

$$\tilde{\epsilon}_c^{ch} = \tilde{\epsilon}_c^{in} = \epsilon - \epsilon_{0c}^{el} \quad (4.7)$$

The method to obtain the damage factors for concrete under compression is described in section 4.1.4.3.

ABAQUS Input: Property Module » Material Editor » Mechanical » Concrete Damaged Plasticity » Compressive Behaviour

#### 4.1.4.2 Tensile Response

The tensile response for concrete is characterized by two relationships between stress vs strain, and stress vs crack opening, for uncracked and cracked concrete respectively. They were discussed in detail in section 3.1.3.

To combine them into the single relationship shown in figure 4.3, the stress vs crack opening relationship needs to be converted into a stress vs plastic strain relationship. As the damaged plasticity model is a smeared crack approach, this is possible by smearing the cracks over the smeared crack length. In other words, the crack opening needs to be modified using equation 4.8.

$$\tilde{\epsilon}_t^{ck} = \frac{\omega}{l_s} \quad (4.8)$$

By adding the plastic strain to the elastic strain, it is possible to define the curve shown in figure 4.3. Within the same figure, two unloading paths for concrete under tension is also displayed. The first path assumes that there is no damage done to the elasticity of the concrete (gradient of  $E_0$ ), whilst the second reflects the unloading path for the damage plasticity model (gradient of  $(1 - d_t)E_0$ ).

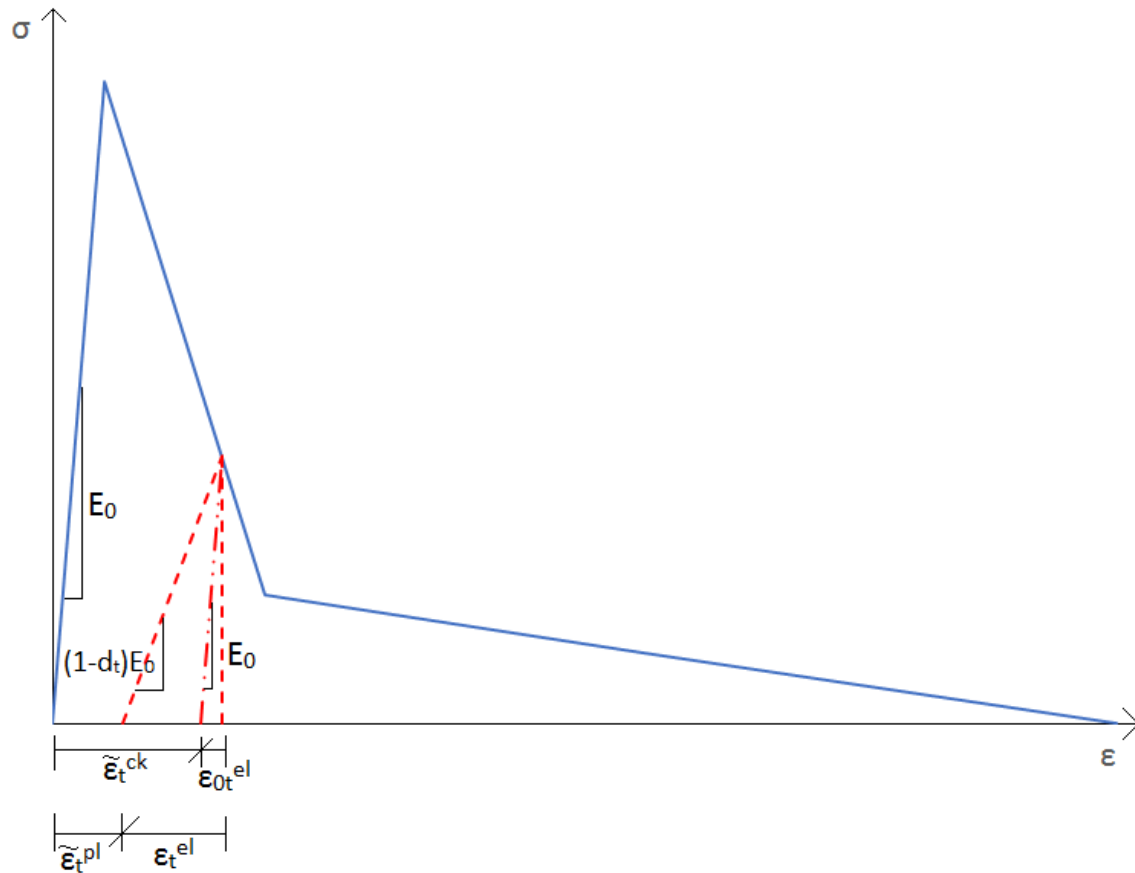


**Figure 4.3:** Concrete Tensile Response, with the effect of the damage factor on elasticity

In a similar way to concrete under compression, the unloading path of concrete prior to yielding follows the elastic modulus ( $E_0$ ). However, once it reaches this point, the elasticity of the beam is affected and the gradient of the unloading path changes to  $(1 - d_t)E_0$ . The damage factor increases from zero after plastic deformation commences, up to a maximum of 1.

The stress at each point of the unloading path can be determined with the help of equation 4.9, which relates the stress to the damage factor and the tensile equivalent strain ( $\tilde{\epsilon}_t^{pl}$ ).

$$\sigma_t = (1 - d_t) \cdot E_0 \cdot (\epsilon_t - \tilde{\epsilon}_t^{pl}) \quad (4.9)$$

The effective cohesion stress is given in equation 4.10, which is the stress which determines the size of the yield surface (Abaqus 2010).

$$\bar{\sigma}_t = \frac{\sigma_t}{(1 - d_t)} = E_0 \cdot (\epsilon_t - \tilde{\epsilon}_t^{pl}) \quad (4.10)$$

Inputting this material behaviour in ABAQUS requires for the definition of the tensile response and the relationship between the damage factors and inelastic strain. There are several ways to input the tensile response curve in ABAQUS, including by strain, displacement or GFI ( $G_F^I$ ). As the relationship between the yield stress and inelastic strain is already known from equation 4.8, this definition is easiest/quickest to use in this case.

The method to obtain the damage factors for concrete under tension is described in section 4.1.4.3.

ABAQUS Input: Property Module » Material Editor » Mechanical » Concrete Damaged Plasticity » Tensile Behaviour » Type: Strain

#### 4.1.4.3 Damage Factors

The damage factors for concrete under tension and compression can be defined by one of the two approaches described below. The two methods of calculating these factors will be compared against each other in section 6, to determine which of the two models is more capable of capturing the material response of concrete, and hence which should be used in subsequent analyses.

##### Method 1

The first approach used to calculate the damage factors is relatively new, and was developed by Alfarah, López-Almansa and Oller. It is somewhat more complicated and time intensive to define than the second approach, however seeks to provide a more accurate, mesh-independent result (Alfarah et al. 2017).

In order to define the damage factors for compression and tension, the material specific coefficients  $a$  and  $b$  must first be defined according to equations 4.11 - 4.14, for both concrete under compression and tension (as indicated by the subscript) (Alfarah et al. 2017).

$$a_c = 2 \cdot (f_{cm}/f_{c0}) - 1 + 2 \cdot \sqrt{(f_{cm}/f_{c0})^2 - (f_{cm}/f_{c0})} \quad (4.11)$$

$$a_t = 2 \cdot (f_{tm}/f_{t0}) - 1 + 2 \cdot \sqrt{(f_{tm}/f_{t0})^2 - (f_{tm}/f_{t0})} \quad (4.12)$$

$$b_c = \frac{f_{c0} \cdot l_s}{G_{ch}} \cdot \left(1 + \frac{a_c}{2}\right) \quad (4.13)$$

$$b_t = \frac{f_{t0} \cdot l_s}{G_F} \cdot \left(1 + \frac{a_t}{2}\right) \quad (4.14)$$

Where:

$f_{cm}$	is the mean compressive strength [MPa]
$f_{c0}$	is the compressive stress at zero concrete crushing [MPa], see eqn. 4.15
$f_{tm}$	is the mean tensile strength [MPa]
$f_{t0}$	is the tensile stress at zero crack width [MPa], see eqn. 4.16
$l_s$	length of the element [mm]
$G_{ch}$	is the crushing energy [MPa], see eqn. 4.17
$G_F$	is the fracture energy [MPa]

$$f_{c0} = 0.4 \cdot f_{cm} \quad (4.15)$$

$$f_{t0} = f_{tm} \quad (4.16)$$

$$G_{ch} = \left(\frac{f_{cm}}{f_{tm}}\right)^2 \cdot G_F \quad (4.17)$$

Once these coefficients have been calculated for the concrete, then the damage factors for compression and tension can be calculated using equations 4.18 and 4.19 respectively (Alfarah et al. 2017).

$$d_c = 1 - \frac{1}{2 + a_c} \cdot \left[ 2 \cdot (1 + a_c) \cdot \exp(-b_c \tilde{\epsilon}_c^{in}) - a_c \cdot \exp(-2 \cdot b_c \cdot \tilde{\epsilon}_c^{in}) \right] \quad (4.18)$$

$$d_t = 1 - \frac{1}{2 + a_t} \cdot \left[ 2 \cdot (1 + a_t) \cdot \exp(-b_t \tilde{\epsilon}_t^{ck}) - a_t \cdot \exp(-2 \cdot b_t \cdot \tilde{\epsilon}_t^{ck}) \right] \quad (4.19)$$

To calculate the inelastic strain and cracking strain for concrete under compression and tension respectively, equations 4.20 and 4.21 should be used, relating the total strain to each of the values required (Alfarah et al. 2017).

$$\tilde{\epsilon}_c^{ch} = \tilde{\epsilon}_c^{in} = \epsilon - \epsilon_{0c}^{el} = \epsilon - \frac{\sigma_c}{E_0} \quad (4.20)$$

$$\tilde{\epsilon}_t^{ck} = \epsilon - \epsilon_{0t}^{el} = \epsilon - \frac{\sigma_t}{E_0} \quad (4.21)$$

## **Method 2**

The second method which will be used to calculate the damage factors was developed by Lubliner et al. (1989). It was used as a base for which the calculations involved in method 1 were built upon, and compared to that method, is rather simple and easy to implement.

To calculate the damage factors for concrete under compression and tension, only equation 4.22 is required (Lubliner et al. 1989).

$$d = 1 - \frac{\sigma}{f} \quad (4.22)$$

Where:

$\sigma$  is the compressive or tensile stress; and  
 $f$  is the mean compressive or tensile stress.

By defining the damage factors in this way, they linearly increase until failure.

### Comparison of Methods

The damaged plasticity values calculated from the two methods above are compared in figures 4.4 and 4.5, for compression and tension respectively. Note, a smeared length of 46mm was taken.

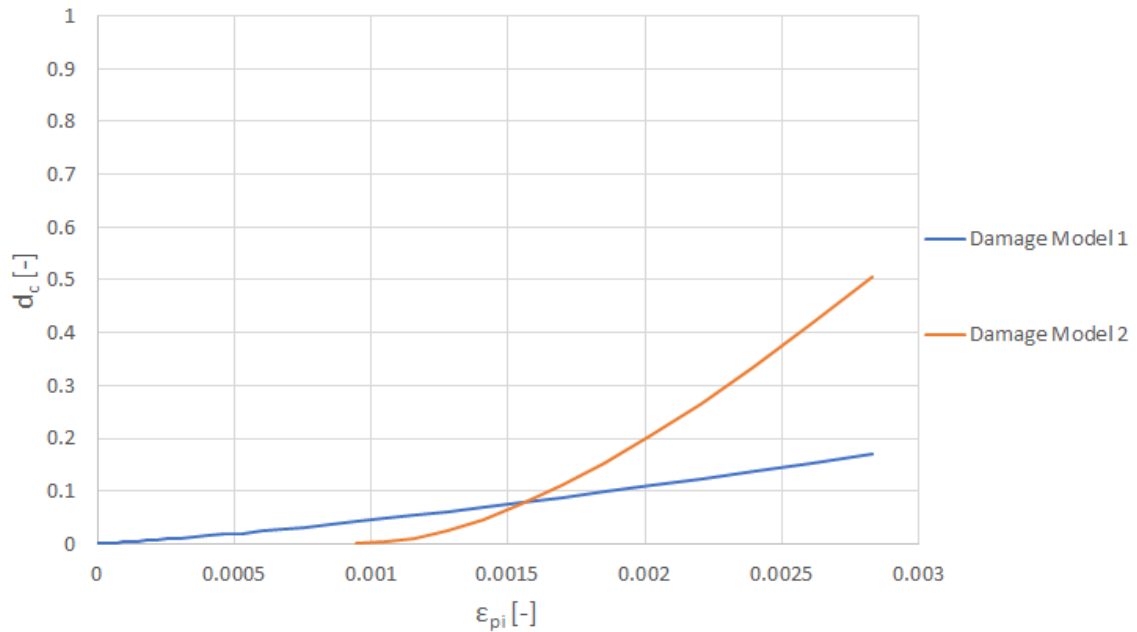


Figure 4.4: Comparison of Compressive Damaged Plasticity Values

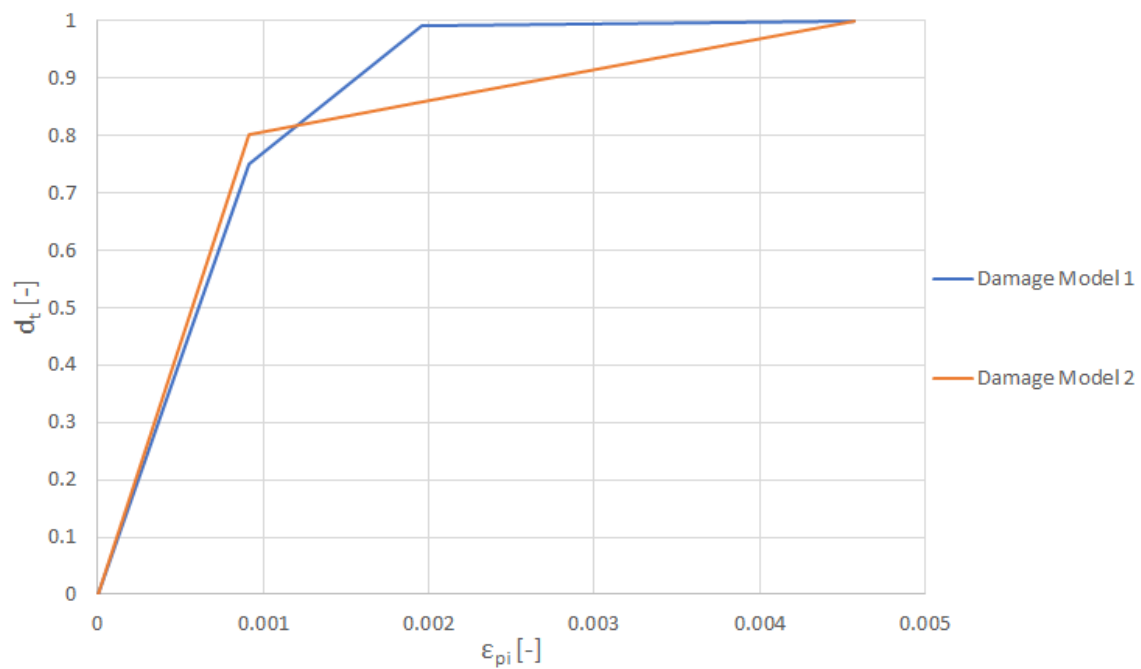


Figure 4.5: Comparison of Tensile Damaged Plasticity Values

The greatest difference in the damage values are seen for the compressive response, with significantly larger values observed for model 2. This would correlate with a greater stiffness loss in the beam at greater levels of stress. There is no significant unloading occurring in the compressive zone of the beam, so minimal influence should exist between these two models.

When considering only the first branch of the tensile response (until plastic strain is approximately 0.001), the difference between the models is less than 0.05. With a smeared length of 100, this difference becomes negligible, whilst for a smeared length of 10, the difference in tensile damage factors is approximately 0.1. As the load-deflection response of the beam is more dependent on the tensile response, then this difference between the damage models should become more apparent at greater levels of loading, with smaller smeared lengths.

It is not possible to state at this stage which model is more reasonable, and hence a comparison in section 6 will be made.

### Input into ABAQUS

For both of the methods discussed above, when the concrete is under tension the damage value will equal to 1 at failure. ABAQUS, however, does not allow for a damage value of 1 to be input (even 0.98 is not accepted due to rounding). Whilst a damage factor can be input close to the value of 1, the analysis will take longer, and is more likely to be cancelled prematurely by the software. Therefore, it is recommended to only include the damage factors for the crack sizes up until the point of the first crack width  $\omega_1$ .

Tension Input:	Property Module » Material Editor » Mechanical » Concrete Damaged Plasticity » Tensile Behaviour » Options » Tensile Damage
Compression Input	Property Module » Material Editor » Mechanical » Concrete Damaged Plasticity » Compressive Behaviour » Options » Compressive Damage

#### 4.1.4.4 Plasticity Parameters

The plasticity parameters defined in the table below must be input in the damage plasticity model in order for it to run.

Parameter	Description	Recommended Value(s)
Dilation Angle ( $\psi$ )	Dilation angle in the p-q plane	between 5 - 40 degrees
Eccentricity ( $\varepsilon$ )	Flow potential eccentricity	0.1
$f_{b0}/f_{c0}$	Ratio of biaxial compressive yield stress to uniaxial compressive yield stress	1.16
K	Ratio of second stress invariant on the tensile meridian vs on the compressive meridian	0.667
Viscosity Parameter	Relaxation time	between 0 - 0.0001

From a literature review it was found that the two plasticity parameters with the greatest variability in their recommended values, is the dilation angle and viscosity parameter.

Michał & Andrzej (2015) performed numerical analyses for uniaxial and bi-axial concrete for different values of dilation angle. They recommend an angle as low as  $5^\circ$  to be taken, with larger values leading to positive volumetric strains under compression, overestimating the load-bearing capacity. Counter to this, Yang (2019) performed numerical analyses on beams similar to the SUREBridge beams, and recommended a dilation angle between  $25^\circ$  and  $45^\circ$ .

Variability in the recommendations surrounding the appropriate value of the viscosity parameter also was found. Michał & Andrzej (2015) provided a good overview as to the effect of taking different viscosity parameter values has on the tensile response of concrete. A value of 0 will result in very clean crack definition, with larger values resulting in a greater spread of the cracking region (i.e. damage will be not be confined to a single line of concrete elements). Whilst they recommend a value very close to 0 to be taken, it appears as though this is not always possible, from a review of other articles. Convergence problems are often experienced, and the viscosity parameter is one way which to avoid them. For this reason, Yang (2019) recommends a value of  $10^{-4}$ .

Due to the high variability in these two values, a sensitivity analysis will be performed in section 6 to determine which values are most appropriate for this specific situation.

ABAQUS Input: Property Module » Material Editor » Mechanical » Concrete Damaged Plasticity » Plasticity

### 4.1.5 Total Strain Crack Model (DIANA)

The total strain crack model is a smeared crack model available in DIANA, which allows for either rotating, fixed or fixed to rotating cracks to be modelled. Compared to the damaged plasticity model available in ABAQUS, the main difference in the material response is that the unloading curve DIANA follows is unaffected by any damage factors. Otherwise, the material response curves are the same, albeit somewhat easier to define in DIANA.

DIANA has several inbuilt curves to define material behaviour, which simplify the definition of different behaviours, as only key data is required to fully define the curve. Outside of these models, it is also possible to define the response manually with stress-strain inputs, in a similar way to how ABAQUS permits.

To find the total crack model in DIANA, it is necessary to select the class *Concrete and Masonry* when adding a material, and then selecting *Total Strain based crack model* as the material model.

#### 4.1.5.1 Rotating vs Fixed Cracks

Unlike the concrete material models available through ABAQUS, the total strain crack model in DIANA allows for the definition of rotating, fixed and rotating to fixed cracks.

As discussed in section 4.1.3.2, by selecting a fixed crack, the location of the crack is saved in the model, and a new crack will not form unless the threshold angle is passed. However, a rotating crack will be aligned to the principle axis and it can 'rotate' through the progression of loading.

The rotating crack model generally is found to correlate to better results in reinforced concrete beams, whilst the fixed crack model exactly captures the physical nature of cracking in reality - as they do not rotate once made. The rotating to fixed crack option attempts to bridge the gap between the two approaches, which may prove to provide the best crack pattern results.

It was not possible to complete a comparison of the results for the three options described given the time constraints in the thesis. Therefore only the rotating crack model will be utilized in this thesis.

DIANA Input: Materials Module » Class: Concrete and Masonry » Material model: Total Strain Crack Model » Total strain based crack model » Crack Orientation: Fixed, Rotating OR Fixed to rotating

#### 4.1.5.2 Compressive Response

The concrete compressive response can be defined with the selection of one of the predefined response curves available in DIANA. A few of the options include an elastic model, multi-linear, the response according to the fib 2010 model code, and according to Eurocode 2, among others.

The stress-strain curve described in section 3.1.2 is based upon the fib 2010 model code, and hence this is the model which was selected for use in this thesis. To utilize this curve, only the young's modulus, compressive strength, yield and ultimate strains must be input for full definition of the response.

#### 4.1.5.3 Tensile Response

The cracked response of concrete under tension can be captured through several predefined models in DIANA. Three of these models have been selected to compare;

- fib 2010 Model code;
- Hordijk; and,
- Exponential.

As the curves which describe the concrete tensile response according to the fib 2010 model code have already been discussed in detail in section 3.1.3, they will not be defined again in this section.

The curves which describe the response according to Hordijk and the exponential relation are presented below, followed by a comparison of all three models.

### Hordijk

The tension stiffening relationship proposed by Hordijk, Cornelissen and Reinhadt is defined by equations 4.23 and 4.24 (TNO DIANA 2015), whereby the stress equals 0 at the ultimate strain ( $\epsilon_{nn.ult}^{cr}$ ).

$$\sigma_{nn}^{cr} = f_t \cdot \left[ \left( 1 + \left( c_1 \cdot \frac{\epsilon_{nn}^{cr}}{\epsilon_{nn.ult}^{cr}} \right)^3 \right) \cdot \exp \left( -c_2 \cdot \frac{\epsilon_{nn}^{cr}}{\epsilon_{nn.ult}^{cr}} \right) - \frac{\epsilon_{nn}^{cr}}{\epsilon_{nn.ult}^{cr}} \cdot (1 + c_1^3) \cdot \exp(-c_2) \right] \quad (4.23)$$

Where:

$$\epsilon_{nn.ult}^{cr} = 5.136 \cdot \frac{G_f^I}{h \cdot f_t} \quad (4.24)$$

and:

$c_1$	= 3
$c_2$	= 6.93
$f_t$	is the mean tensile strength [MPa]
$\epsilon_{nn}^{cr}$	is the cracking strain [-]
$\epsilon_{nn.ult}^{cr}$	is the ultimate cracking strain [-]
$G_f^I$	is the mode I fracture energy, from equation 3.10
$h$	is the crack band width [mm]

### Exponential

The exponential response is defined by equations 4.25 and 4.26 (TNO DIANA 2015). The stress at ultimate strain is not equal to 0 in this relation, unlike for Hordijk. Instead, the crack is considered to be fully open when  $\epsilon_{nn}^{cr} > 2\epsilon_{nn.ult}^{cr}$ .

$$\sigma_{nn}^{cr} = f_t \cdot \exp \left( -\frac{\epsilon_{nn}^{cr}}{\epsilon_{nn.ult}^{cr}} \right) \quad (4.25)$$

Where:

$$\epsilon_{nn.ult}^{cr} = \frac{G_f^I}{h \cdot f_t} \quad (4.26)$$

### Comparison of Models

For a given smeared length ( $h$ ), the response from the three concrete tensile relations has been plotted in figure 4.6.

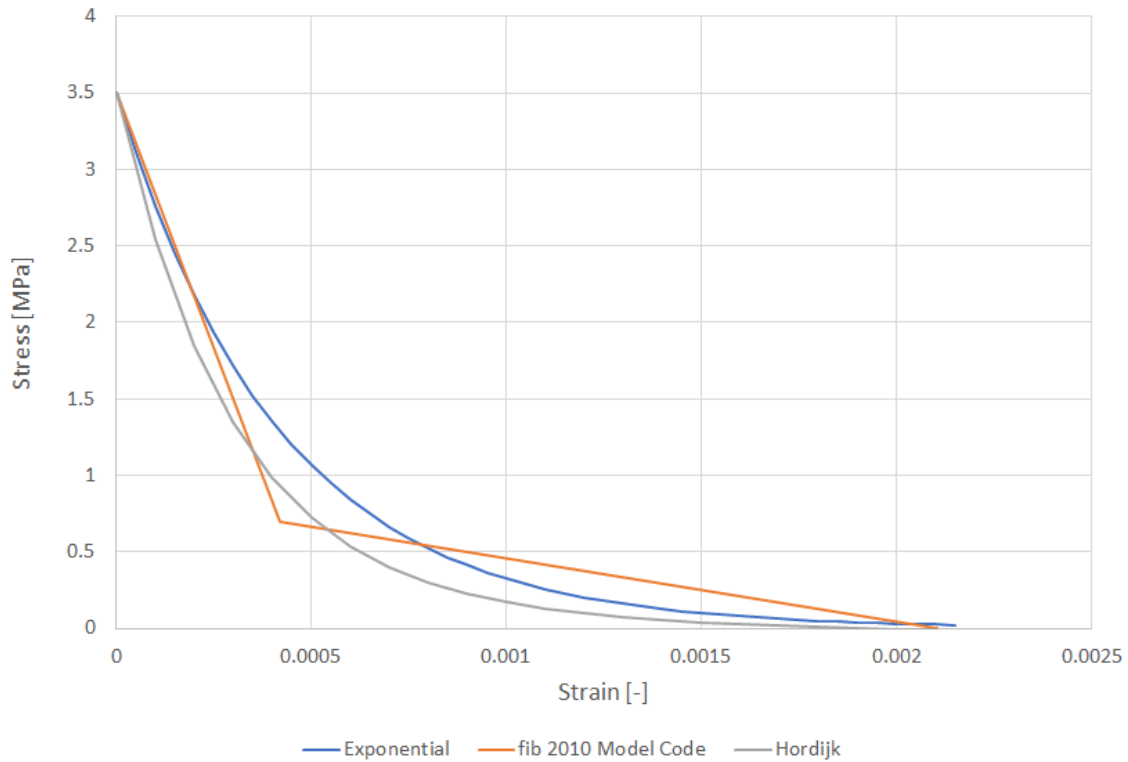


**Figure 4.6:** Concrete Tensile Softening Relations in DIANA

The three tension softening curves behave in a similar manner, whereby the ultimate stress and strain is approximately equal between the models. Compared to the exponential model, the model proposed by Hordijk characterizes a smaller crack opening at similar levels of stress.

The fib 2010 model code appears to roughly approximate the behaviour of the other two curves, however may relate to higher crack width sizes at higher (earlier) stress levels.

A comparative analysis between the three models will be performed in section 6, to determine which results in more accurate crack analysis results.

### 4.1.5.4 Shear Retention

Within the smeared crack approach, DIANA provides the option to specify a shear retention factor. This factor decreases the shear modulus of the concrete, stimulating its degradation which occurs in real life when cracking develops. It is possible to not only identify a reduction of the shear modulus as they develop but also for existing cracks which may have closed.

Some of the available models include the damage and aggregate based models, the Maekawa shear retention model and the normal crack strain-based model, among others.

No shear retention factor is specified in the analyses.

## 4.2 Steel Material Model

Whilst it is possible to directly input the non-linear stress-strain curves from section 3.2 into the FE software, it is not the approach adopted in this thesis. This is because the models which will be analyzed are complex enough without over-defining the steel response. Most importantly, it was determined that the benefits obtained from inputting the exact steel response was outweighed by the increased analysis time. Instead, a simplified bi-linear model, such as what is displayed in figure 4.7 will be used.

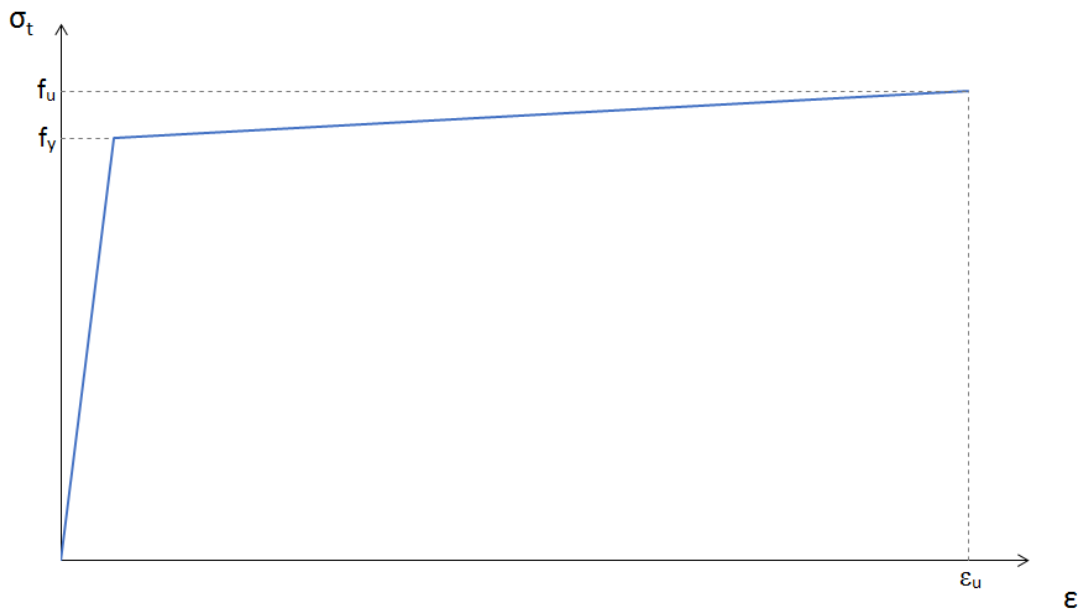


**Figure 4.7:** Elastic-Plastic Material Model for Steel

In the same way as the actual material response, the bi-linear (elastic-plastic) model is linear elastic until yield stress is reached. Once yield is reached, the steel behaves plastically, and the stress-strain slope changes.

### 4.2.1 Elastic Behaviour

The linear elastic behaviour of steel can directly be input in both ABAQUS and DIANA by the specification of the Young's Modulus and Poisson's ratio.

DIANA Input:     Materials Module » Class: Reinforcements and pile foundations » Material Model: Von Mises Plasticity » Linear Elasticity

ABAQUS Input:    Property Module » Material Editor » Mechanical » Elasticity » Elastic

### 4.2.2 Plastic Behaviour

In ABAQUS, the plastic response is input as a relationship between the yield strength and plastic strain. As the stress-strain relationship is linear after yielding, only the definition of the start and end points of the curve are required to fully define the behaviour. ABAQUS interpolates between these two values for any values undefined. Hence, only the yield stress and ultimate stress need to be input, with their corresponding plastic strain values.

In DIANA, the Von Mises plasticity model is used, whereby it is possible to define the same relationship between the yield strength and plastic strain.

DIANA Input:     Materials Module » Class: Reinforcements and pile foundations » Material Model: Von Mises plasticity » Von Mises plasticity

ABAQUS Input:   Property Module » Material Editor » Mechanical » Plasticity

### 4.2.3 Bond-slip Relationship

The bond-slip relationship between concrete and steel, according to Fib (2013), is shown in figure 4.8.

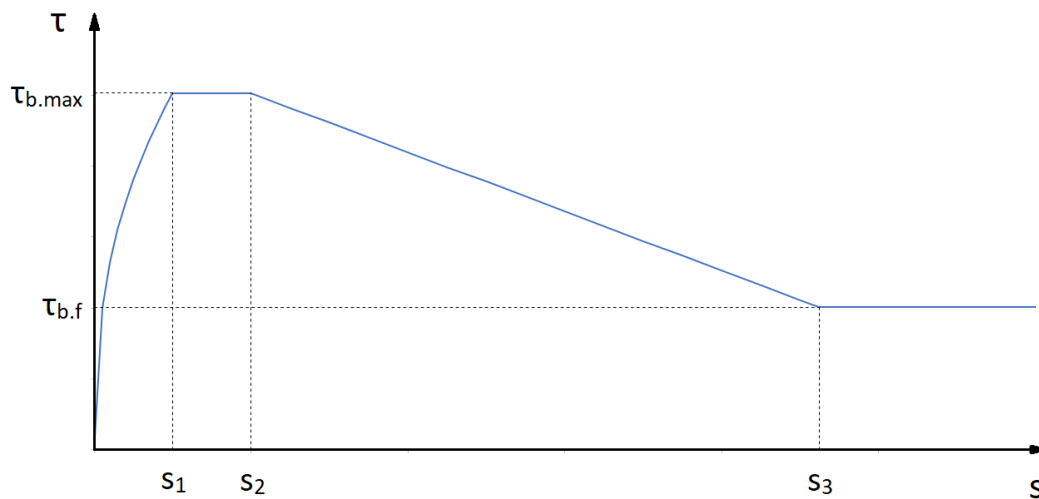


**Figure 4.8:** Bond-slip relationship between Steel and Concrete

This is characterized by the following set of equations (Fib 2013):

$$\begin{aligned}
 \tau_b &= \tau_{b.max} \cdot (s/s_1)^\alpha & \text{for } 0 \leq s \leq s_1 \\
 \tau_b &= \tau_{b.max} & \text{for } s_1 \leq s \leq s_2 \\
 \tau_b &= \tau_{b.max} - (\tau_{b.max} - \tau_{b.f}) \cdot (s - s_2)/(s_3 - s_2) & \text{for } s_2 \leq s \leq s_3 \\
 \tau_b &= \tau_{b.f} & \text{for } s_3 < s
 \end{aligned}$$

Ribs run along the steel reinforcement bars, allowing for the concrete and steel to be interlocked together. Under loading these ribs will cause local stress peaks in the concrete located between them, eventually causing concrete crushing and micro-cracking. As loading increases, the concrete between the ribs is sheared off, damaging the bond between the steel and concrete.

Depending on the quality of the bond between the concrete and steel surfaces, the level of slip occurring at different shear stress levels can change (Fib 2013). The bond quality is affected by the surface of the steel (size and spacing of ribs), quality of the concrete (strength, cover size), and the position and orientation of the bar at the time of casting, among others (Fib 2013). Fib (2013) considers two states of bond; good bond and other bond. The key parameters defining each of these states of bond quality is in table 4.1.

Parameter	Good Bond	Other Bond
$\tau_{b.max}$	$2.5 \cdot \sqrt{f_{cm}}$	$1.25 \cdot \sqrt{f_{cm}}$
$\tau_{b.f}$	$0.4 \cdot \tau_{b.max}$	$0.4 \cdot \tau_{b.max}$
$s_1$	1 mm	1.8 mm
$s_2$	2 mm	3.6 mm
$s_3$	9.24 mm	9.24 mm
$\alpha$	0.4	0.4

**Table 4.1:** Steel Bond-slip values for good and all other bond conditions

Note: The mean rib distance ( $s_3$ ) from the experiments was unknown, so a value from literature was input in its place (Lundgren 1999).

Additionally, it should be emphasized that the same bond-slip relationship also exists for negative shear stresses (Ma & Kwan 2015). Hence, the full bond-slip model should be included in the FE models.

Good bond is assumed between the concrete and the steel for all SUREBridge beams.

### 4.3 CFRP Material Model

As discussed in section 2, failure of the concrete at the level just above the CFRP bonding location caused the CFRP laminates to be removed from the base of the concrete.

This simplifies the modelling of the CFRP, as no failure mechanism needs to be accounted for, as the material itself did not fail. Therefore, only the linear elastic response needs to be defined.

#### 4.3.1 Elastic Response

As truss elements are utilized, only axial force is resisted by them. The material model in this case is then an isotropic linear elastic model, where only the elasticity in the direction of axial load is required. As the truss elements are aligned to the direction of the fibres in the matrix, then only this elasticity needs to be input. This is the elasticity which was determined from the experimental testing of the CFRP, which was discussed in section 3.3.

ABAQUS Input: Property Module » Material Editor » Mechanical » Elastic » Elasticity » Type: Isotropic  
DIANA Input: Materials module » Class: Composites and rubber » Material Model: Linear Elastic Isotropic » Linear material properties

## 4.4 Epoxy Material Models (CFRP to Concrete)

The CFRP laminates are bound to the bottom surface of the concrete with the help of an adhesive. There are two possible ways to model the presence of this adhesive; either directly or by using a traction-separation law between the two surfaces.

If the epoxy is modelled directly, the material properties provided by the supplier can be used to define the elastic behaviour. However, as Chen & Teng (2001) have found through a literature study, the adhesive rarely fails. Instead in the majority of cases the concrete located a few millimeters above the adhesive will fail instead, mainly due to the high strength adhesives which bond well to the FRP and concrete surfaces. Therefore, several bond-slip models have been proposed to replicate this behaviour.

### 4.4.1 Epoxy

When the epoxy is directly modelled, only the linear elastic response is modelled. The Young's Modulus and Poisson's ratio provided by the distributor are directly input into the model.

ABAQUS Input: Property Module » Material Editor » Mechanical » Elastic » Elasticity  
DIANA Input: Materials Module » Class: Composites and rubber » Material model: Linear elastic isotropic » Linear material properties

### 4.4.2 Bond-Slip Model

As an alternative to the method above, it is possible to describe a bond-slip relationship between the CFRP and concrete surface.

Lu et al. (2005) proposed two new bond-slip models based on several existing models which were used at that time. One model was more precise, yet more complicated than the other, which was bi-linear.

Comparing the results from both the new and existing models against the results from 253 pull out tests, the accuracy of each model was able to be compared. They found the newly proposed models outperformed all others, with the precise model matching results with an  $R^2 = 0.9099$  and the bi-linear model with an  $R^2 = 0.9083$  (Lu et al. 2005).

As the accuracy of both models are similar, yet the implementation is more challenging with the precise model, the bi-linear model will be proposed for use in this thesis. The bi-linear model is displayed in figure 4.9.

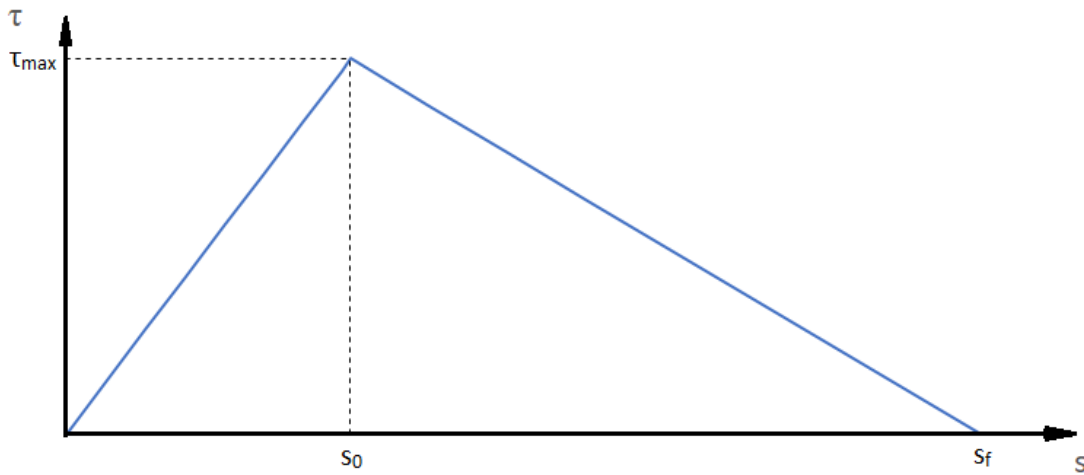


**Figure 4.9:** Bond-slip relationship between CFRP and Concrete

It is characterized by the following set of equations (Lu et al. 2005):

$$\begin{aligned} \tau &= \tau_{max} \cdot \frac{s}{s_0} & \text{for } s \leq s_0 \\ \tau &= \tau_{max} \cdot \frac{s_f - s}{s_f - s_0} & \text{for } s_0 < s \leq s_f \\ \tau &= 0 & \text{for } s > s_f \end{aligned}$$

Where:

$$\tau_{max} = \alpha_1 \cdot \beta_w \cdot f_t$$

$$\alpha_1 = 1.5$$

$$\beta_w = \sqrt{\frac{2.25 - b_f/b_c}{1.25 + b_f/b_c}}$$

$$s_0 = 0.0195 \cdot \beta_w \cdot f_t$$

$$s_f = 2 \cdot G_f / \tau_{max}$$

and:

$b_f$  is the width of the laminate

$b_c$  is the width of the concrete beam

$f_t$  is the tensile strength of the concrete

In was also the case for the other bond-slip models, the full bond-slip curve should be defined when used. This means that also negative shear stress and slip should be accounted for.

## 4.5 GFRP Material Model

In section 3.4, three possible approaches for defining the material properties of GFRP were presented. They are briefly summarized below:

1. Component based: All components are defined with their respective properties
2. Assuming an equivalent section of a web and two flanges: The edges, flutes and flats are smeared across the mid-section creating an equivalent web core
3. Assuming equivalent properties: flats and top and bottom skins are retained, assuming equivalent properties for all sections.

Whilst approach 1 reflects reality, it does require for all components to be modelled in the cross section. This is challenging when modelling the 3D section in the 2D plane, and hence is not used in this thesis.

Both approach 2 and 3 simplify the modelling of the GFRP panels in FE software. Approach 2 contains less simplifications in the material response than approach 3, and for this reason it was used in this thesis.

### 4.5.1 Elastic Behaviour

By adopting approach 2 in the modelling of GFRP panels, the material properties in table 3.5 can be input into ABAQUS and DIANA. This requires for a linear elastic, orthotropic material model to be used.

In ABAQUS, a linear elastic model is selected, with lamina behaviour. In DIANA, a composite material model is defined, with orthotropic (plane stress) behaviour.

ABAQUS Input: Property Module » Material Editor » Mechanical » Elastic » Type: Lamina  
DIANA Input: Materials Module » Class: Composites and rubber » Material model: Linear elastic orthotropic » Linear material properties » Element type: Plane stress

### 4.6 Epoxy Material Model (GFRP to Concrete)

In beam 2, the same epoxy which was used to connect the CFRP to the base of the beam was also used to connect the GFRP panels. However, unlike the CFRP connection, this epoxy was located close to the neutral axis, and hence didn't resist high forces through loading. Therefore, there is no need to include any bond-slip relationship in the modelling of this epoxy. Additionally, the epoxy is 10mm thick, significantly thicker than what is used with the CFRP.

The epoxy is therefore modelled as a linear elastic, isotropic material. Only the specification of the Young's Modulus and Poisson's ratio is required.

ABAQUS Input: Property Module » Material Editor » Mechanical » Elastic » Elasticity  
DIANA Input: Materials Module » Class: Composites and rubber » Material model: Linear elastic isotropic » Linear material properties

### 4.7 Mortar Material Model

For beams 3 and 4, a mortar is used to connect the GFRP sandwich panels to the concrete beam, in the place of the epoxy. Similarly to the epoxy, it also is located close to the neutral axis, and hence does not resist high forces through loading. Therefore, no bond-slip or failure mechanism needs to be included in the material modelling.

The mortar is therefore modelled as a linear elastic, isotropic material. Only the specification of the young's modulus and Poisson's ratio is required.

ABAQUS Input: Property Module » Material Editor » Mechanical » Elastic » Elasticity  
DIANA Input: Materials Module » Class: Concrete and masonry » Material model: Linear elastic isotropic » Linear material properties

# 5

## Finite Element Models

Seven finite element models, based off the SUREBridge experiments, were developed in the commercial programs ABAQUS and DIANA. A short description of the beams can be found below:

- Beam 1      Reinforced Concrete;
- Beam 2.1    Reinforced Concrete, Pretensioned CFRP laminates, Longitudinal GFRP panels, GFRP attached via an epoxy;
- Beam 2.2    Reinforced Concrete, Longitudinal GFRP panels, GFRP attached via an epoxy;
- Beam 3.1    Reinforced Concrete, Pretensioned CFRP laminates, Longitudinal GFRP panels, GFRP attached via a mortar;
- Beam 3.2    Reinforced Concrete, Longitudinal GFRP panels, GFRP attached via a mortar;
- Beam 4.1    Reinforced Concrete, Pretensioned CFRP laminates, Transverse GFRP panels, GFRP attached via a mortar; and
- Beam 4.2    Reinforced Concrete, Transverse GFRP panels, GFRP attached via a mortar.

As beam 1 is a simple reinforced concrete beam, it was used as a reference beam for modelling, allowing for the response of the concrete and steel to be verified prior to the addition of CFRP and GFRP.

As discussed in section 2.4.3.1, when testing beams 2 - 4 in the laboratory it was found that the CFRP debonded from the base of the beams, due to the shearing off of the concrete at the layer just above the epoxy. It is not possible to include this failure mechanism in a single FE model without extensive work. Therefore, it was determined that capturing this behaviour was outside the scope of the thesis. In order to capture the full response, the analysis of each of the beams 2 - 4 were split into two models to replicate the response prior to CFRP failure and after. Beam 2.1 is therefore used to model the response with pretensioned CFRP laminates, whilst beam 2.2 captures the response of the beam after the debonding of the CFRP. As the strain levels in the CFRP were recorded throughout loading, they will be used to determine the failure point of beams 2.1, 3.1 and 4.1.

This chapter will systematically progress through the steps required to develop the finite element models, whilst section 7 displays the results. Where differences between the development of the FE models in ABAQUS and DIANA exist, they are be pointed out in the relevant sections.

## 5.1 Geometry

The beams were modelled in the 2D plane, with plane stress and truss elements. Only half of the beams were modelled due to symmetry, thereby reducing the computation time of the analysis. An overview of the general model setup is shown in figure 5.1.

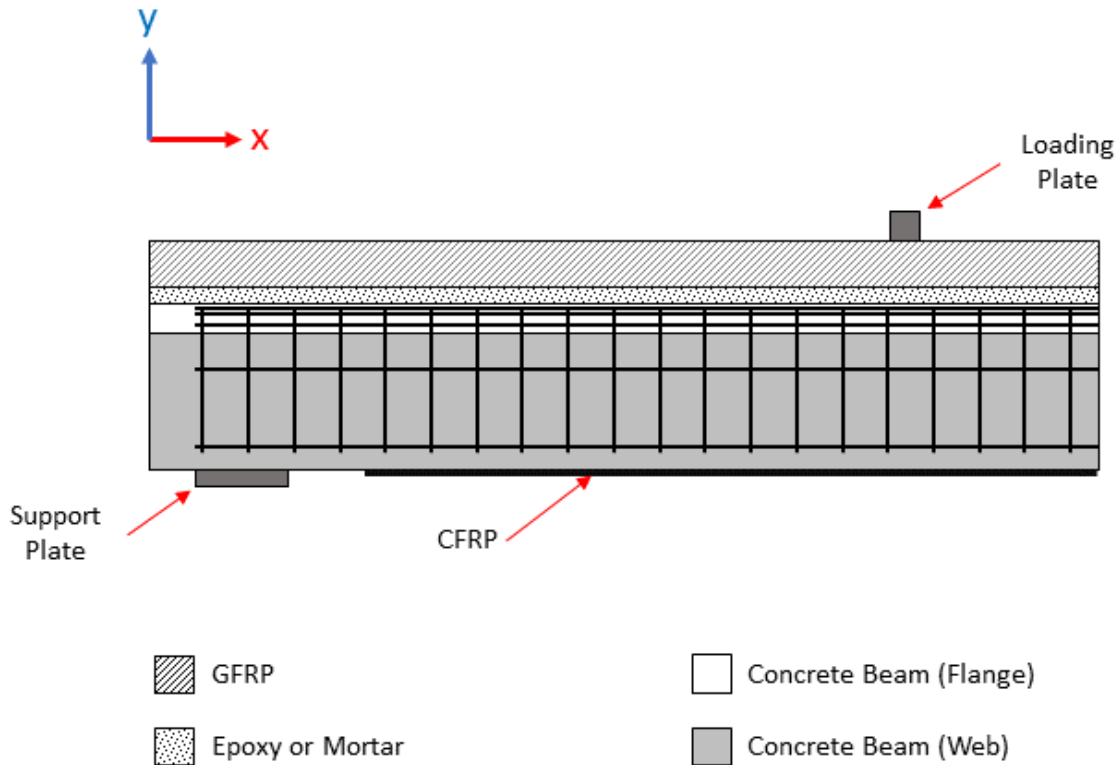


**Figure 5.1:** Beam Geometry for beams 2 - 4

There is one notable difference between the beams tested in the laboratory setting, and those tested in the software, and that is the addition of loading and support plates. They were added to the FE models in order to reduce the local concrete crushing which results from high stresses at the point of load and support applications. The plates have a greater ductility than that of the beam, and so will soften the impact of the load and support condition.

There are five layers of longitudinal reinforcement included in the concrete beam, as well as two different sized stirrups, which are placed at regular intervals along the length. The cross section of the concrete beam exclusively is displayed in figure 5.2, where these features are labelled.

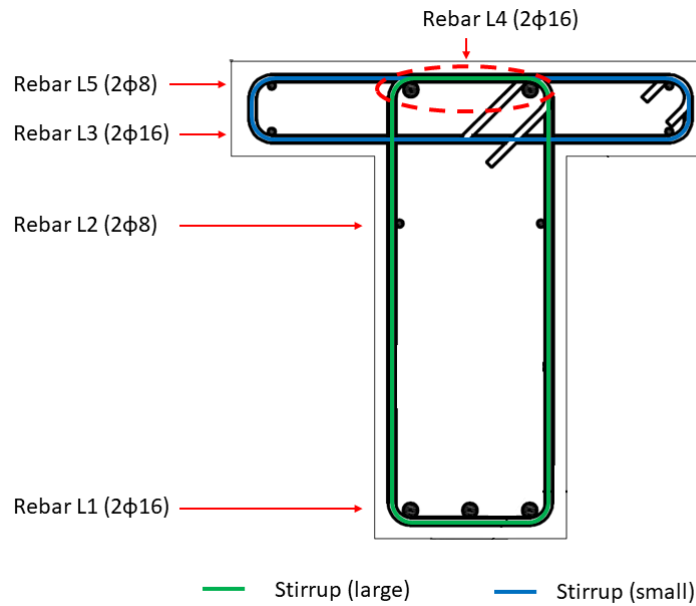


**Figure 5.2:** Cross Section of the Reinforced Concrete Beam

The transformation of the 3D section into the 2D plane requires for some changes to the reinforcement to be made. In the 2D model, the vertical component of the stirrups affect the shear capacity of the beam, whilst the horizontal components have very little contribution. Therefore, to convert the stirrups from 3D to 2D, the height of the vertical components was kept, and the total area of the cross sections was doubled (to account for the two vertical components). In the FE model, the large stirrups are modelled separately from the small stirrups.

Each layer of longitudinal reinforcement was modelled by a single wire feature, which has the same area as the total area of the reinforcement in that layer.

The dimensions of each component for the four beams is listed in table 5.1, with the exception of the GFRP panels, whose properties are listed in table 5.2. As some of the geometry did not change between the different beam models, only the difference in geometry will be noted for subsequent beams. For example, the dimensions of the concrete and rebar does not change between beams, so is only stated for beam 1, however is present in all beams. One notable exception is the epoxy in beam 2 is replaced by the mortar in beams 3 + 4.

Part	Length [mm]	Depth [mm]	Height [mm]	Diameter [mm]	Spacing [mm]
<b>Beam 1</b>					
Concrete Beam (Web)	3000	200	400	-	-
Concrete Beam (Flange)	3000	500	100	-	-
L1 Rebar	2950	-	-	3 $\phi$ 16	-
L2 Rebar	2950	-	-	2 $\phi$ 8	-
L3 Rebar	2950	-	-	2 $\phi$ 8	-
L4 Rebar	2950	-	-	2 $\phi$ 16	-
L5 Rebar	2950	-	-	2 $\phi$ 8	-
Stirrup (Large)	-	-	472	2 $\phi$ 8	150
Stirrup (Small)	-	-	72	2 $\phi$ 8	150
Support Plate	150	200	20	-	-
Loading Plate	50	500	50	-	-
<b>Beam 2</b>					
CFRP	2650	82	1.45	-	-
Epoxy (GFRP)	3000	500	10	-	-
<b>Beam 3 + 4</b>					
Mortar (GFRP)	3000	500	30	-	-

**Table 5.1:** Dimensions of each component in the four beam models, excl. GFRP

Component	Length [mm]	Depth [mm]	Height [mm]
<b>Beam 2</b>			
Top Flange	3000	500	16.7
Bottom Flange	3000	500	19.8
Web	3000	500	111
<b>Beam 3</b>			
Top Flange	3000	500	17.6
Bottom Flange	3000	500	16.4
Web	3000	500	111
<b>Beam 4</b>			
Top Flange	3000	500	19.9
Bottom Flange	3000	500	17.9
Web	3000	500	111

**Table 5.2:** Dimensions of the GFRP Panels

## 5.2 Boundary Conditions

As only half of the beam was modelled, a symmetry condition was applied to the cut section of the beam whereby the x-displacement is fixed. This was applied to the concrete beam, CFRP, GFRP and the connection (epoxy or mortar) between the GFRP and concrete beam.

The support condition which was attached to the support plate constrains the beam in the vertical direction. In order to release any additional stresses which may buildup and exactly replicate the four-point bending conditions, no other degree of freedom was constrained at this point.

An additional support condition was applied at the location of the load application, for the DIANA analysis only. This is a software requirement, however was only active when this load is applied (deactivated for all other load cases).

All three of these boundary conditions can be seen in figure 5.3.

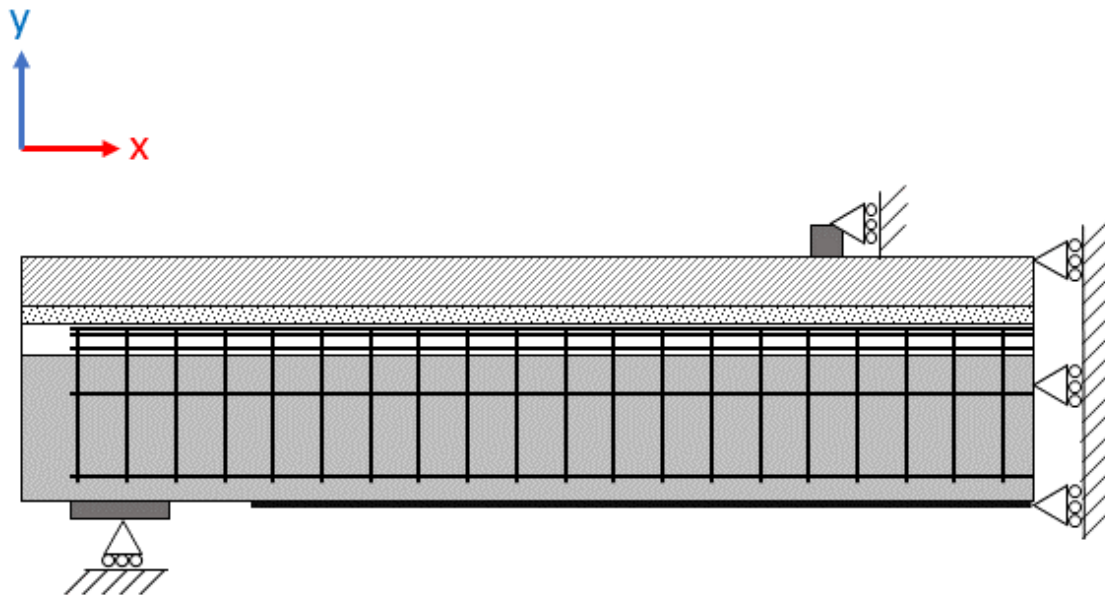


**Figure 5.3:** Boundary Conditions in the FE Models. From left to right; support, loading and symmetry conditions

## 5.3 Loading Conditions

There are four loads which were accounted for in the model:

- Pretensioning the CFRP (2 x loads)
- Self-weight
- Four point bending load

### 5.3.1 Pretensioning the CFRP Laminates

There are two loads related to the pretensioning of the CFRP laminates which needed to be included in the model; the actual pretensioning loads, and an anchorage load.

In the laboratory, the pretensioning device was attached to the beam through two anchor bolts, located 100 mm from the base of the beam. As the pretensioning was applied to the CFRP laminates, an equal reaction force acted at this location, cambering the beam.

Due to some relaxation, the stress along the CFRP laminates decreased. Jincheng Yang calculated the adjusted pretensioning loads for a similar SUREBridge beam, where 100kN pretensioning was also utilized. These adjusted pretensioning loads were used for this thesis, which are listed in table 5.3.

Load	Load Value [kN]
$P_1$	14.404
$P_2$	13.756
$P_3$	12.500
$P_4$	10.076
$P_5$	9.108
$P_6$	9.721
$P_7$	10.489
$P_8$	9.575
Anchorage	89.600

**Table 5.3:** Pretensioning Loads used in FE

It is expected that the actual pretensioning loads would have slightly changed from the values Jincheng Yang calculated, however this adjustment was not made for these analyses.

The location of the loads along the CFRP is according to the pretensioning device dimensions. Figure 5.4 displays the location of the point loads.

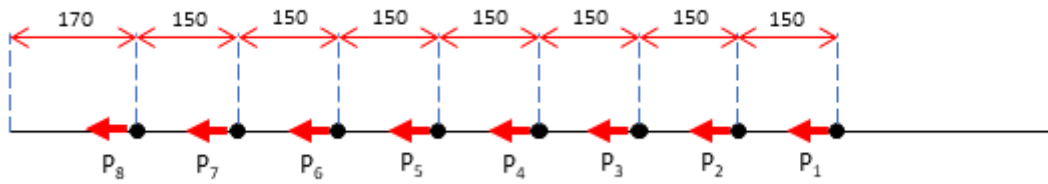


**Figure 5.4:** Pretensioning Loads and Positions [mm]

In both DIANA and ABAQUS, the CFRP laminates were pretensioned by the application of point loads along their length.

The anchorage load was applied through a small steel anchor plate, to prevent local concrete crushing at this location (in the same way the load and support plates prevent crushing).

### 5.3.2 Self-weight

The dead load of the beams was also included in the analysis. This was calculated from the material densities input for each of the materials. As the specific densities of all materials is not known, the density of concrete was increased to take into account the density from all other parts.

### 5.3.3 Four-point bending

For the analysis of all four beams, the load from the four-point bending test was applied as a prescribed displacement, in order to capture the post-beam behaviour of the material.

## 5.4 Bond between the Steel Reinforcement and Concrete Beam

The steel reinforcement bars can be connected to the concrete in several ways. The simplest way is to embed the rebar into the concrete, assuming a perfect bond between the two materials, and hence allowing no relative motion between them. However, this grossly oversimplifies the behaviour which occurs in reality, so a more complicated method of modelling of their connection can be used, based on the bond-slip relationship presented in section 4.2.3. The main benefits to including this relationship in the model is the improvement in the crack patterns and maximum crack width results.

There are different methods to integrate the bond-slip behaviour in ABAQUS, compared to DIANA. Therefore the approaches in each of the software are presented independently from one another in the sections below.

### 5.4.1 Perfect Bond

By embedding the rebar into the concrete, perfect bond between the two materials is assumed. When the software analyses the concrete, it will detect which concrete elements the embedded steel runs through, and will strengthen them in the direction the reinforcement bars are orientated.

No separate elements or degrees of freedom are required to model this bond behaviour, meaning that it is the simplest case to model.

DIANA Input:     Element Geometries » Shape type: Reinforcement lines  
                  » Element Class: Bar reinforcements » Reinforcement  
                  type: Embedded

ABAQUS Input:    Interaction module » Create Constraint » Embedded  
                  region » choose embedded and host region in subsequent  
                  steps

### 5.4.2 Bond-slip Modelling in ABAQUS

There are several possible ways to include bond-slip in ABAQUS, such as through the use of spring, connector or adhesive elements. There are other less common methods, like the bond-zone model, which will also be discussed below, however its ability to fully capture the bond-slip relationship and the cracking pattern is still to be determined.

### 5.4.2.1 Springs

From a literature review of 20 articles where the bond-slip between concrete and steel was included, only 2 were found to have used non-linear springs. However, as one of the articles utilized a combination of non-linear springs and zero-thickness adhesive elements to model bond-slip, it is difficult to know the exact effect the springs themselves had on the results (Yao & Wu 2016).

The remaining article by Chen et al. (2011) utilized non-linear springs to model bond-slip between steel and concrete in beams externally reinforced by FRP. They found that the inclusion of the springs had a significant impact on the cracking behaviour of the beam, and hence when the FRP would fail (Chen et al. 2011). Additionally, they recommend that a mesh size of <20mm be utilized, to obtain more accurate load-deflection and cracking results (Chen et al. 2011).

### Defining Springs in ABAQUS

To define the bond-slip behaviour in ABAQUS using springs, the user must insert SPRING2 elements along the length of the reinforcing bar, between nodes of the concrete and steel. This can be a cumbersome procedure if the user must manually connect the nodes by hand. Therefore, in large-scale models it is recommended to use a script to adjust the input file just prior to analysis to include the presence of these springs.

The behaviour of any spring is generally described by equation 5.1.

$$F(u) = k \cdot \Delta u \tag{5.1}$$

Where:

- $\Delta u$  is the relative displacement;
- $F(u)$  is the force in the spring; and
- $k$  is the spring constant.

It is possible to describe either a linear or non-linear relationship between the force and relative displacement in the spring. However, it is important to note that modelling using the CAE for 2D models will only allow for linear spring properties to be assigned, and all non-linear behaviour will need to be defined through the input file. If a linear relationship is selected to model, then only the ascending branch of the bond-slip relationship described in section 4.2.3 can be input, by the definition of the spring constant. If a non-linear relationship is defined with the input file, it is possible to define the full bond-slip relationship by defining force and relative displacement couples.

### **Limitations and Considerations**

There are some limitations and considerations to be made when using this method. Firstly, in ABAQUS the coordinate axis are fixed to locations in space, not to elements. Therefore if the elements which lie below a coordinate axis deform under load, the axis is unaffected. Hence, whilst the direction of the spring may be aligned correctly prior to the loading, it will not be aligned after loading. However, for small deformations this will have minimal influence.

Additionally, the number of springs along the interface will also have an influence on the bond-slip relationship observed. This is because the rebar is only connected to the concrete at set points along the beam. This is also true in reality, as the rebar is connected to the concrete by the ribs along its surface. However, unless there are a similar number of springs as ribs, then there will be a greater bond-slip reaction further along the bar than there exists in reality (as all slip of a certain length will accumulate in 1 connector). This still oversimplifies the reality, as the length between the ribs still contributes to the overall behaviour.

It is recommended to complete a sensitivity analysis to determine the optimum number of springs. However, as this method was not used to model bond-slip in this thesis, it will not be performed.

#### **5.4.2.2 Connector Elements (translator)**

From a literature review, it was found that a significant portion of bond-slip models utilized the connector element called translator. However, as some of these models were in the 3D plane (Issa & Masri 2015, Du 2016, Li et al. 2014) or utilized plane stress elements to model the reinforcement (Gooranorimi 2016), their relevance to this specific modelling case is unclear.

Of the two articles which modelled in the 2D plane with truss elements for the rebar, one makes vague mention of a "bond-link element" (Coronelli & Gambarova 2004), which is assumed to reference another connector element called the link element. The second article clearly references the translator element, however only the effect on the load-deflection diagrams was investigated (Li et al. 2014).

Considering all articles which referenced the use of the translator element, only Gooranorimi (2016) investigated the effect on the cracking behaviour, however only limited comparisons were made to experimental data. It is therefore unclear what influence the translator element has on the cracking behaviour, although load-deflection results have been shown to correlate well.

Due to the closeness in the behaviour of non-linear springs and translator elements, it could be argued that some of the conclusions drawn on the accuracy of cracking behaviour seen by using non-linear springs would also be observed from utilizing translators. This however, remains to be seen.

### Defining Translators in ABAQUS

The translator element, shown in yellow in figure 5.5, aligns the coordinate systems of the two connected nodes (shown in blue) and allows relative motion between them in the selected direction (in this case  $u_1$ ).

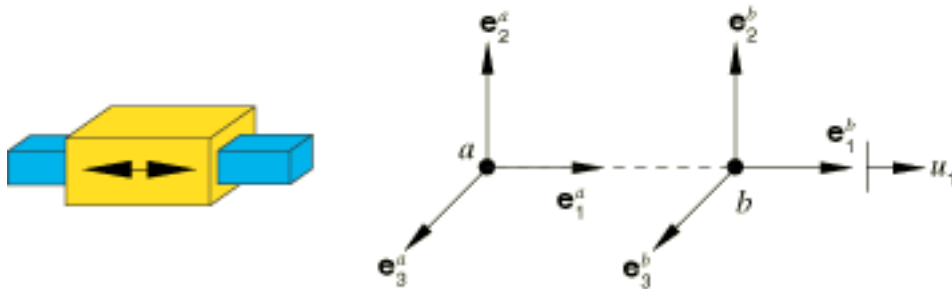


**Figure 5.5:** Overview of the translator behaviour in ABAQUS

It is possible to define elastic, plastic and damaged translator behaviour. Fully elastic behaviour was utilized for this thesis due to simplicity, however plastic behaviour and damage factors should ideally be specified to more closely replicate the bond which exists in reality.

The full bond-slip curve which was described in section 4.2.3 can be defined through non-linear elastic behaviour, by the specification of force-displacement pairs. Unlike non-linear springs, non-linear translators can be specified in the CAE, making them an attractive option for non-coding users of ABAQUS.

To include connectors within the model, the following steps must be followed:

1. Partition the beam and reinforcement bars
2. Create wire elements between the nodes of the beam and the rebar
3. Assign connector behaviour to the wires individually.

In *step 1*, the beam and the wire are equally partitioned along their length, so that the partitions of the beam and the bars are aligned. It is important that the distance between partitions are kept constant, so that only a single translator behavior needs to be defined in step 3.

It is also important to note that with a greater number of partitions, more translators will need to be defined in step 2, and the finer the mesh will need be in the model. These two points will mean that the modelling time, and analysis time will both greatly increase.

In *step 2*, wire elements are added between the beam and the bar, at the location of each partition.

In *step 3*, the wire elements are assigned translator properties. Figure 5.6 displays an example of a translator connection between the concrete beam and the steel rebar.

In the actual model, the length of the wire is zero (as the node of the concrete overlaps the steel), however they have been separated for clarity in this figure.

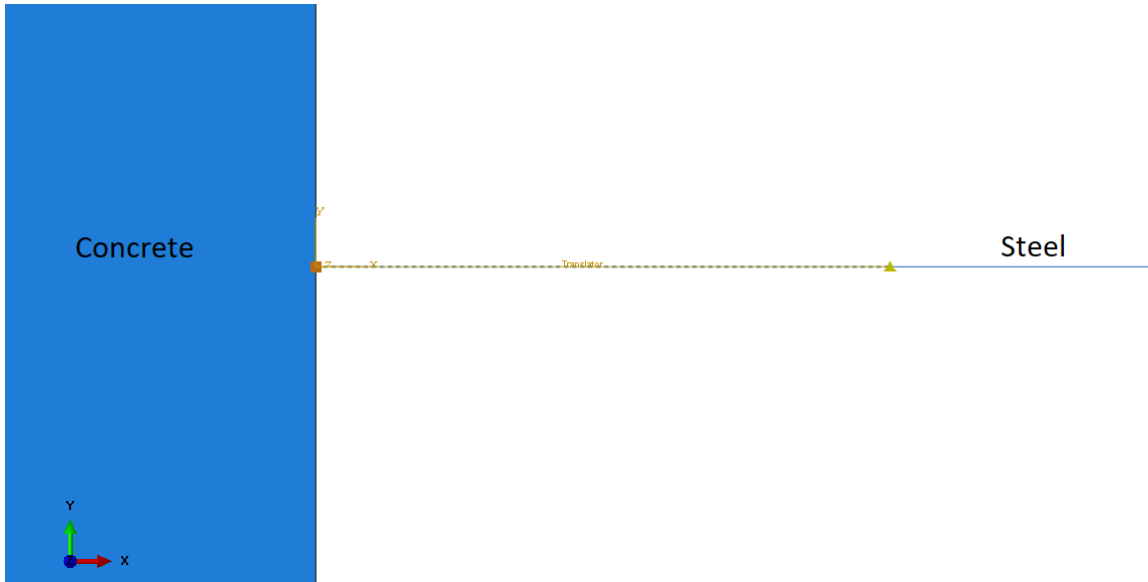


**Figure 5.6:** Translator element in ABAQUS

To assign the translator properties, ABAQUS requires an input of a force-relative displacement relationship. To obtain this relationship, the bond-slip curve must be adjusted. The following calculations must be performed:

To convert shear stresses into shear forces, equation 5.2 needs to be used. It is important to define the full bond-slip curve, for tension and compression in this way.

$$P = \tau \cdot (n \cdot 2 \cdot \pi \cdot r \cdot l_{partition}) \quad (5.2)$$

Where:

- P is the shear force [N]
- $\tau$  is the shear stress [MPa]
- n is the number of reinforcement bars at that level
- r is the radius of the reinforcement bars [mm]
- $l_{partition}$  is the distance between partitions [mm]

### Limitations and Considerations

In the same way that springs suffer from some shortfalls, translator elements do as well. Alike springs, it does require for the manual partition of the beam and reinforcement bars in order to define connectors between them. This can be time intensive.

This method of modelling was used in this thesis to model the bond-slip relationship between the concrete beam and steel reinforcement bars. It is important to note that only the lowest level of reinforcement (L1) has bond-slip assigned. This is because it will have the most influence on the cracking behaviour, and hence the maximum crack size and crack pattern should not be overly affected by the remaining steel bars being embedded. It was determined that the amount of time required to include bond-slip for all reinforcement bars and stirrups in the model was too great.

To emphasize this point, figure 5.7 has been included. It shows the model from ABAQUS, which has several vertical partitions along the bottom-most reinforcement bar. In order to have a mesh density of 11x11mm, the spacing of the reinforcement bars needed to be also spaced at 11mm. Hence, 256 connectors were defined to include bond-slip for just this one longitudinal bar.

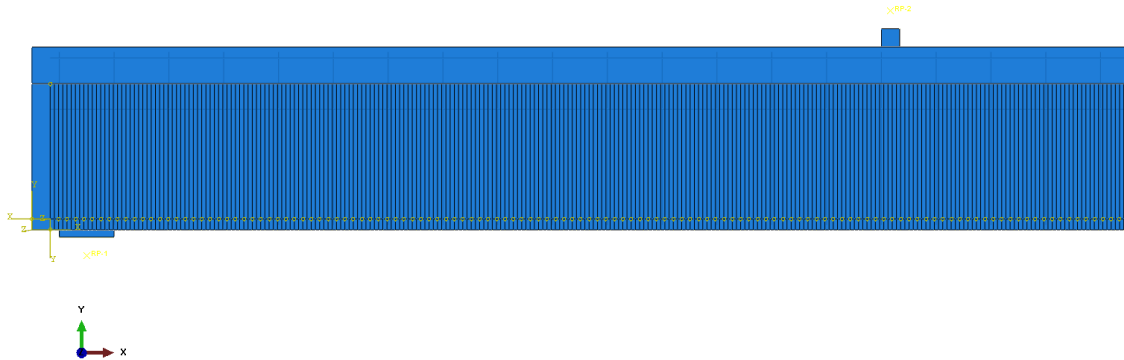


**Figure 5.7:** Partitions for defining bond-slip in ABAQUS

Because of the mix of bond-slip and embedded elements, it is expected that there will still be some mesh dependency of the results. This is discussed further in section 5.4.4.

### 5.4.2.3 Adhesive Elements

Another method of defining the bond-slip behaviour between concrete and steel utilizes cohesive elements. Cohesive elements are defined through the parts module, unlike the springs and translators which are defined through the interactions module. The elements provide a connection to the concrete for the steel, and the material properties define the bond-slip relationship.

In some ways this method can prove to be more complicated to model in ABAQUS than using springs or connectors, however it can be included in the model much quicker. The complication in modelling the cohesive elements is in the understanding of the traction-separation laws to define the adhesive behaviour. However, a simple tie between the elements and the steel and concrete reduces the time taken to define several springs/translators.

From a literature review, several instances where zero-thickness adhesive elements were used to model bond-slip were found. Whilst one of these articles dealt with modelling in 3D (Mang et al. 2015), the remainder modelled in the 2D plane. From these, only two compared the crack patterns/size against laboratory data, however both found good correlations between the two (Chen et al. 2011, Yao & Wu 2016). In addition, there were several articles which discussed the importance of including bond-slip when modelling FRP strengthened beams, as it perfect bond would usually overestimate the strength of the beam.

Due to the complexity in modelling, adhesive elements were not utilized in this thesis.

### 5.4.2.4 Bond Zone Models

A fourth approach was also investigated as a possible alternative to the methods listed above. Somewhat simpler, it only requires some adjustment to the material models of either the concrete or the steel to replicate the bond-slip between them.

#### Modified Concrete

Ziari & Kianoush (2014) proposed a method whereby the concrete material properties of a small area surrounding the reinforcement bars is adjusted; reducing the fracture energy and tensile strength. The steel however, is still embedded in the section. The core concept behind this approach is that in reality, the steel reinforcement exerts compressive, not tensile forces due to bond-slip on the surrounding concrete (Ziari & Kianoush 2014). Hence, by reducing the tensile strength and fracture energy of this small region in the FE model, this phenomenon can be replicated. They found that through trial and error, the ideal depth of this zone is equal to half of the bar diameter (Ziari & Kianoush 2014).

Replicating experimental tests performed by other authors, they compared the steel strain variation along the span, and generally found good results (Ziari & Kianoush 2014). They also compared crack sizes, however only between the experimental

data, the bond zone model and perfect bond model. Between the bond zone model and perfect bond, slightly better results were obtained from the bond zone model, however it still only generally matched the experimental results (Ziari & Kianoush 2014).

From a critical analysis of the article, several questions are raised as to the validity of this method. Firstly, the depth of the zone they propose is based from trial and error, as is the values selected for the tensile strength and fracture energy, so whether they are model dependent is still unknown.

The FE comparisons made in the article are for pull-out tests, with unconfined steel reinforcement bars, so there likely will be additional cracks forming for a beam under flexure when utilizing this method. Additionally, as the steel is still embedded in the concrete, crack patterns will still not be accurate.

In summary, this method appears to attempt to present a simplified adhesive model, however whether the simplifications made in the model are reasonable is still outstanding. With no other sources appearing to utilize this method, and the shortcomings discussed above, this method was not utilized in this thesis.

### **Modified Steel**

Dehestani & Ojarestaghi (2015) proposed a similar model, whereby the steel properties are adjusted to increase the ductility of the rebar in order to replicate bond-slip. Properties adjusted include the elastic modulus, yield strength and the slope of the stress-strain relation in the plastic range (Dehestani & Ojarestaghi 2015). The steel is still embedded in the concrete in this method.

Whilst load deflection results generally correlate well, there is no comparison of crack width sizes, nor crack patterns. As the steel is embedded in the concrete, it is expected to suffer from the same shortfalls as perfect bond models when cracking is concerned, and for this reason, it will not be used in this thesis.

### 5.4.3 Bond-slip Modelling in DIANA

The inclusion of the bond-slip relationship between the concrete and steel is much simpler in DIANA than in ABAQUS. The fib 2010 Bond-slip model is a predefined cohesive model which can be used in the software.

#### 5.4.3.1 fib 2010 Bond-slip Model

Bond-slip can be included in DIANA by selecting the appropriate material model, element geometry and element data for the steel bars. It requires for no additional elements to be modelled by the user, rather DIANA will include interface elements between the two elements to simulate the bond between them.

By creating the steel material under the class *Reinforcements* and selecting a *Bond-slip reinforcement* as the material model, it is possible to define the bond-slip interface using the fib 2010 Bond-slip Model. It requires for the definition of the normal stiffness and shear stiffness moduli, as well as the key values from the bond-slip curve, which was defined in section 4.2.3. Unlike ABAQUS, it doesn't require for the shear stress to be converted into the shear forces.

To define the shear stiffness value, equation 5.3 was used. A normal stiffness of  $1000N/mm^3$  was used for the normal stiffness.

$$K_{ss} = \tau_{max}/s_0 \quad (5.3)$$

Where:

$\tau_{max}$  is the maximum shear stress from the bond-slip relationship [MPa]  
 $s_0$  is the slip for a small initial displacement [mm]

The element geometry must also reflect that bond-slip is included in the model, but selecting a reinforcement type of *Truss bondslip*. The cross-sectional area of the bar must be provided, as well as the contact perimeter, for the correct bond-slip behaviour to be recognized.

Finally, the element data type *INTERF* must be selected, with the specification of a truss interface.

#### 5.4.4 Smearred Length

In section 4.1.3.2, two recommendations were made for which smeared length to take depending on whether perfect or bond-slip was included in the model.

Whilst including bond-slip in DIANA is very straightforward and requires little additional modelling time, the method in ABAQUS is significantly more challenging. The following question was then posed:

*If only the lowest level of reinforcement was modelled with bond-slip, which smeared length should be adopted?*

From a review of literature, only one case was found where a beam was modelled with several layers of reinforcement, and only bond-slip defined on the tensile steel layer (Li et al. 2014). In this case, the smeared crack length taken was equal to the length of the element, and translator elements defined the bond-slip (Li et al. 2014). Unfortunately, only the load-deflection results were compared, which did show good correlation, however tended to exhibit slightly stiffer behaviour prior to yielding (Li et al. 2014).

As this case didn't include any stirrups, it's unknown what effect it might have when they are still embedded in the concrete.

For the first of the beams, a series of investigations will need to be performed in ABAQUS to determine whether it is appropriate to utilize a smeared crack length equal to the length of an element, when some reinforcement is still embedded. The following analyses must be performed:

1. Smeared Crack length = length of element
2. Smeared Crack length greater than length of element

From the literature review, step 1 is expected to correlate well with the laboratory results. This would mean that the remaining embedded reinforcement has little effect on the cracking behaviour. If however the results don't correlate well, then the investigation progresses onto step 2. Step 2 would assume that whilst a beam with all rebar modelled with bond-slip would have a smeared crack length equal to the length of an element, a beam with fully embedded rebar would have it equal to 100mm. When a beam is modelled with a combination of both, the appropriate smeared crack length must exist between the two values.

The results in DIANA, whereby bond-slip is included for all longitudinal rebar and stirrups, would then act as a benchmark for the results in ABAQUS.

## 5.5 Bond between the CFRP laminates and the Concrete Beam

In the laboratory tests, the CFRP laminates were connected to the concrete beam via an epoxy. This method of connection can be included in the model by either modelling the epoxy itself, or by including a bond-slip relationship between the beam and the laminates. Both approaches will be investigated in this section, for each software.

### 5.5.1 Modelling the Epoxy in 2D

By modelling the epoxy using 2D stress elements, the connection which exists in reality between the CFRP and concrete can be exactly replicated in the FE software. The epoxy is then tied to the concrete on one side, and tied to the CFRP on the other.

As the epoxy only exists after the pretensioning of the CFRP laminates, it must not be active for the first stages of the analysis, but switched on for later steps. This can present a challenge in ABAQUS due to the limitations in the software, however it easily performed in DIANA by phased solutions.

In ABAQUS, it is not possible to switch on/off constraints or parts for different steps of the analysis. To work around this obstacle, surface-to-surface contact can be modelled between the CFRP and the epoxy. This can be switched on and off at different steps, allowing for the connection to only be switched on after the CFRP has been pretensioned. To replicate a perfect bond in the surface-to-surface contact interaction, the stiffness of the bond must be incredibly high.

### 5.5.2 Bond-slip

#### 5.5.2.1 In ABAQUS

Instead of modelling the epoxy itself, the bond-slip relationship which was presented in section 4.4.2, can be included instead. This requires for a surface-to-surface contact interaction to be defined between the concrete and CFRP surfaces which is only switched on after the CFRP has been pretensioned.

The surface-to-surface interaction is defined by a contact interaction property with cohesive behaviour. The definition of this cohesive behaviour is based upon the traction-separation relationship defined in equation 5.4.

$$t = \begin{bmatrix} t_n \\ t_s \\ t_t \end{bmatrix} = \begin{bmatrix} K_{nn} & K_{ns} & K_{nt} \\ K_{ns} & K_{ss} & K_{st} \\ K_{nt} & K_{st} & K_{tt} \end{bmatrix} \cdot \begin{bmatrix} \delta_n \\ \delta_s \\ \delta_t \end{bmatrix} \quad (5.4)$$

Uncoupled behaviour is selected, where normal separation does not cause traction forces in the shear direction, and vice versa. Hence only the values  $K_{nn}$ ,  $K_{ss}$  and  $K_{tt}$  need to be defined in ABAQUS. They are calculated from equations 5.5 and 5.6.

$$K_{nn} = E_{epoxy} \cdot d_{CFRP} \quad (5.5)$$

$$K_{ss} = K_{tt} = \left( \frac{\tau_{max}}{s_0} \right) \cdot d_{CFRP} \quad (5.6)$$

Where:

$E_{epoxy}$	Young's Modulus of the Epoxy [MPa], see section 3.3
$d_{CFRP}$	Depth of CFRP into the page, which is in contact with beam [mm]
$\tau_{max}$	Maximum shear stress [MPa], see section 4.4.2
$s_0$	Slip value [mm], see section 4.4.2

It is important to note that it is only possible to define a single set of stiffness values, and hence it is impossible to define stiffness degradation using this method. Therefore only the ascending branch of the bond-slip relationship described in section 4.4.2 is able to be defined.

### 5.5.2.2 In DIANA

In DIANA, the bond-slip behaviour between the CFRP laminates and the concrete beam can be defined by an interface between the two surfaces. Compared to the method in ABAQUS, the entire bond-slip relation defined in section 4.4.2 can be input.

To define the bond-slip relation, a 2D interface material must be defined, with elastic and bond-slip property definition. The linear elastic properties required for DIANA are different to the elastic properties required for ABAQUS, as the user defines the thickness of the interface layer in DIANA, so it only requires stiffness with the units  $N/mm^3$ . The method of calculation is displayed in equations 5.7 and 5.8.

$$K_{nn} = E_{epoxy}/0.001 \quad (5.7)$$

$$K_{ss} = \tau_{max}/s_0 \quad (5.8)$$

Where:

$E_{epoxy}$	Young's modulus for epoxy [MPa], see section 3.6
$\tau_{max}$	Maximum shear stress [MPa], see section 4.4.2
$s_0$	Slip value [mm], see section 4.4.2

By defining these elastic properties, the same epoxy definition exists between ABAQUS and DIANA. However, by additionally defining a bond-slip model, the full definition of the curve from section 4.4.2 can be achieved.

A multi-linear bond-slip model is therefore included, through the input of relative displacement and shear stress pairs. It is important to note that the full definition of the bond-slip curve needs to be input, that is, for positive and negative shear stresses and relative displacements.

### 5.6 Analysis Procedure

The analysis is decomposed into the following five steps:

1. Pretensioning of CFRP
2. Attachment of the CFRP to the concrete beam
3. Removal of the pretensioning load
4. Application of the dead load
5. Application of displacement control

For some of the beams analyzed, the analysis procedure is slightly adjusted due to the absence of CFRP laminates. This is the case for beams 1, 2.2, 3.2, and 4.2, when only steps 4 and 5 are utilized.

In *step 1*, the pretensioning loads are activated - both the point loads along the CFRP laminate, and the anchor load. The epoxy which is located between the CFRP and the concrete beam is turned off in this step.

In *step 2*, the epoxy layer is switched on. This replicates the application and drying of the epoxy in the laboratory.

In *step 3*, the pretensioning loads are deactivated. As in reality, when the pretensioning device is removed from the beam, the reaction force applied to the beam is removed (anchor load), and the CFRP laminate is no longer being externally loaded. Some relaxation of the force in the CFRP laminates will occur in this step.

In *step 4*, the dead load is applied to the beam.

In *step 5*, displacement control is applied to the beam at the location of the loading plate. The dead load is not deactivated in this step, as it still exists in reality.

## 5.7 Mesh

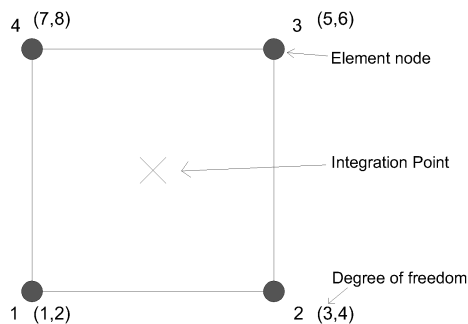
For both the analyses in ABAQUS and DIANA, 2D plane stress elements and 1D truss elements were utilized. A short summary of the different elements used in each software is provided in the sections below.

### 5.7.1 Elements in ABAQUS

Two elements were utilized in the construction of the ABAQUS models:

- CPS4R
- T2D2

#### CPS4R



CPS4R is a 4-node bi-linear plane stress element, with reduced integration and hourglass control. It is used to model the concrete beam, the support, load and anchorage plates and the GFRP panels. As the out of plane stresses are negligible for these sections, it is appropriate to use 2D plane stress elements to model them. The thicknesses assigned are according to the dimensions listed in section 5.1.

CPS4R has two degrees of freedom for each node. Reduced integration is used to prevent shear locking during bending. Full integration elements tend to experience overly stiff behaviour, resulting from energy going into shearing the element, rather than bending it.

#### T2D2

T2D2 is a 2-node linear displacement, truss element. Hence, only axial load is transmitted by this element. It is used to model the longitudinal reinforcement bars, stirrups and CFRP laminates. As the thicknesses of all of these components is relatively thin, it is appropriate to utilize 2D truss elements. The area assigned to each of the sections is representative of the sum of the areas of the sections out-of-plane. For example, Rebar L1 represents three 16mm reinforcement bars, and hence the area assigned to this section is equal to the sum of the total areas.

T2D2 has two degrees of freedom for each node.

### 5.7.2 Elements in DIANA

Three elements were utilized in the construction of the DIANA models:

- Q8MEM
- T6MEM
- L2TRU

#### Q8MEM

Q8MEM is a higher order, four-node quadrilateral plane stress element (TNO DIANA 2010), similar to CPS4R in ABAQUS. It is based on linear interpolation and Gauss integration (TNO DIANA 2010). It is used to model the concrete beam, the support, load and anchorage plates, and the GFRP Panels.

#### T6MEM

T6MEM is a three-node triangular plane stress element, based on linear interpolation and Gauss integration (TNO DIANA 2010).

It was not possible to solely use Q8MEM elements to model the concrete beam in very fine meshes, so in some locations a T6MEM element was used. An example is provided in figure 5.8, whereby the T6MEM elements are highlighted in red (near the base of the beam).

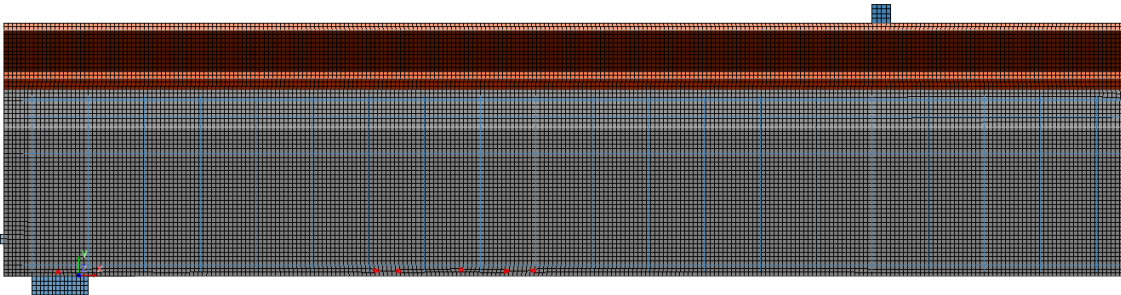


**Figure 5.8:** Location of T6MEM elements in a mesh from DIANA (highlighted in red)

#### L2TRU

L2TRU is a two node truss element (TNO DIANA 2012), similar to the T2D2 element available in ABAQUS. This was utilized for modelling the longitudinal reinforcement bars, the stirrups and the CFRP laminates.

### 5.7.3 Mesh Density

It is important to choose a mesh density which whilst ensuring accurate results, does not take excessive time to run.

Yang et al. (2018) recommended a mesh size of 25 x 25 mm when running the analyses of earlier SUREBridge FE models. However, as only load-deflection results were compared in this case, this may not be fine enough for observe accurate crack patterns.

The recommendations made by Chen et al. (2011) may be more relevant to this modelling case, as they modelled reinforced concrete beams with externally bonded FRP. They recommend a mesh size of less than 20 mm, for more accurate cracking and load-deflection results (Chen et al. 2011).

Mesh sensitivity analyses will therefore be performed at different stages of the analysis process to determine the most appropriate mesh density to obtain accurate results.

## 5.8 Iteration Method

The implicit iteration method used in both ABAQUS and DIANA is the Newton-Raphson method, or full Newton Method.

### In ABAQUS

In ABAQUS, automatic loading is applied. That is, the step size is not explicitly provided by the user, rather ABAQUS will automatically determine the appropriate step size so that convergence is reached at each step of the analysis. If convergence is not reached, then the analysis will be cancelled by the software. The following parameters were input to limit the analysis:

- Maximum number of iterations: 1000000
- Increment size (Initial): 0.1
- Increment size (Minimum):  $10^{-10}$
- Increment size (Maximum): 0.1

### In DIANA

In DIANA, the user is able to either explicitly state the step size and number of steps, or rely on automatic adaptive loading. If the latter is adopted, then the software will adopt the step size until convergence is met for each step in the analysis. Alternatively, if the step sizes are explicitly given, the user can select the option *continuation method*, so that if convergence is not found for a given step, the analysis does not stop.

For the analysis in this thesis, explicit step sizes were input for the analysis, allowing a maximum of 80 iterations to occur before moving onto the next iteration, even if convergence wasn't found. By running a few analysis to begin with to determine the appropriate step size, convergence is found for most steps. When concrete cracking occurs, convergence usually isn't reached for a step or two, however doesn't affect the results significantly. This choice was made due to the large computation time associated with the automatic adaptive loading choice.

## 5.9 Convergence of Solutions

There are several reasons why problems arise related to convergence in both ABAQUS and DIANA, including incorrect modelling, analysis or input choices made by the user. A literature review of the common sources of convergence and recommendations for each case is discussed below.

### 5.9.1 Elastic Analysis

As with any finite element analysis, it is prudent to first run a linear elastic analysis of the model to determine whether there are incorrect boundary conditions, material inputs or interactions which might cause issues in the non-linear analysis of the model (Palacio 2013). Comparing against hand calculations for ultimate limit state will assist in verifying the model response.

### 5.9.2 Step size

It is important that the step size is adequately small when running non-linear analyses, in order to prevent abrupt changes in the model, which would prevent the software from reaching convergence.

This is not an issue in ABAQUS, as adaptive step sizes was selected, and hence the software will self-adjust the size of the step until convergence is reached.

This is an issue in DIANA, as explicit step sizes was used for the analysis. Particularly at loading stages where concrete cracking occurred, it is critical to reduce the step size down until convergence is reached. As the step sizes are adequately small, it is not a large concern if convergence is not reached for a single step, so long as it is reached for the steps following it.

### 5.9.3 Viscosity Parameter (ABAQUS)

The viscosity parameter was introduced in section 4.1.4.4, as one of the parameters required to be specified in the damage plasticity model in ABAQUS. This parameter is set to the default value of 0 by ABAQUS (Abaqus 2010), however by setting a larger value ( $10^{-4}$  or  $10^{-5}$ ), it can assist the analysis to reach convergence.

This is an issue related to ABAQUS/standard, as it does not cope well with sudden changes in the model (Abaqus 2010). When materials with softening behaviour are included in the model, the software will often have difficulties finding convergence (Abaqus 2010). By utilizing viscoplastic regularization, stresses are permitted to be outside of the yield surface (Abaqus 2010).

It is recommended to choose a small value of the viscosity factor compared to the time increment (Abaqus 2010), so that:

$$\frac{t}{\mu} \rightarrow \infty \quad (5.9)$$

Where:

$\mu$  is the viscosity factor; and  
 $t$  is the time step

Malm (2006) modelled reinforced concrete beams utilizing the concrete damaged plasticity material model, and was only able to obtain limited results post-brittle failure, even when utilizing viscoplastic regularization. They concluded that when analyzing statically, ABAQUS does not capture the behaviour as well as other FE software, such as Atena (Malm 2006).

A sensitivity analysis on the viscosity parameter will be performed to determine the effect on the results, in section 7.

### 5.9.4 Alternative Solution Methods

As an alternative to viscoplastic regularization, analyzing the model through ABAQUS/Explicit can also prevent convergence issues from arising. This is because it generally is more capable to analyze models where large discontinuities occur.

As discussed above, Malm (2006) had difficulties capturing the post-brittle failure behaviour of a reinforced concrete beam. Whilst they found better convergence in the program Atena, they also analyzed the model in ABAQUS/Explicit, and were able to achieve a better definition of post-peak behaviour, then any viscoplastic regularization gave them in ABAQUS/Standard.

They are not the only author to experience these difficulties. Chen et al. (2011, 2015) also reported issues when modelling reinforced concrete beams with externally bonded FRP. By utilizing a dynamic solution process, convergence issues could be overcome, and the definition of the concrete failure and FRP debonding was well maintained. They even go so far to claim that their model, utilizing dynamic analysis, is far superior to all previous models capturing intermediate crack-induced debonding failure, due to its accuracy of capturing post-peak behaviour, and the precision of the load-deflection and cracking results Chen et al. (2011).

As the debonding of the CFRP laminates is not contained within a single model in this thesis, there is little need to result to utilizing ABAQUS/Explicit or dynamic solutions. It is however recommended that in the case where this debonding is desired to be captured in a single FE model, that ABAQUS/Explicit or dynamic analysis is utilized.

# 6

## Sensitivity Analyses

Several sensitivity analyses were formed on beam 1 to determine the most appropriate material and model parameters to use in the analysis of the SUREBridge beams in section 7. The results from these sensitivity analyses is presented in this chapter, as well as a discussion of the findings.

As the bond-slip relationship between steel and concrete is one of the more challenging relationships to model, the analyses progressed ignoring this bond initially, and then comparing the result which are obtained from including it.

The laboratory results obtained from Jincheng Yang has been included in all figures for ease of comparison.

### 6.1 Perfect Bond

When the bond between the steel reinforcement bars and the concrete beam is assumed to be perfect, five sensitivity analyses were performed. They were conducted to measure the effect of:

- Mesh density on the results from ABAQUS and DIANA;
- Smear length on the results from ABAQUS and DIANA;
- Damage model on the results from ABAQUS;
- Dilation angle on the results from ABAQUS; and
- Viscosity parameter on the results from ABAQUS.

In the sensitivity analyses performed, the following parameters were utilized in the FE models, unless stated otherwise (especially in the case where the sensitivity of one of the parameters was tested):

- Mesh density: 25 x 25 mm
- Smear Length: 100 mm (ABAQUS), 150 mm (DIANA)
- Damage Model: 1 (ABAQUS only)
- Dilation angle: 30° (ABAQUS only)
- Viscosity parameter:  $10^{-4}$  (ABAQUS only)

Only the load-deflection curves are compared in each of these sensitivity analyses. This is because of the low quality cracking information available when no bond-slip is included in the model.

### 6.1.1 Effect of Mesh Density

Four different mesh densities were compared in both ABAQUS and DIANA. The densities which were tested include:

- 100 x 100 mm
- 50 x 50 mm
- 25 x 25 mm
- 10 x 10 mm

#### 6.1.1.1 Results

The resulting load-deflection curves for each mesh density is displayed in figures 6.1 and 6.2, for ABAQUS and DIANA respectively.

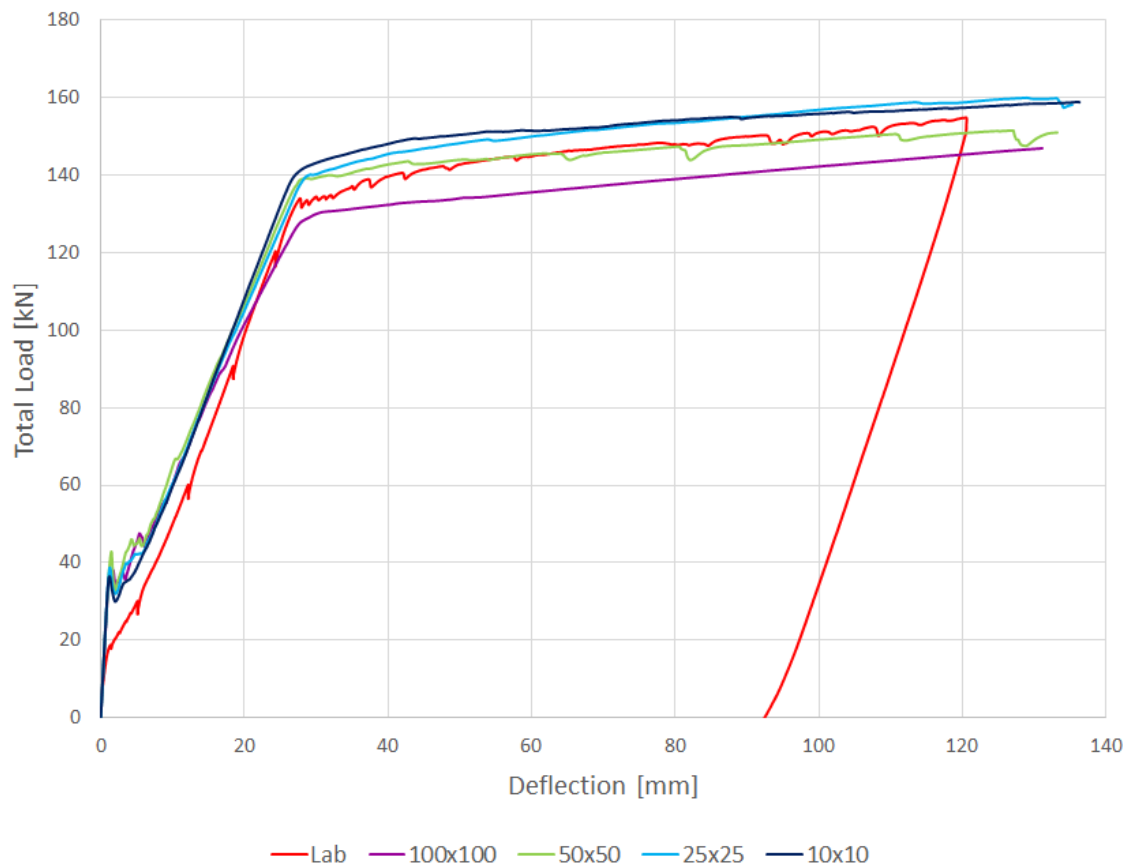


**Figure 6.1:** B1: Effect of different mesh densities on the load-deflection curves in ABAQUS, Perfect Bond

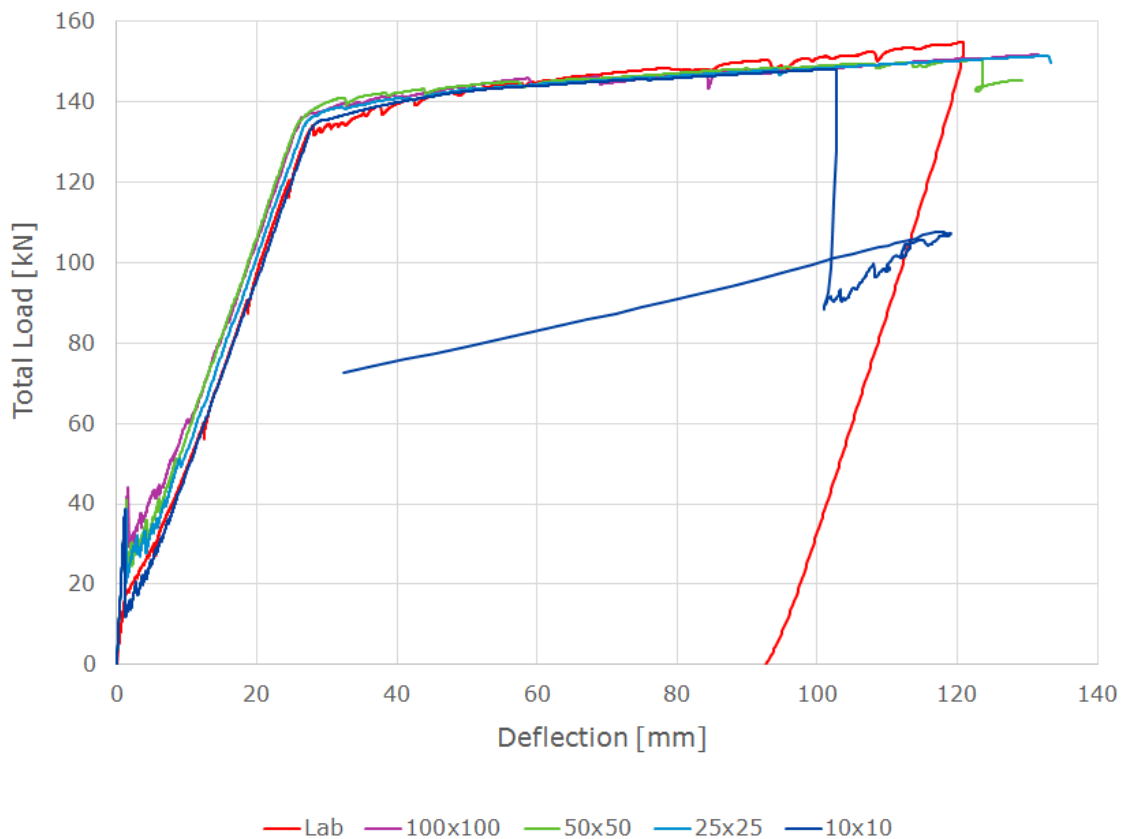


**Figure 6.2:** B1: Effect of different mesh densities on the load-deflection curves in DIANA, Perfect Bond

In the mesh sensitivity study performed in DIANA, convergence problems occurred for the mesh density of 10 x 10 mm. This is evident in the load-deflection result found in figure 6.2, as the total load dramatically falls at just over 100mm. This was caused by the crushing of the concrete at this point (i.e. failure).

#### 6.1.1.2 Discussion of Results

From looking at figures 6.1 and 6.2, it is clear that greater variations of the results occur for the different mesh densities in ABAQUS, than in DIANA.

In ABAQUS, the gradient of the load-deflection curves prior to reaching yield is consistent between different mesh densities. However, large variations exist in the load value corresponding to the yield point, particularly for the coarsest mesh which significantly underestimates it. The yield point of the remaining three densities are similar, however deviations occur in the post-yield response of the 50 x 50 mm mesh. It was therefore concluded that a mesh density of 25 x 25 mm or 10 x 10 mm would provide the most accurate results in ABAQUS.

In DIANA, only slight variations in the load-deflection curves can be observed. There is little variance in the yield point, nor gradient of the pre- or post- yield

response. Whilst the mesh densities of 10 x 10 mm and 25 x 25 mm displayed a closer response to the laboratory result, the premature failure of the former meant that further analyses would be performed considering a 25 x 25 mm mesh.

The adoption of the 25 x 25 mm mesh size for further analyses in both software is in line with the recommendations made by Jincheng Yang, for earlier SUREBridge beams (Yang et al. 2018).

### 6.1.2 Effect of the Smeared Length

The effect which the smeared length has on the results was compared in both ABAQUS and DIANA. The different smeared lengths which were tested are as follows:

- 150 mm
- 100 mm
- 50 mm
- 36.4 mm ( $\sqrt{2A}$ )
- 25 mm

#### 6.1.2.1 Results

The resulting load-deflection curves for each smeared length is displayed in figure 6.3 for ABAQUS and figures 6.5 and 6.4 for DIANA.

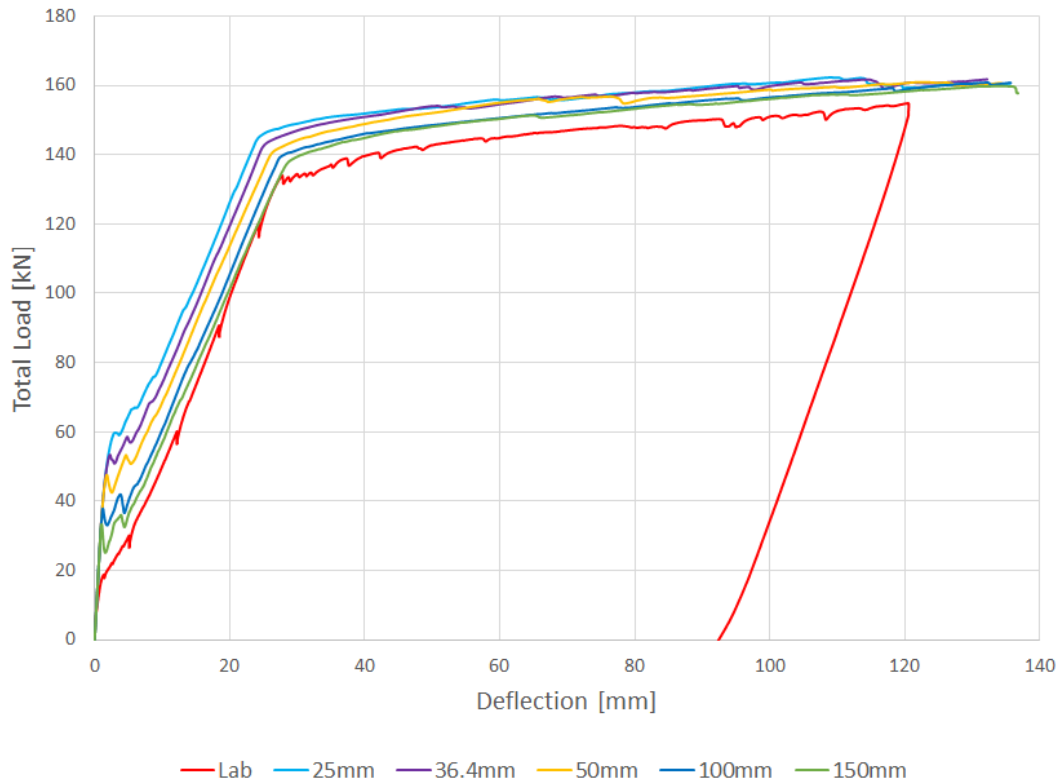


**Figure 6.3:** B1: Effect of different smeared lengths on the load-deflection curves in ABAQUS, Perfect Bond

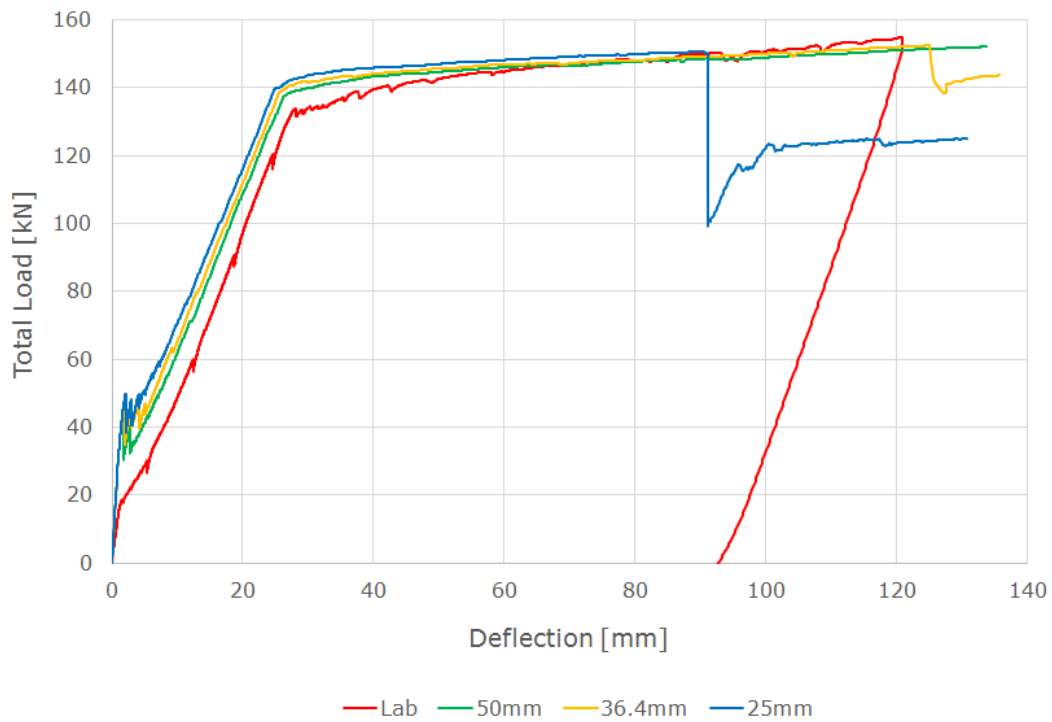


**Figure 6.4:** B1: Effect of different smeared lengths on the load-deflection curves in DIANA, Perfect Bond, for smeared lengths 25 - 50 mm

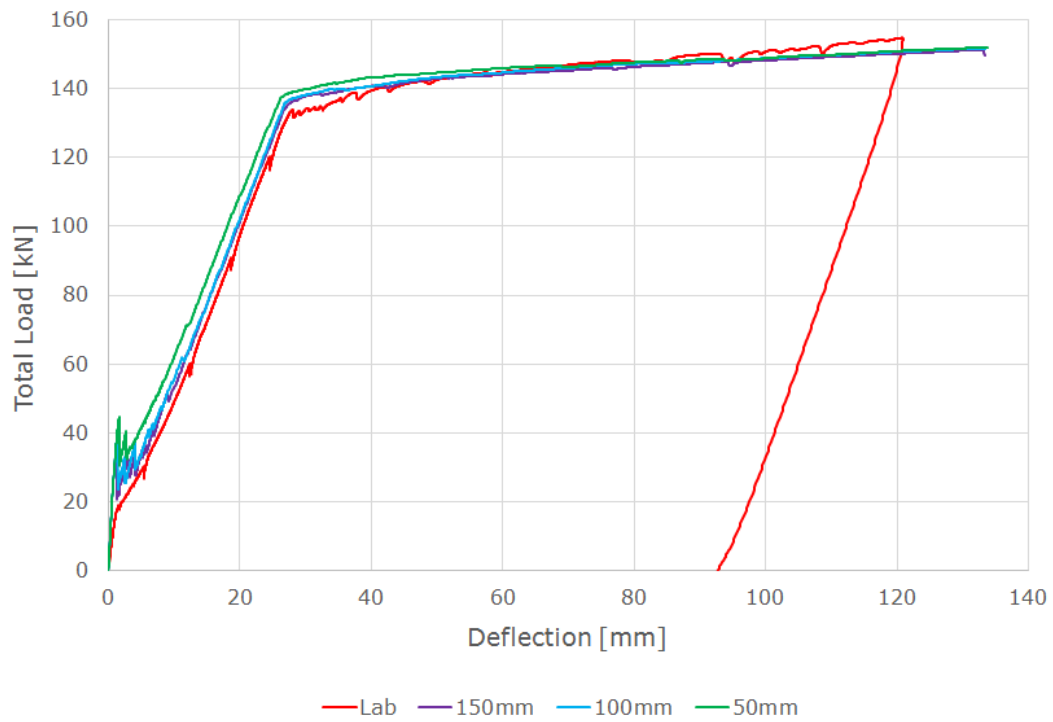


**Figure 6.5:** B1: Effect of different smeared lengths on the load-deflection curves in DIANA, Perfect Bond, for smeared lengths 50 - 150 mm

For the smeared length of 25mm in DIANA, convergence issues occurred at the deflection of approximately 90mm, due to crushing of the concrete (i.e. failure).

### 6.1.2.2 Discussion of Results

Section 4.1.3.2 briefly touched on two schools of thought in regard to the specification of the smeared crack length for embedded reinforcement. One concept is that it is mesh dependent, and that the length of the element should be the smeared crack length, whilst the second is that it is material dependent.

Comparing the results in figures 6.3, 6.5 and 6.4, it is clear that for ABAQUS and DIANA, a value of 100 - 150 mm provides the best fit to the experimental data.

If instead a smeared length of approximately 25 mm (equal to  $l_{el}$ ) is taken, then the load-deflection results would not be as accurate. Therefore, it can be confidently stated that the smeared length is material dependent when embedded reinforcement is utilized, not mesh dependent.

Furthermore, if utilizing DIANA with embedded reinforcement, the smeared length should be input manually by the user, otherwise the default Rots method will be adopted ( $l_s = \sqrt{2A}$  or  $\sqrt{A}$ ).

A smeared length of 100 mm was selected in ABAQUS as the 150 mm result undercut the laboratory results slightly near yield. A smeared length of 150 mm was selected for future analyses in DIANA, as it provided the best match to laboratory results.

This is consistent with the recommendations made by Jincheng Yang for a similar strength concrete.

### 6.1.3 Effect of the Damage Model (ABAQUS)

Two methods of calculating the damage plasticity factors was proposed in section 4.1.4.3. A comparison of the methods is performed in this section, based on a mesh size of 25 x 25 mm.

#### 6.1.3.1 Results

The load deflection results calculated according to the two damage models are displayed in figure 6.6.

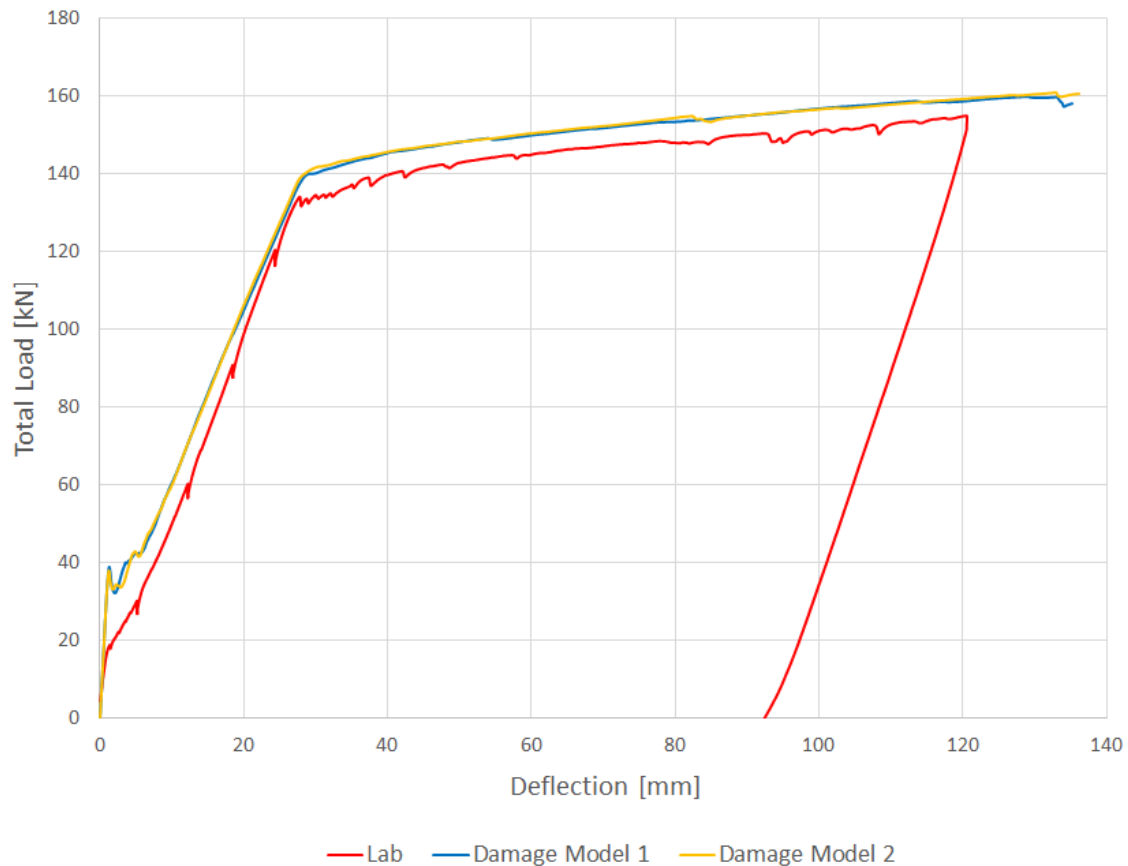


**Figure 6.6:** B1: Effect of different damage models on the load-deflection results in ABAQUS, Perfect Bond, Mesh 25 x 25 mm

#### 6.1.3.2 Discussion of Results

Two methods of calculating the damage plasticity values was presented in section 4.1.4.3. When comparing the load-deflection results, no difference is observed between the results. However, it should be noted that the run time of the second damage model was approximately 10 minutes longer than the first model. This was the determining factor which lead to damage model 1 being selected for further analyses. However for the average user, utilizing the mathematically more simpler model (2) will not affect the results obtained.

It should also be mentioned that when inputting values for the damage plasticity model in ABAQUS, values close to 1 will result in long running times and convergence issues. This is only an issue in describing tension values, as they equal to 1 at ultimate strain. It is recommended to only define the tension damage factor up until the first cracking strain ( $\omega_1$  from section 4.1.4.2).

The reason as to why ABAQUS has such problems with larger damage values is that as the values get larger, more elasticity is lost in the unloading. This results in a much more sudden change in the model, which ABAQUS/Standard has difficulty analyzing. It might be possible to specify larger damage values, however the viscosity parameter would need to decrease in order to achieve convergence. This in turn would increase analysis time. Alternatively, ABAQUS/Explicit might be otherwise employed to overcome these discontinuity problems.

### 6.1.4 Effect of the Dilation Angle (ABAQUS)

The effect of four different dilation angles on the results in ABAQUS were compared. The tested dilation angles are:

- $15^\circ$
- $20^\circ$
- $30^\circ$
- $40^\circ$

#### 6.1.4.1 Results

Figure 6.7 displays the load-deflection results for all dilation angles. As convergence issues occurred for the angles of  $15^\circ$  and  $20^\circ$  at approximately 2 mm deflection, the graph is restricted to only view until this point. Figure 6.8 displays the full load-deflection curves for  $30^\circ$  and  $40^\circ$ , which did not suffer from the same convergence issues.

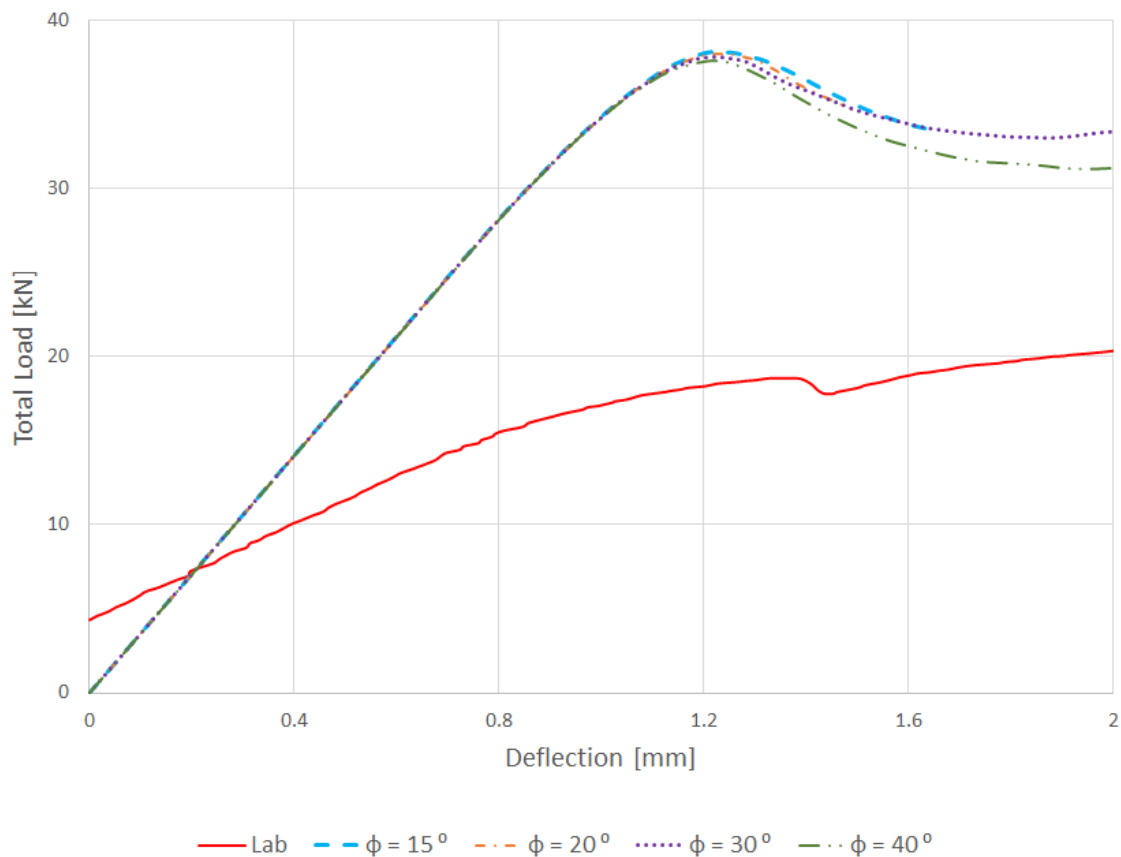


**Figure 6.7:** B1: Effect of different dilation angles on the load-deflection curves in ABAQUS, Perfect Bond (zoomed in)

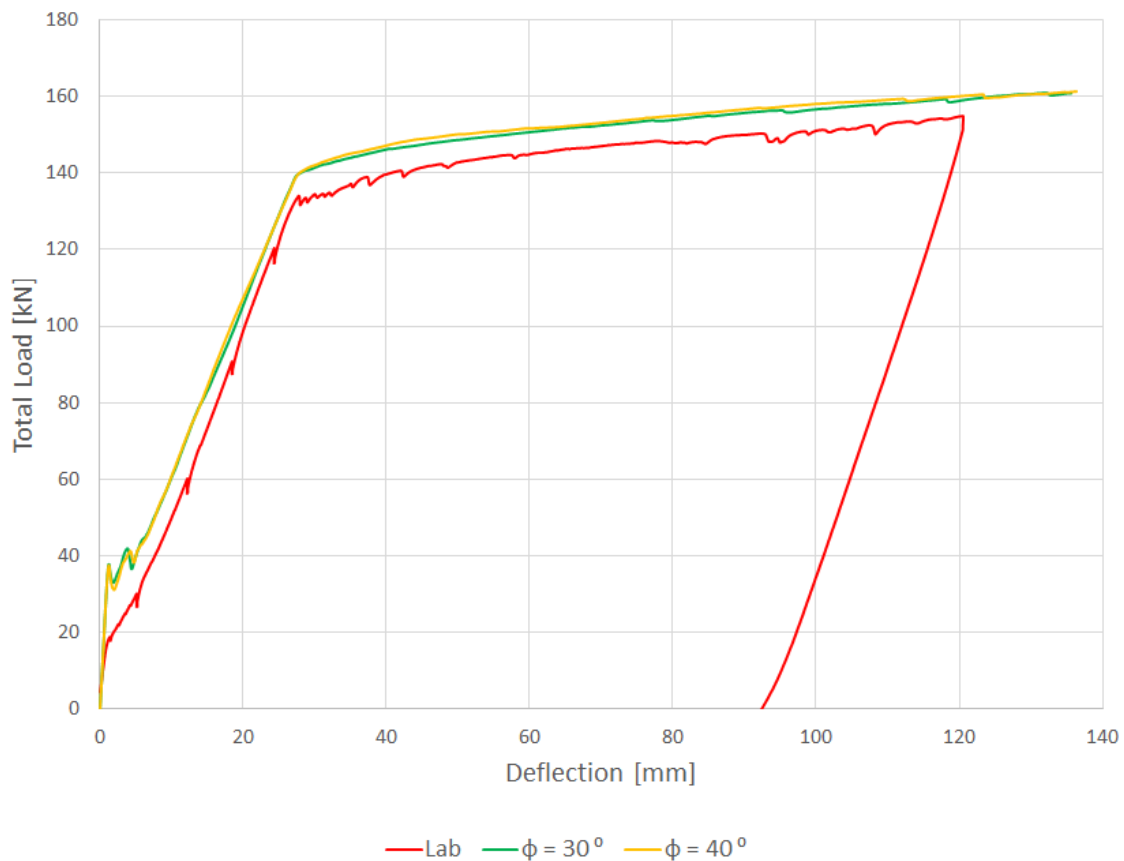


**Figure 6.8:** B1: Effect of different dilation angles on the load-deflection curves in ABAQUS, Perfect Bond (zoomed out)

#### 6.1.4.2 Discussion of Results

Section 4.1.4.4 discussed which dilation angle might be most appropriate for modelling the SUREBridge beams. Whilst Michał & Andrzej (2015) recommended a value of  $5^\circ$  it is evident from our analyses that angles lower than  $20^\circ$  will not run due to convergence issues.

Greater values in the range of  $30^\circ$  and  $40^\circ$  result in similar load-deflection results, which is consistent with the findings of Yang et al. (2018). There is some variability in the cracking responses, however this would need further investigation to draw further conclusions.

The dilation angle of  $30^\circ$  is selected for further analyses.

### 6.1.5 Effect of the Viscosity Parameter (ABAQUS)

The effect of the viscosity parameter on the analyses is compared in this section. Three different viscosity parameter values were tested:

- $10^{-2}$
- $10^{-3}$
- $10^{-4}$

#### 6.1.5.1 Results

The load-deflection results are displayed in figure 6.9.

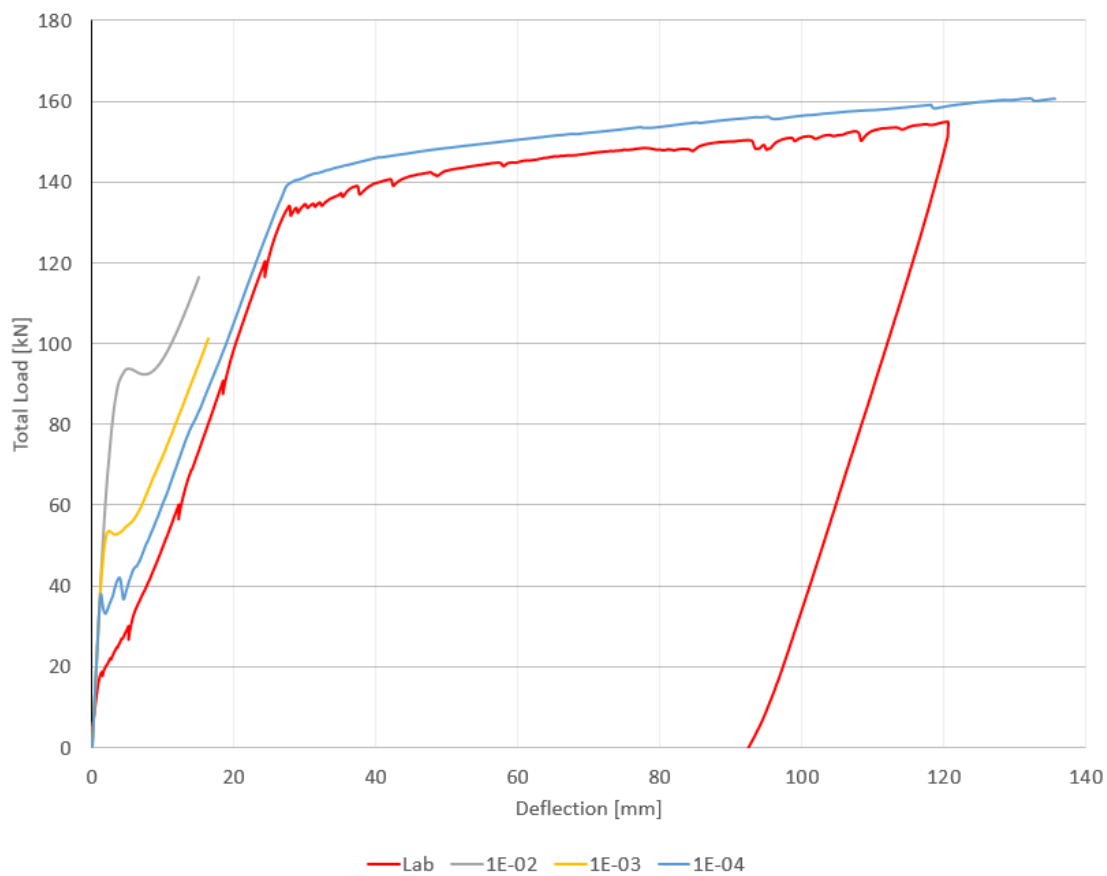


**Figure 6.9:** B1: Effect of different viscosity parameters on the load-deflection curves in ABAQUS, Perfect Bond

Convergence issues occurred when analyzing with the viscosity parameter set to  $10^{-2}$  and  $10^{-3}$ , and hence the load-deflection curves in figure 6.9 end abruptly before the yield point.

### 6.1.5.2 Discussion of Results

From figure 6.9, it is clear that taking a viscosity parameter greater than  $10^{-4}$  will lead to convergence problems. Even for the small portion of results which were obtained for larger viscosity parameters, it is clear that the load-deflection curve is dilated vertically as values increase.

This somewhat contradicts the recommendations by Li et al. (2014), that the viscosity parameter can be between the range of  $10^{-3}$  to  $10^{-5}$  without compromising results. From the load-deflection curves, it is clear that  $10^{-3}$  is too large to obtain accurate results. On the other end of the spectrum, if a viscosity parameter of  $10^{-5}$  is adopted, the run time would be expected to increase. It is therefore recommended that a value of  $10^{-4}$  be utilized in the analyses, unless convergence issues occur, in which case a value of  $10^{-5}$  should be used.

## 6.2 Bond-Slip Included

When the bond-slip relationship between the steel and concrete was included in the model, four sensitivity analyses were performed. They were performed to measure the effect of:

- Mesh density on the results from ABAQUS and DIANA;
- Smear Length on the results from ABAQUS and DIANA;
- Tension Model on the results from DIANA; and
- Damage plasticity models on the results from ABAQUS.

In the sensitivity analyses performed, the following parameters were utilized in ABAQUS, unless stated otherwise:

- Mesh density: 11 x 11 mm
- Smear Length: 11 mm
- Damage Model: 1
- Dilation angle: 30°
- Viscosity parameter:  $10^{-4}$

The following parameters were utilized in DIANA, unless stated otherwise:

- Mesh Density: 11 x 11 mm
- Smear Length: 11 mm
- Tension Model: Hordijk

The sensitivity analyses compare the effect different parameters have on the load-deflection curves, maximum crack size and the crack pattern.

### 6.2.1 Effect of the Mesh Density

The effect which four different mesh densities have on the results from ABAQUS and DIANA are found in this section. As the mesh density is dependent on the spacing of the translator elements in ABAQUS, this spacing has been adopted in DIANA for a direct comparison between the two programs. The four mesh densities are as follows:

- 92 x 92 mm
- 46 x 46 mm
- 23 x 23 mm
- 11 x 11 mm

The smear length used in each of the analyses was equal to the length of the element (i.e. for a mesh density of 92 x 92 mm, the smear length was 92).

#### 6.2.1.1 Results

The effect of changing the mesh density on the load-deflection curves is displayed in figures 6.10 and 6.11 for ABAQUS and DIANA respectively.

## 6. Sensitivity Analyses

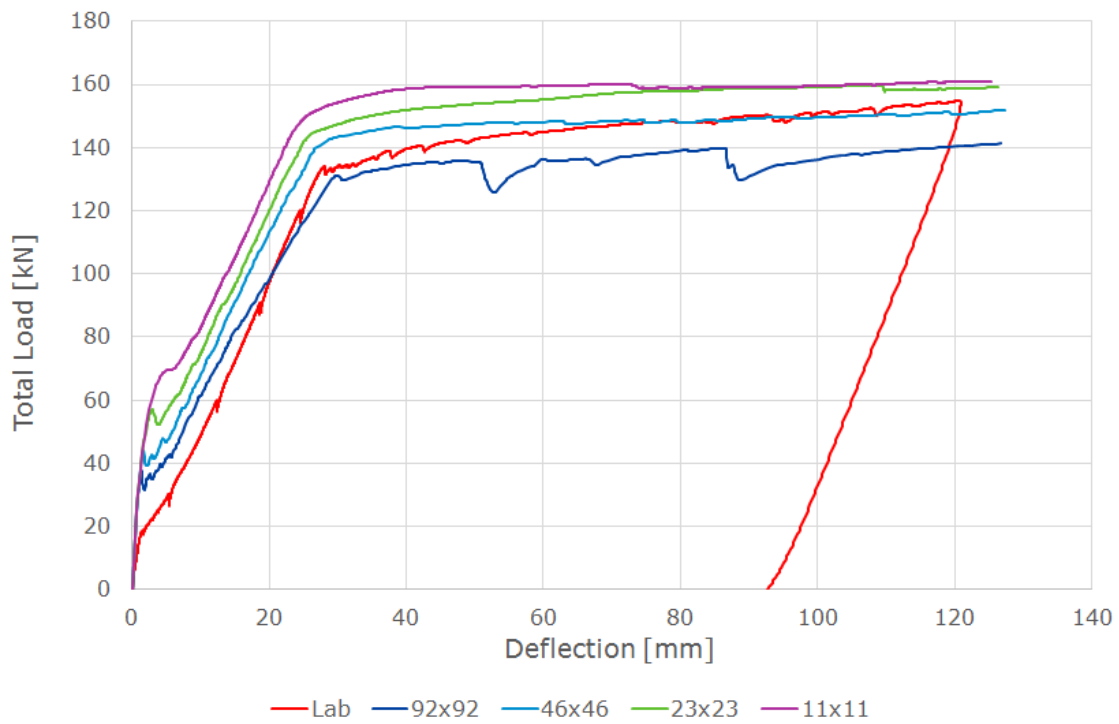


**Figure 6.10:** B1: Effect of different mesh densities on the load-deflection curves in ABAQUS, with Bond-Slip

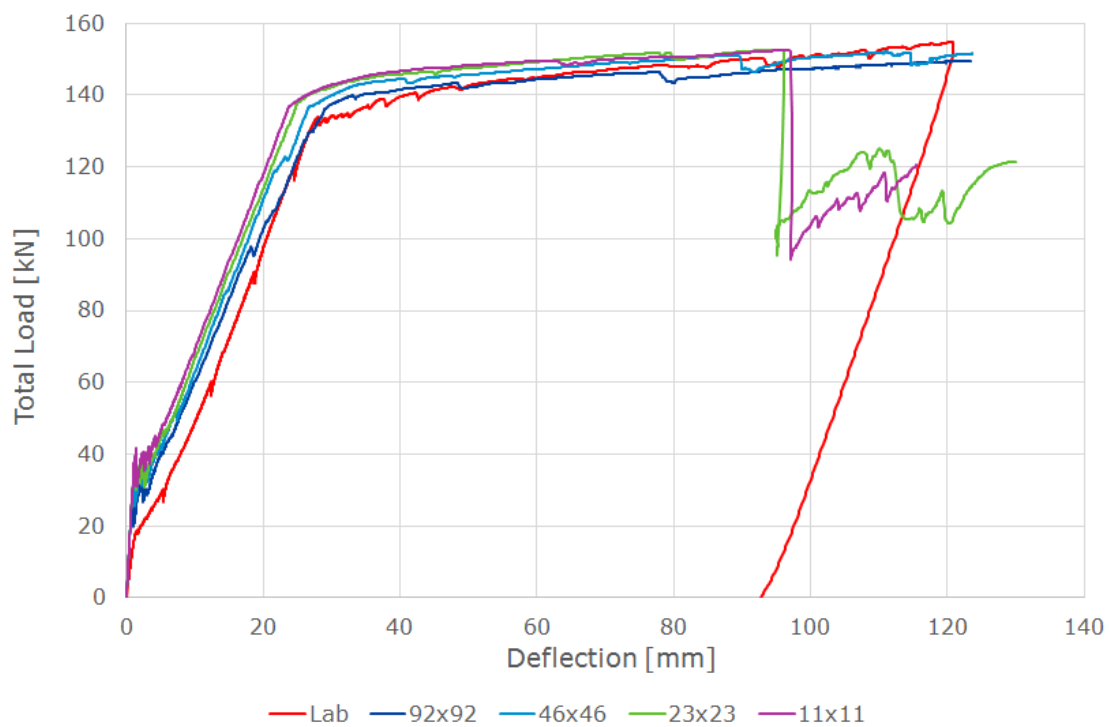


**Figure 6.11:** B1: Effect of different mesh densities on the load-deflection curves in DIANA, with Bond-Slip

For the mesh sizes 11 x 11 mm and 23 x 23 mm in DIANA, crushing of the concrete at a deflection of approximately 95mm has caused the load-deflection diagrams to suddenly drop at this level.

The maximum crack width sizes for each of the mesh densities in ABAQUS and DIANA are displayed in table 6.1 for the load levels of 30 kN, 60kN, 90kN and 120kN. These values have not been arbitrarily chosen, rather they are the load levels at which images were taken of the crack patterns, and measurements of the maximum crack widths were made in the laboratory.

Mesh Size	30 kN [mm]	60 kN [mm]	90 kN [mm]	120 kN [mm]
<b>ABAQUS</b>				
92x92	0.12	0.46	0.68	1.01
46x46	0.01	0.30	0.46	0.67
23x23	0.00	0.24	0.37	0.55
11x11	0.00	0.02	0.25	0.38
<b>DIANA</b>				
92x92	0.30	0.65	0.89	1.20
46x46	0.12	0.39	0.57	0.80
23x23	0.08	0.33	0.48	0.62
11x11	0.09	0.24	0.39	0.59
<b>Lab</b>				
	0.12	0.20	0.26	0.33

**Table 6.1:** B1: Maximum crack width size, according to mesh size

The crack patterns related to each of these load levels and mesh densities, for each software, are provided in full in section A.1.1.

### 6.2.1.2 Discussion of Results

#### Load-deflection

Four mesh densities were compared in ABAQUS and DIANA. When comparing the load-deflection results from both software, it is obvious that the greatest variations occur within ABAQUS.

From the mesh study for perfect bond, in section 6.1.1, the main effect of changing mesh densities in ABAQUS was the change in the yield point. Whilst this is also seen when the mesh density is changed and bond-slip is included, there is also an additional difference; a change in cracking loads. This effect was observed in another sensitivity study performed for perfect bond, that is, when the smeared length was changed.

In ABAQUS, as only the bottom layer of longitudinal reinforcement had bond-slip included, uncertainties arose as to whether this was appropriate (mixing embedded and bond-slip reinforcement), and if it were, which smeared length should be taken. This was discussed in detail in section 5.4.2. At that point, two concepts were proposed (assuming that the combination is okay):

1. Smeared Crack Length = length of element
2. Smeared Crack Length > length of element

The ABAQUS models in this section utilized approach 1. It is evident that either the smeared crack length was incorrectly taken (i.e. approach 2 should have been used), or that there is an issue including embedded and bond-slip in a single model. The results at first glance appear to support the first conclusion. Given that approach 2 should be used, then a smeared length somewhere between  $l_{el}$  and 100 mm should be taken. For larger mesh sizes, the difference in the two recommended values is small (92 vs 100 mm), and hence the results are closer to the experimental. As the mesh becomes finer, then the difference between the two values becomes greater (11 vs 100 mm), and the results become more inaccurate.

This will be explored more fully in section 6.2.3 when a greater smeared length is taken for the 11 x 11 mm mesh.

For both ABAQUS and DIANA, it should be noted that the inaccuracy of the results for the analyses with the coarser mesh is also likely in part due to the poor mesh quality. It is easier to understand when looking at the elements in the figures showing the crack patterns in section A.1.1. As the distance from the level of the bottom longitudinal reinforcement bar to the base of the beam is 30 mm, taking a mesh size of 46 or 92 mm will mean that for the lowest layer of elements, their length is 1.5 to 3 times greater than their height. This is a poor mesh, and hence would have contributed to the poor quality of the results.

Looking back at the load-deflection curves from DIANA, it is clear that there is less variation in the results when adjusting the mesh density. If only the load-deflection results for the 23 x 23 mm mesh and 11 x 11 mm mesh are compared (ignoring the larger two due to poor mesh quality), then there is very little difference in the results. Both mesh densities yield at approximately the same point, and also fail at similar points as well. The reason they fail "prematurely" (that is, at lower deflections than the lab beam shows) is that the bond-slip relationship introduces too much stiffness into the analyses, or perhaps that a shear retention factor should have been introduced.

### **Maximum Crack Widths**

Caution should be made when comparing the crack sizes and patterns at early states of loading to the laboratory beams. This is because those beams tested in the laboratory were already cracked due to drying shrinkage before loading began.

It is unsurprising that the maximum crack sizes on average decreases as the mesh density decreases. When a coarse mesh is used to capture cracking, several cracks

which would exist in reality would be contained within a single element are combined into a single crack.

Whilst the finest mesh density in ABAQUS shows a very good agreement with the laboratory results in later loading stages, it is questionable whether this is just coincidence, given the inaccuracy of the load-deflection results. The lack of crack sizes at early stage of loading is a result from the delayed onset of cracking as the mesh sizes decrease, as seen in figure 6.10 (load related to the initiation of cracking increases, with finer mesh).

In DIANA, where bond-slip is utilized for all longitudinal and stirrup bars, the mesh size providing the most accurate crack sizes is 11 x 11 mm. Greater differences occur for later loading points, however for early cracks, it captures the size well. The reason why it does not capture the maximum crack sizes so well at later load stages becomes more apparent when viewing the crack patterns. At later load stages, the DIANA models do not fully develop some cracks, hence leading to the cracks in the surrounding area to grow larger than they should, overestimating the maximum crack sizes.

### **Cracking Patterns**

Looking at the crack patterns from the beams in ABAQUS, it is clear that the large amount of early cracking of the experimental beams has not been captured by the FE models, further enforcing their appearance is from non-experiment related reasons. From 60 kN of loading onwards, similar numbers of cracks are observed in the 46 x 46 mm and 23 x 23 mm mesh, however with better definition in the latter sized mesh. The cracking behaviour of all beams is not consistent with the laboratory results, however the mesh size 23 x 23 mm appears to match best from all, given crack location.

Interesting behaviour is observed through all load stages in the 11 x 11 mm mesh, whereby a cross-style (or inverted-V) cracking pattern occurs in the mid-span. It commences at the end of the stirrups, which are embedded in this case. This cracking pattern is likely caused by the combination of embedded and bond-slip reinforcement. In reality, the ends of the stirrups would experience some slip, however as they are embedded in this case, cracking commences there.

Looking at the cracking patterns in DIANA, a mesh density of 23 x 23 mm or 11 x 11 mm is necessary to capture the full definition of the cracking pattern. Comparing the results at load level 120 kN it is clear that the 11x11 mm mesh captures the results best. Given how closely the cracks are situated to each other in the laboratory beam, it is unsurprising that a finer mesh is required to achieve similar definition.

### 6.2.2 Effect of the Smeared Length (DIANA)

In section 4.1.3.2, two smeared lengths were proposed for concrete modelling where bond-slip is included, where:

- $l_s = \sqrt{A}$ , and
- $l_s = \sqrt{2A}$ .

To measure the effect of different smeared lengths have on the results, one mesh density is tested with two smeared lengths. Due to the high computation time of running the 11 x 11 mm mesh, the 23 x 23 mm mesh was selected instead.

This mesh was run in DIANA, with the smeared lengths of:

- 23mm, and
- 32.6mm.

#### 6.2.2.1 Results

The load-deflection results are displayed in figure 6.12, and the maximum crack widths for the load levels 30, 60, 90 and 120 kN are listed in table 6.2

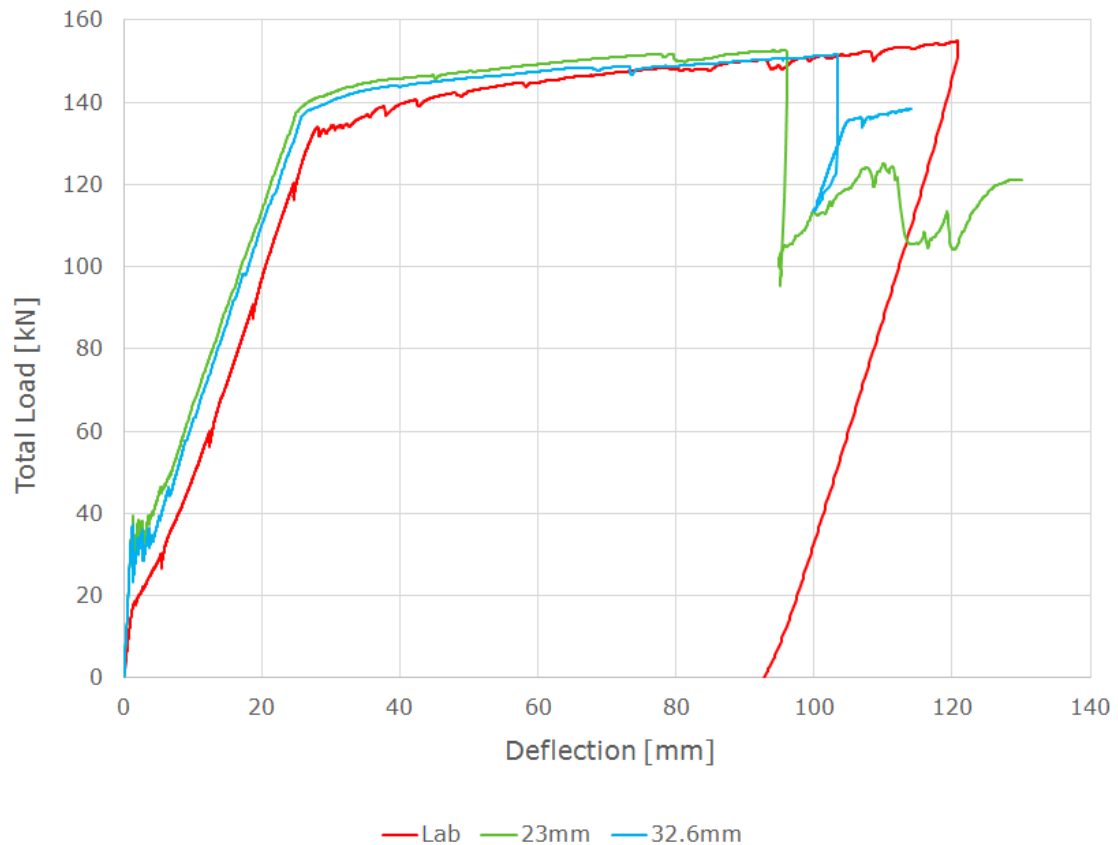


**Figure 6.12:** B1: Effect of different smeared lengths on the load-deflection curves in DIANA, with Bond-Slip

Smeared Length [mm]	30 kN [mm]	60 kN [mm]	90 kN [mm]	120 kN [mm]
<b>DIANA</b>				
23	0.08	0.33	0.48	0.62
32.6	0.22	0.47	0.67	0.91
<b>Lab</b>				
	0.12	0.20	0.26	0.33

**Table 6.2:** B1: Maximum crack width size, according to smeared length (DIANA)

The crack patterns related to each of these load levels is provided in full in section A.1.2.

### 6.2.2.2 Discussion of Results

This section compared the two approaches for the smeared length, where it could either be defined as either:

- $\sqrt{A}$
- $\sqrt{2A}$

#### Load-deflection

Comparing the results using a 23 x 23 mm mesh, there is only minimal impact on the load-deflection results. Utilizing a smeared length of 32.6 mm ( $\sqrt{2A}$ ) will move the load-deflection curve down and right slightly. Whilst this captures a slightly closer result to the lab result in relation to the deflection prior to yielding, the yielding load and the ultimate deflection, it does fail at a lower ultimate load.

The "ultimate" load of the laboratory beam (keep in mind that it didn't fail at this load, it was just unloaded) is 153.8kN, whilst for the smeared length of 23 mm it is 153.5 kN, and for the 32.6 mm smeared length it is 151.43 kN.

It is likely that the reinforcement amount in the finite element models is somewhat lower than that from the lab, however, even in the case where there were more reinforcement bars, the same relationship could be expected. That is, the ultimate load is somewhat underestimated when using a larger smeared length. In this situation, it leads to an underestimation of the ultimate load.

#### Maximum Crack Widths

The effect on the maximum crack size is significantly greater, with more inaccurate results being obtained from a smeared length of 32.6 mm, for all load levels. It resulted in a maximum crack width approximately 30% larger than for a smeared length of 25 mm.

### **Crack Patterns**

It is clear from looking at the crack patterns as to why there are such large variations in the maximum crack widths. Between the two beams, there is very little difference between the crack patterns themselves. The same numbers of cracks are on average seen, with only small variations in their general locations and direction of growth. As greater deflections were seen from the load-deflection curve for the smeared length of 32.6 mm, however no changes in the numbers of cracks, then it is clear that these cracks only opened further to allow for overall greater deflections in the beam.

With minimal changes in the crack patterns and load-deflection results, but more significant differences in the maximum crack size, a smeared length of  $\sqrt{A}$  is taken for future analyses.

Our results are consistent with the findings of Rots, given that higher order elements were used for the analyses in DIANA, a smeared length of  $\sqrt{A}$  should be used (Rots 1988).

### 6.2.3 Effect of the Smear Length (ABAQUS)

As was discussed in section 5.4.2, the decision was made to only include bond-slip on the bottom-most layer of longitudinal reinforcement, due to the high modelling time required to include it. The remainder of the reinforcement is embedded in the concrete.

Assuming that it is appropriate to mix embedded reinforcement with those including bond-slip, there are no recommendations in literature as to which smeared length should be taken. Theoretically, it should be a value which is greater than the value which would be taken if it had been fully bond-slip ( $l_s = l_{element}$ ), but less than what would have been taken if it was fully embedded ( $l_s = 100\text{ mm}$ ).

The two smeared lengths that were selected are:

- 11 mm; and
- 46 mm.

#### 6.2.3.1 Results

The load-deflection results are displayed in figure 6.13, and the maximum crack width size from the two analyses are displayed in table 6.3.

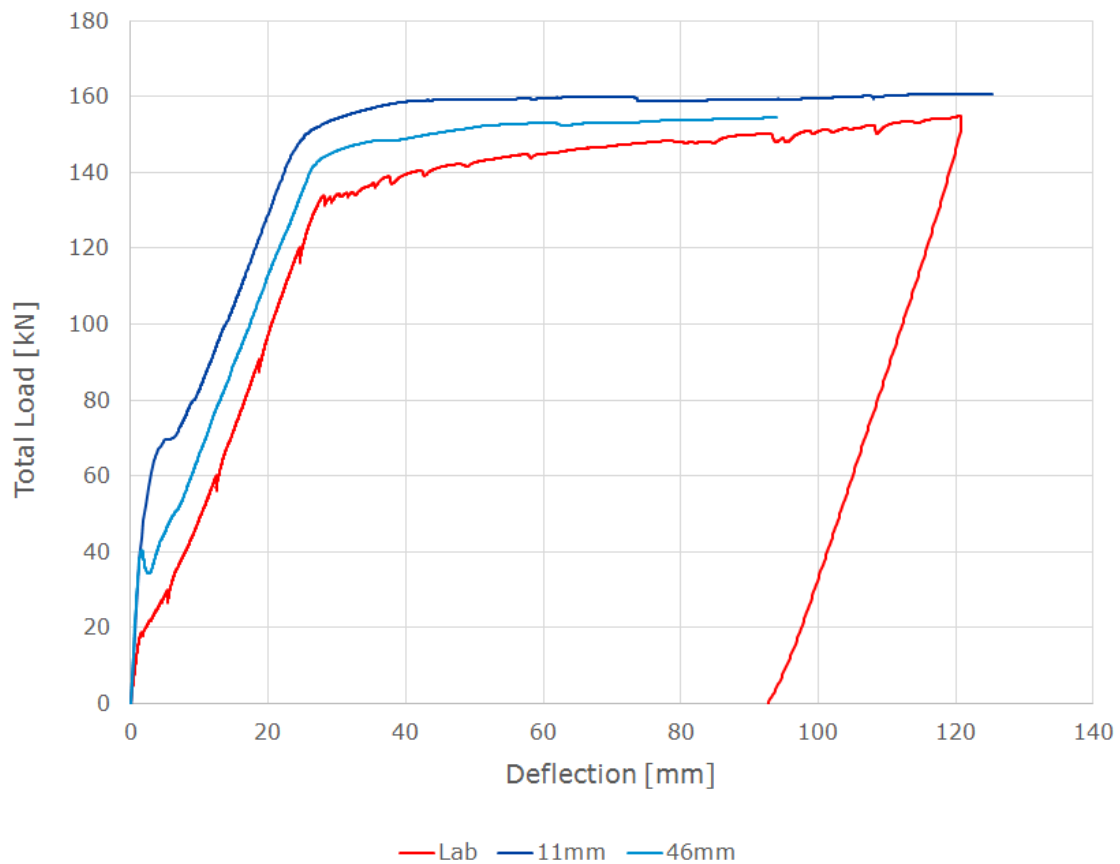


**Figure 6.13:** B1: Effect of different smeared lengths on the load-deflection curves in ABAQUS, with Bond-Slip

Note that the analysis of the smeared length of 46 mm was cancelled prematurely due to an unrelated issue in the computer running the analysis. Due to the longer run-time and the limitations of time on the thesis, it was not reanalyzed.

Smeared Length [mm]	30 kN [mm]	60 kN [mm]	90 kN [mm]	120 kN [mm]
<b>ABAQUS</b>				
11	0.00	0.02	0.25	0.38
46	0.01	0.79	1.29	1.77
<b>Lab</b>				
	0.12	0.20	0.26	0.33

**Table 6.3:** B1: Maximum crack width size, according to smeared length (ABAQUS)

The crack patterns related to each of these load levels and smeared lengths, is provided in full in section A.1.3.

### 6.2.3.2 Discussion of Results

#### Load-deflection

As was discussed in section 6.2.1, the appropriateness of combining embedded and bond-slip reinforcement is still to be determined. It was found in that section that utilizing a smeared length equal to the length of the element does not yield accurate load-deflection results. It was proposed that a smeared length with a value greater than the length of the element might prove more accurate, as an appropriate value would have to lie somewhere between the length of the element (full bond-slip) and 100 mm (full embedded), due to the combination of bond-slip and embedded. Hence a value of 46 mm was tested.

From the load-deflection curve in figure 6.13, it is clear that utilizing a smeared length of 46 mm yields a more accurate result compared to that 11 mm. It affects all points of the load-deflection graph, from the cracking load, yield point and the post-yield response. The result from utilizing 46 mm aligns closer to the expected result, when comparing against the results obtained from the embedded reinforcement load-deflection curves. From load-deflection results solely, it is already clear that a smeared length of 46 mm is more appropriate in this case.

#### Maximum Crack Widths

Whilst the load-deflection results show a more accurate result utilizing a smeared length of 46 mm, the opposite response is observed when comparing the maximum crack width sizes. In this case, using a smeared length of 46 mm results in highly inaccurate crack widths.

As no case was found in literature where a combination of embedded stirrups and a bond-slip longitudinal reinforcement bar was used, it is difficult to know what effect combining them may have. It is likely that it was just coincidence that the smeared length of 11 mm yielded more accurate results, as the overall beam deflection is much less at these load levels than any other beam analysis. Hence, it shouldn't be unexpected that the crack width sizes should be this small.

### **Crack Patterns**

When comparing the crack patterns, much improved behaviour is observed when utilizing a smeared length of 46 mm. As was already observed from the load-deflection result, the cracking load is significantly increased when a smeared length of 11 mm is used. It is therefore unsurprising that at 60kN of loading, there are no cracks observed for 11 mm, but already 6-10 cracks in the 46 mm beam. It isn't until 90 kN that distinct cracks are observed, and even at that point, the number severely lags behind the 46 mm beam.

For both beam models, the same cross/inverted-V pattern is observed, with cracks initiating from the ends of the stirrups. As was mentioned in a previous section this was likely due to the combination of embedded and bond-slip reinforcement in the beams. As the ends of the stirrups should experience some slip in reality, as they are embedded in this case, they cause cracking at these locations.

When comparing against the experimental data at 120 kN of loading, the 46 mm model shows the greatest correlation. In the lab beam, after the location of the load-plate, 4 cracks can be seen. Only 3 are seen in the 11 mm beam, whilst the 46 mm beam captures 4 cracks. For the remainder of the span, the beam tested in the laboratory shows 10 cracks, whilst the 11 mm beam shows 6 and the 46 mm shows 8. The locations are more consistent with a smeared length of 46 mm as well.

When considering the improvement in load-deflection results, alongside the accurate cracking patterns, the smeared length of 46 mm will be utilized in further models with a mesh density of 11 x 11 mm. The non-correlation of the crack widths is put down as a side effect of including embedded reinforcement in the beam with bond-slip.

### 6.2.4 Effect of the Tension Model (DIANA)

In section 4.1.5.3, three tension response curves were proposed for concrete tensile modelling in DIANA. They were:

- fib 2010 model code;
- Hordijk; and
- Exponential.

The influence of these three models on the results is tested in DIANA, with a constant fracture energy of 0.1474 N/mm.

#### 6.2.4.1 Results

Figure 6.14 displays the influence on the load-deflection diagram with each tension curve.

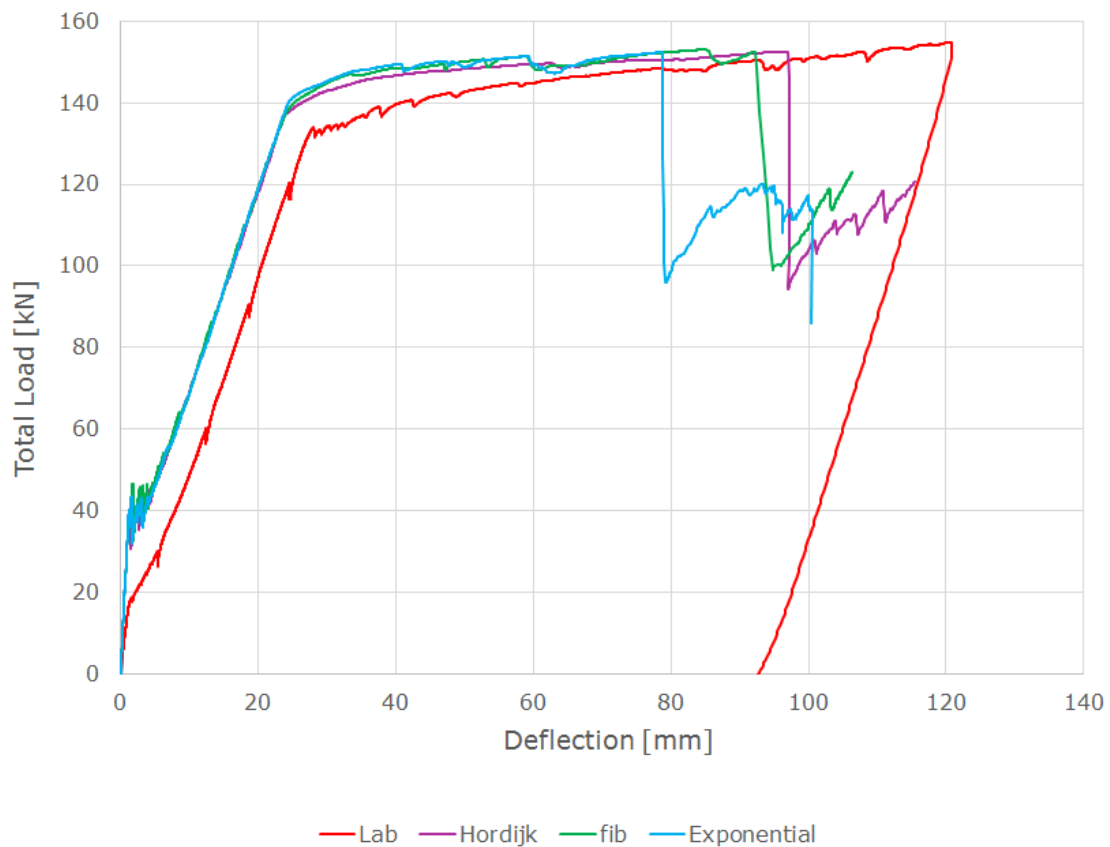


**Figure 6.14:** B1: Effect of different tension models on the load-deflection curves in DIANA, with Bond-Slip

The maximum crack width size at 30kN, 60kN, 90kN and 120kN is displayed in table 6.4.

Tension Model	30 kN [mm]	60 kN [mm]	90 kN [mm]	120 kN [mm]
<b>DIANA</b>				
Hordijk	0.09	0.24	0.39	0.59
fib	0.12	0.28	0.47	0.63
Exponential	0.11	0.27	0.43	0.58
<b>Lab</b>				
	0.12	0.20	0.26	0.33

**Table 6.4:** B1: Maximum crack width size, according to tension model (DIANA)

The crack patterns related to each of these load levels and tension models is provided in full in section A.1.4.

#### 6.2.4.2 Discussion of Results

##### Load-deflection

Looking at the load-deflection curves for different tension models in DIANA, there are only minor differences in the results. Most notably is the failure point, however there is also a slight difference in the yield point.

Comparing the failure point, the failure load is the same between the different curves. The exponential model however failed earliest at a deflection of approximately 79 mm, followed by the fib curve at 92 mm, and the Hordijk curve at 97 mm. The laboratory beam was not loaded until failure, so it is not possible to directly compare against this result. Furthermore, it is suspected that the amount of reinforcement in the FE models was less than that in the experimental tests.

Whilst improvements in all curves might be obtained by adjusting the bond-slip model input, the same general relationships seen here would likely also be observed in that case. Therefore, it is likely that the Hordijk curve would likely correlate closer to that from the lab result in relation to failure deflection. However, as the rebar amount may change, this may not hold true.

As well as changes in failure deflection, there is also a minor difference in the yield point between curves. The Hordijk curve is slightly closer than the other two curves, however minor advantages would only be observed from this.

Generally, when comparing the load-deflection curves of the three tension models available in DIANA, little difference is observed. However, more pronounced differences exist between the maximum crack width results, and the crack patterns.

### **Maximum Crack Width**

In terms of the maximum crack size, the results from the Hordijk tension curve are the closest to the laboratory results, with the exception of the earliest load level. The stress-strain relationship in figure 4.6 can provide some insights as to why there are such differences in the crack sizes for later loading levels. Assuming a similar cracking pattern, it could be assumed that the stress level in one crack would be consistent between tension models. At lower levels of stress in the tension softening relations, the strain level in the Hordijk curve is lower than the other two, with the fib curve displaying the greatest strain levels. This matches what is observed in the results.

### **Crack Patterns**

The crack patterns reveal some interesting differences between the different tension models. At 30 kN of loading, the same single crack can be observed in all three models, at approximately the same location along the beam.

However, at 60 kN the differences between the models becomes more apparent. The Hordijk model displays the greatest number of cracks (approximately 9), whilst the fib model shows the least (7-8). This comes at no surprise given the results on the maximum crack sizes. It is logical that the fib model will display less, albeit larger cracks. The distribution of cracks is better in the Hordijk model as well, more closely resembling the experimental results.

For the load levels of 90 and 120 kN, the crack patterns of the Hordijk and exponential tension models more closely are related to the experimental results, with similar distributions and numbers of cracks. In the mid point of the span, both models capture the same number of cracks, however not all cracks are as fully developed as those in the lab beam. Whilst the lab beam shows 4 fully developed cracks after the load-plate, the Hordijk shows 3 fully developed and 1 half-developed crack, and the exponential and fib show 2 fully developed and 2 half-developed cracks. Whilst the Hordijk tension curve relates closer to the lab result, there are still cracks which do not fully develop, causing the maximum crack width size to be overestimated.

The fib model appears to display a repetitive cracking pattern along the span, with equally spaced large and small cracks. Whilst the number of cracks approximately match what is observed in the laboratory, the pattern of large-small cracks is unusual.

The Hordijk curve was adopted for future models, largely due to having the most accurate maximum crack width sizes, but also as the crack patterns were as, if not more, accurate than the other models at all levels of loading.

### 6.2.5 Effect of the Damage Model (ABAQUS)

In section 4.1.4.3, two methods of calculating the damage plasticity factors was discussed. The influence these two models have on the results in ABAQUS is presented in this section.

#### 6.2.5.1 Results

Figure 6.15 displays the influence the two damage models have on the load-deflection curve.

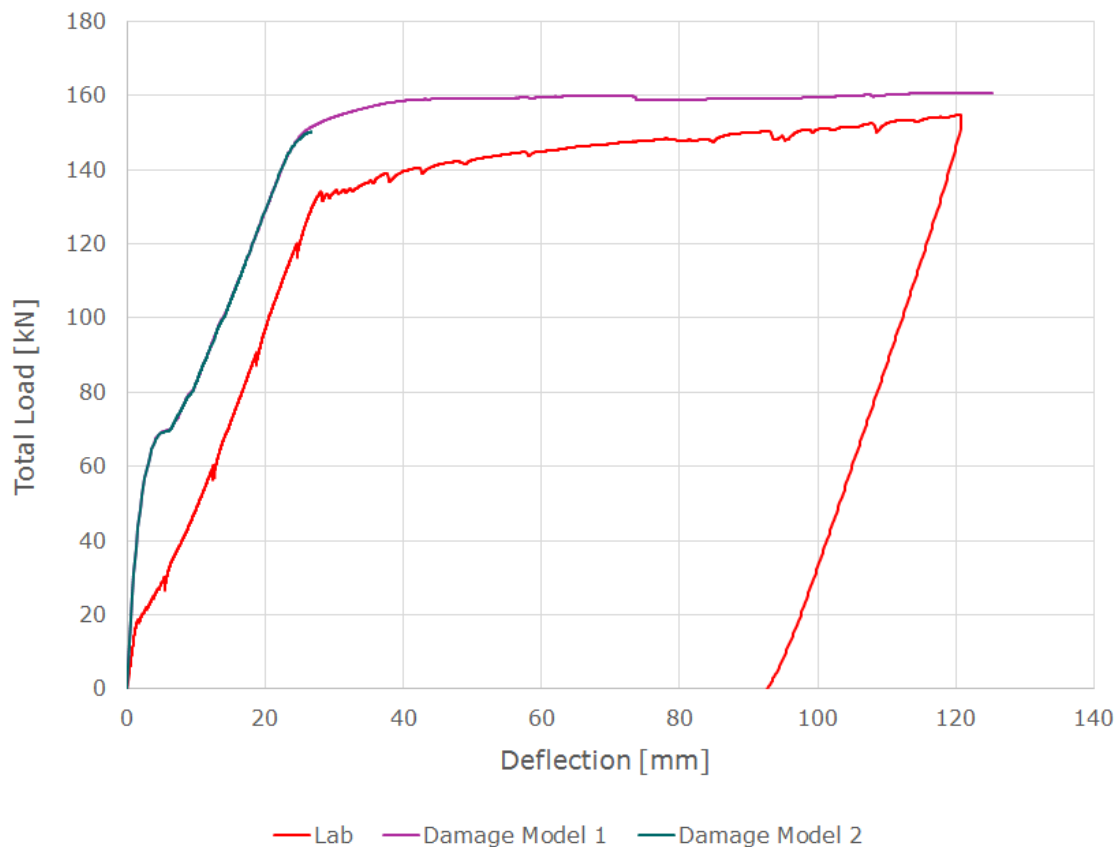


**Figure 6.15:** B1: Effect of different damage models on the load-deflection curves in ABAQUS, with Bond-Slip

The analysis for damage model 2 stopped due to convergence issues at a deflection of approximately 27mm. It is possible that the analysis may have continued beyond this point if a smaller viscosity parameter was specified, but the time required to run the analysis would have increased dramatically, and the choice was made not to do so.

The maximum crack widths at the load levels of 30, 60, 90 and 120 kN is displayed in table 6.5.

Damage Model	30 kN [mm]	60 kN [mm]	90 kN [mm]	120 kN [mm]
<b>ABAQUS</b>				
1	0.00	0.02	0.25	0.38
2	0.00	0.01	0.29	0.42
<b>Lab</b>				
	0.12	0.20	0.26	0.33

**Table 6.5:** B1: Maximum crack width size, according to damage model (ABAQUS)

The crack patterns related to each of these load levels and damage models is provided in full in section A.1.5.

### 6.2.5.2 Discussion of Results

#### Load-deflection

Whilst no difference was observed in the load-deflection results of the two models when the reinforcement was embedded, that is not the case when bond-slip is included. Specifically, damage model 2 suffered from convergence issues and terminated prematurely at the yield point.

A comparison of the two damage models was performed in section 4.1.4.3, which showed the difference in the tension damage factors became close to 0.1 at the first crack size  $\omega_1$ , when a smeared length of 10 mm is used. This would mean a greater loss of elasticity in the cracked section with unloading. ABAQUS/Standard does not cope well with sudden changes in the model, which would have occurred in this case. Whilst decreasing the viscosity parameter in this case might have meant a full load-deflection curve could have been obtained, it would have come at a computational cost.

#### Maximum Crack Width & Crack Pattern

Comparing the crack width sizes, it is clear that damage model 1 produces slightly more accurate results. Little difference is observed for the crack patterns however.

Damage model 1 was selected for the following analyses, mainly due to its ability to reach convergence in the smallest period of time, and resulting in the most accurate crack sizes.

# 7

## Finite Element Results & Discussion

Prior to any discussion of the results of the SUREBridge beams, it should be re-emphasized that the exact reinforcement amount in the beams tested in the laboratory was unknown. The ultimate load capacity is also unknown, all were unloaded prior to it being reached.

For the analyses of beam 1, only the longitudinal reinforcement layers 1, 2 and 4 were active, with the remaining layers (3 and 5) inactive. This was a decision made early in the modelling process, however was changed to include layers 3 and 5 for later analyses of beams 2 - 4. It was determined that the amount of time to rerun the results of beam 1 would be too great, and only little changes would have been observed in the results, as reinforcement layers 3 and 5 lie close to the neutral axis for this case.

Comparison of the finite element results and the experimental data will progress assuming the reinforcement amount is the same between them, however in reality it may have been different. Therefore, any difference between experimental and FE results could also be accounted for in part by this.

Photographs of the cracks in the web of the laboratory beams were provided to the authors by Jincheng Yang. The figures shown in this section of these cracking patterns (from the lab) were developed from these photographs by the authors. It should be emphasized that only the web of the concrete beams are shown for comparison (not the full SUREBridge beams).

The laboratory result obtained from Jincheng Yang has been included in all figures for ease of comparison.

## 7.1 Beam 1

### 7.1.1 Perfect Bond

From the sensitivity analyses performed in section 6, the best-fit results from ABAQUS and DIANA were determined.

For ABAQUS, the result which best fits to the experimental data has the following features:

- Mesh density: 25 x 25 mm
- Smear length: 100 mm
- Damage model: 1
- Dilation angle: 30°
- Viscosity parameter:  $10^{-4}$

For DIANA, the result which best fits the experimental data has the following features:

- Mesh density: 25 x 25 mm
- Smear length: 150 mm

#### 7.1.1.1 Load-Deflection Results

The load-deflection results for both ABAQUS and DIANA are displayed together in figure 7.1 with the results from the laboratory testing.

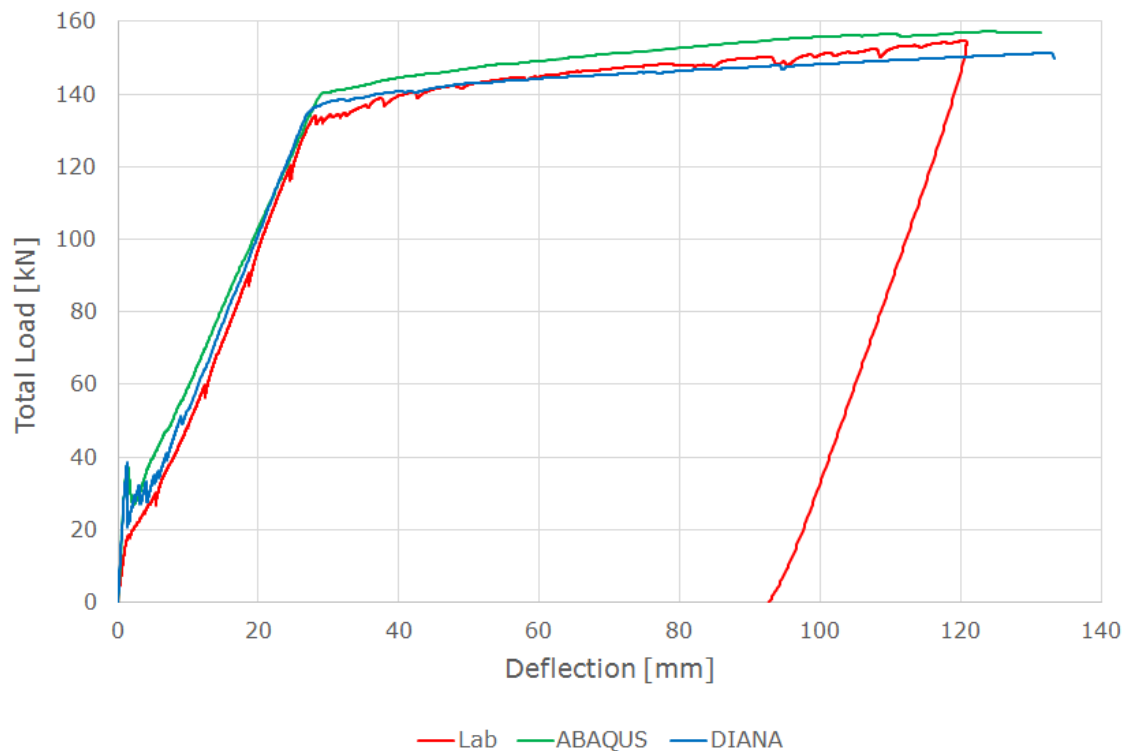


**Figure 7.1:** B1: Load-deflection of beam 1, Perfect bond

### 7.1.1.2 Discussion of Results

Due to the low quality cracking data when reinforcement is embedded in the concrete, only the load-deflection results can be compared for this case. From figure 7.1, it is clear that the same general behaviour is obtained from both the model from ABAQUS and from DIANA. Prior to yielding, there is some difference in the gradient of the FE curves; DIANA tends to capture the gradient of the experimental result better than what ABAQUS does, however they converge around the yield point of the experimental result.

The yield points captured by both software are also different; DIANA almost matches the experimental result, whilst ABAQUS overestimates it by approximately 7 kN. Additionally, the gradient of the post-yield response in ABAQUS matches that of the experimental, whilst the DIANA model underestimates it.

It is important to note that the exact reinforcement design of the experimental beam was unknown, so the finite element analyses progressed assuming three layers of reinforcing bars. If the experimental beams were proven to contain more reinforcement, it could in fact be the case that with this adjustment in FE, the DIANA model would more closely match the results.

As the beam was tested in the laboratory weren't loaded until their ultimate point, it is somewhat difficult to make comparisons for the late-stage loading.

Given the ability of both ABAQUS and DIANA to capture the load-deflection response of the experimental beam given embedded reinforcement, these same model and material parameters will be used for the analysis of beams 2, 3 and 4.

### 7.1.2 Bond-Slip Included

From the sensitivity analyses performed in section 6, the best-fit results from ABAQUS and DIANA was determined.

For ABAQUS, the result which best fits to the experimental data has the following features:

- Mesh density: 11 x 11 mm
- Smeared Length: 46 mm
- Damage Model: 1
- Viscosity parameter:  $10^{-4}$
- Dilation angle:  $30^\circ$

For DIANA, the result which best fits the experimental data has the following features:

- Mesh density: 11 x 11 mm
- Smeared Length: 11 mm
- Tension Model: Hordijk

#### 7.1.2.1 Load-Deflection Results

The load-deflection results for both software are displayed together in figure 7.2 with the load-deflection curve from the laboratory testing.

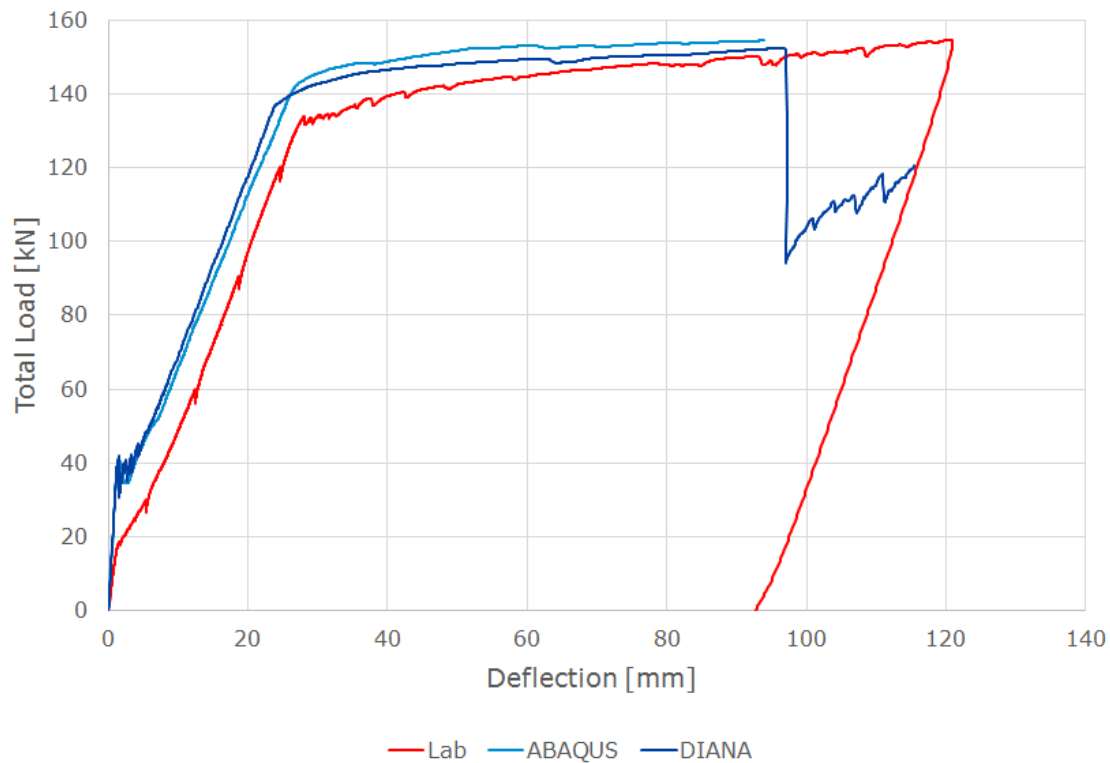


**Figure 7.2:** B1: Final Curves in ABAQUS and DIANA, with Bond-Slip

The analysis in ABAQUS was terminated prematurely due to an unrelated computer issue. Unfortunately due to time constraints, it was not repeated, however it would be expected to progress past this point.

The analysis in DIANA failed at approximately 97mm of loading due to concrete crushing.

#### 7.1.2.2 Maximum Crack Width Results

The maximum crack widths for these analyses is displayed in table 7.1.

Source	30 kN [mm]	60 kN [mm]	90 kN [mm]	120 kN [mm]
ABAQUS	0.01	0.79	1.29	1.77
DIANA	0.09	0.24	0.39	0.59
Lab	0.12	0.20	0.26	0.33

**Table 7.1:** B1: Maximum crack width size

#### 7.1.2.3 Crack Patterns

The crack patterns from both analyses at load levels 90 and 120 kN are compared against the cracking pattern obtained from the laboratory in figures 7.3 and 7.4 respectively.

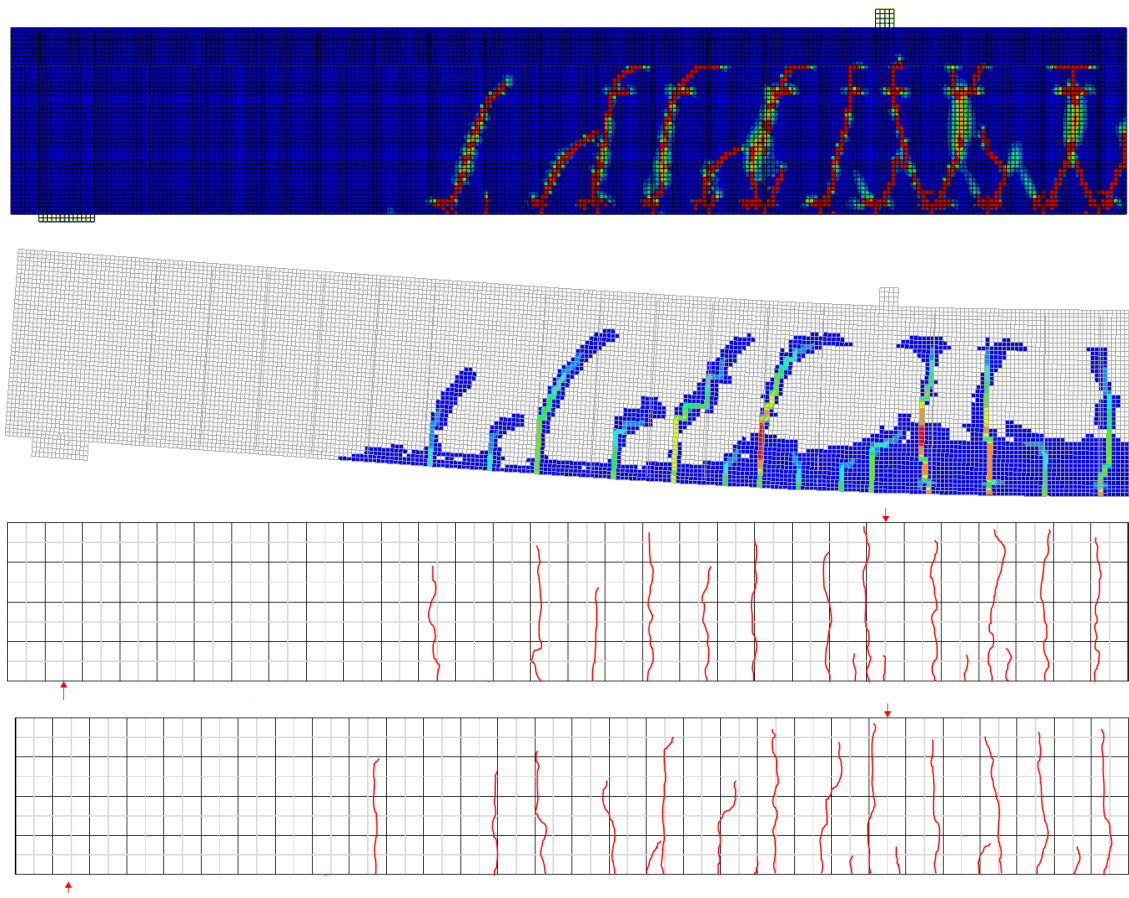


**Figure 7.3:** B1: Crack Patterns at 90 kN. From top to bottom: ABAQUS, DIANA, Lab (LHS) and Lab (RHS)

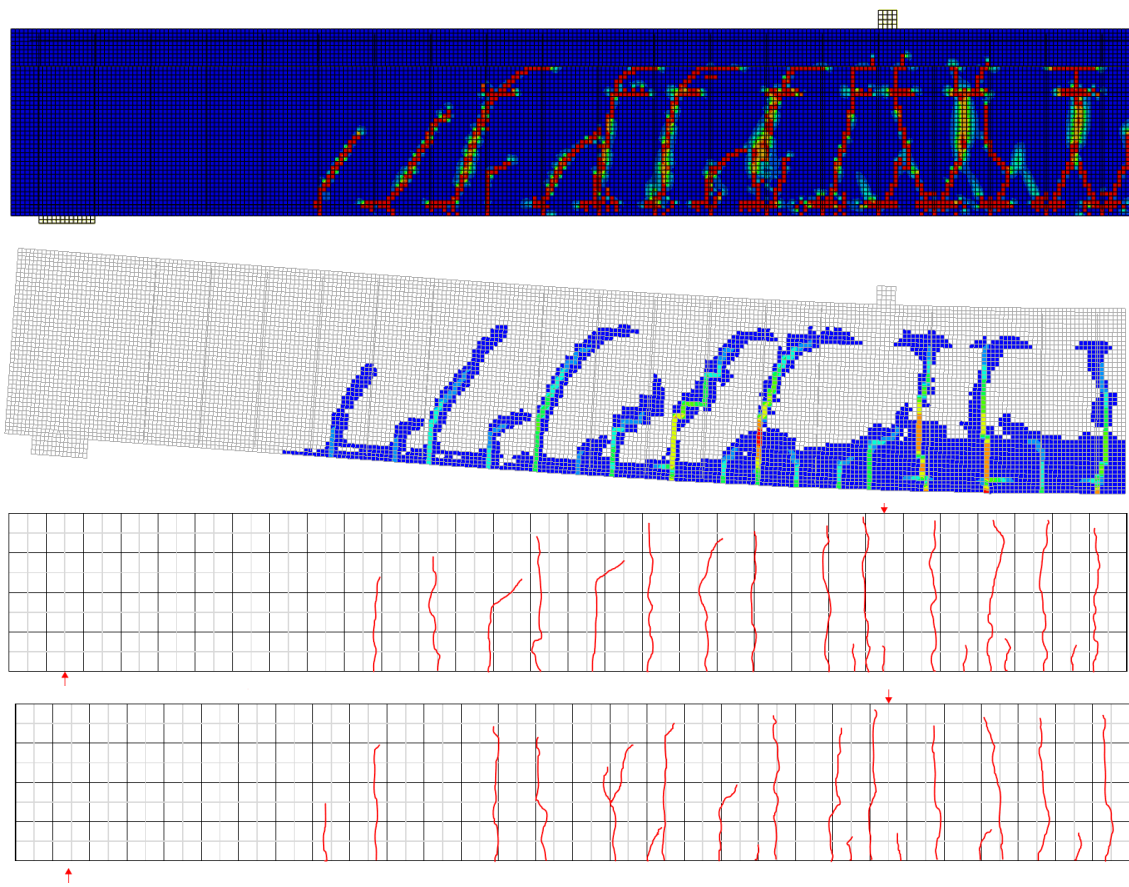


**Figure 7.4:** B1: Crack Patterns at 120 kN. From top to bottom: ABAQUS, DIANA, Lab (LHS) and Lab (RHS)

### 7.1.2.4 Discussion of Results

#### Load-deflection

The load-deflection results when including bond-slip are not as closely aligned to the laboratory results as they were when perfect bond was assumed. However, it is important to keep in mind that as the exact reinforcement amount is unknown in the experimental beams, it is difficult to directly compare the results and draw conclusions.

Both ABAQUS and DIANA overestimate the yield point of beam 1, however tend towards a similar "ultimate point" (i.e. the point when the beam was unloaded in the lab). The gradient of the pre-yield stage matches that of the laboratory result well for both software.

The bond-slip relationship used in both of the models is from the fib 2010 model code. It assumes good bond behaviour between the concrete and steel. It is clear however, that by including this relationship, the elasticity of the beam has been changed. It might have been worthwhile to investigate whether the "all other bond condition" defined in section 4.2.3 might have yielded better results, otherwise the difference may also have something to do with the bond-slip curve itself. The values are obtained from pull-out tests, however a slightly different curve may show a better relationship for loading in this specific case (bending).

Alternatively, whether the introduction of a shear retention factor would have improved the situation, to reduce the shear stiffness of the beam after cracking, remains to be seen.

The DIANA model includes bond-slip in a different way to the ABAQUS model. All longitudinal reinforcement and stirrups have bond-slip defined in DIANA, whilst only longitudinal reinforcement layer 1 has it included in ABAQUS. Comparing the load-deflection curves, it appears as though it is possible to obtain similar results when combining bond-slip and embedded rebar by taking a larger smeared length (46 mm in this case).

#### Maximum Crack Width

Comparing the maximum crack sizes, it appears that there is some crack definition lost when not all steel bars are modelled with bond-slip, as the maximum crack widths more than triple under some load conditions.

In DIANA, the crack width sizes correlate well for the lower load levels, however are nearly double the experimental results at later loads. This difference can be accounted for by the differing crack patterns. Comparing the crack patterns in the laboratory beam against those of DIANA, at the load level of 120 kN, it is clear that there are locations whereby some cracks have not developed. As some cracks have not fully developed, then the cracks in the vicinity have grown larger instead. This has led to an overestimation of the crack width size in DIANA.

For the ABAQUS model, it is clear that the combination of embedded and bond-slip rebar has caused inaccurate crack width readings.

### **Crack Patterns**

Figures 7.3 and 7.4 compare the crack patterns in ABAQUS and DIANA against the crack patterns obtained from the lab. Both left and right sides of the lab beam is included to provide some insight in the variability of cracking behaviour concrete has, largely due to the influence of aggregates and the non-homogeneous nature of the material in reality. Only two later load levels are compared, as some of the early cracking observed in the lab beams was due to drying shrinkage, so is hard to compare against the FE results.

It should be emphasized that only the general cracking features can be compared between the lab and FE beams, due to this variability in cracking behaviour.

At the load level of 90 kN, the lab beams show four large cracks in the mid-span, following the load plate. In both ABAQUS and DIANA, three large cracks are observed, with a fourth half developed crack. The locations are generally consistent with the laboratory beams as well. The definition of cracks in the bottom half of the web for the ABAQUS model is not so clearly defined. Cracking begins at the ends of the stirrups, creating a cross or inverted-V pattern. This is likely caused by the stirrups being modelled as embedded. As they would in reality experience some bond-slip, embedding them has caused localized concrete cracking at their ends.

In the remainder of the span, the lab beams show 8 - 9 cracks half or fully formed. In ABAQUS, 7 cracks are visible, whilst in DIANA approximately 6 - 7 cracks are visible, with an additional 3 smaller cracks also forming. The general crack pattern is consistent between the FE beams and the lab beams, except in the section just left of the loading plate, as ABAQUS only shows 1 crack, DIANA shows 3 small cracks, and the lab beams show 2 fully formed.

At the load level of 120 kN, ABAQUS displays several more fully developed cracks than DIANA (9 vs 7 cracks), with the numbers of cracks more closely aligned to those in the lab beams (12 cracks). In DIANA, whilst the number of fully developed cracks are somewhat less, the crack initiating locations (the points along the base of the beam which they develop) are consistent to the lab results, however some of the cracks do not form as fully as they should.

When focusing on the mid-span following the load plate, it is clear that the DIANA model matches exactly the number and location of cracks, however one of these does not obtain the same height as it has in both lab beams. The ABAQUS beam on the other hand captures the same number of fully developed cracks, but the location is not consistent with either half of the lab beams.

Considering that only longitudinal reinforcement level 1 is included with bond-slip in the ABAQUS model, the load-deflection results and the crack patterns are consistent with the results for a beam whereby bond-slip is included for all bars in the

model. Whilst further in-depth investigation should be performed to conclusively state whether it is possible to combine embedded and bond-slip reinforcement with an adjusted smeared length, from these results it suggests it might be feasible.

## 7.2 Beam 2

### 7.2.1 Perfect Bond

This section will present the results for beam 2 when the bond-slip between the concrete and the steel is assumed to be perfect. For the models in ABAQUS and DIANA, the mesh density taken was 25 x 25 mm.

Additional material properties taken for the analyses in ABAQUS are as follows:

- Smear length: 100 mm
- Damage Model: 1
- Dilation angle: 30°
- Viscosity parameter:  $10^{-4}$

Additional material properties taken for the analyses in DIANA are as follows;

- Smear Length: 150 mm
- Tension Model: Hordijk

#### 7.2.1.1 Load-Deflection Results

The load-deflection results from both ABAQUS and DIANA are displayed in figure 7.5, together with the result obtained from the laboratory testing.

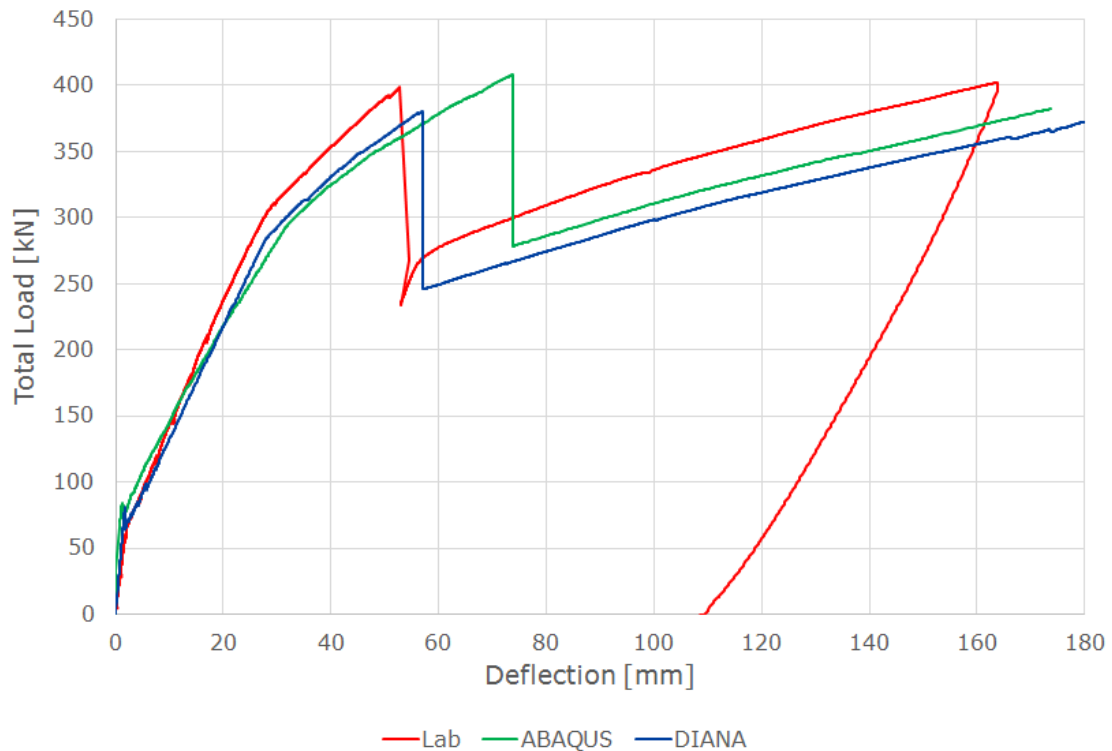


**Figure 7.5:** B2: Load-deflection of beam 2, Perfect bond

As discussed in section 5 the analysis of beam 2 was completed with the use of two FE models; one to capture behaviour prior to CFRP failure, and one to capture post-failure. The point of failure of model 2.1 was determined according to the level of strain in CFRP. As strain gauges were utilized in the laboratory, the level of strain related to the delamination of the CFRP was recorded. This was approximately 0.010866.

When running beam 2.1 beyond this point in ABAQUS, no delamination is observed. However, the model in DIANA was able to capture this behaviour, as well as the post-delamination behaviour. The load-deflection results from DIANA are displayed in figure 7.6, alongside the laboratory result. At the point of failure, the strain in the CFRP laminates was 0.01155.

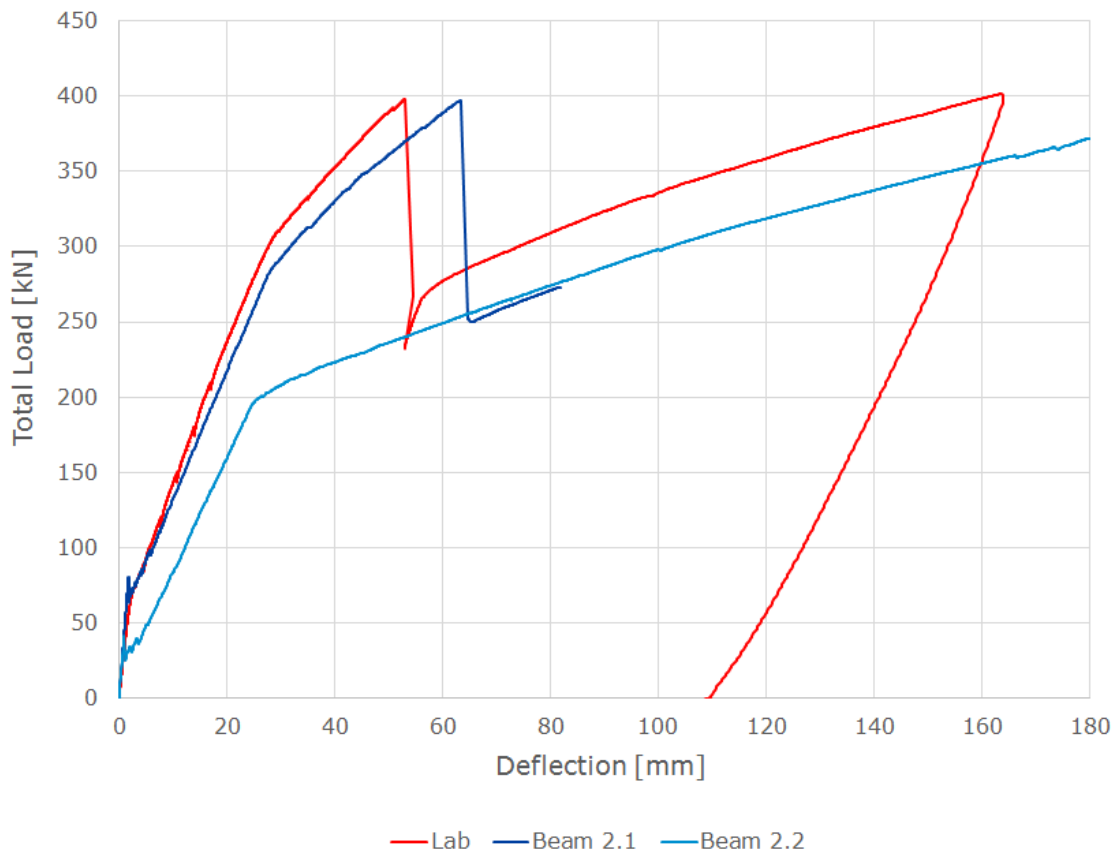


**Figure 7.6:** B2: Load-deflection of Beam 2.1 and 2.2 in DIANA, Perfect Bond

Note: the analysis of beam 2.1 was terminated prematurely by the author, and it is expected that the curve would continue beyond this point in a similar manner as beam 2.2.

In the step just prior to the failure of the CFRP in the model, the crack pattern was as displayed in figure 7.7 and the slip in the interface was as displayed in figure 7.8.

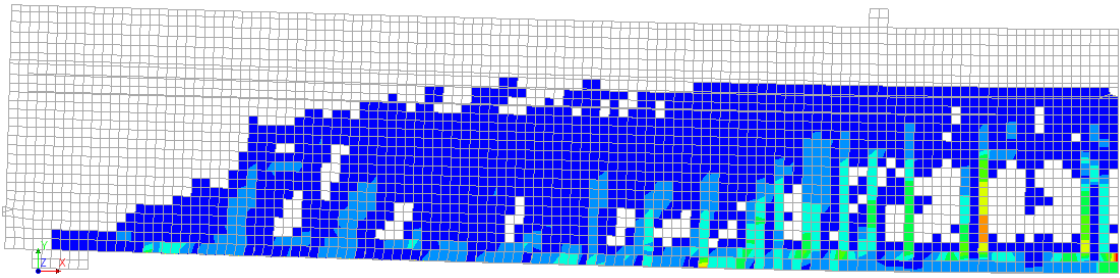


**Figure 7.7:** B2: Crack Pattern in beam 2.1 in DIANA, just prior to failure, Perfect

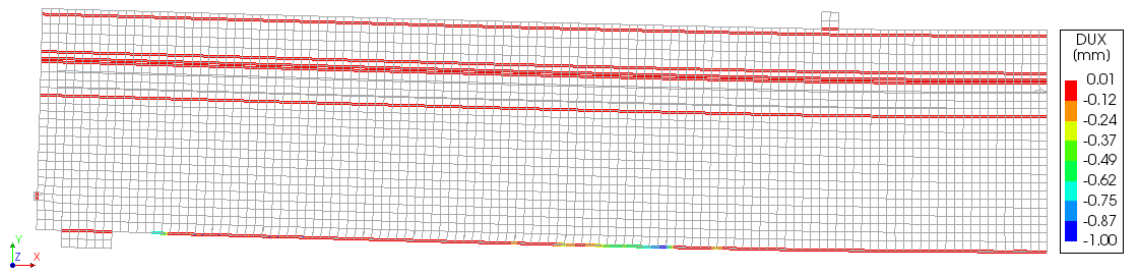


**Figure 7.8:** B2: Slip in the interface in beam 2.1 in DIANA, just prior to failure, Perfect

After failure, the slip in the interface was as displayed in figure 7.9.

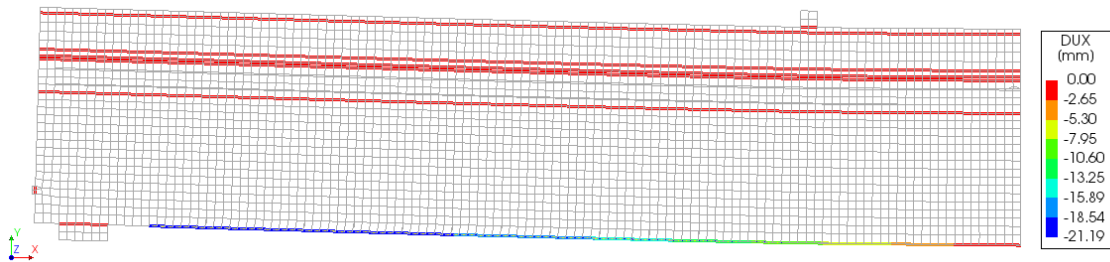


**Figure 7.9:** B2: Slip in the interface in beam 2.1 in DIANA, just following failure, Perfect

### 7.2.1.2 Discussion of Results

Comparing the load-deflection results obtained from the ABAQUS and DIANA models in figure 7.5, there are some significant differences in the behaviour captured by the models. Looking at the gradient of the load-deflection curves prior to the CFRP delamination, little variation can be seen between the two results, however compared to the lab beam, both show greater levels of deflection throughout loading. One possible explanation for this behaviour is that there are significantly more cracks being formed when the reinforcement is embedded, leading to small levels of slip occurring along a greater length of the CFRP and hence leading to the total deflection of the beam to be overestimated.

The most significant difference between the two models is the point at which delamination occurs. One potential explanation for this difference comes from the definition of the bond-slip between the CFRP and the concrete. In ABAQUS, only the ascending branch is defined, whilst in DIANA, the full curve is input. This difference would mean that smaller amounts of slip would occur due to concrete crack formation in ABAQUS, and hence the overall strain in the CFRP would be lower than in DIANA. The failure point would therefore be identified earlier for the DIANA model, which is what is observed in figure 7.5.

When running the ABAQUS model of beam 2.1, no debonding of the CFRP was captured by the analysis. It was therefore necessary to find the failure point of the model by finding the same level of strain in the CFRP at which failure occurred for in the lab. The DIANA model, on the other hand, was capable of capturing the delamination of the CFRP itself, as well as the post-failure response. The reason why the DIANA model was able to predict the delamination point, and the ABAQUS model could not lies in the definition of the epoxy layer between the CFRP and concrete.

In DIANA, the full bond-slip curve in section 4.4.2 was defined, whilst in ABAQUS, only the ascending branch was defined. Without the descending branch input in the model, then the CFRP cannot fail from debonding. To understand why, it is important to understand the mechanism leading to the CFRP debonding.

Along the base of the beam, cracks will begin to form in the concrete through the course of the loading. If you consider the largest of these cracks, it is bonded to the CFRP through this interface layer. As the stiffness of the CFRP is greater than that of the forming crack, the level of strain in the CFRP located over this crack will be less than the crack itself. Hence, as the crack dilates, the CFRP will deform to a lesser degree, causing shear stresses to build up in the interface layer between the CFRP and the crack. These shear stresses building up on either side of the crack opening will cause the CFRP to "slip" into the crack from both sides.

In ABAQUS, as only the ascending branch of the bond-slip behaviour is included, then shear stresses are allowed to continue to build up, only allowing progressive amounts of slip to occur at larger shear stresses.

In DIANA, the full bond-slip relationship is defined, and hence it will reach a point at which infinite slip will occur at zero shear stress (essentially removing the CFRP from the model). In figure 7.8 it is possible to see the amount of slip in the interface just prior to failure. The location of maximum slip aligns with the largest crack size opening on the base of the beam shown in figure 7.7. At the next step in the analysis, the full CFRP interface fails (i.e. reaches the point where infinite slip will occur), which is evident from the slip values registered in figure 7.9.

The importance of including the full CFRP bond-slip relationship is impressed by comparing the ABAQUS and DIANA models. Whilst the failure point of the ABAQUS model can still be determined with the laboratory results, it does make it fully reliant on their existence and accuracy. It also means that if the behaviour of a beam with slightly different dimensions is needed, then laboratory testing would need to occur. The DIANA model is therefore superior to the ABAQUS model in this regard.

When comparing the delamination deflection of the FE models against that of the laboratory beam, it is clear that there are large differences. This likely comes down to the embedding of the steel reinforcement. When comparing the delamination load, both ABAQUS and DIANA captured similar results to the laboratory.

The load related to delamination in the laboratory was 397 kN, whilst in DIANA it was 394 kN (ignoring the ABAQUS model as it didn't predict failure itself). With less than 0.76% difference in results, it can be concluded that an model with embedded steel will still obtain an accurate result for the failure load. This is a promising conclusion, as it would mean that more simplified models could be employed when designing using the SUREBridge solution, reducing computation and modelling time, without a cost to the result. Only the deflection is inaccurate in this case, which would hold no importance in design at ultimate limit state.

Furthermore, the ability of the post-peak response to be captured by the DIANA model is also incredible. It aligns well to the same response from the beam 2.2 model from DIANA, which is to be expected. The reason why this behaviour was able to be captured is due to the analysis options used. Explicit step sizes were defined and a continuation method was specified. Hence, even when convergence isn't reached for a single step, the analysis will still continue. Convergence wasn't reached immediately after the peak response, however it was reached again at a later point.

Following failure, the gradient of the curves are similar, however both underestimate the response from the lab. This is likely due the simplifications made in modelling the GFRP panel. This will be discussed further in section 7.2.2.

## 7.2.2 Bond-Slip Included

This section will present the results for beam 2 when the bond-slip between the concrete and the steel was included in the model. For the models in ABAQUS and DIANA, the mesh density taken was 11 x 11 mm.

Additional material properties taken for the analyses in ABAQUS are as follows:

- Smear length: 46 mm
- Damage Model: 1
- Dilation angle: 30°
- Viscosity parameter:  $10^{-4}$

Additional material properties taken for the analyses in DIANA are as follows:

- Smear Length: 11 mm
- Tension Model: Hordijk

### 7.2.2.1 Load-Deflection Results

The load-deflection results from both ABAQUS and DIANA are displayed in figure 7.10, alongside the result obtained from the laboratory testing.

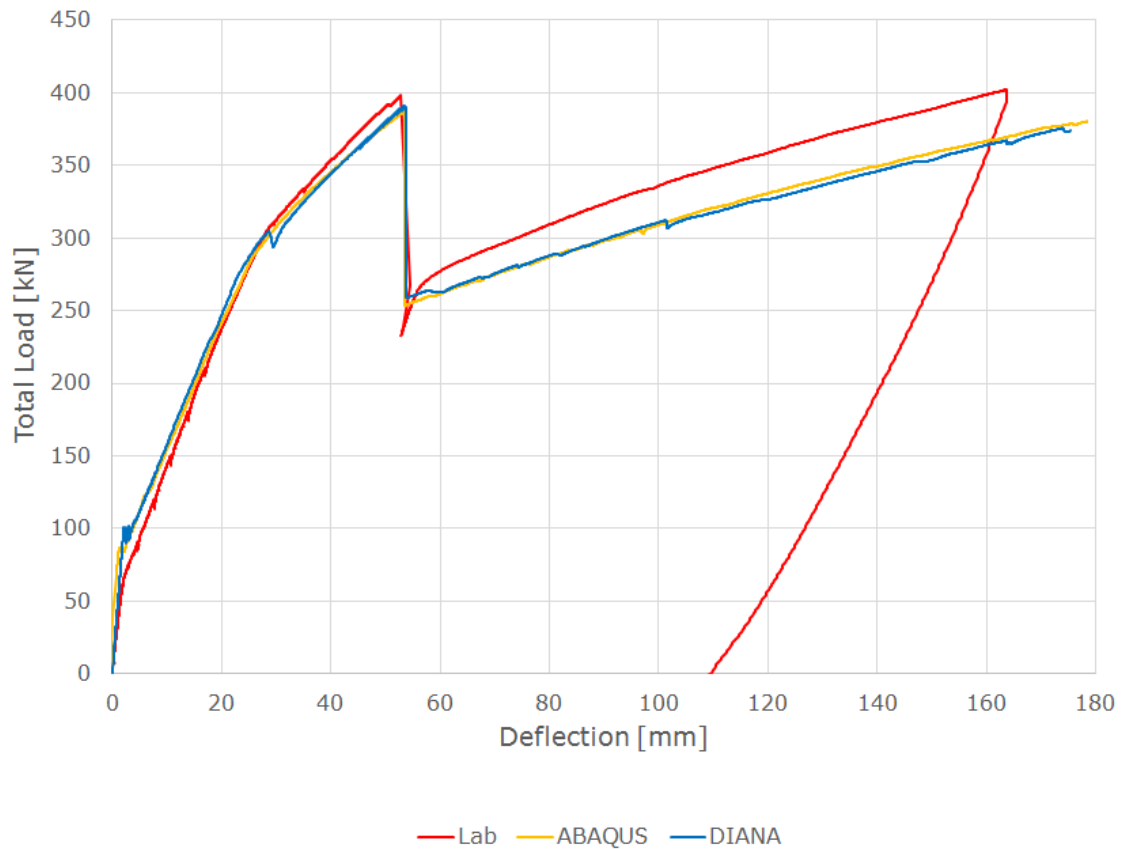


**Figure 7.10:** B2: Final Curves in ABAQUS and DIANA, with Bond-Slip

As discussed in section 5, the analysis of beam 2 was divided into two sections; pre-CFRP failure and post-CFRP failure. The failure point of beam 2.1 was to be determined according to the strain level in the CFRP. In the laboratory testing, the CFRP delaminated from the concrete beam at a strain level of approximately 0.010866, and hence in the FE models "failure" is reached when the CFRP reaches this level.

In figure 7.10, the failure point of the ABAQUS result was calculated according to this method. When the model was left to run after this point, no CFRP delamination was observed. In the DIANA model however, the model itself failed due to delamination. The strain in the CFRP at this point was approximately 0.010934. The model did not run beyond this point, and signalled that there were convergence issues.

Just prior to the failure point, the cracking pattern was as displayed in figure 7.11, with the slip between the CFRP and concrete as displayed in figure 7.12.

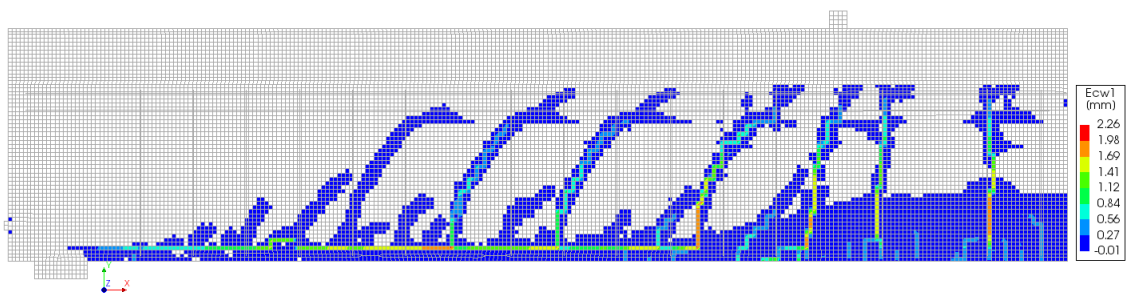


**Figure 7.11:** B2: Crack Pattern just prior to Failure point of DIANA Model, with Bond-Slip

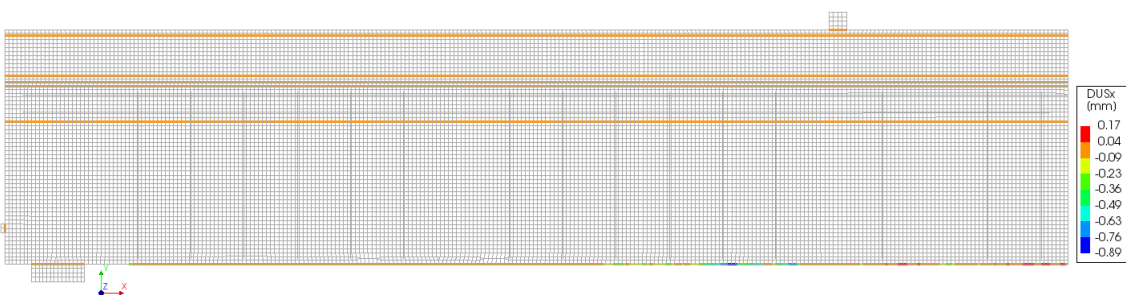


**Figure 7.12:** B2: Interface Slip just prior to Failure point of DIANA Model, with Bond-Slip

Just following the failure point, the cracking pattern was as displayed in figure 7.13, with the slip between the CFRP and concrete as displayed in figure 7.14. It should be emphasized though that convergence was not reached for this step, so these values are not accurate (however they can signal the attempt at a solution).

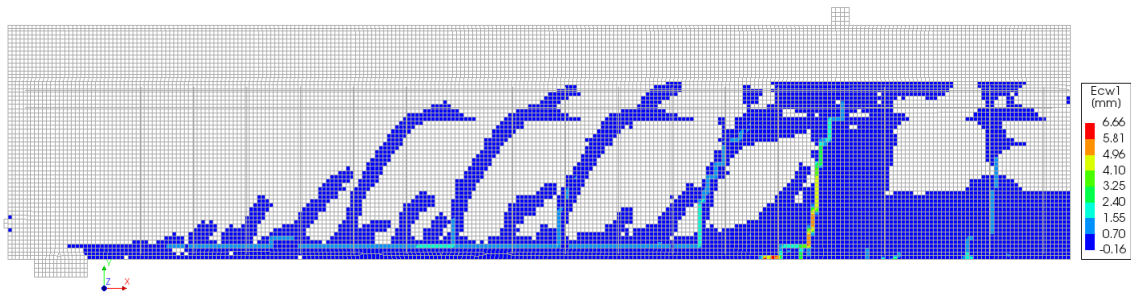


**Figure 7.13:** B2: Crack Pattern just following Failure point of DIANA Model, with Bond-Slip

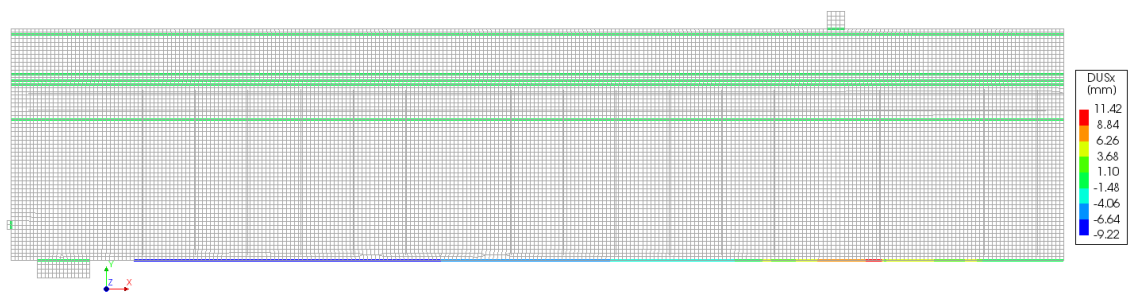


**Figure 7.14:** B2: Interface Slip just following Failure point of DIANA Model, with Bond-Slip

### 7.2.2.2 Maximum Crack Width Results

The maximum crack width size for each of the models is presented in table 7.2, for the load levels of 90, 120, 150 and 180 kN. These load values have not been arbitrarily selected, rather they are the load levels at which images were taken of the crack patterns, and measurements of the maximum crack width were made in the laboratory.

Source	90 kN [mm]	120kN [mm]	150kN [mm]	180kN [mm]
ABAQUS	0.54	0.74	0.99	0.93
DIANA	0.077	0.20	0.29	0.37
Laboratory	0.08	0.12	0.16	0.18

**Table 7.2:** B2: Maximum crack width size

### 7.2.2.3 Crack Patterns

The crack patterns for both analyses at load levels 150 and 180 kN is compared against the cracking pattern obtained from the laboratory in the figures 7.15 and 7.16 respectively.

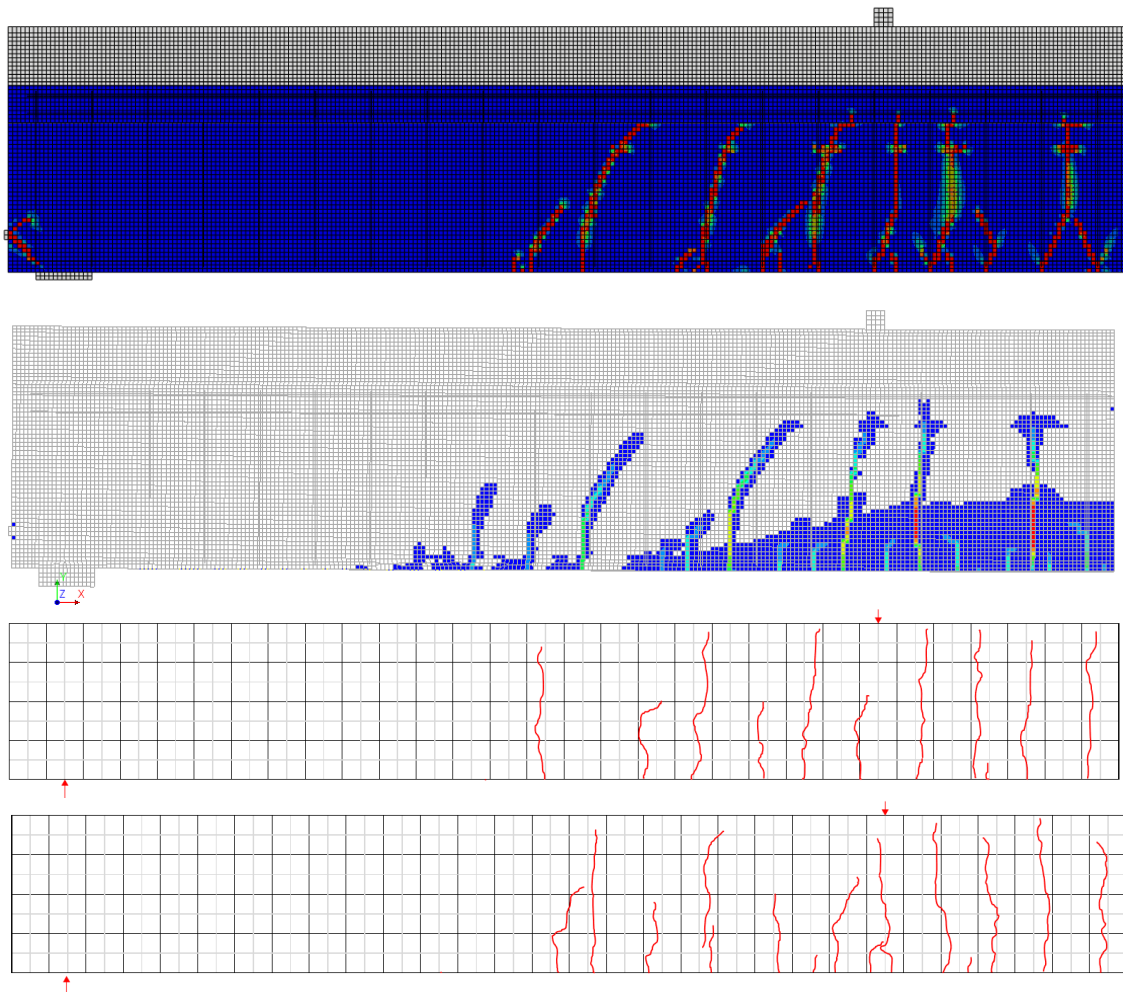


**Figure 7.15:** B2: Crack Patterns at 150 kN. From top to bottom: ABAQUS, DIANA, Lab (LHS) and Lab (RHS)

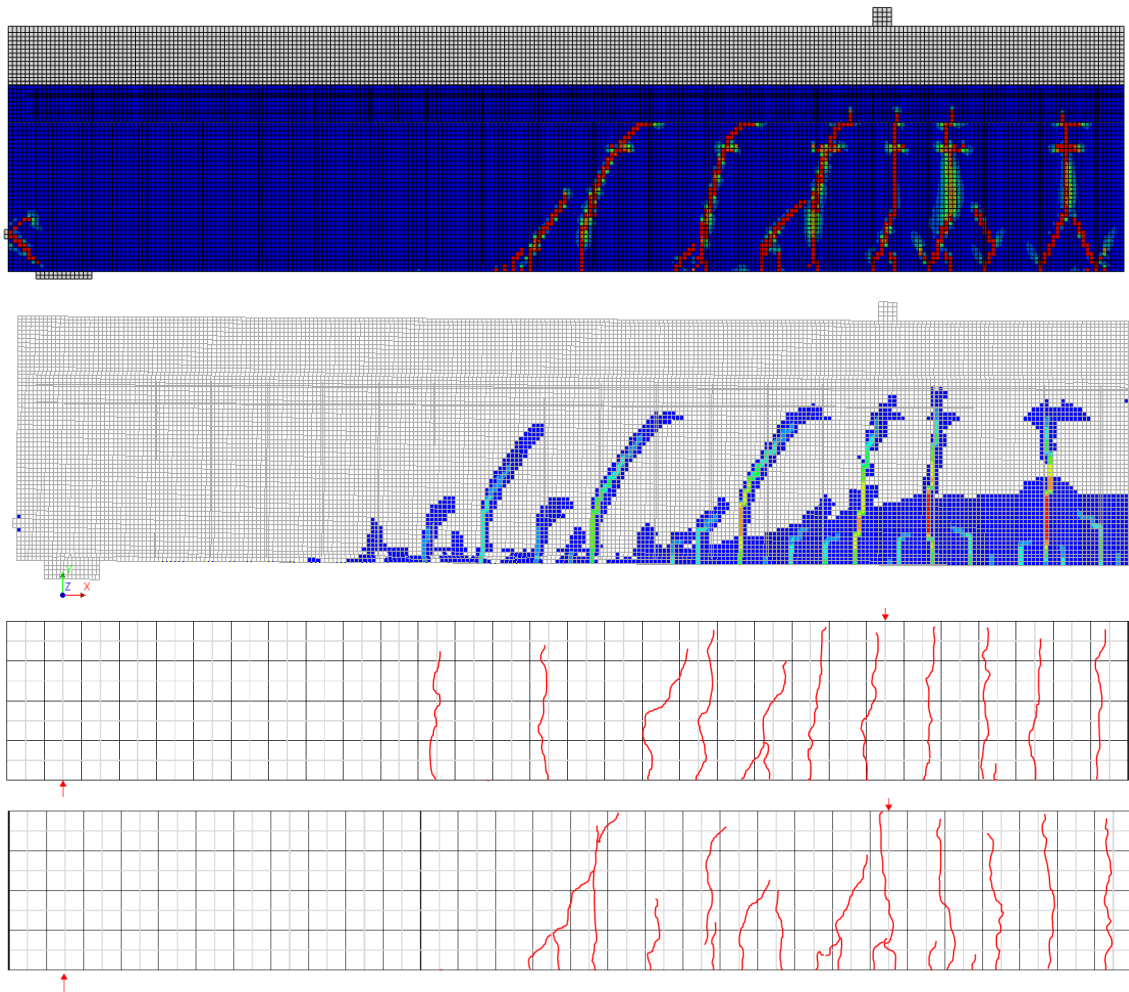


**Figure 7.16:** B2: Crack Patterns at 180 kN. From top to bottom: ABAQUS, DIANA, Lab (LHS) and Lab (RHS)

#### 7.2.2.4 Discussion of Results

##### Load-deflection

Comparing the load deflection results of the models including bond-slip and those with perfect bond, little difference can be observed for the general global behaviour. The point of failure of the beam 2.1 models is better captured when bond-slip is included between the concrete and the steel, than when it was not. This supports some of the conclusions made by other literature (Chen et al. 2011). That is, as the debonding of the CFRP is highly dependent on the cracking of the concrete, it is vitally important to include bond-slip between the steel and the concrete to capture the failure point.

As was discussed for the perfect bond results in section 7.2.1, the delamination point of beam 2.1 in ABAQUS had to be determined from the strain levels in the CFRP from the lab testing. In the same way that the perfect bond model in DIANA was able to capture the delamination failure of the CFRP, the bond-slip model from DIANA is also able to, however unlike the former, it wasn't able to capture the post-peak behaviour. This is likely due to the more complex responses occurring due to bond-slip, which the software wasn't capable to analyze implicitly.

The failure point of both the ABAQUS and DIANA models are very similar. The strain level of the CFRP in the DIANA model at delamination was 0.010934, which is close to the actual strain in the CFRP when it failed in the laboratory (0.010866).

Looking at the level of slip in the interface just prior to delamination failure point, as shown in figure 7.12, it is clear that there are several cracks along the base of the beam which are causing localized slip. This is also evident from the crack patterns observed in figure 7.11. From the level of slip, it can be concluded that these locations have experienced localized delamination, and with one more step, full global delamination occurs. It becomes evident from figure 7.13 which crack was responsible for instigating the failure of the CFRP, that is, one of the cracks just left of the loading plate.

Comparing the delamination load of the DIANA model (390kN) to the experimental beam (397kN), only 1.76% difference between values is observed. Whilst slightly less accurate than the result achieved when the steel was embedded, it was capable of capturing the failure deflection with significant more accuracy.

The load deflection results for the post-CFRP failure behaviour in both software do not correspond well with the response measured from the laboratory. The difference likely results from the definition of the GFRP panels. In section 3.4 three ways of defining the GFRP properties was made:

1. Component based
2. Equivalent web
3. Equivalent stiffness

Approach 1 was not possible, as it would have required the definition of each of the components which exist in 3D in the 2D plane. This would be overly complicated.

The second and third approaches were both simplifications of reality in one way or another. Approach 2 was utilized in this model. This meant that the components which lay between the two flanges were smeared across the whole width, giving it equivalent properties. It was not clear in the calculations received by the company how many webs were smeared along what depth of panel. Nor did it note how many flats and edges were included in the calculation. In the lab, beam 2 had four longitudinal webs in the GFRP panels, whilst five were in beam 3. The differences are summarized in the table below. No account for these differences were made in the FE modelling.

	<b>Beam 2</b>	<b>Beam 3</b>
Number of Webs [-]	4	5
Total Web Thickness [mm]	38.5	56.1

Furthermore, the web material properties are obtained from smearing the edges, flats and flutes across the width. Depending on what proportion of these components were included in the lab, and their thickness, the material properties would differ greatly. If an edge (with an  $E = 21GPa$ ) was included in the GFRP panel of beam 2, then the overall elasticity of the section would increase, compared to if it were just composed of flats (with  $E = 12GPa$ ).

It is therefore suspected that the simplifications made in the modelling of the GFRP panels is responsible for the difference in these curves. Additionally, it could also have something to do with the reinforcement amount. This will be discussed further in section 7.3.2, where the results from beam 3 with bond-slip are presented and discussed.

### **Maximum Crack Width**

Looking at the maximum crack width results, the DIANA model was capable of capturing sizes much closer to the experimental results than ABAQUS was able to. This is hardly a surprise given this same relationship was observed in the results for beam 1. For lower load levels, the results are more accurate, however on average are double the values measured from the test beams.

The inaccuracy of the ABAQUS model is likely due to the combination of embedded and bond-slip reinforcement. For the DIANA model, it becomes apparent when looking at the crack patterns why there are deviations in the maximum crack width size at later load levels. This is because in some areas of the beam, some cracks do not fully develop their height, and hence the cracks in the surrounding areas grows larger. This causes the overestimation at later load levels.

### **Crack Patterns**

Comparing the crack patterns for the load levels of 150 kN and 180 kN, the FE models captured fewer fully developed cracks than the lab beams. For the load of

150 kN, 4 cracks are observed in the mid-span of the lab beams after the load plate. In ABAQUS, only 3 fully developed cracks are observed, however a fourth is half developed. The location of the cracks from ABAQUS are not as close to those in the laboratory as those from DIANA. In DIANA, only two cracks are seen, however there are several smaller cracks in the same location as those in the lab beams. Outside of the mid-span, the crack locations for both FE models are similar enough, and generally coincide with the results from the lab.

For the load level of 180 kN, only little changes are observed in the ABAQUS model compared to the previous load step, however the DIANA has developed more cracks in the length near the support. The cracks in the ABAQUS model more closely resemble the results from the right-hand side of the lab beam, whilst the DIANA model captures the cracks from the left-hand side of the beam. The height of the DIANA cracks are still somewhat lacking in the mid-span, which was also evident from the analysis of beam 1 results.

In the finite element analyses performed by Ma & Kwan (2015), a special crack queuing algorithm was employed, which, after each load application, would search for the concrete element with the highest tensile stress to strength ratio and determine whether it had cracked. By utilizing this method where the stress distribution is step-wise analyzed within the same load step, it is claimed to result in fewer cracks, with more realistic widths. Whether this could be implemented for the analyses in DIANA is to be investigated, however it could result in fewer undeveloped cracks being modelled.

Alternatively, it might be worthwhile investigating whether a shear retention factor might reduce the shear stiffness in the cracked concrete, allowing further development of some of the cracks.

## 7.3 Beam 3

### 7.3.1 Perfect Bond

This section will present the results for beam 3 when the bond-slip between the concrete and the steel is assumed to be perfect. For the models in ABAQUS and DIANA, the mesh density taken was 25 x 25 mm

Additional material properties taken for the analyses in ABAQUS are as follows:

- Smear Length: 100 mm
- Damage Model: 1
- Dilation angle 30°
- Viscosity parameter:  $10^{-4}$

Additional material properties taken for the analyses in DIANA are as follows:

- Smear Length: 150 mm
- Tension Model: Hordijk

#### 7.3.1.1 Load-Deflection Results

The load-deflection results from both ABAQUS and DIANA are displayed in figure 7.17, together with the result obtained from the laboratory testing.

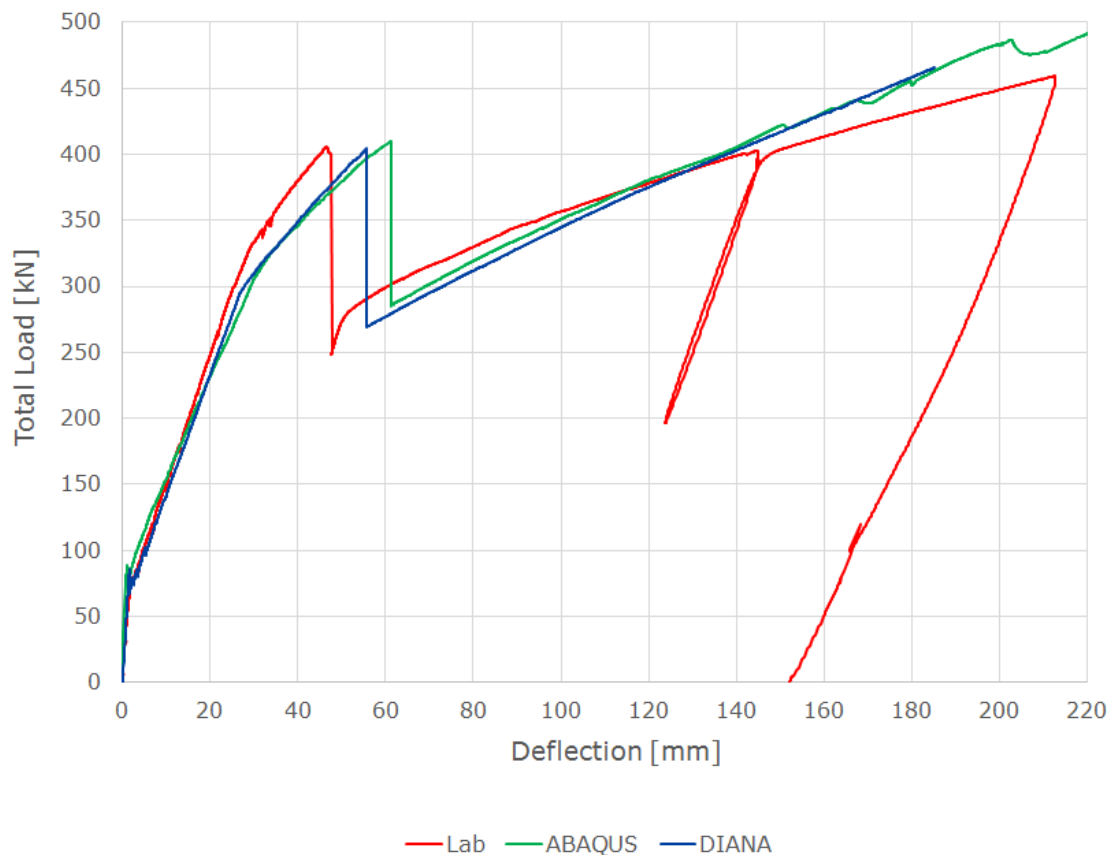


**Figure 7.17:** B3: Load-deflection of beam 3, Perfect Bond

Note: the non-linear response from the ABAQUS model, at late stages of loading, is caused by high compressive stresses in the upper flange.

The failure point of beam 3.1 was determined according to the level of strain in the CFRP laminates. At the strain of approximately 0.010935, it was deemed that "failure" had occurred.

When running beam 3.1 beyond this point in ABAQUS, no delamination is observed. However, in DIANA, both the delamination of the CFRP and the post-peak behaviour was able to be captured. The load-deflection result from beam 3.1 in DIANA is displayed in figure 7.18 alongside the laboratory result.

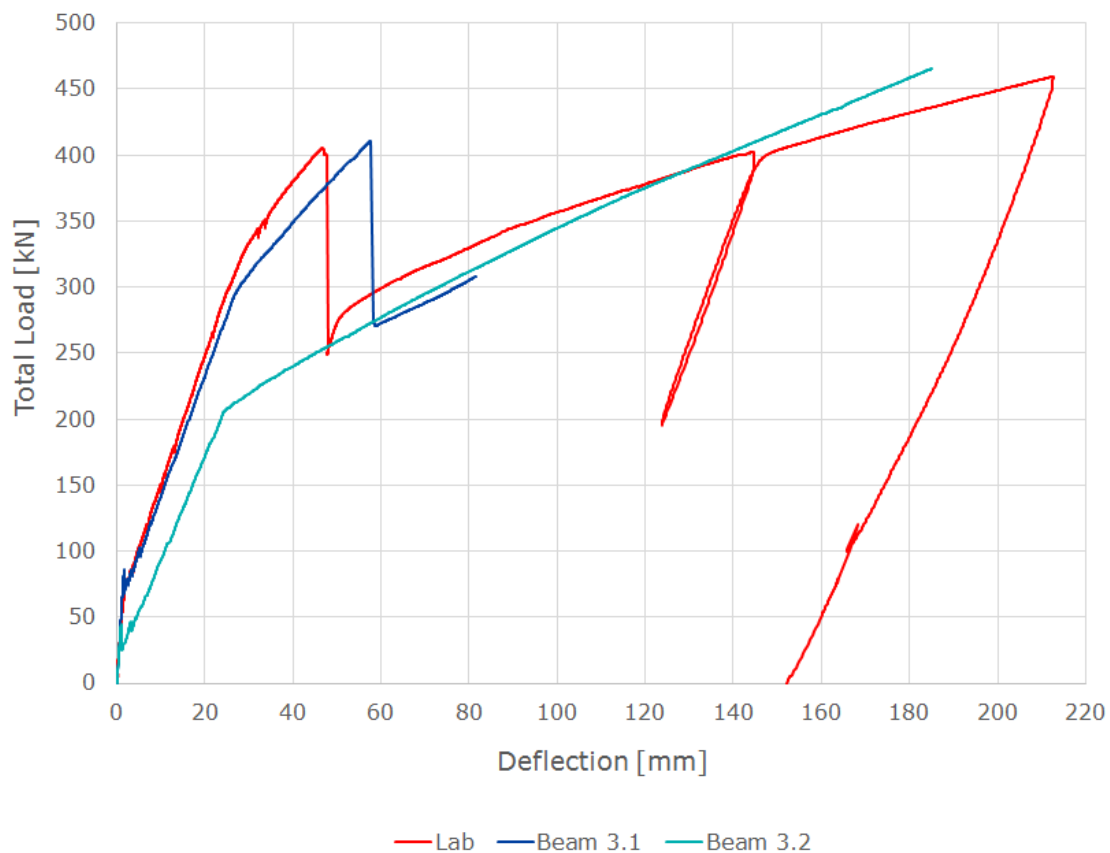


**Figure 7.18:** B3: Load-deflection of beam 3.1 in DIANA, Perfect Bond

Note: the analysis of beam 3.1 was terminated prematurely by the author.

In the step just prior to the failure of the CFRP in the model, the crack pattern was as displayed in figure 7.7 and the slip in the interface was as displayed in figure 7.20.

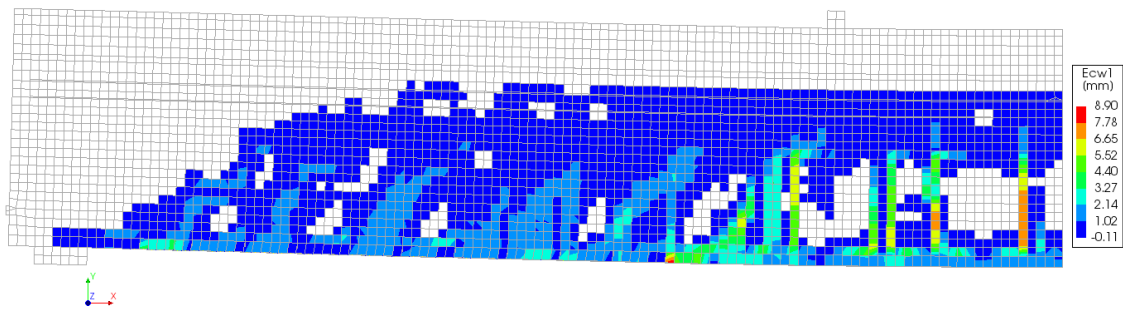


**Figure 7.19:** B3: Crack Pattern in beam 3.1 in DIANA, just prior to failure, Perfect

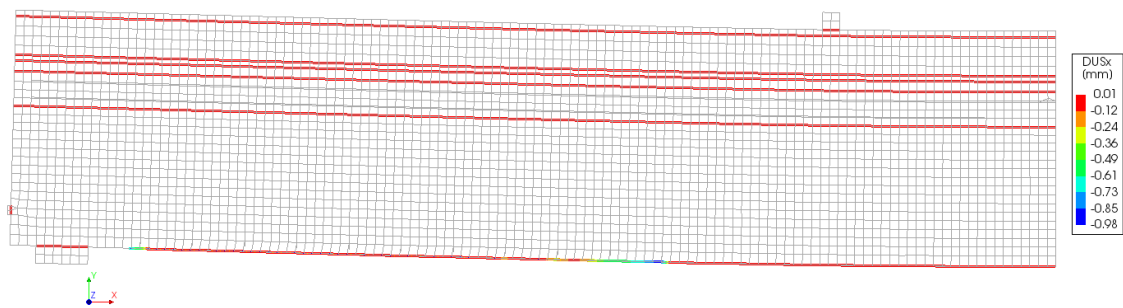


**Figure 7.20:** B3: Slip in the interface in beam 3.1 in DIANA, just prior to failure, Perfect

After failure, the slip in the interface was as displayed in figure 7.21.

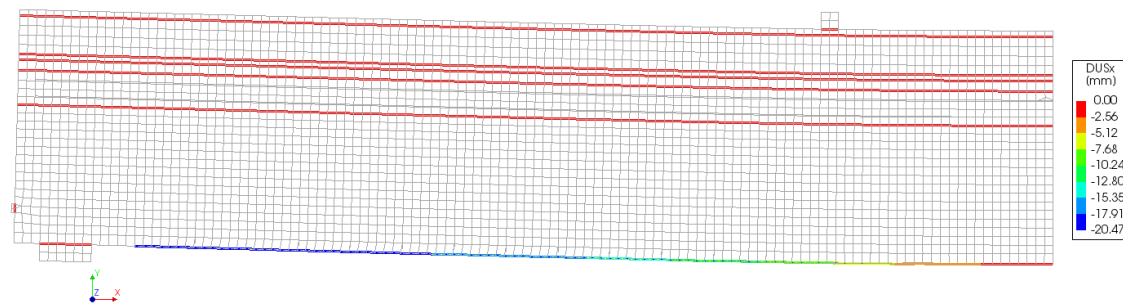


**Figure 7.21:** B3: Slip in the interface in beam 3.1 in DIANA, just following failure, Perfect

### 7.3.1.2 Discussion of Results

Comparing the load-deflection results obtained from ABAQUS and DIANA in figure 7.17, to the experimental results, some differences can be seen. Most notable is the difference between the failure points, and the gradient of the post-peak response. Whilst the load level related to the failure point is consistent between the three sources, the degree of deflection for the FE models is 10 - 15 mm greater than that of the lab. This same observation was made in the analysis of beam 2, perfect bond. The difference is in part due to the non-inclusion of bond-slip between the concrete and steel, but also due to the partial definition of the CFRP bond-slip curve in ABAQUS.

When comparing the load related to delamination, the DIANA model records it at 404 kN, whilst the lab records it at 402 kN (ignoring the ABAQUS result as it didn't predict failure itself). This is a difference of less than 0.5%. Whilst the level of deflection is inaccurate when embedding the steel, it doesn't affect the ultimate load of the beam. Furthermore, when designing to ultimate loads, the deflection is not taken into consideration. This is consistent with the findings for beam 2, and would mean a simplified model for design purposes could be used.

Due to the simplifications in the modelling of the GFRP panels, the results from the beam 3.2 models are not likely to be accurate. On average the response is consistent between the experimental and FE beams, however it wouldn't be expected to capture the correct ultimate capacity without a more accurate representation in the model. As the smeared web approach was taken for the specification of the properties of the GFRP deck, there is no variation in properties or width of the web to account for the differing number or size of the webs which were present in the laboratory, between beam 2 and 3. The same geometry and material properties of the web was consistent between the two models, however this was not the case for the lab beams. This was discussed more in detail in section 7.2.2.

In the same way which DIANA was capable of capturing the delamination failure point of beam 2.1, it was also able to capture the delamination for beam 3.1. From looking at the crack pattern of the beam just prior to the delamination in figure 7.19, it is evident that there is one concrete element on the base of the beam which has a larger crack opening than that of the others. At this location, in figure 7.20, it is possible to see that the slip in this area has already surpassed maximum (greater than 0.23mm, which is the ultimate slip value in the bond-slip relationship). Hence, it can be concluded that local delamination has occurred in this area. With one further step, full delamination of the CFRP occurs, which is what is evident from figure 7.21.

From figure 7.6, it is clear that the post-peak behaviour captured from beam 3.1 is very similar to the response from beam 3.2 at that point. It is expected that if the analysis of beam 3.1 were to continue, it would likely follow a similar path to that of beam 3.2. In that way, the model of beam 3.1 has fully captured the response of the full beam. As mentioned prior, its inability to capture the exact failure point of

the CFRP is likely due to the lack of steel-concrete bond-slip in the model. Ignoring this shortfall, it has captured the general load-deflection response well.

### 7.3.2 Bond-Slip Included

This section will present the results for beam 3 when the bond-slip between the concrete and the steel was included in the model. For the models in ABAQUS and DIANA, the mesh density taken was 11x11mm.

Additional material properties taken for the analyses in ABAQUS are as follows:

- Smear length: 46 mm
- Damage Model: 1
- Dilation angle: 30°
- Viscosity parameter:  $10^{-4}$  (Beam 3.1),  $10^{-5}$  (Beam 3.2)

Note: due to convergence problems, the viscosity parameter for the analysis of beam 3.2 had to be decreased by 1 order of magnitude.

Additional material properties taken for the analyses in DIANA are as follows:

- Smear Length: 11 mm
- Tension Model: Hordijk

#### 7.3.2.1 Load-Deflection Results

The load-deflection results are displayed in figure 7.22 for both ABAQUS and DIANA, alongside the laboratory results.

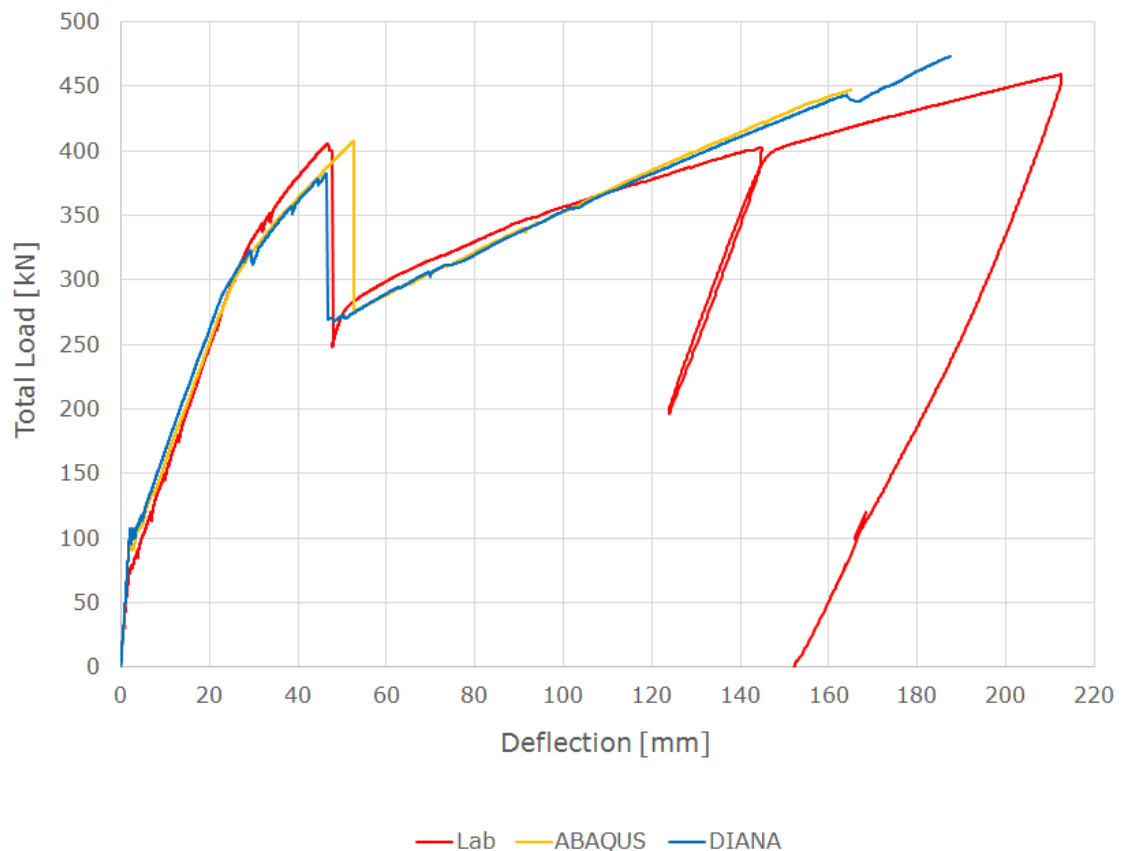


**Figure 7.22:** B3: Load-deflection of Beam 3, with Bond-Slip

The failure point for the analysis in ABAQUS was determined according to the level of strain occurring in the CFRP at failure in the laboratory. This strain level was 0.010935. For the analysis in DIANA however, failure due to delamination was observed instead. The strain level in the CFRP was approximately 0.010328 at this point.

Whilst convergence wasn't found in the analysis of the DIANA model of beam 3.1 for two steps after delamination occurred, it was found for all steps following. The load-deflection results for the two models in DIANA are displayed in figure 7.23.

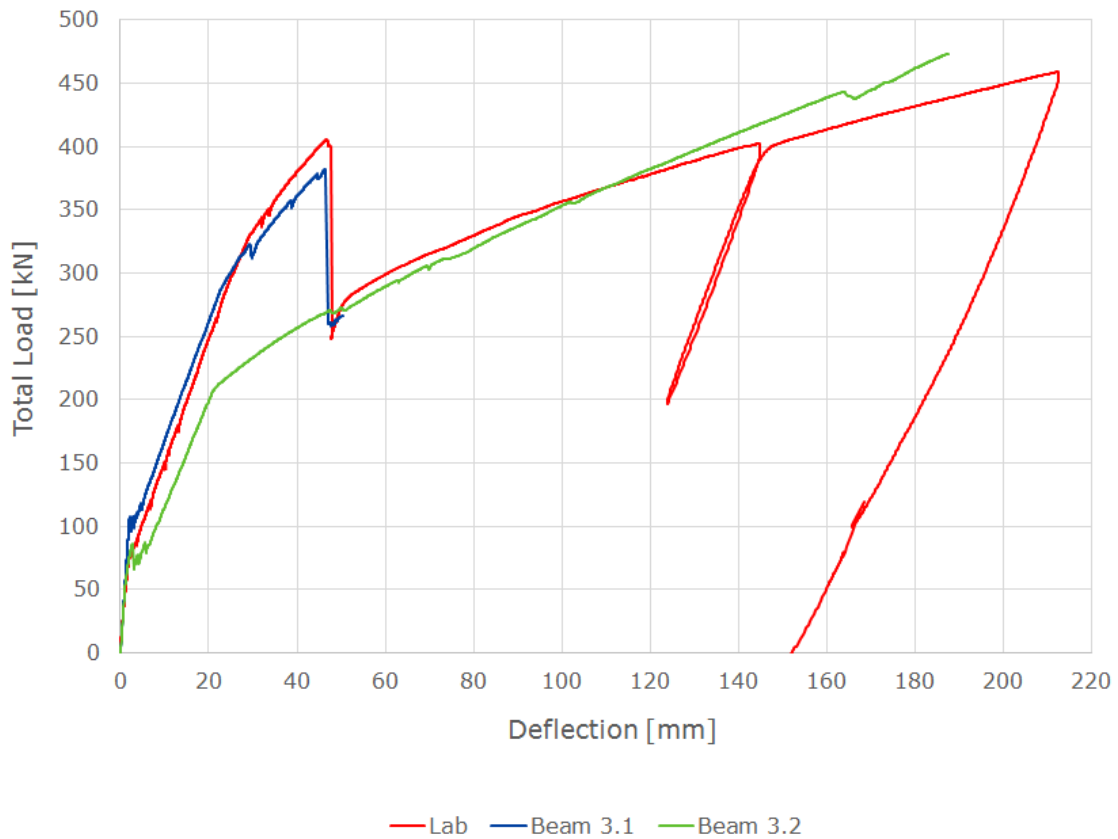


**Figure 7.23:** B3: Beam 3.1 and 3.2 results from DIANA, with Bond-Slip

The analysis was stopped prematurely by the authors, so further results were not obtained past the point shown.

The crack pattern just prior to delamination is displayed in figure 7.24, with the level of slip in the interface between the CFRP and the concrete displayed in figure 7.25.

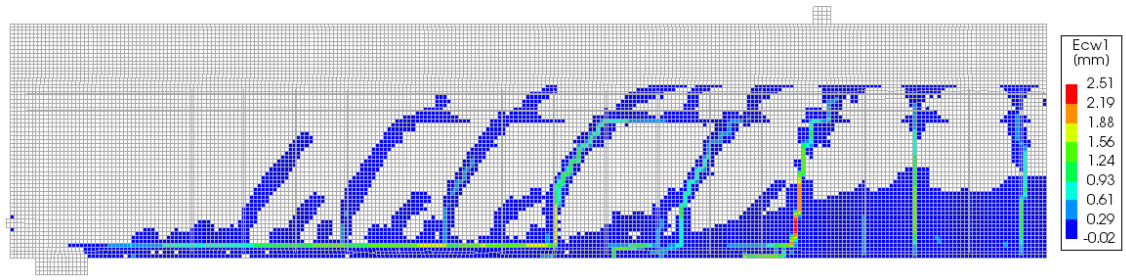


**Figure 7.24:** B3: Crack Pattern just prior to Failure Point of DIANA model, with Bond-Slip

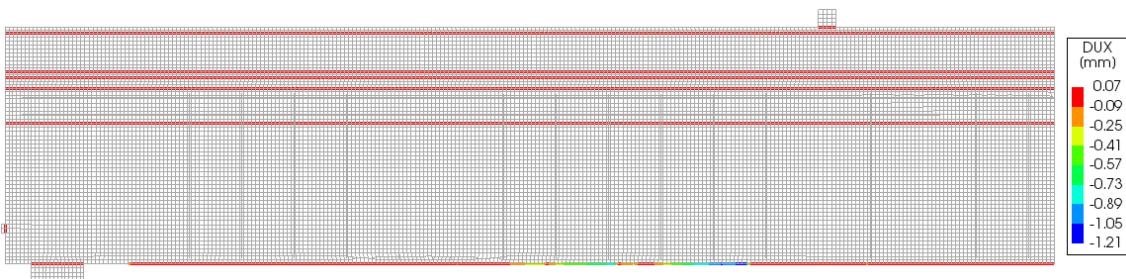


**Figure 7.25:** B3: Slip just prior to Failure Point of DIANA model, with Bond-Slip

For the step following delamination, the crack pattern and level of slip in the interface was as shown in figures 7.26 and 7.27 respectively.

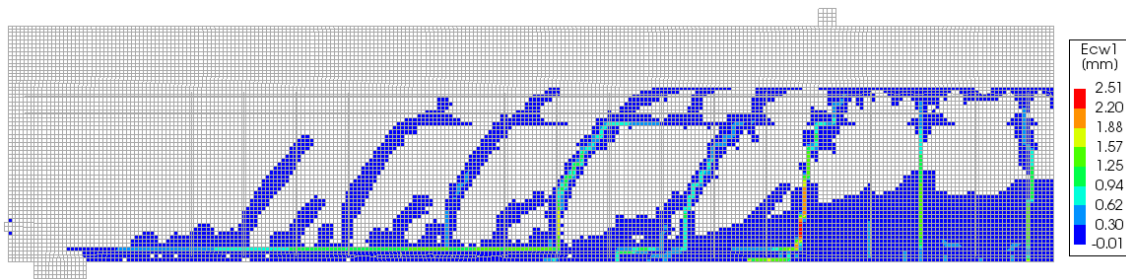


**Figure 7.26:** B3: Crack Pattern just prior to Failure Point of DIANA model, with Bond-Slip

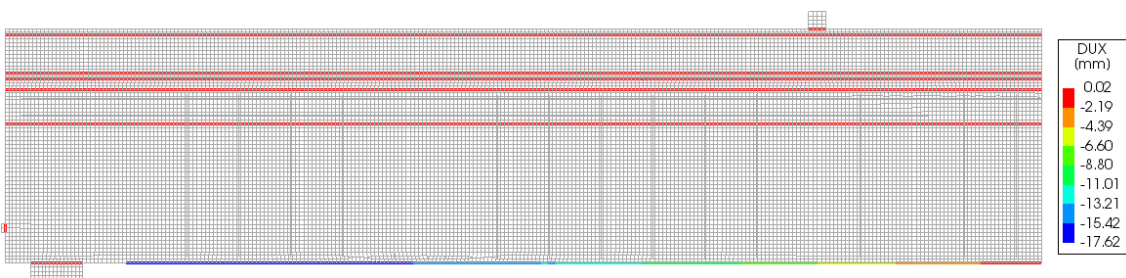


**Figure 7.27:** B3: Slip at Failure Point of DIANA model, with Bond-Slip

### 7.3.2.2 Maximum Crack Width Results

The maximum crack width size for each of the models is presented in table 7.3 for the load levels of 90, 120, 150 and 180 kN.

Source	90 kN [mm]	120kN [mm]	150kN [mm]	180kN [mm]
ABAQUS	0.39	0.67	0.85	1.06
DIANA	0.0004	0.20	0.30	0.41
Laboratory	0.06	0.12	0.18	0.22

**Table 7.3:** B3: Maximum crack width size

### 7.3.2.3 Crack Patterns

The crack patterns for both analyses at load levels 150 and 180 kN is compared against the cracking pattern obtained from the laboratory in the figures 7.28 and 7.29 respectively.

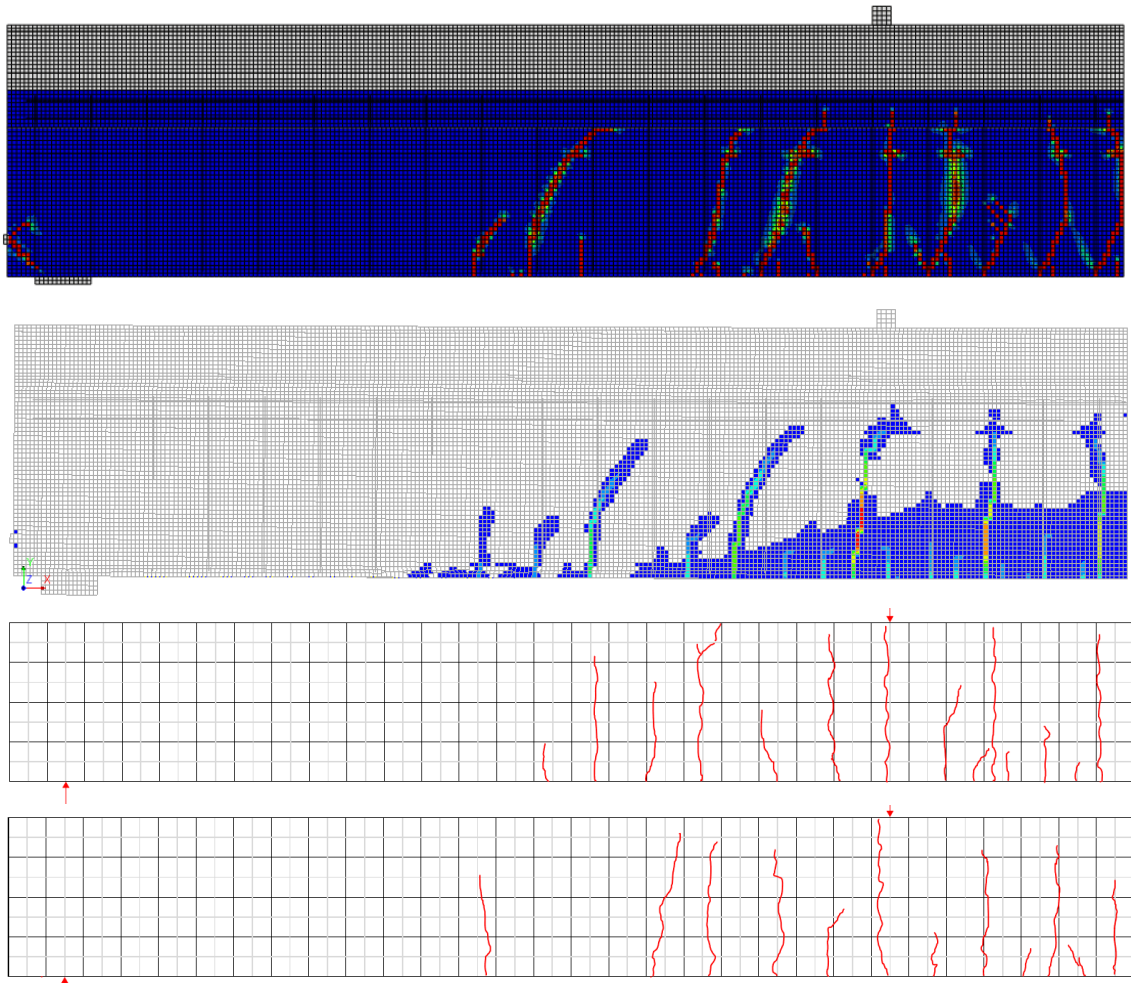


**Figure 7.28:** B3: Crack Patterns at 150 kN. From top to bottom: ABAQUS, DIANA, Lab (LHS) and Lab (RHS)

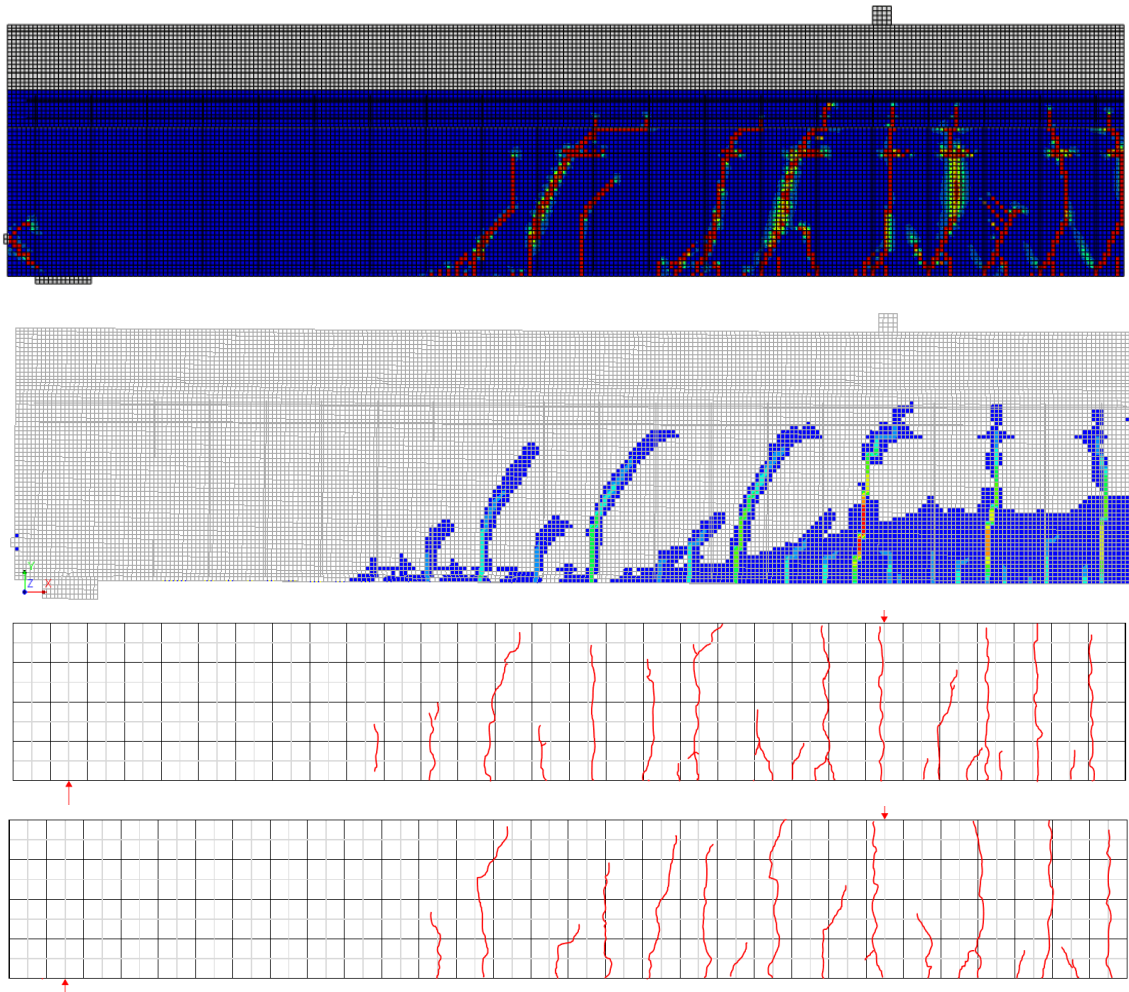


**Figure 7.29:** B3: Crack Patterns at 180 kN. From top to bottom: ABAQUS, DIANA, Lab (LHS) and Lab (RHS)

### 7.3.2.4 Discussion of Results

#### Load-deflection

Comparing the load-deflection curves for the case where perfect bond was included (figure 7.17) against those where bond-slip was included (figure 7.22), the general response is consistent between the two cases. When bond-slip is included, the response near the delamination failure of the CFRP is closer to the experimental results, supporting the notion that bond-slip is necessary to capture the correct failure point. Following CFRP failure, very little difference is observed.

It is interesting to note though, that whilst the deflection of the delamination point wasn't captured in the perfect bond models, the load level was, with a 0.5% accuracy. Compared to the DIANA model with bond-slip, where the delamination load was 381 kN (5.7% difference to lab), the embedded model provides a more accurate result than the bond-slip model. From a design point of view, it could motivate the use of the embedded steel model over the bond-slip model, not just from the point of view to save time (modelling and analysis), but also as the ultimate load can be calculated with a greater level of accuracy. This is consistent with the findings from the analysis of beam 2.

Comparing the load-deflection response of beam 3.2 to the experimental data in figure 7.22, it is clear that the gradient of the two curves are different. This is likely due to the simplifications made in modelling the GFRP panel. The gradient of the experimental curve is non-linear, whilst the FE models display a purely elastic response. Significant simplifications were made in the modelling of the GFRP sandwich decks, which may not be accurate enough to capture the full response when loaded to this degree. With a more accurate representation of this component, it is likely that the response of the FE models prior to the CFRP debonding might have been closer to that of the experimental result. This would mean an adjustment to both the material properties and also how the webs are represented in the models. With thin webs, there should be some local effects at later load levels (which were potentially captured by the lab beams, through the non-linearity of the response).

Comparing the full load-deflection curves from the beams in ABAQUS and DIANA, it is clear that the gradient of the curves are consistent, with the only difference being the point of failure of the laminates. In the ABAQUS model, the point of failure had to be determined from the laboratory results, whilst the DIANA model failed by its own volition. Unless damage initiation and damage evolution is specified in the surface-to-surface interaction between CFRP and concrete in ABAQUS, then the descending branch of the bond-slip relationship cannot be defined, and hence no predictive failure can be made. This limits the usefulness of the ABAQUS model in its current form.

Looking at figures 7.24 and 7.25, the cracks responsible for the delamination failure of the CFRP in the DIANA model can correctly be identified as those located just left of the load plate. This is because of the slip at this section has already

exceeded the maximum defined slip value of the bond-slip relationship. Hence, local delamination failure has already started to occur at this location.

Looking at the load step following delamination failure, it is clear that the CFRP has fully debonded from the surface of the concrete, from looking at figure 7.27. This is because the level of slip in some locations exceed 17 mm.

Somewhat surprisingly, the DIANA model was capable of capturing the post-delamination behaviour, as shown in figure 7.23.

The reason why this behaviour was able to be captured by this model and no other bond-slip model comes down to three reasons:

1. Step Size
2. Continuation Method
3. Iteration number

The load step was reduced so that for each step approximately 0.01 mm of deflection was added. By using a continuation method, it allows for the analysis to continue even if convergence isn't found in one step. With a maximum allowable number of iterations set to 80 per step size, it provided the software time to find the convergent solution. Whilst for two steps following delamination, no solution was found, it was for every step following these.

As a downside to this method, the total number of steps was into the 1000s, and the size of the result file was over 60GB. Hence, if this were to be repeated, and continued for a longer period of loading following delamination, then only data from every few steps should be saved to reduce the size of the analysis. Even with this in mind, the time required to analyze until this point in DIANA was significant, reaching over 2 days. It is for this reason that it is recommended to instead switch over to an explicit analysis instead.

Looking at the small amount of the post-delamination behaviour captured by the DIANA model of beam 3.1, it is clear that it responds similarly to that of beam 3.2, however without more data, it cannot be confirmed that it would follow the same response.

### **Maximum Crack Width**

Comparing against the experimental maximum crack width sizes, the results obtained from DIANA are more accurate than those from ABAQUS. This is due the the combination of embedded and bond-slip reinforcement in the ABAQUS model, causing the results to be highly inaccurate.

There is still some difference in the maximum crack width sizes between the DIANA model and the lab beam. When comparing the crack patterns, it is clear that there are several cracks which do not fully develop in the DIANA model, hence leading to an overestimation of the maximum crack widths. This is consistent with the findings from beam 1 and 2.

### **Crack Patterns**

Comparing the crack patterns from the two halves of the experimental beam, it is clear that there is some significant "randomness" in the cracking behaviour, and hence only the general response should be compared between the FE and lab data.

Looking at the load level of 150 kN, 2-3 significant cracks are found in the area between the mid-span and the load plate in the lab beams. In ABAQUS, 3 cracks are located in this area, and generally correlate well in terms of location. In DIANA, only 2 cracks are observed, with several smaller cracks well located, but not as developed. Consistent with the lab data, both software show a significant crack under the load plate. The remainder of the beam in ABAQUS correlates well to the cracking pattern on the right-hand side of the lab beam, whilst DIANA correlates better to the left-hand side.

At the load level of 180 kN, the ABAQUS result displays good cracking definition in the mid-span after the load plate, generally matching well with the experimental cracking in terms of height and general location. For the remainder of the span significantly less cracks are observed in the ABAQUS model, however the locations of the cracks do correlate well to those observed from the right-hand side of the lab beam.

In DIANA, the number of well developed cracks lags behind the lab beams, both in the mid-span and the remainder of the beam. The crack locations are still fairly consistent with those found in the lab however. The main issue of the DIANA model lies in the development of the cracks at these later load levels. Whether a crack queuing algorithm should be employed, or a shear retention factor, is still to be determined.

When looking at the angle of the cracks, it is clear in all FE beams that the cracks generally are rotated more towards the load plate than what is shown in the lab beams. Whether this could be corrected by not utilizing a rotating crack model, it is unclear. Further research should be done to determine whether this can be corrected.

## 7.4 Beam 4

### 7.4.1 Perfect Bond

This section will present the results for beam 4 when the bond-slip between the concrete and the steel is assumed to be perfect. For the models in ABAQUS and DIANA, the mesh density taken was 25 x 25 mm.

Additional material properties taken for the analyses in ABAQUS are as follows:

- Smear length: 100 mm
- Damage Model: 1
- Dilation angle: 30°
- Viscosity parameter  $10^{-4}$

Additional material properties taken for the analyses in DIANA are as follows:

- Smear length: 150 mm
- Tension Model: Hordijk

#### 7.4.1.1 Load-Deflection Results

The load-deflection results from both ABAQUS and DIANA are displayed in figure 7.30, together with the result from the laboratory testing.

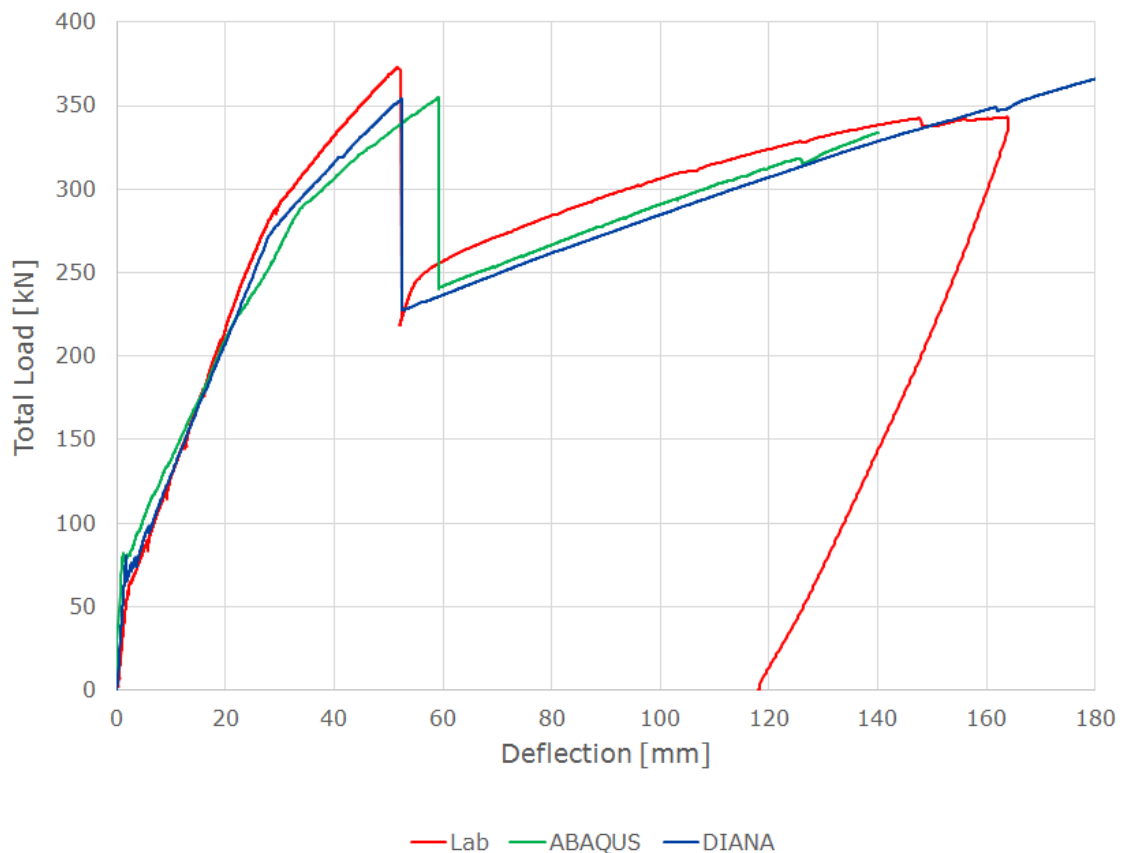


**Figure 7.30:** B4: Load-deflection of beam 4, Perfect Bond

The failure point of beam 4.1 was determined according to the level of strain in the CFRP laminates. In the laboratory, failure occurred at a strain level of approximately 0.010363, and hence this was the point of "failure" for the FE analyses in figure 7.30.

When running beam 4.1 beyond this point in ABAQUS, no delamination failure was observed. However, in DIANA, both the delamination of the CFRP and the post-peak behaviour was able to be captured. The load-deflection result from beam 4.1 in DIANA is displayed in figure 7.31, alongside the laboratory result.

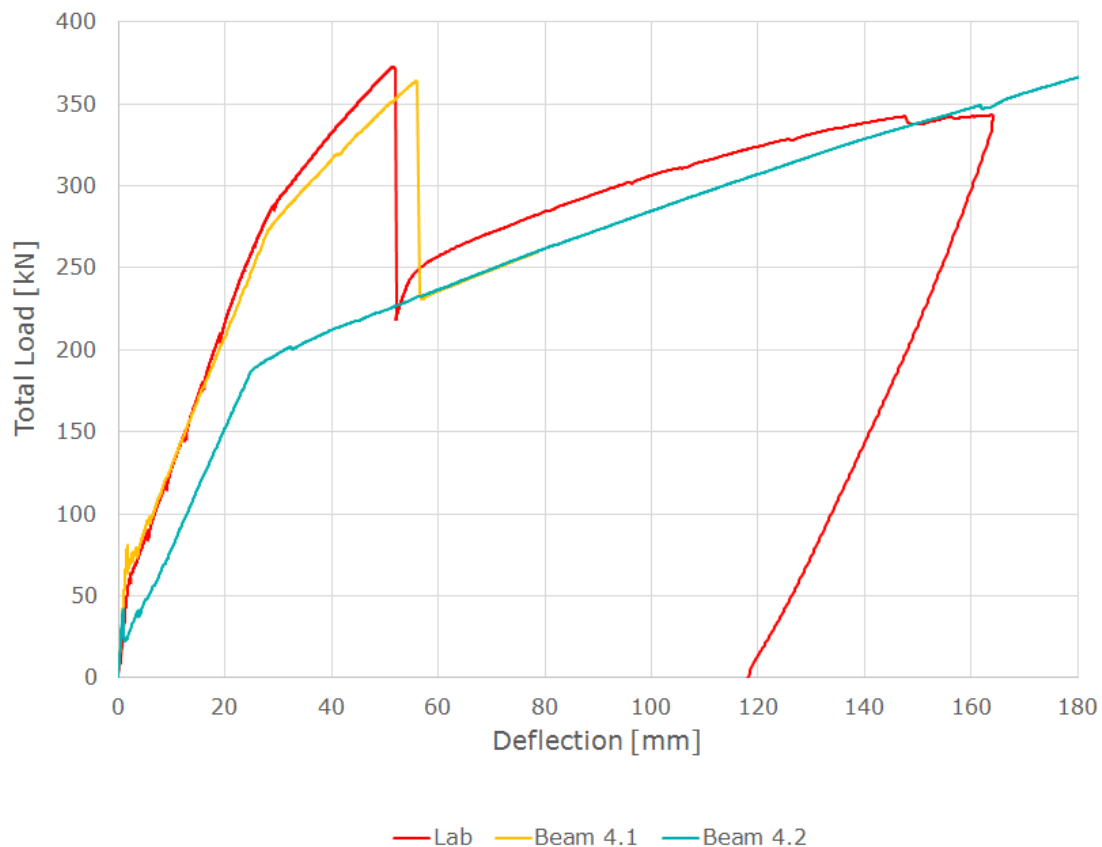


**Figure 7.31:** B4: Load-deflection of beams 4.1 and 4.2 in DIANA, Perfect Bond

Note: the analysis of beam 4.1 was terminated prematurely by the author.

In the step just prior to the delamination of the CFRP in the model, the crack pattern was as displayed in figure 7.32, with the slip in the interface layer between the CFRP and the concrete as shown in figure 7.33.

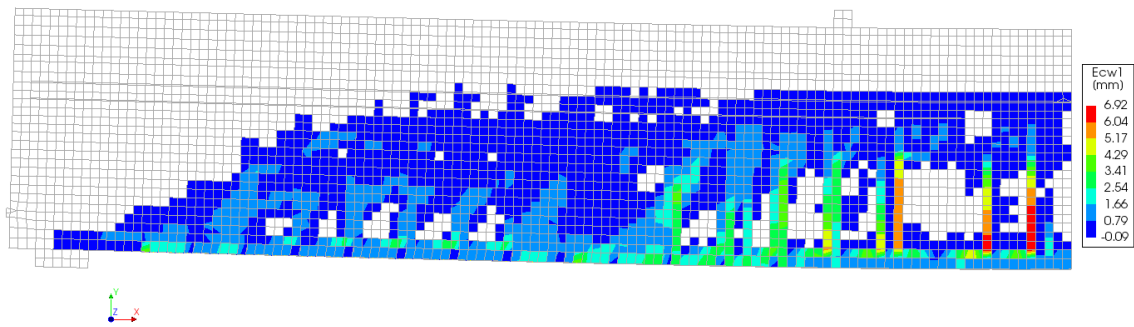


**Figure 7.32:** B4: Crack Pattern in beam 4.1 in DIANA, just prior to failure, Perfect

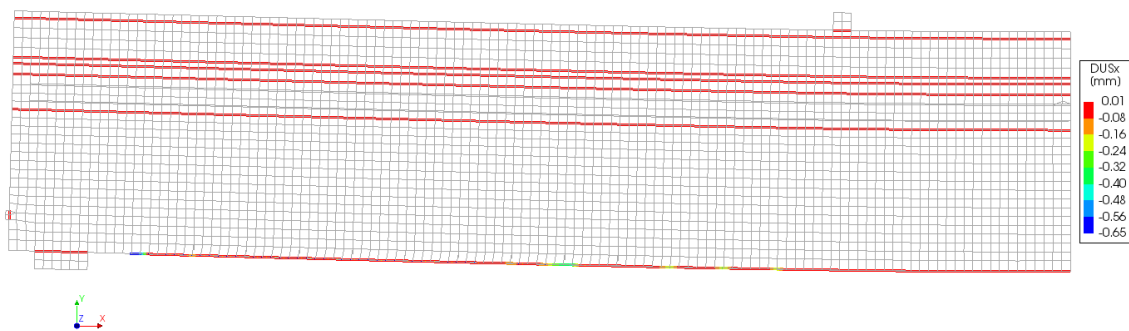


**Figure 7.33:** B4: Slip in the interface in beam 4.1 in DIANA, just prior to failure, Perfect

At failure, the slip in the interface was as displayed in figure 7.34.

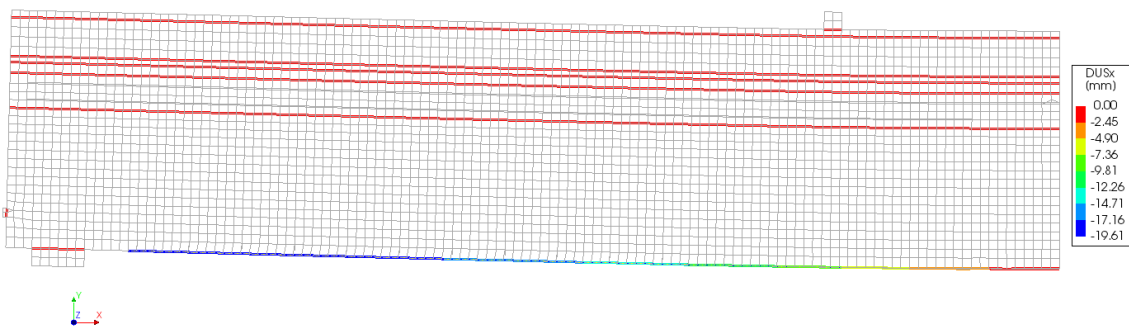


**Figure 7.34:** B4: Slip in the interface in beam 4.1 in DIANA, just following failure, Perfect

#### 7.4.1.2 Discussion of Results

Comparing the load-deflection results from ABAQUS and DIANA in figure 7.30, there are several notable differences between them. Focusing on the behaviour prior to the delamination of the CFRP, little difference is seen in the gradients until yielding, at which point the ABAQUS curve shows greater levels of deflection. This behaviour was also present in the analysis of beams 2 and 3, and at that point it was proposed that the cause of their divergence was due to differing definitions of the epoxy between the CFRP and the beam. In ABAQUS only the ascending branch is defined, whilst in DIANA, the full bond-slip curve was input. By only defining the ascending branch, further amounts of slip will only occur at high shear stresses, causing less slip into cracks, and hence lower strain levels in the CFRP compared to that in DIANA.

Differences would also be expected between the experimental results and the embedded FE results, due to the differing crack definition. More cracks are observed along the base of the beam, which will directly influence the level of strain in the CFRP through loading, and hence the failure point. The strain gauges attached to the CFRP on the experimental beams were not located over any cracks, but in the embedded FE models it was impossible to avoid cracks as the entire base of the beam appeared cracked (see figure 7.32). This would have influenced the point of failure measured as well.

Interestingly enough, there is a greater variation in the failure loads of the embedded models for beam 4, than there was for beams 2 and 3. For the DIANA model, the failure load was determined to be 364 kN, whilst for the lab it was 372 kN (ignoring the ABAQUS result, as it didn't predict failure). The difference is 2.2%.

In the same way that DIANA was able to capture the delamination failure of the CFRP for beams 2 and 3, it was also able to capture it for beam 4 as well. This was due to the full definition of the bond-slip relationship between the CFRP and the concrete in the model. Unlike the other beams which delaminated just prior to the load-plate, beam 4 delamination occurred at the end of the CFRP laminate (left-hand side). This is evident from the slip at that point has already exceeded the maximum defined value of 0.23mm (ultimate slip value) locally in figure 7.33. Due to the longitudinal reinforcement being embedded, the crack definition on the base of the beam is difficult to analyze in figure 7.32. In the step following this, delamination occurs, which is clear from the slip readings in figure 7.34.

Looking at the post-delamination responses in figure 7.30, the response from ABAQUS and DIANA are similar, and generally correlate well with the experimental results. Whilst the FE models display fully linear response, the experimental data is more non-linear. This is likely due to some local effects coming into play for the experimental beams, from having slender webs in the GFRP panels. In the FE model, an equivalent web section was used for the GFRP. This significantly simplified the modelling, however removes any local responses which may have affected the global behaviour (i.e. lateral deflections in the web), as well as simplifying the material properties in such a way which may prove incorrect. Although, as the contribution

to the flexural resistance of the panel is low for webs oriented in the tangential direction, less difference is observed for beam 4, than what was observed in beams 2 and 3. Hence, the approximate modelling of the webs in this way is sufficient.

## 7.4.2 Bond-Slip Included

This section will present the results for beam 4 when the bond-slip between the concrete and the steel was included in the model. For the models in ABAQUS and DIANA, the mesh density taken was 11 x 11 mm.

Additional material properties taken for the analyses in ABAQUS are as follows:

- Smear length: 46 mm
- Damage Model: 1
- Dilation angle: 30°
- Viscosity parameter:  $10^{-4}$  (Beam 4.1),  $10^{-5}$  (Beam 4.2)

Note: due to convergence problems, the viscosity parameter for the analysis of beam 4.2 had to be decreased by 1 order of magnitude.

Additional material properties taken for the analyses in DIANA are as follows:

- Smear Length: 11 mm
- Tension Model: Hordijk

### 7.4.2.1 Load-Deflection Results

The load-deflection results are displayed in figure 7.35 for both ABAQUS and DIANA, alongside the laboratory results.

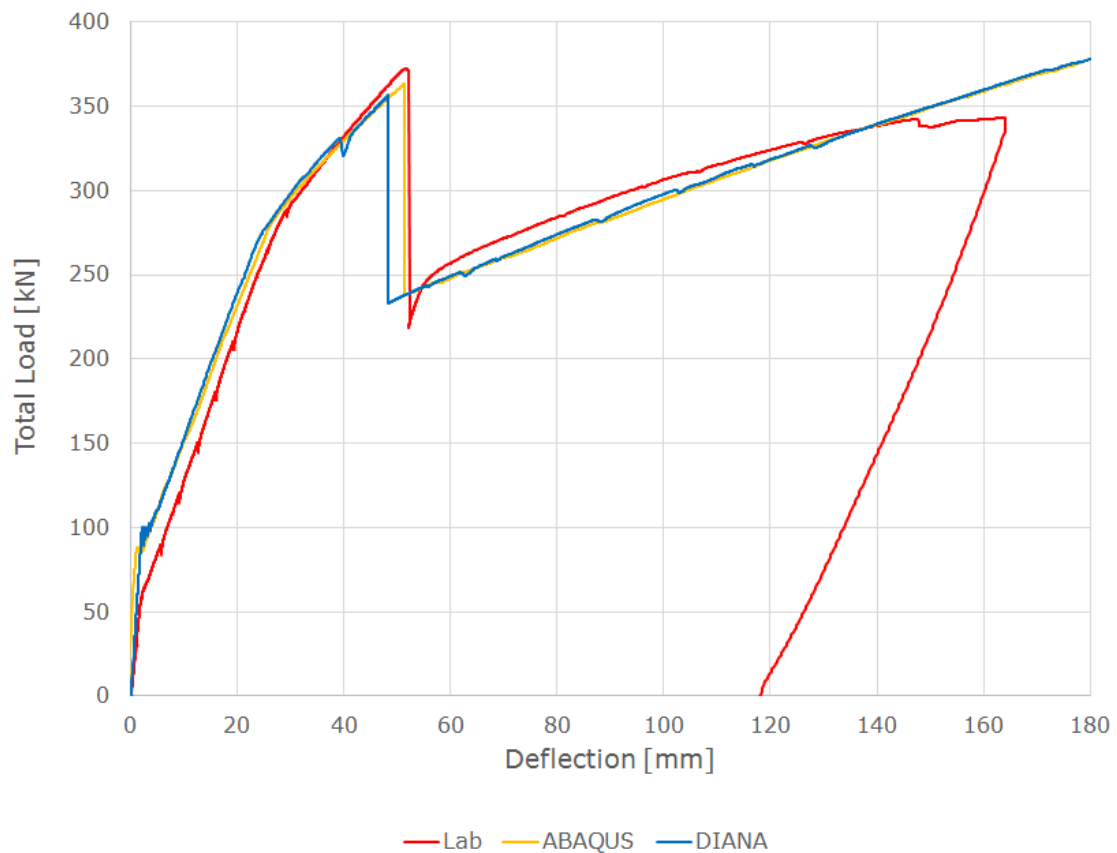


**Figure 7.35:** B4: Final Curves in ABAQUS and DIANA, with Bond-Slip

The failure point of beam 4.1 was determined according to the level of strain in the CFRP. In the laboratory, the CFRP debonded from the beam at a strain level of approximately 0.010363, and hence when the strain in the CFRP reached this level in the FE models, it was determined that "failure" was reached.

When running beam 4.1 beyond this failure point in ABAQUS, no concrete failure was observed (and hence no debonding of the CFRP). However, in DIANA, debonding of the CFRP did occur just later than the point shown in figure 7.35. Adjusting the load-deflection curve to the point of failure captured by DIANA, the result can be seen in figure 7.36.

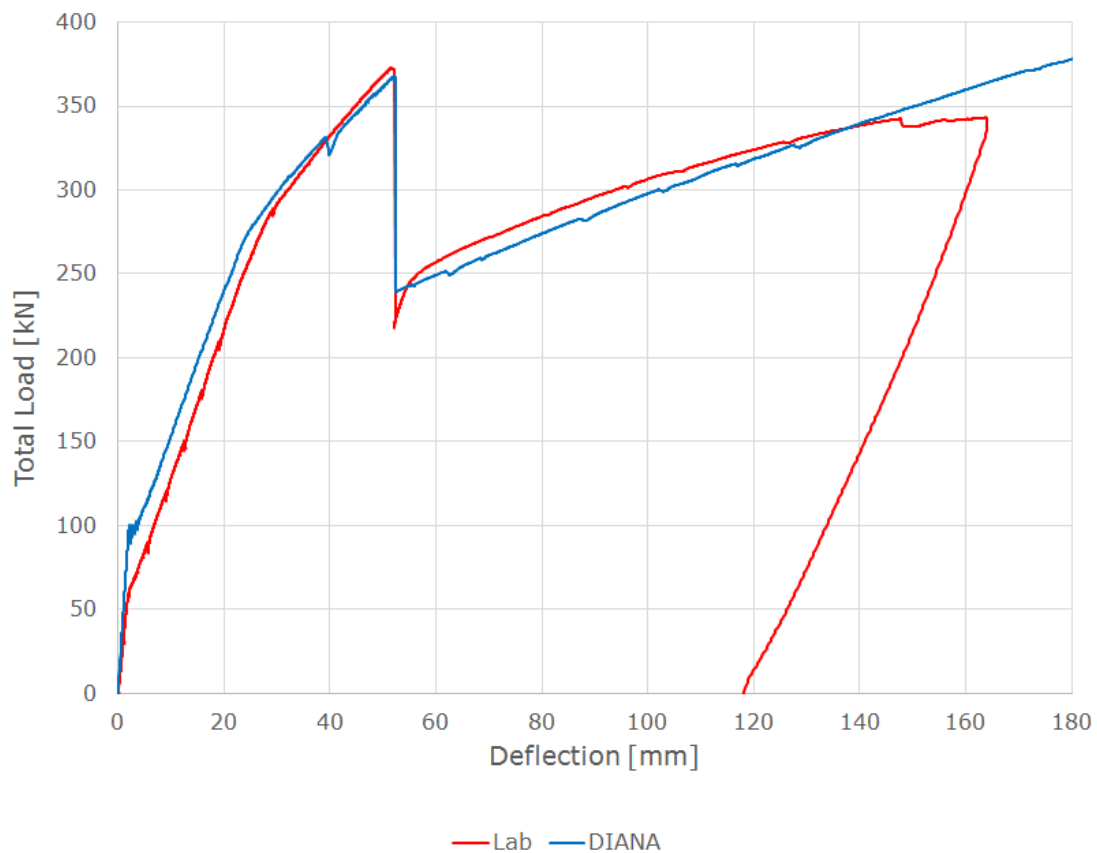


**Figure 7.36:** B4: Failure point of the DIANA model, with Bond-Slip

Strain readings for this failure point varied from 0.011012 to 0.010396, within a space of 10 cm. Given the location of the cracks, the strain readings can highly vary.

At the point of failure in the DIANA model, the crack pattern was as displayed in figure 7.37, with the slip in the interface as shown in figure 7.38.

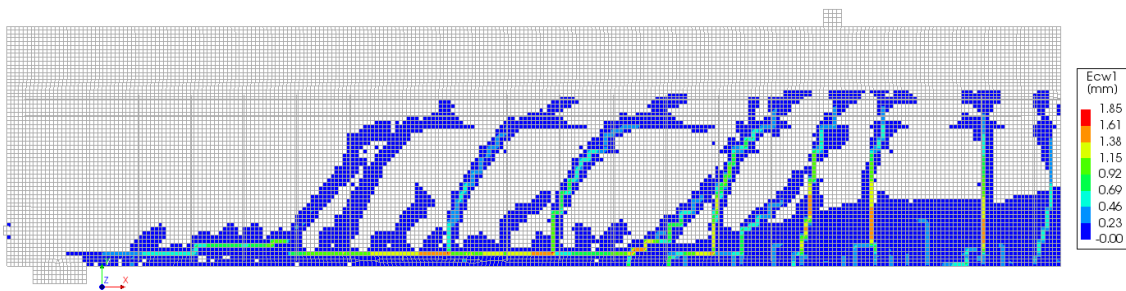


**Figure 7.37:** B4: Crack Pattern just prior to failure, with Bond-slip

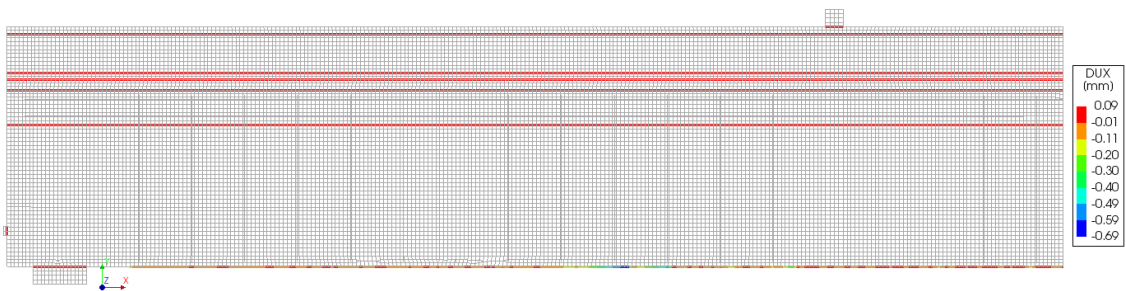


**Figure 7.38:** B4: Slip in the interface just prior to failure, with Bond-slip

At failure, no convergence was found in the model, and the analysis was cancelled. The crack pattern at this point was as displayed in figure 7.39, and the slip in the interface was as displayed in figure 7.40.

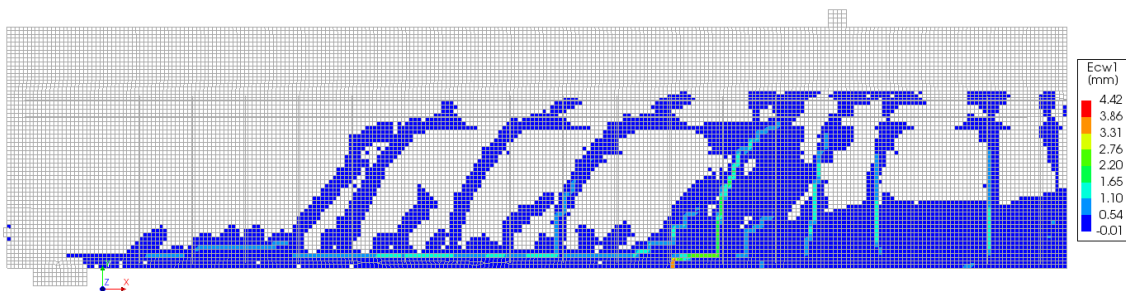


**Figure 7.39:** B4: Crack Pattern just following failure, with Bond-slip

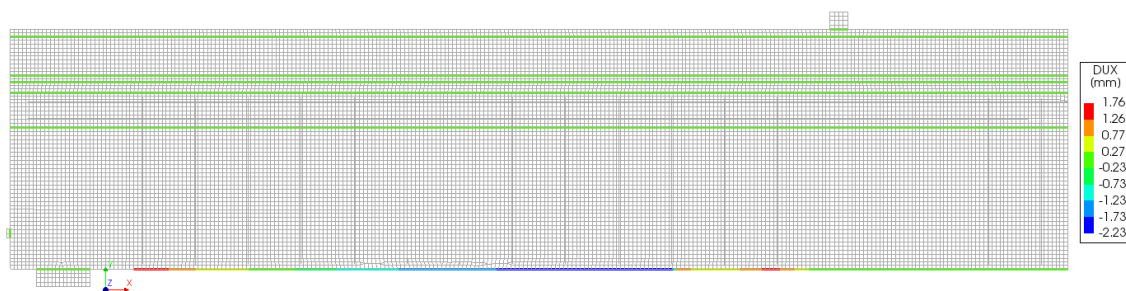


**Figure 7.40:** B4: Slip in the interface just following failure, with Bond-slip

### 7.4.2.2 Maximum Crack Width Results

The maximum crack width size for each of the models is presented in table 7.4, for the load levels of 90, 120, 150 and 180 kN.

Source	90 kN [mm]	120kN [mm]	150kN [mm]	180kN [mm]
ABAQUS	0.50	0.82	1.19	1.22
DIANA	0.08	0.19	0.30	0.37
Laboratory	0.10	0.15	0.22	0.25

**Table 7.4:** B4: Maximum crack width size

### 7.4.2.3 Crack Patterns

The crack patterns for both analyses at load levels 150 and 180 kN is compared against the cracking pattern obtained from the laboratory in the figures 7.41 and 7.42 respectively.

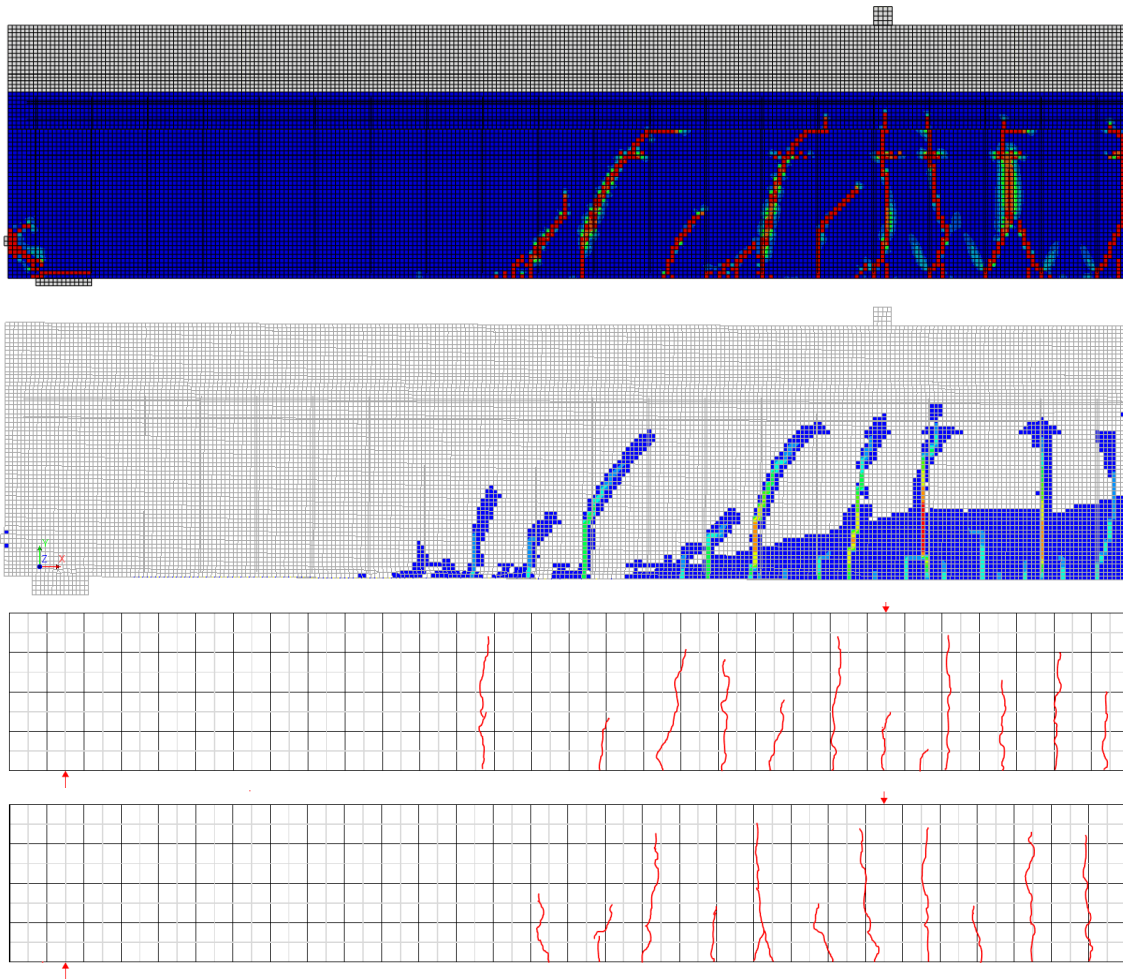


**Figure 7.41:** B4: Crack Patterns at 150 kN. From top to bottom: ABAQUS, DIANA, Lab (LHS) and Lab (RHS)

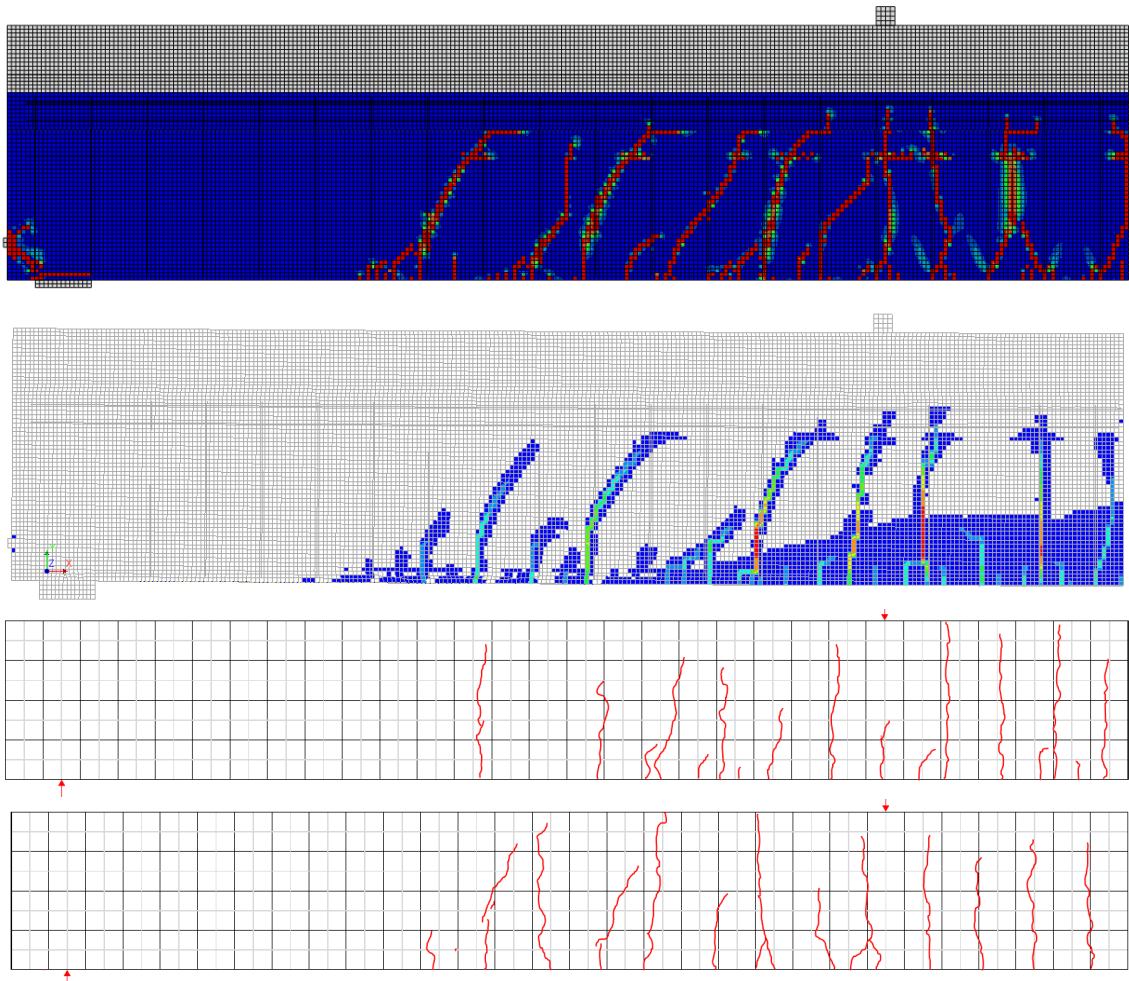


**Figure 7.42:** B4: Crack Patterns at 180 kN. From top to bottom: ABAQUS, DIANA, Lab (LHS) and Lab (RHS)

#### 7.4.2.4 Discussion of Results

##### Load-deflection

Looking at the load-deflection results in figure 7.35, the only significant difference in the results from ABAQUS and DIANA is the delamination point. In this figure, the delamination point was determined according to the level of the strain in the CFRP. When it was equal to the value measured in the laboratory at CFRP delamination, then "failure" was deemed to have occurred. When running the DIANA model past this point, it fails at the point shown in figure 7.36. It is arguable that the strain in the CFRP at this later point does actually equal to that failure point measured in the laboratory. Difficulty arises however in determining the appropriate point in the CFRP to measure failure. Some nodes measured strains of 0.010396, which is incredibly close to the lab value of 0.010363. Other nodes measured much higher values of 0.011012. Given the variance, it could be argued that because the measurement in the laboratory was taken over a non-cracked section, the lowest strain value of the mid-point in the FE should be taken. Hence, the failure strains correlate very well.

The delamination deflection is captured well by both software, as well as the delamination load. In DIANA, this was found to be 365 kN, whilst in the lab it was 372 kN. This is a difference of only 1.88%, proving that including the bond-slip between the steel and the concrete will lead to a more accurate prediction of the maximum load. The counter was true however for beams 2 and 3. As the variation is below 2.5% overall when embedding the steel, it is still the recommended choice if a deck were to be designed utilizing the SUREBridge solution. Whilst there might be small variations in the accuracy of the results, significant time is saved from modelling and analyzing the models.

Comparing the location of the critical crack in the embedded and bond-slip models, there are significant differences. For the bond-slip model, the critical crack location is just left of the loading plate (either the orange crack in figure 7.39, or that just left of it in figure 7.37). In the embedded model, however, the critical crack responsible for delamination is located at the end of the CFRP, closest to the support (see the maximum slip in figure 7.33). The only differences between these two DIANA models is the inclusion of bond-slip around the steel reinforcement. By embedding the steel, significantly more cracks are displayed, which can incorrectly cause delamination failure of the CFRP. It is therefore of prime importance to include bond-slip between the steel and the concrete, if both the deflections and failure cracks wish to be determined with accuracy.

Assuming the failure point shown in figure 7.31 for DIANA, the result of ABAQUS and DIANA align well to the results from the experimental test. There is still some variation in the load-displacement response of the beam after the delamination of the CFRP, however it correlates better than those results for beam 2 and 3. This is likely due to the more negligible influence of the web in the response of the GFRP. In this case, the webs run along the transverse plane, and hence do not contribute overly to the flexural resistance in this case. The non-linearity of the curve also

may not be captured with the current definition of the GFRP panels, as the webs are entirely smeared over the length and width. This removes all secondary effects which may occur (i.e. deflection of the webs).

Whilst the DIANA model was capable of capturing the delamination point, it was not able to run past this point and capture any post-peak behaviour. Compared to the beam 4.1 model with embedded reinforcement (which was capable of running after delamination), the behaviour within the bond-slip model is notably more complicated. Once the CFRP debonds in the bond-slip model, the stiffness in the model changes immediately. The bond-slip between the steel and the concrete needs to find equilibrium, which is difficult with such a sudden change. If instead this was analyzed explicitly, then it might be possible to capture post-peak failure, and hence only require 1 FE model.

### **Maximum Crack Width**

Comparing the maximum crack width results obtained from FE, against those measured in the lab, it is clear that the accuracy of the DIANA model is higher than that of the ABAQUS model. This is the same conclusion made for the beams 1, 2 and 3, and is likely caused by the combination of embedded and bond-slip reinforcement. Whilst outside the scope of this thesis, it would be interesting to compare the results when bond-slip is included for all rebar in ABAQUS. The difference in the results from ABAQUS and DIANA should be minimal in that case however.

### **Crack Patterns**

Comparing the crack patterns at the load level of 150 and 180 kN, the results for both ABAQUS and DIANA show good correlation with the results obtained from the lab tests. At the load level of 150 kN the cracking displayed in the DIANA beam almost completely correlates to those cracks in the right-hand side of the laboratory beam. A strong correlation is also seen with the result in ABAQUS, however some cracks in the mid-span after the load plate are not located as well as those from DIANA.

At the load level of 180 kN, the correlation is not as strong between the DIANA beam and the experimental, due to DIANA's inability to obtain the same crack height in the mid-span after the load plate. This is a common comment made from the analysis of all DIANA beams. The crack locations between ABAQUS and DIANA do correlate well, however ABAQUS does show several more well developed cracks in the length of span between the support and load plate.

It is important to note the difference in cracks of this location between the two sides of the laboratory beams. On the right-hand side, significantly more fully developed cracks are observed, whilst on the left-hand side, there are more half-developed cracks. This assists in highlighting that it isn't always possible to capture the exact cracking pattern of concrete; it is highly variable.

# 8

## Conclusions

The aim of this master thesis was to replicate the results from the experimental tests of the SUREBridge beams in two FE programs; ABAQUS and DIANA, and to provide extensive documentation of the process.

From the results, it was found that the inclusion of the full bond-slip relationship between both the concrete and the steel reinforcement, and the concrete and the CFRP laminates, is critical to accurately predict the delamination failure point of the CFRP. However, the delamination load can accurately be predicted with a deviation of less than 2.5% by modelling embedded steel reinforcement. With this consideration, it is recommended to utilize embedded reinforcement when designing to ultimate limit state using the SUREBridge solution, due to the significant savings in time due to modelling and analysis. Whilst inaccurate values of deflection will be determined, this is of no concern when designing to ultimate limit state.

More in-depth modelling is however required for the GFRP panels, as the simplified models were not capable of capturing the same response as the laboratory beams.

Furthermore, given that the reinforcement design is able to be verified, then more accurate comparisons can be made between the FE analyses and experimental data.

Finally, when comparing the modelling processes of ABAQUS and DIANA, the authors determined that given the range of behaviour able to be input with relative ease, DIANA was the preferred modelling software for this situation.



# 9

## Future Studies

From the findings in this master thesis, there are several areas where the authors believe that there may be benefits from conducting further research.

Further development should be made to the models created in this thesis, in order to obtain the full response curves from a single model which can accurately predict delamination failure. This would mean the development of an explicit analysis, to overcome some of the shortfalls of the current implicit analyses. Namely, it's inability to cope with sudden stiffness changes in the models. This would allow for the full load-deflection response to be obtained from a single model.

The modelling of the GFRP sandwich panels should be upgraded to better represent the properties of the panels tested in the laboratory.

Whilst this thesis slightly investigated whether it is possible to combine embedded and bond-slip reinforcement in a single model, no solid conclusions can be drawn without further study. It is therefore the recommendation of the authors that further research should be conducted into this area.



# Bibliography

- Abaqus (2010), ‘Abaqus Manual: Concrete damaged plasticity’.  
**URL:** <https://abaqus-docs.mit.edu/2017/English/SIMACAEMATRefMap/simamat-c-concretedamaged.htm>
- Alfarah, B., López-Almansa, F. & Oller, S. (2017), ‘New methodology for calculating damage variables evolution in Plastic Damage Model for RC structures’, *Engineering Structures* **132**, 70–86.
- Chen, G. M., Teng, J. G. & Chen, J. F. (2011), ‘Finite-Element Modeling of Intermediate Crack Debonding in FRP-Plated RC Beams’, *Journal of Composites for Construction* **15**(3), 339–353.
- Chen, G. M., Teng, J. G., Chen, J. F. & Xiao, Q. G. (2015), ‘Finite element modeling of debonding failures in FRP-strengthened RC beams: A dynamic approach’, *Computers and Structures* **158**, 167–183.  
**URL:** <http://dx.doi.org/10.1016/j.compstruc.2015.05.023>
- Chen, J. F. & Teng, J. G. (2001), ‘Anchorage Strength Models for FRP and Steel Plates Bonded to Concrete’, *Journal of Structural Engineering* **127**(7), 784–791.
- Coronelli, D. & Gambarova, P. (2004), ‘Structural Assessment of Corroded Reinforced Concrete Beams: Modeling Guidelines’, *Journal of Structural Engineering* **130**(8), 1214–1224.
- de Almeida, M. I. A. & M. (2009), ‘Structural behaviour of composite sandwich panels for applications in the construction industry’, (October).
- Dehestani, M. & Ojarestaghi, S. S. M. (2015), ‘Modified Steel Bar Model incorporating bond-slip effects for embedded element method’, *Construction and Building Materials* **81**(2015), 284–290.
- Ditcher, A. K. & Webber, J. P. H. (1981), ‘BEHAVIOUR OF CARBON FIBRE REINFORCED PLASTIC LAMINATES’, pp. 43–51.
- Du, Q. (2016), Finite element modelling of steel/concrete bond for corroded reinforcement, PhD thesis, University of Ottawa.
- Fib (2013), *fib Model Code for Concrete Structures 2010*, Wilhelm Ernst & Sohn, Berlin.
- Forsberg, F. (2017), ‘Increased Traffic Loads on Swedish Highway Bridges : A Case

- study of the bridge at highway interchange Värö'.  
**URL:** <http://www.diva-portal.org/smash/record.jsf?pid=diva2%3A1074665&dswid=7895>
- Gooranorimi, O. (2016), Investigation of Bond, Microstructure and Post-Fire Behavior of GFRP Reinforcement for Concrete, PhD thesis, University of Miami.  
**URL:** [http://scholarlyrepository.miami.edu/oa\\_dissertations/1693](http://scholarlyrepository.miami.edu/oa_dissertations/1693)
- Issa, C. A. & Masri, O. (2015), 'Numerical simulation of the bond behavior between concrete and steel reinforcing bars in specialty concrete', *International Journal of Civil, Environmental, Structural, Construction and Architectural Engineering* **9**(6), 767–774.
- Li, C. Q., Yang, S. T. & Saafi, M. (2014), 'Numerical Simulation of Behavior of Reinforced Concrete Structures considering Corrosion Effects on Bonding', *Journal of Structural Engineering* **140**(12), 04014092.
- Lu, X. Z., Teng, J. G., Ye, L. P. & Jiang, J. J. (2005), 'Bond – slip models for FRP sheets / plates bonded to concrete', *Engineering Structures* **27**, 920–937.
- Lubliner, J., Oliver, J., Oller, S. & Oñate, E. (1989), 'A plastic-damage model for concrete', *International Journal of Solids and Structures* **25**(3), 299–326.
- Lundgren, K. (1999), Three-dimensional modelling of bond in reinforced concrete, PhD thesis, Chalmers University of Technology.
- Ma, F. J. & Kwan, A. K. (2015), 'Crack width analysis of reinforced concrete members under flexure by finite element method and crack queuing algorithm', *Engineering Structures* **105**, 209–219.
- Malm, R. (2006), Shear cracks in concrete structures subjected to in-plane stresses, PhD thesis, Royal Institute of Technology (KTH).  
**URL:** <https://www.diva-portal.org/smash/get/diva2:11277/FULLTEXT01.pdf>
- Mang, C., Jason, L. & Davenne, L. (2015), 'A new bond slip model for reinforced concrete structures: Validation by modelling a reinforced concrete tie', *Engineering Computations (Swansea, Wales)* **32**(7), 1934–1958.
- Michał, S. & Andrzej, W. (2015), 'Calibration of the CDP model parameters in Abaqus', *The 2015 World Congress on Advances in Structural Engineering and Mechanics* pp. 25–29.  
**URL:** [http://www.i-asem.org/publication\\_conf/asem15/3.CTCS15/1w/W1D.1.AWinnicki.CAC.p](http://www.i-asem.org/publication_conf/asem15/3.CTCS15/1w/W1D.1.AWinnicki.CAC.p)
- Palacio, K. (2013), 'Practical Recommendations for Nonlinear Structural Analysis in DIANA', *TNO DIANA BV*.
- Palander, T. & Kärhä, K. (2017), 'Potential Traffic Levels after Increasing the Maximum Vehicle Weight in Environmentally Efficient Transportation System: The Case of Finland', *Journal of Sustainable Development of Energy, Water and Environment Systems* **5**(3), 417–429.  
**URL:** <http://www.sdewes.org/jsdewes/pid5.0154>
- Ricci, F. & Valvo, P. S. (2018), D4.4 Analysis of the prototype, Technical report,

- SUREBridge work group.  
**URL:** [surebridge.eu](http://surebridge.eu)
- Rots, J. G. (1988), Computational Modeling of Concrete Fracture, PhD thesis, Delft University of Technology, Delft.  
**URL:** <https://pdfs.semanticscholar.org/7c3d/e6d3483dbcf00b6ab0637b018531ea973633.pdf>
- Rots, J. G. (1989), ‘Crack Models for Concrete: Discrete or Smeared? Fixed, Multi-directional or Rotating?’, *HERON* **34**(1).
- Sto Scandinavia AB (2019), ‘StoPox SK 41’.  
**URL:** [http://www.sto.se/sv/produkter\\_system/produktkatalog/productdetail\\_161210196.html](http://www.sto.se/sv/produkter_system/produktkatalog/productdetail_161210196.html)
- Täljsten, B., Blanksvärd, T. and Sas, G. (2016), Kompositförstärkning av betong (Composite strengthening of concrete. In Swedish), Halmstad: Bulls Graphics AB.
- TNO DIANA (2010), ‘Plane Stress Elements’.  
**URL:** <https://dianafea.com/manuals/d942/ElmLib/node95.html>
- TNO DIANA (2012), ‘Regular Elements’.  
**URL:** <https://dianafea.com/manuals/d944/ElmLib/node36.html>
- TNO DIANA (2015), ‘Tension Softening Relations’.  
**URL:** <https://dianafea.com/manuals/d96/MatLib/node315.html#crack:theo:TenSof>
- Wallenberger, F.T and Bingham, P.A., E. (2010), *Fiberglass and Glass Technology, Energy-Friendly Compositions and Applications*, Springer, New York, 2010.  
**URL:** <https://link-springer-com.proxy.lib.chalmers.se/book/10.1007%2F978-1-4419-0736-3>
- Yang, J. (2019), Flexural Strengthening of Reinforced Concrete Beams Using Externally Bonded CFRP.
- Yang, J., Haghani, R. & Al-emrani, M. (2018), Flexural FRP Strengthening of Concrete Bridges Using an Innovative Concept.
- Yao, L.-Z. & Wu, G. (2016), ‘Nonlinear 2D Finite-Element Modeling of RC Beams Strengthened with Prestressed NSM CFRP Reinforcement’, *Journal of Composites for Construction* **20**(4), 04016008.
- Zhou, A., Lun, C. & Lau, D. (2018), ‘Structural behavior of GFRP reinforced concrete columns under the influence of chloride at casting and service stages’, *Composites Part B* **136**(October 2017), 1–9.  
**URL:** <https://doi.org/10.1016/j.compositesb.2017.10.011>
- Ziari, A. & Kianoush, M. R. (2014), ‘Finite-Element Parametric Study of Bond and Splitting Stresses in Reinforced Concrete Tie Members’, *Journal of Structural Engineering* **140**(5), 04013106.
- Zoghi, M., ed. (2013), *The International Handbook of FRP Composites in Civil Engineering*, CRC Press.  
**URL:** <https://www.taylorfrancis.com/books/9781420003741>



# A

## Appendix 1

### A.1 Beam 1 Results

#### A.1.1 Crack Patterns According to Mesh Density

The cracking patterns of the beams analyzed in section 6.2.1 are displayed in this section. For first ABAQUS and then DIANA, the cracking patterns at each load levels for each mesh density are displayed.

For those analyses performed in ABAQUS, the crack pattern is found by displaying the tension damage factors for each concrete element. Once cracking has commenced in an element, the tension damage factor is greater than 0.

For those analyses performed in DIANA, the crack pattern is found by displaying the crack width size (calculated internally by DIANA).

A.1.1.1 ABAQUS, Crack Patterns at 30 kN

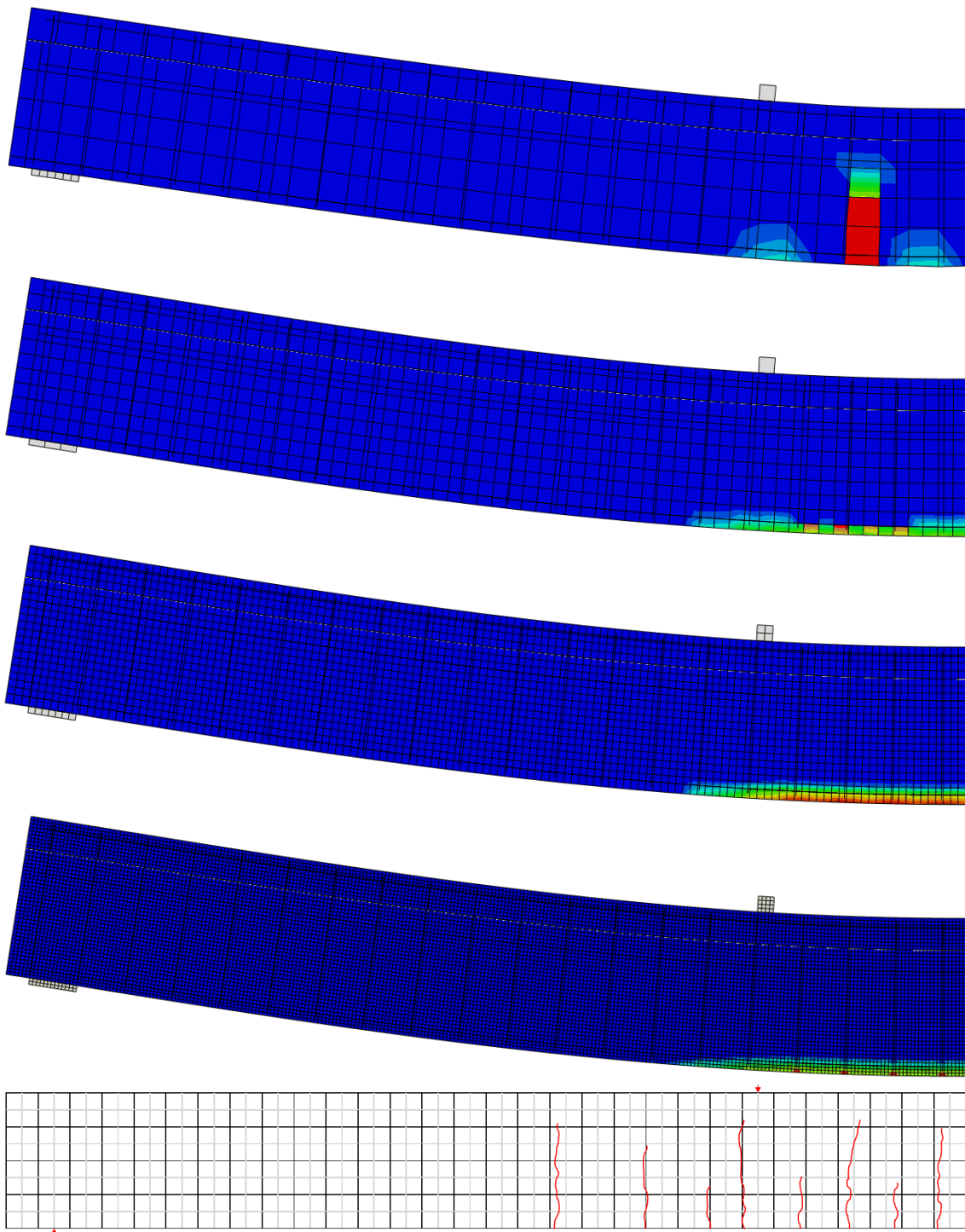


**Figure A.1:** B1: Crack Patterns at 30 kN in ABAQUS. From top to bottom: Mesh 92x92, 46x46, 23x23, 11x11 and from Lab

## A.1.1.2 ABAQUS, Crack Patterns at 60 kN

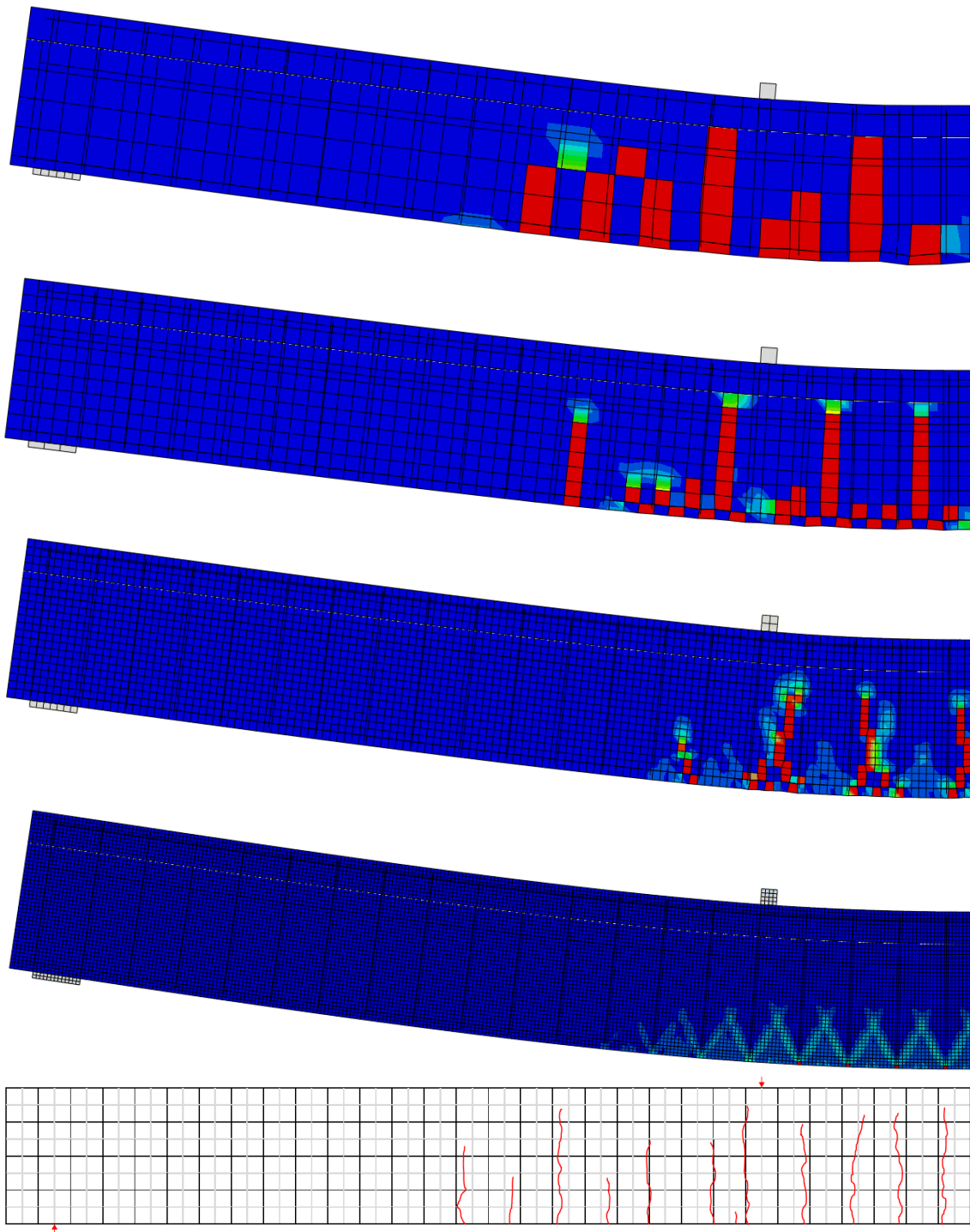


**Figure A.2:** B1: Crack Patterns at 60 kN in ABAQUS. From top to bottom: Mesh 92x92, 46x46, 23x23, 11x11 and from Lab

### A.1.1.3 ABAQUS, Crack Patterns at 90 kN

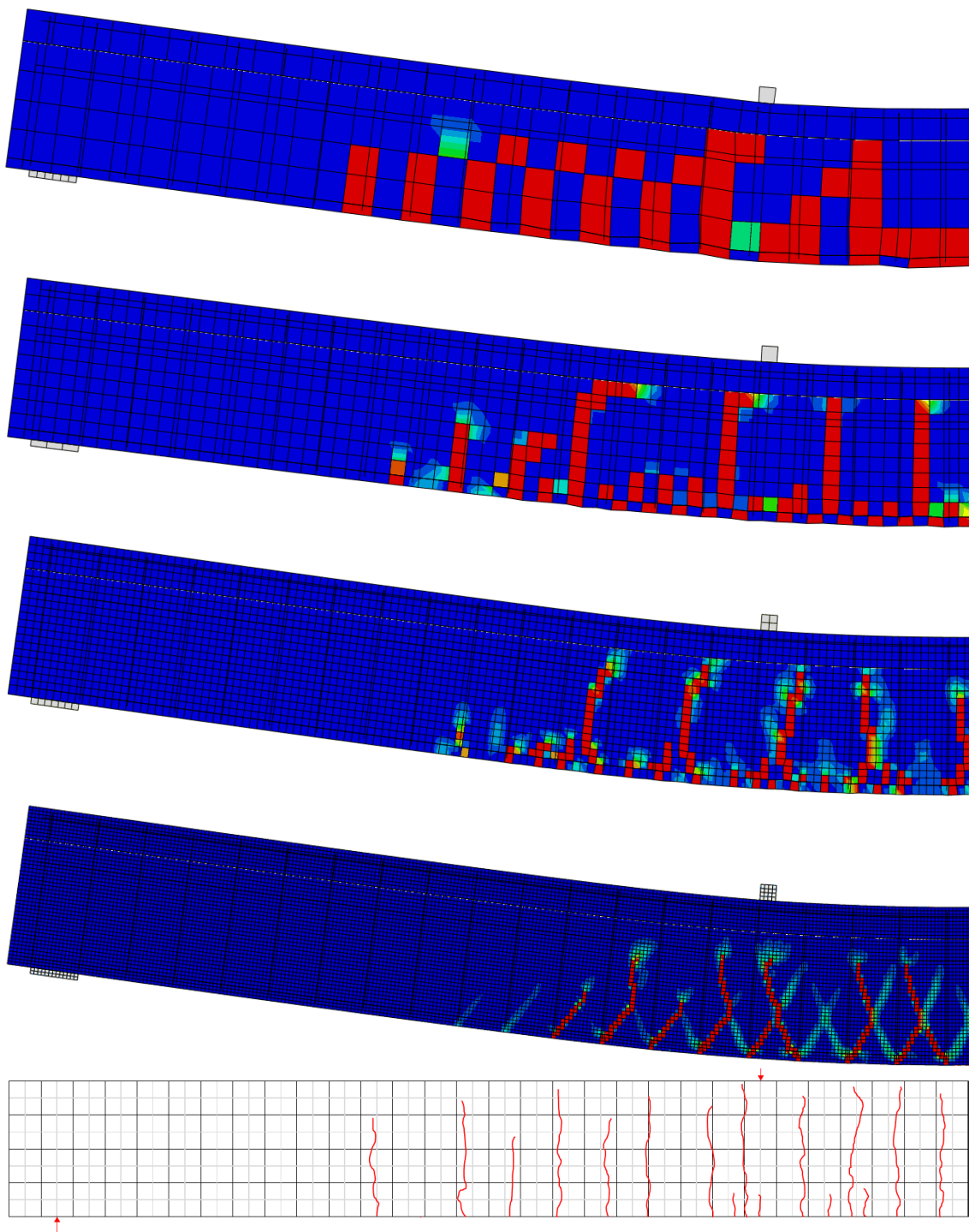


**Figure A.3:** B1: Crack Patterns at 90 kN in ABAQUS. From top to bottom: Mesh 92x92, 46x46, 23x23, 11x11 and from Lab

## A.1.1.4 ABAQUS, Crack Patterns at 120 kN

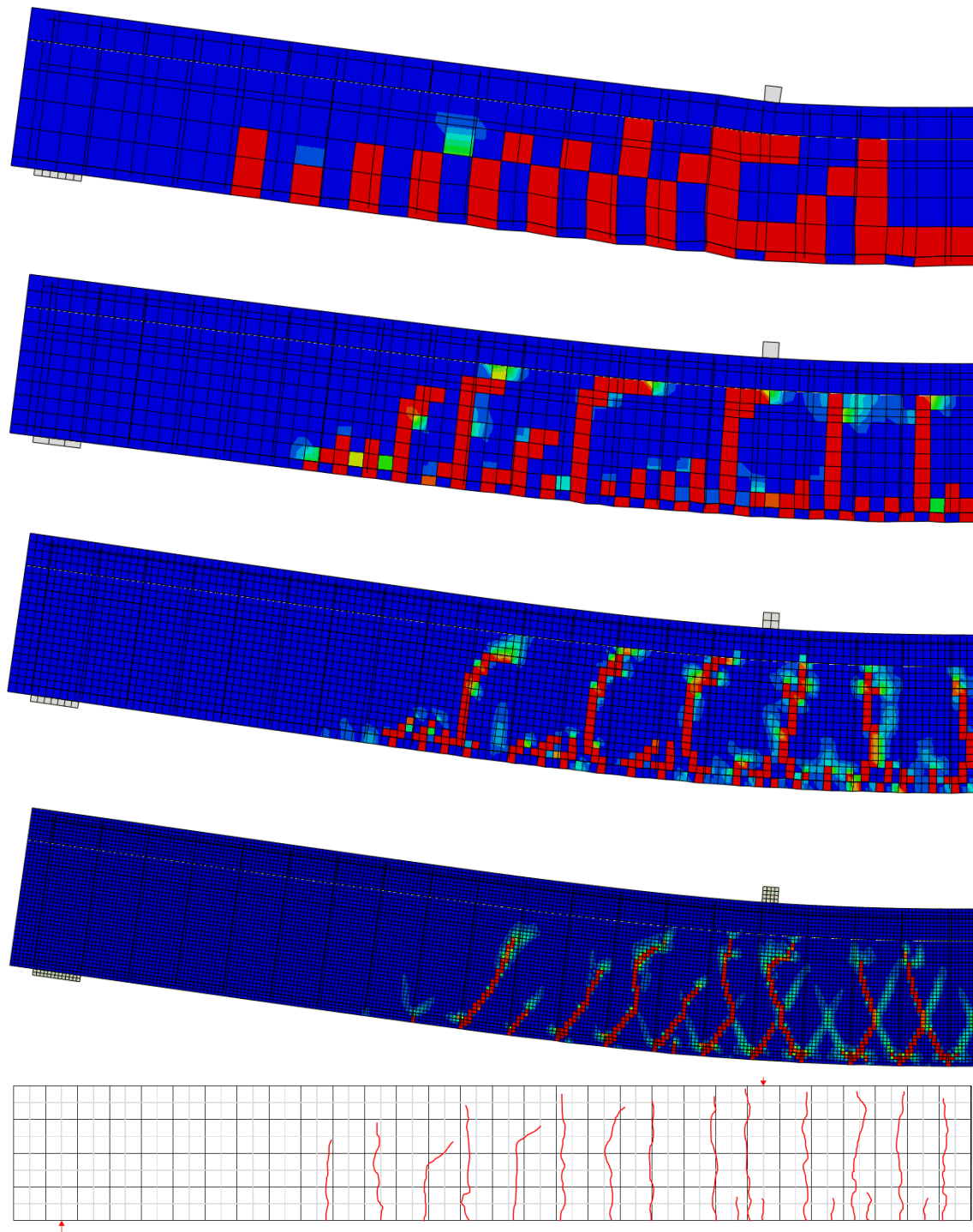


**Figure A.4:** B1: Crack Patterns at 120 kN in ABAQUS. From top to bottom: Mesh 92x92, 46x46, 23x23, 11x11 and from Lab

### A.1.1.5 DIANA, Crack Patterns at 30 kN

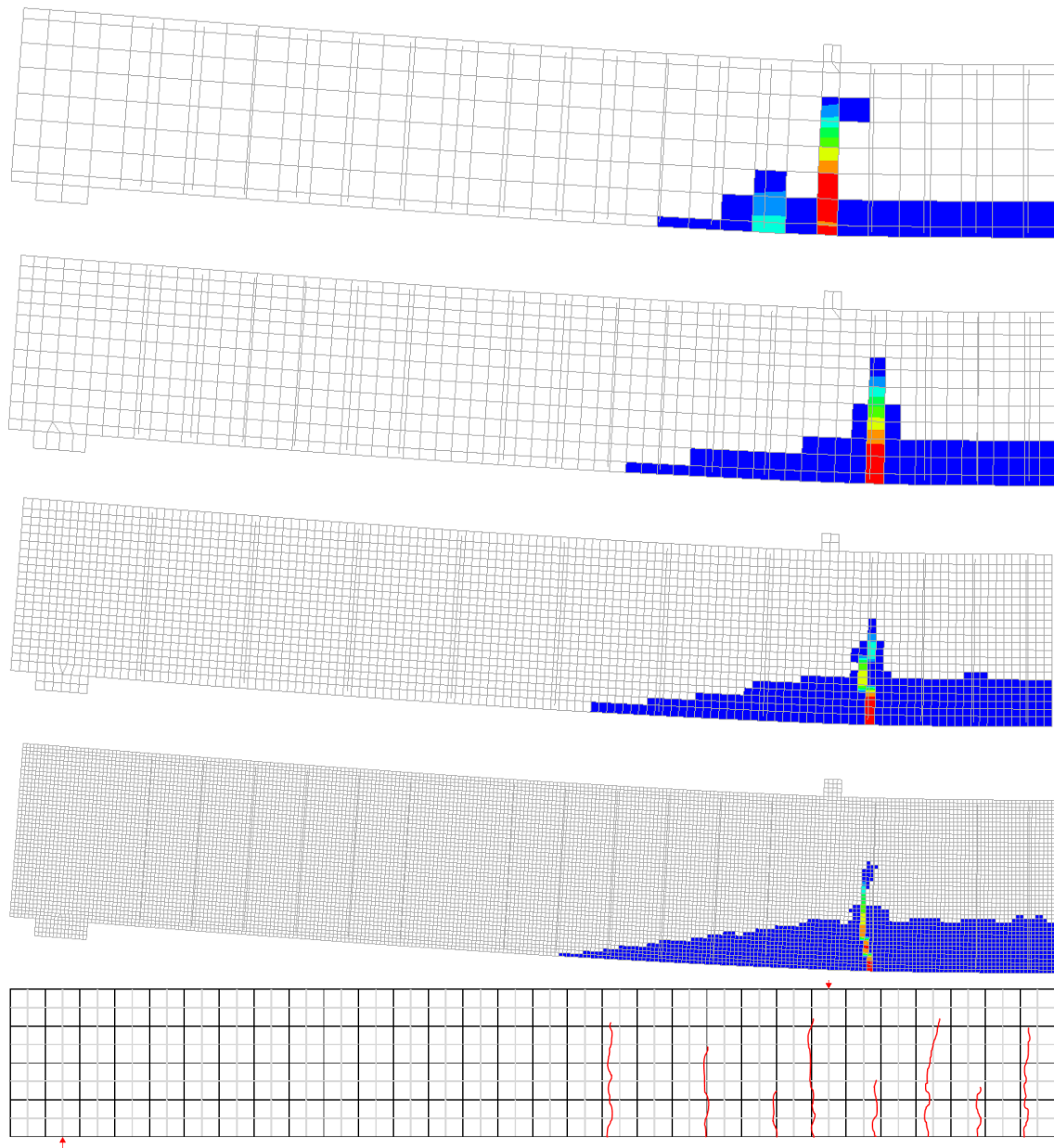


**Figure A.5:** B1: Crack Patterns at 30 kN in DIANA. From top to bottom: Mesh 92x92, 46x46, 23x23, 11x11 and from Lab

## A.1.1.6 DIANA, Crack Patterns at 60 kN

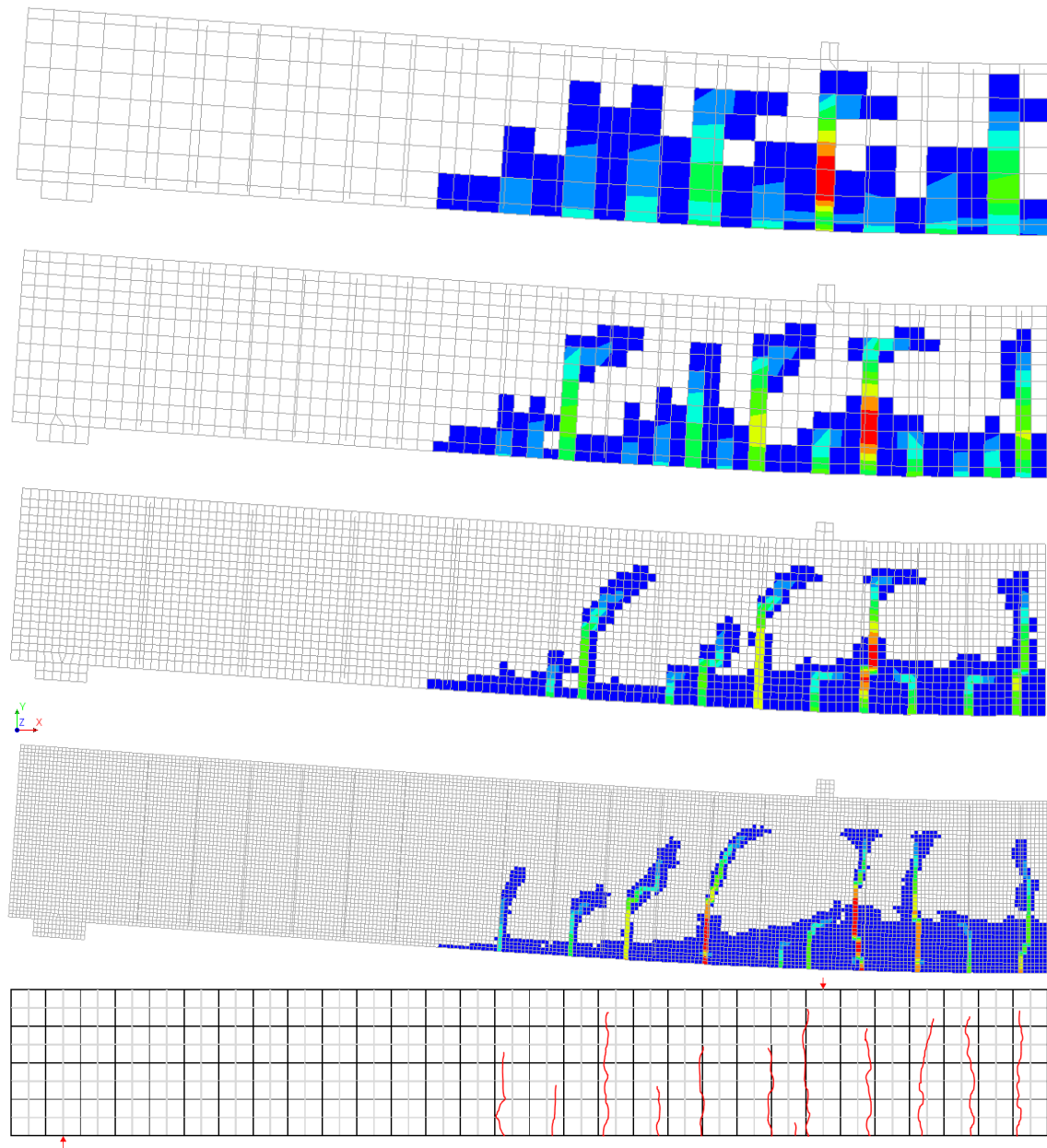


**Figure A.6:** B1: Crack Patterns at 60 kN in DIANA. From top to bottom: Mesh 92x92, 46x46, 23x23, 11x11 and from Lab

A.1.1.7 DIANA, Crack Patterns at 90 kN

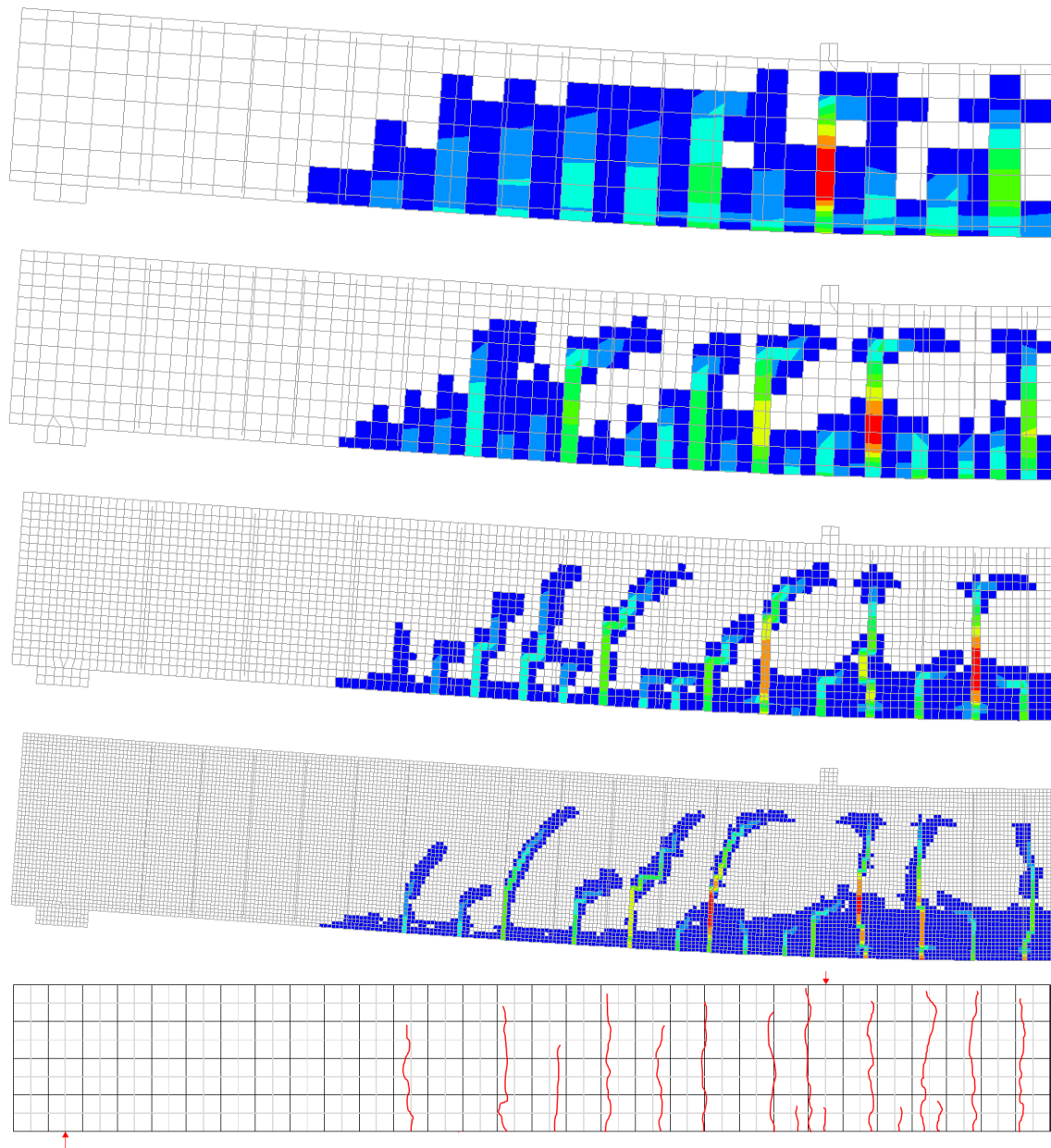


**Figure A.7:** B1: Crack Patterns at 90 kN in DIANA. From top to bottom: Mesh 92x92, 46x46, 23x23, 11x11 and from Lab

## A.1.1.8 DIANA, Crack Patterns at 120 kN

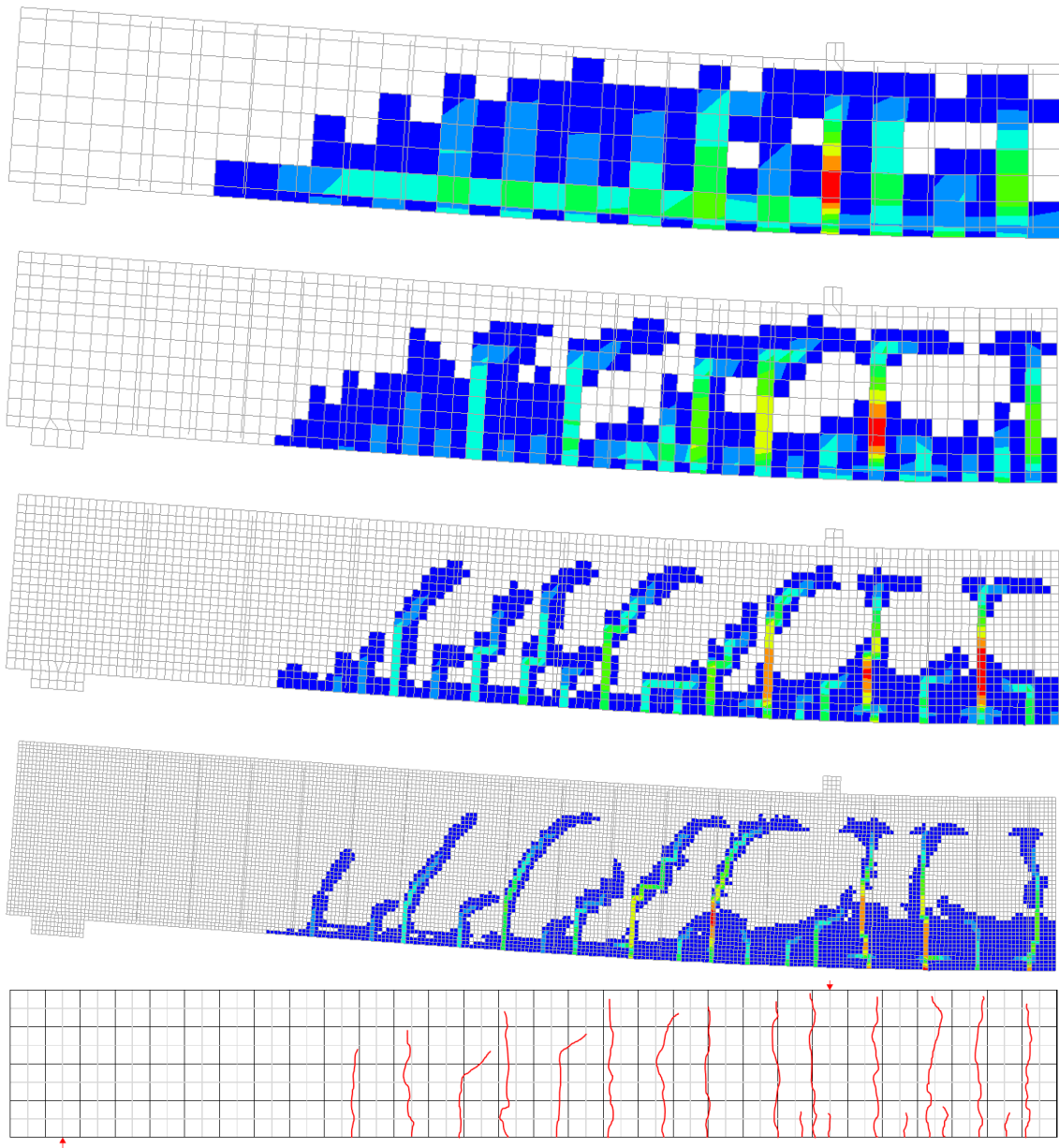


**Figure A.8:** B1: Crack Patterns at 120 kN in DIANA. From top to bottom: Mesh 92x92, 46x46, 23x23, 11x11 and from Lab

## A.1.2 Crack Patterns According to Smear Length (DIANA)

The cracking patterns of the beams analyzed in section 6.2.2 are presented in this section.

### A.1.2.1 DIANA, Crack Patterns at 30 kN

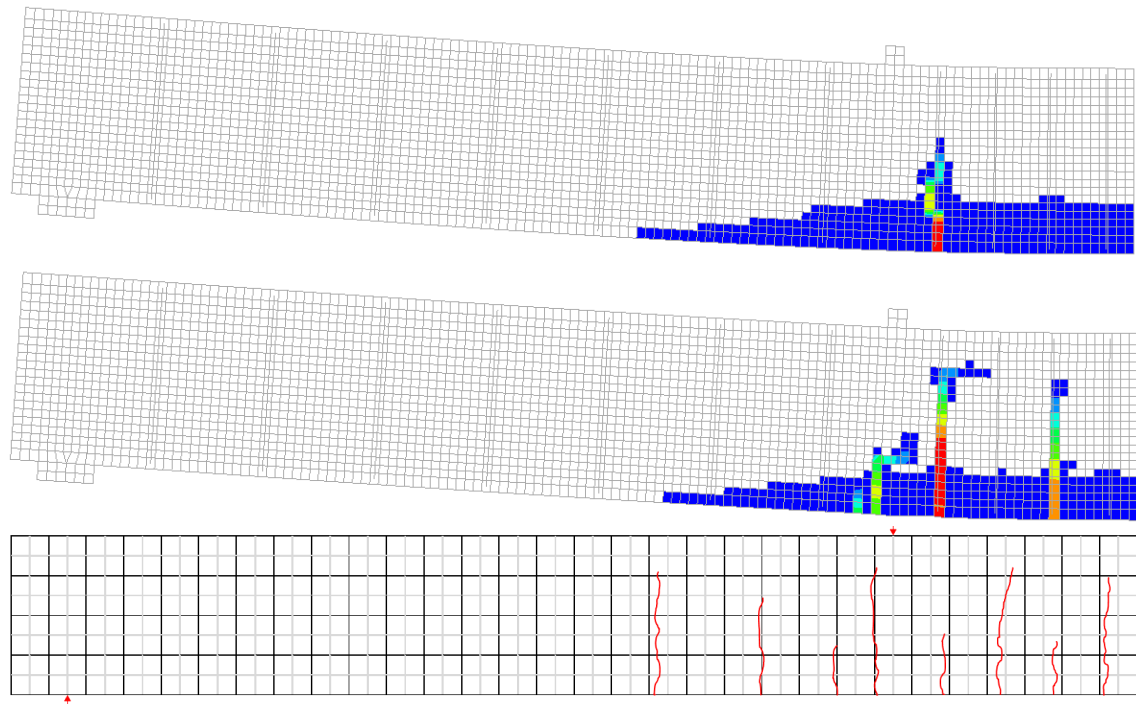


**Figure A.9:** B1: Crack Patterns at 30 kN in DIANA. From top to bottom: Smear Length 23 mm, 32 mm and result from Lab

## A.1.2.2 DIANA, Crack Patterns at 60 kN

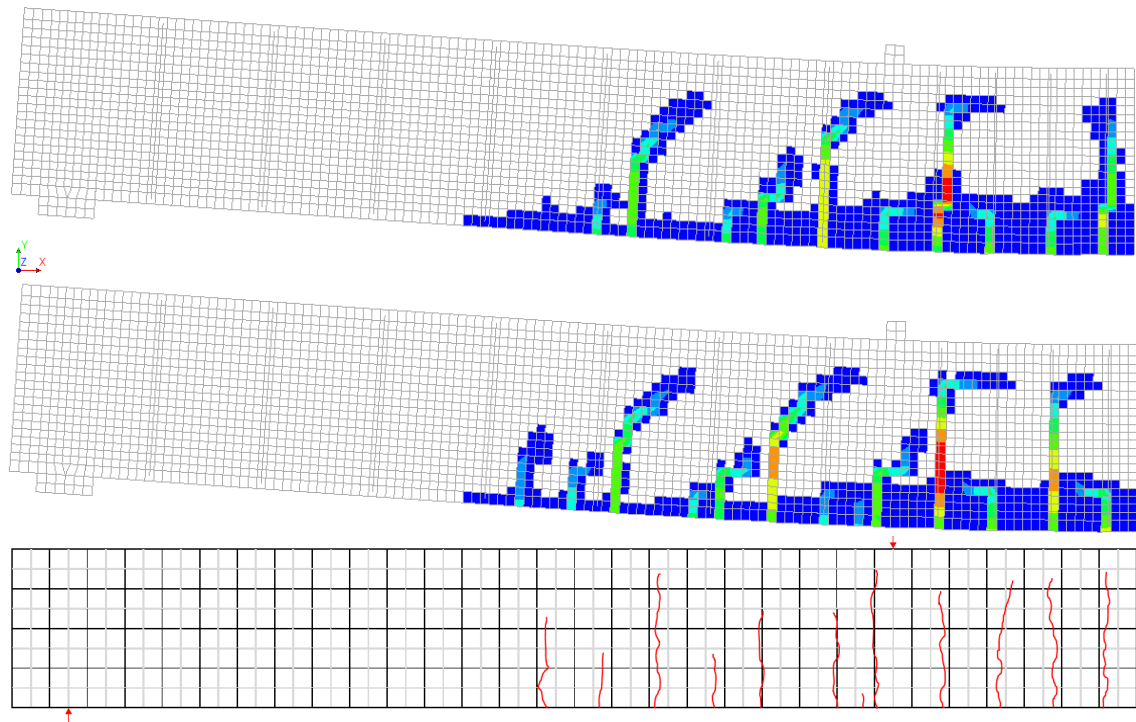


**Figure A.10:** B1: Crack Patterns at 60 kN in DIANA. From top to bottom: Smear Length 23 mm, 32 mm and result from Lab

### A.1.2.3 DIANA, Crack Patterns at 90 kN

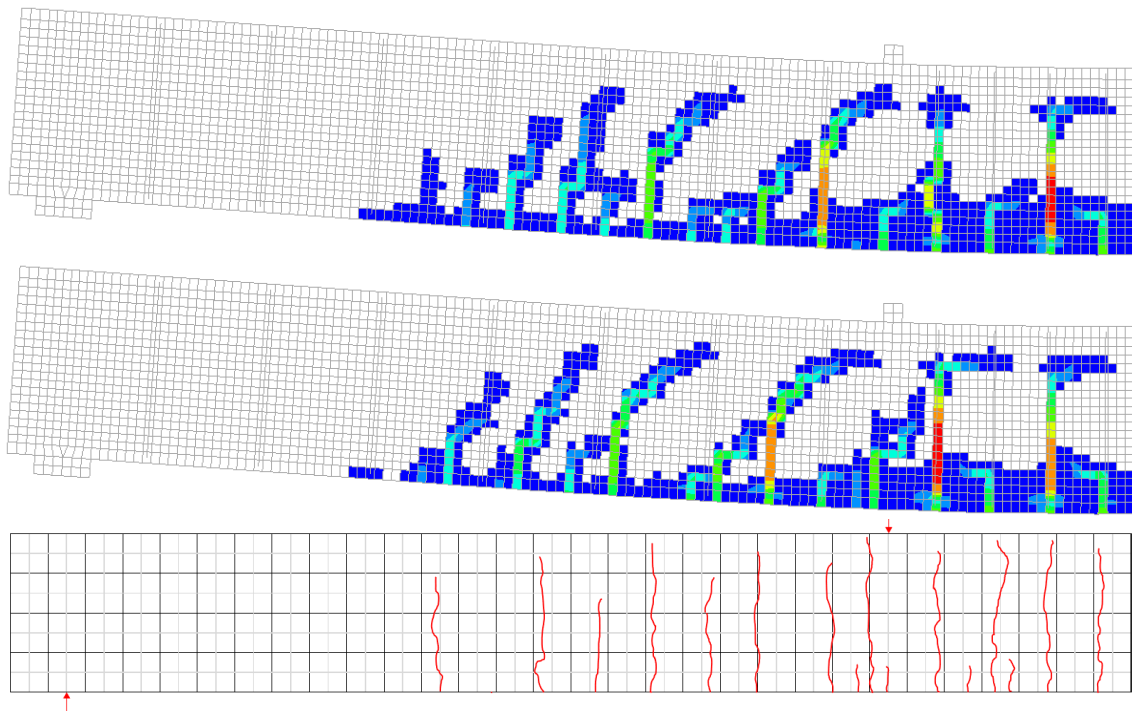


**Figure A.11:** B1: Crack Patterns at 90 kN in DIANA. From top to bottom: Smeared Length 23 mm, 32 mm and result from Lab

## A.1.2.4 DIANA, Crack Patterns at 120 kN

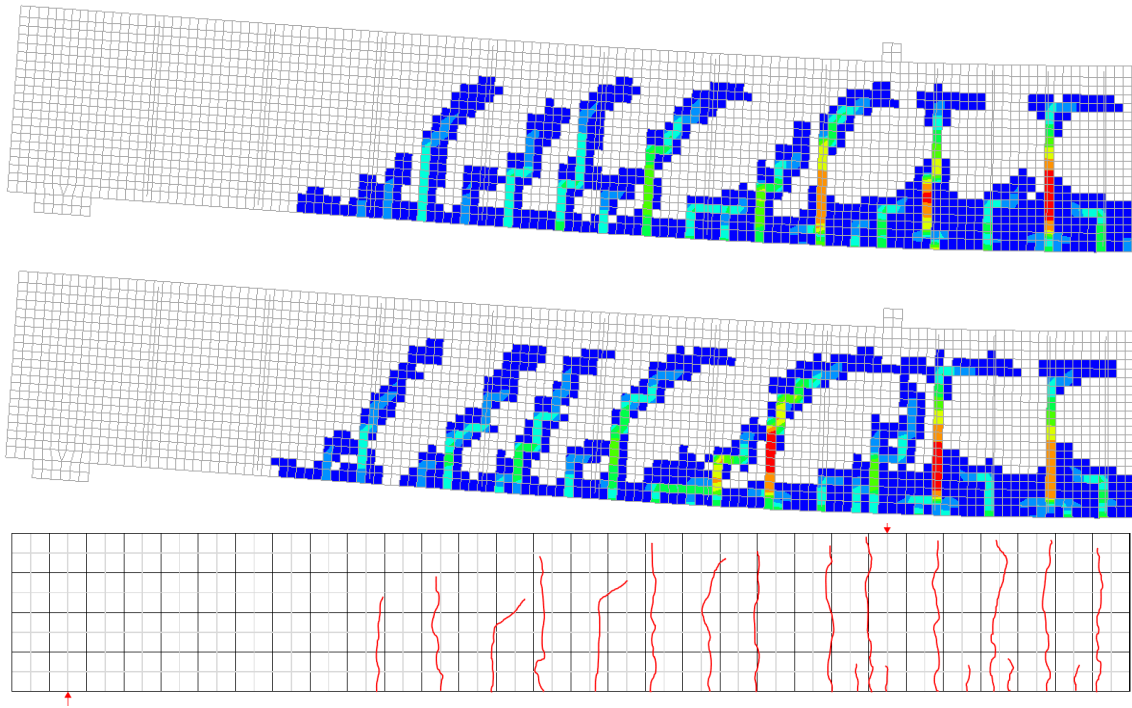


**Figure A.12:** B1: Crack Patterns at 120 kN in DIANA. From top to bottom: Smear Length 23 mm, 32 mm and result from Lab

### A.1.3 Crack Patterns According to Smeared Length (ABAQUS)

The cracking patterns of the beams analyzed in section 6.2.3 are presented in this section.

#### A.1.3.1 ABAQUS, Crack Patterns at 30 kN

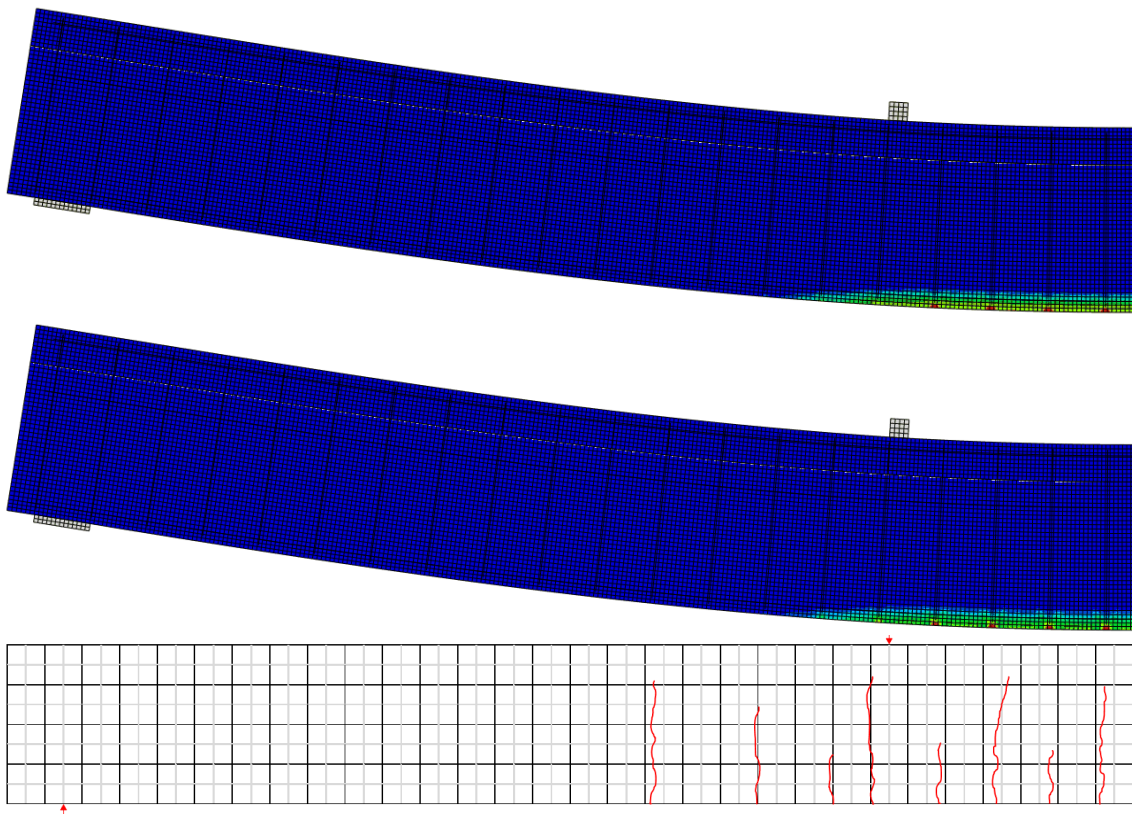


**Figure A.13:** B1: Crack Patterns at 30 kN in ABAQUS. From top to bottom: Smeared Length 11 mm, 46 mm and result from Lab

## A.1.3.2 ABAQUS, Crack Patterns at 60 kN

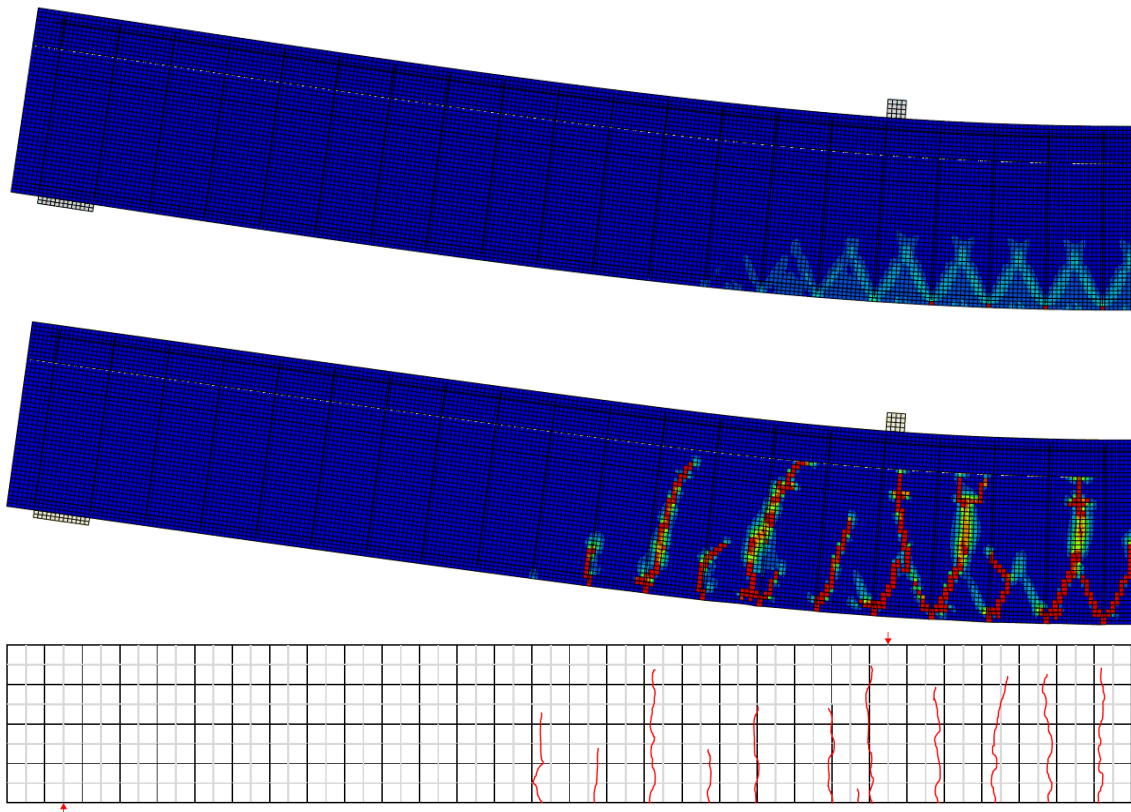


**Figure A.14:** B1: Crack Patterns at 60 kN in ABAQUS. From top to bottom: Smearred Length 11 mm, 46 mm and result from Lab

### A.1.3.3 ABAQUS, Crack Patterns at 90 kN

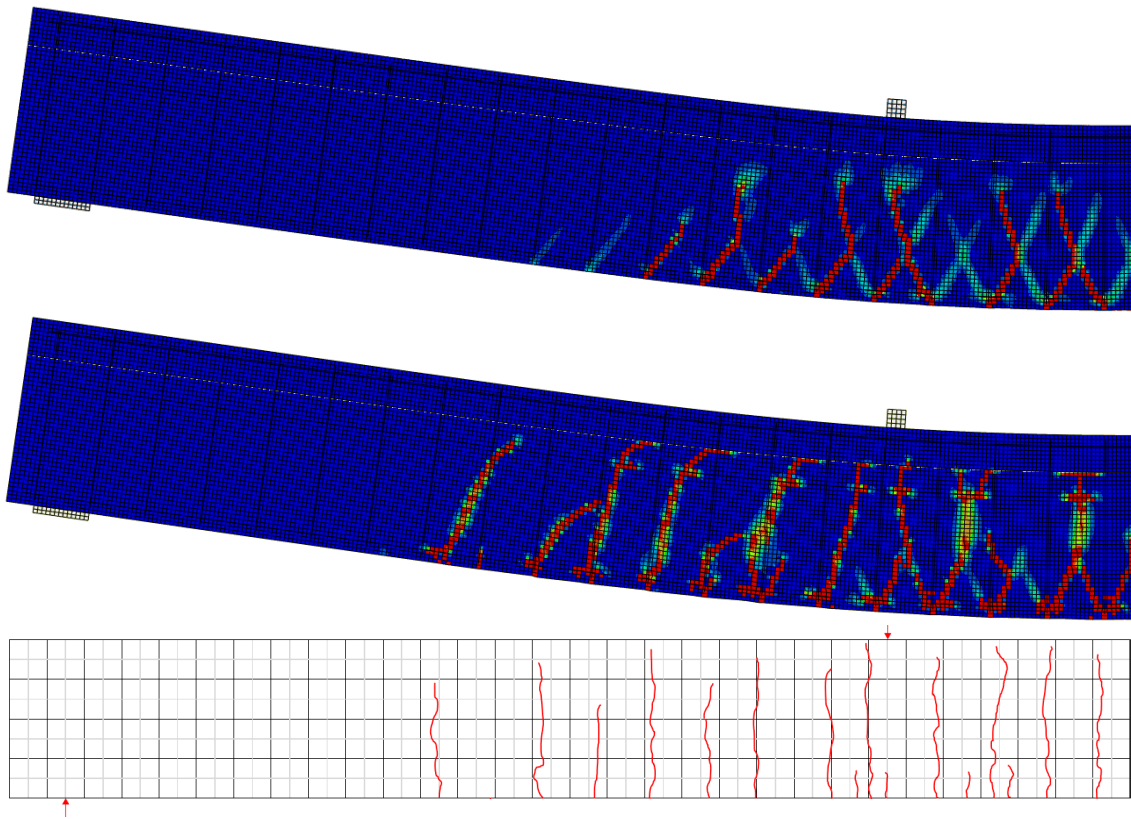


**Figure A.15:** B1: Crack Patterns at 90 kN in ABAQUS. From top to bottom: Smear Length 11 mm, 46 mm and result from Lab

## A.1.3.4 ABAQUS, Crack Patterns at 120 kN

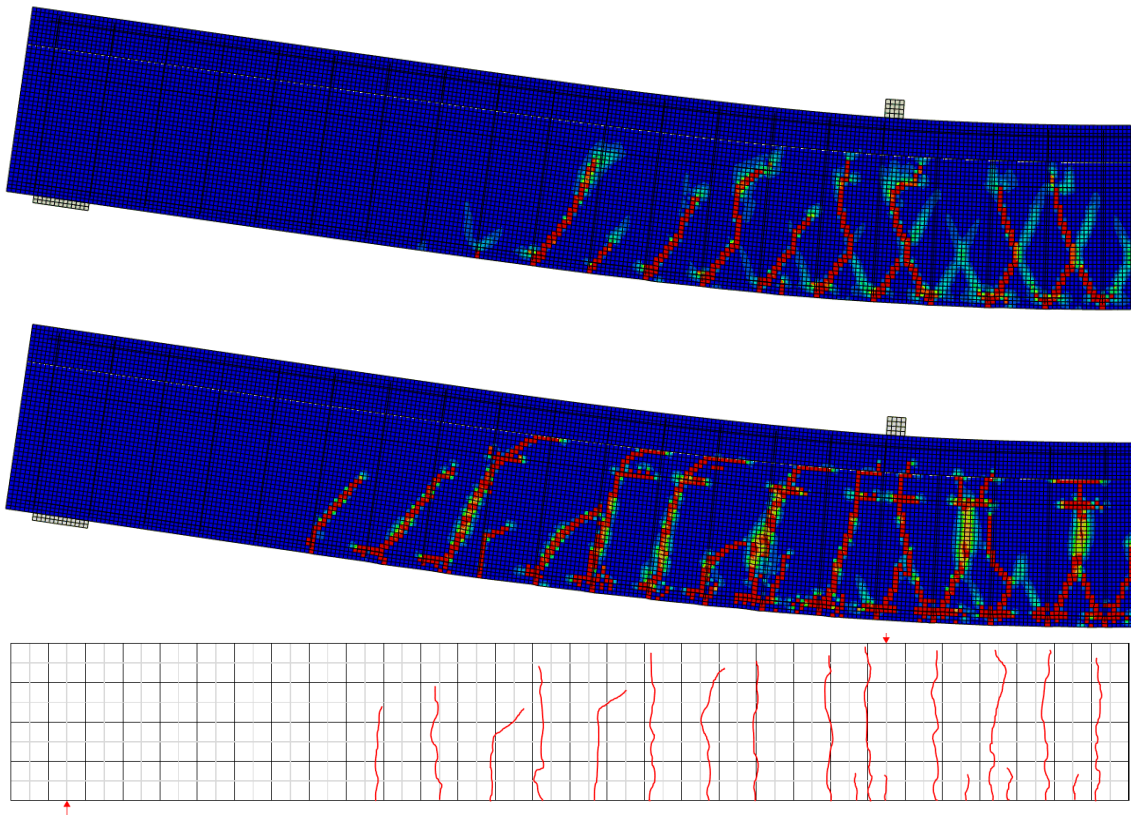


**Figure A.16:** B1: Crack Patterns at 120 kN in ABAQUS. From top to bottom: Smeared Length 11 mm, 46 mm and result from Lab

### A.1.4 Crack Patterns According to Tension Curves (DIANA)

The cracking patterns of the beams analyzed in section 6.2.4 are presented in this section.

#### A.1.4.1 DIANA, Crack Patterns at 30 kN

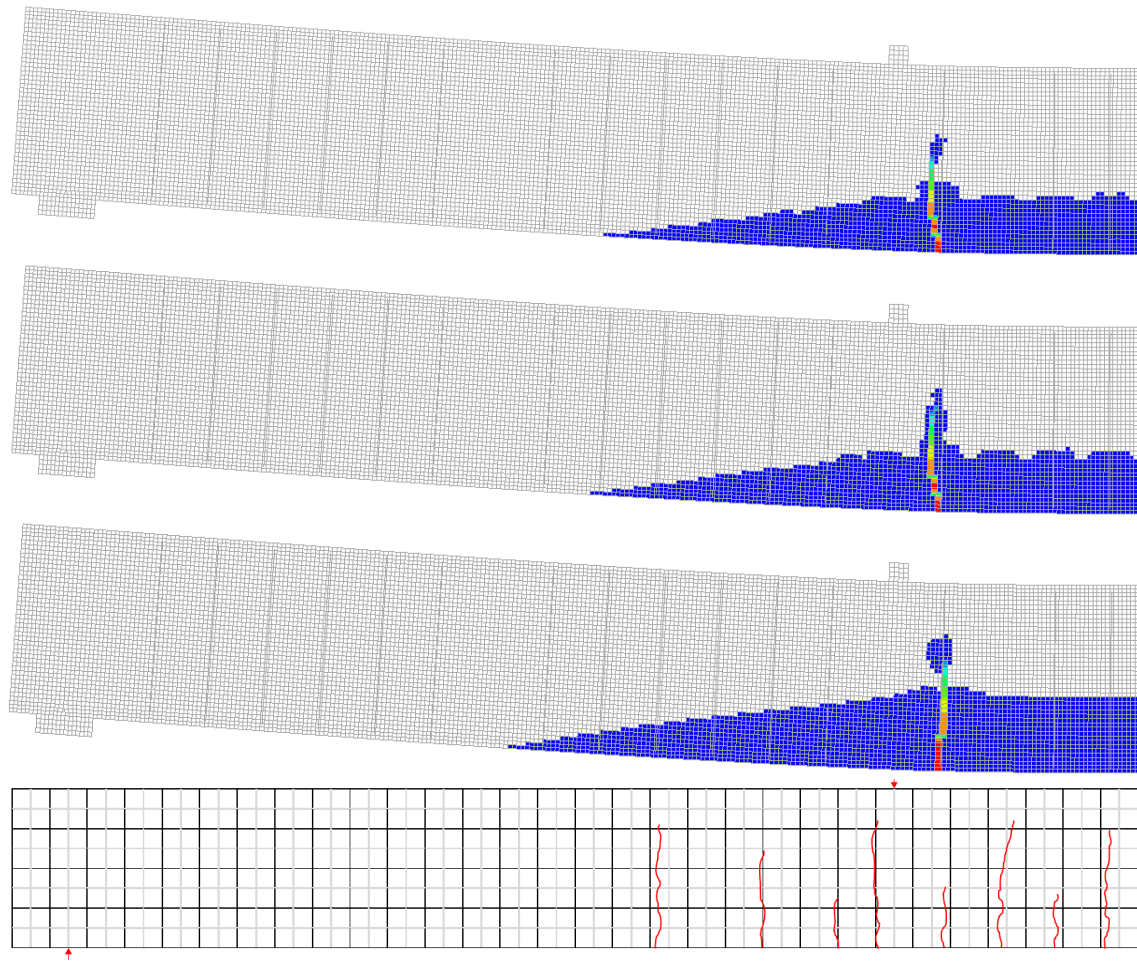


**Figure A.17:** B1: Crack Patterns at 30 kN in DIANA. From top to bottom: Tension model Hordijk, Exponential and fib, and result from Lab

## A.1.4.2 DIANA, Crack Patterns at 60 kN

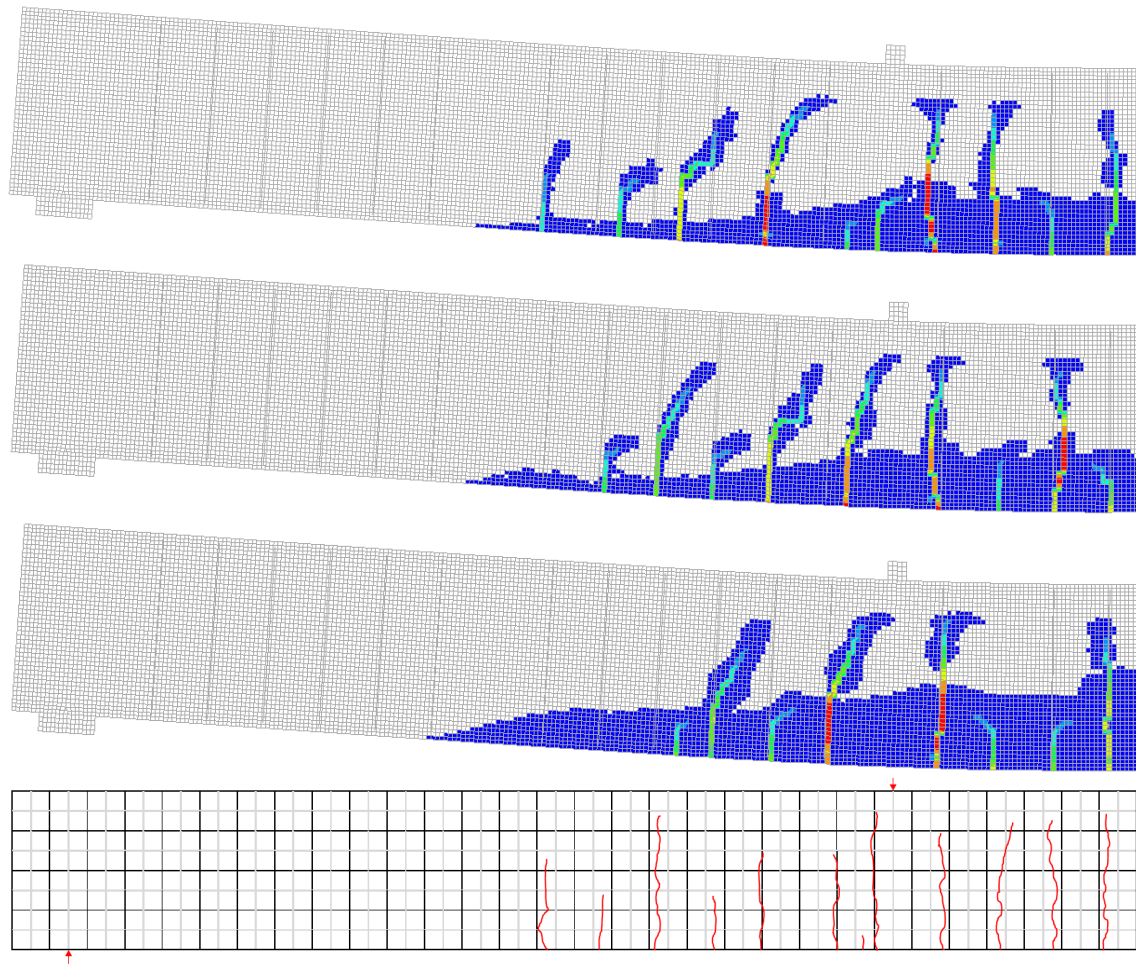


**Figure A.18:** B1: Crack Patterns at 60 kN in DIANA. From top to bottom: Tension model Hordijk, Exponential and fib, and result from Lab

### A.1.4.3 DIANA, Crack Patterns at 90 kN

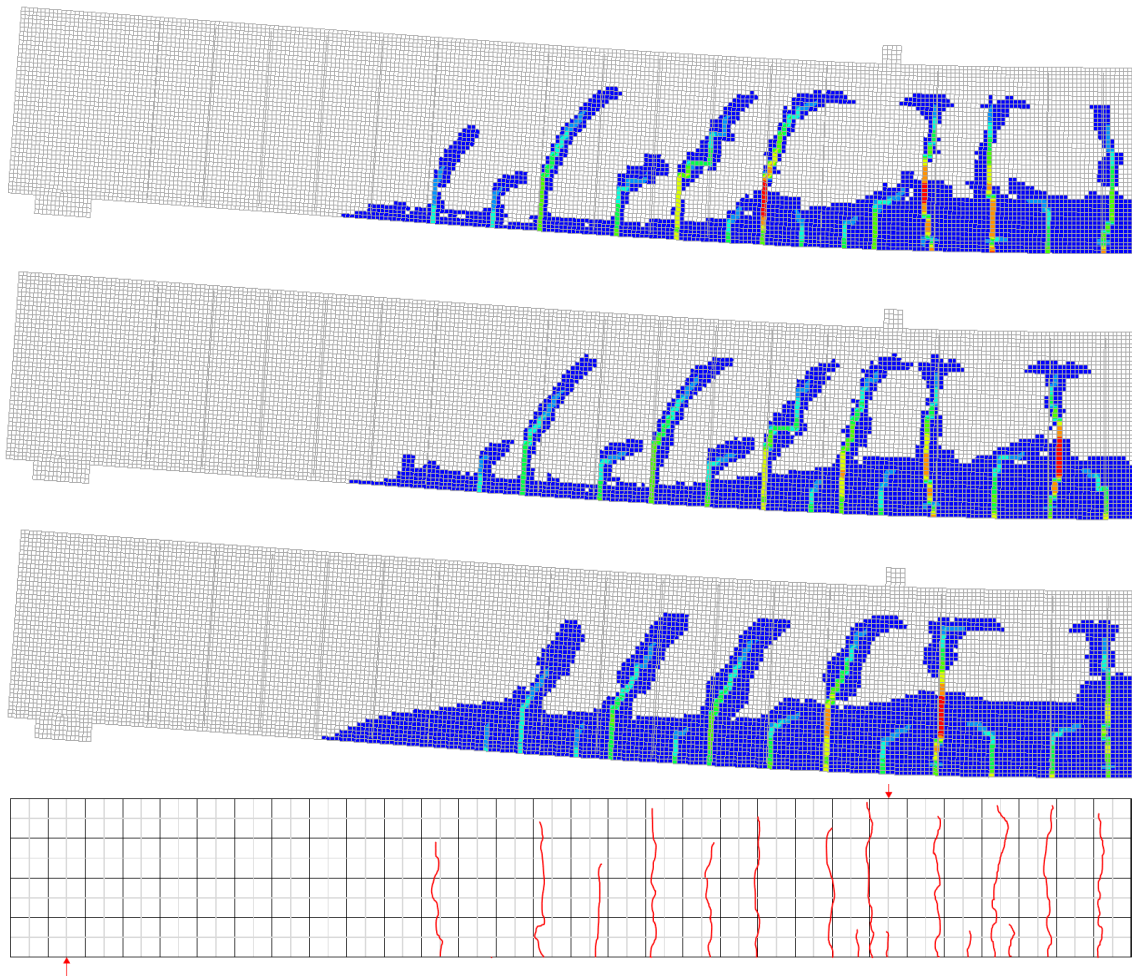


**Figure A.19:** B1: Crack Patterns at 90 kN in DIANA. From top to bottom: Tension model Hordijk, Exponential and fib, and result from Lab

## A.1.4.4 DIANA, Crack Patterns at 120 kN

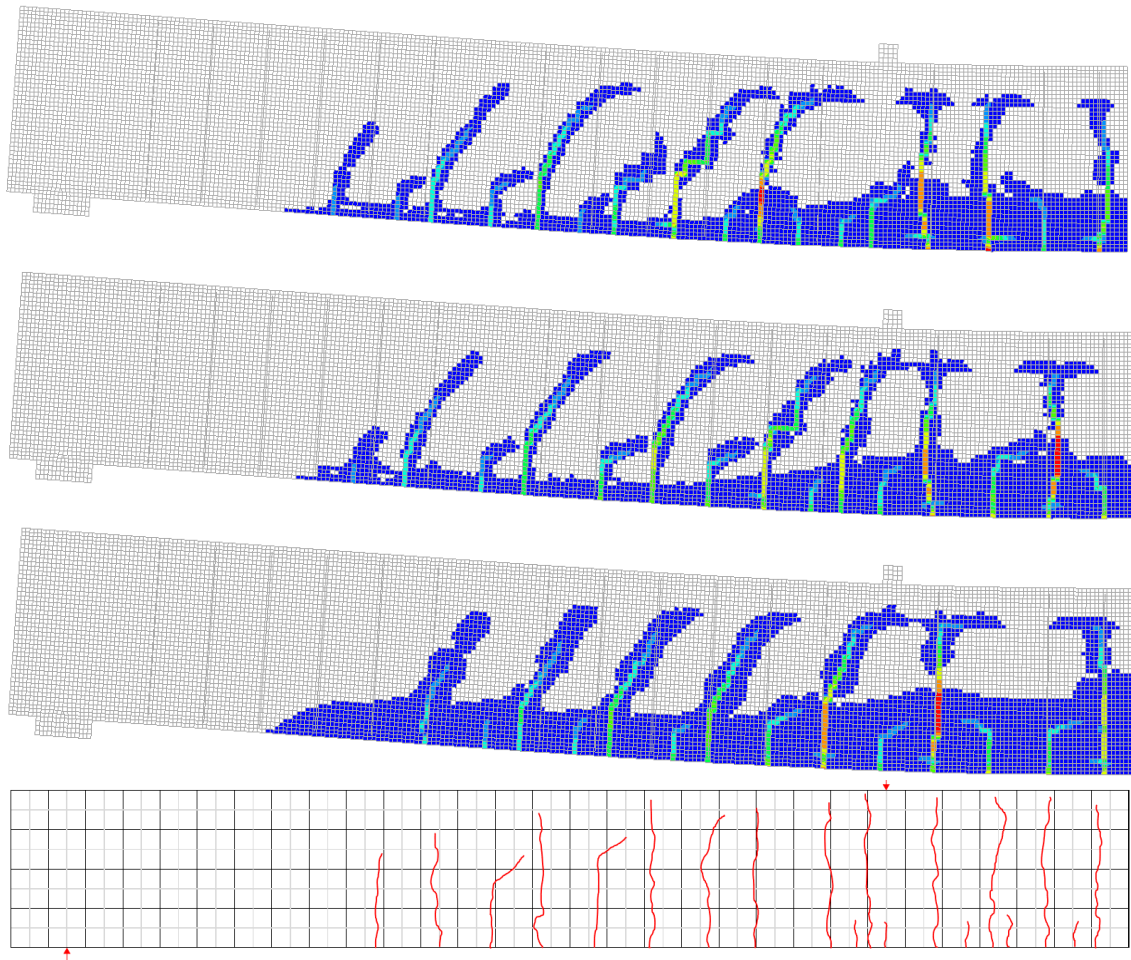


**Figure A.20:** B1: Crack Patterns at 120 kN in DIANA. From top to bottom: Tension model Hordijk, Exponential and fib, and result from Lab

### A.1.5 Crack Patterns According to Damage Models (ABAQUS)

The cracking patterns of the beams analyzed in section 6.2.5 are presented in this section.

#### A.1.5.1 ABAQUS, Crack Patterns at 30 kN

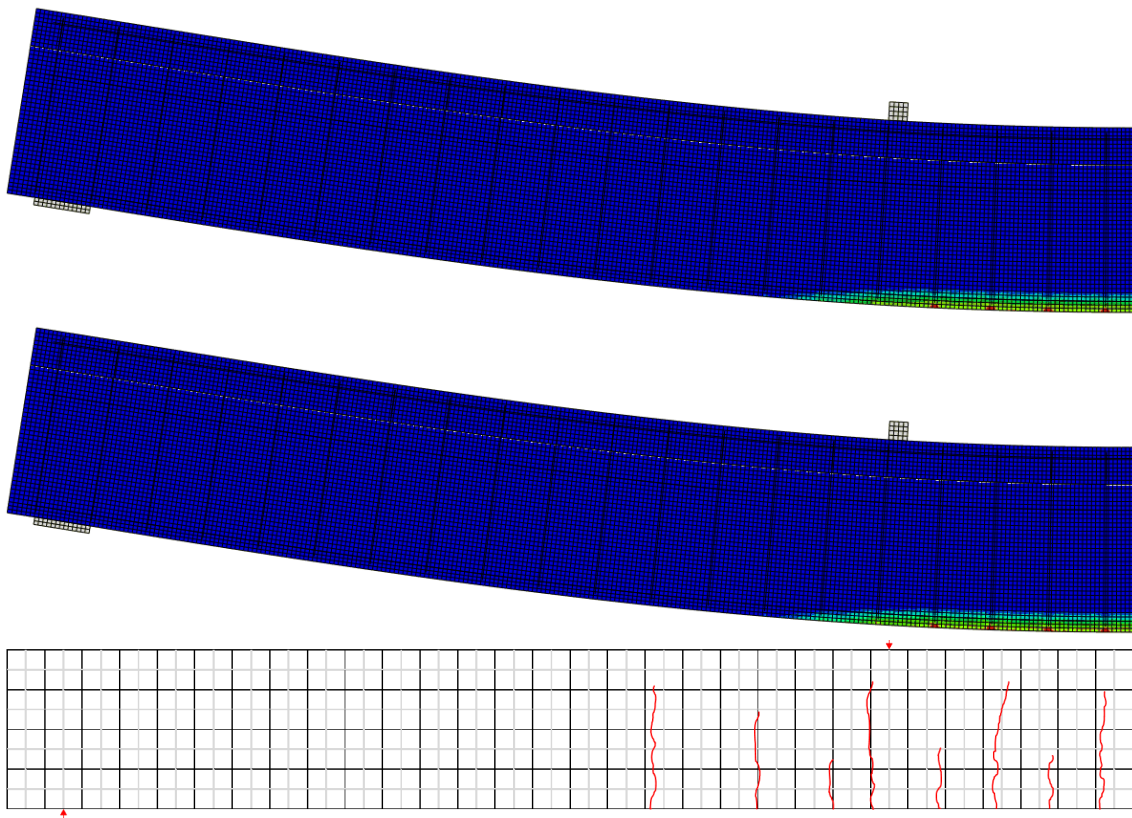


**Figure A.21:** B1: Crack Patterns at 30 kN in ABAQUS. From top to bottom: Damage model 1 and 2, and result from Lab

## A.1.5.2 ABAQUS, Crack Patterns at 60 kN

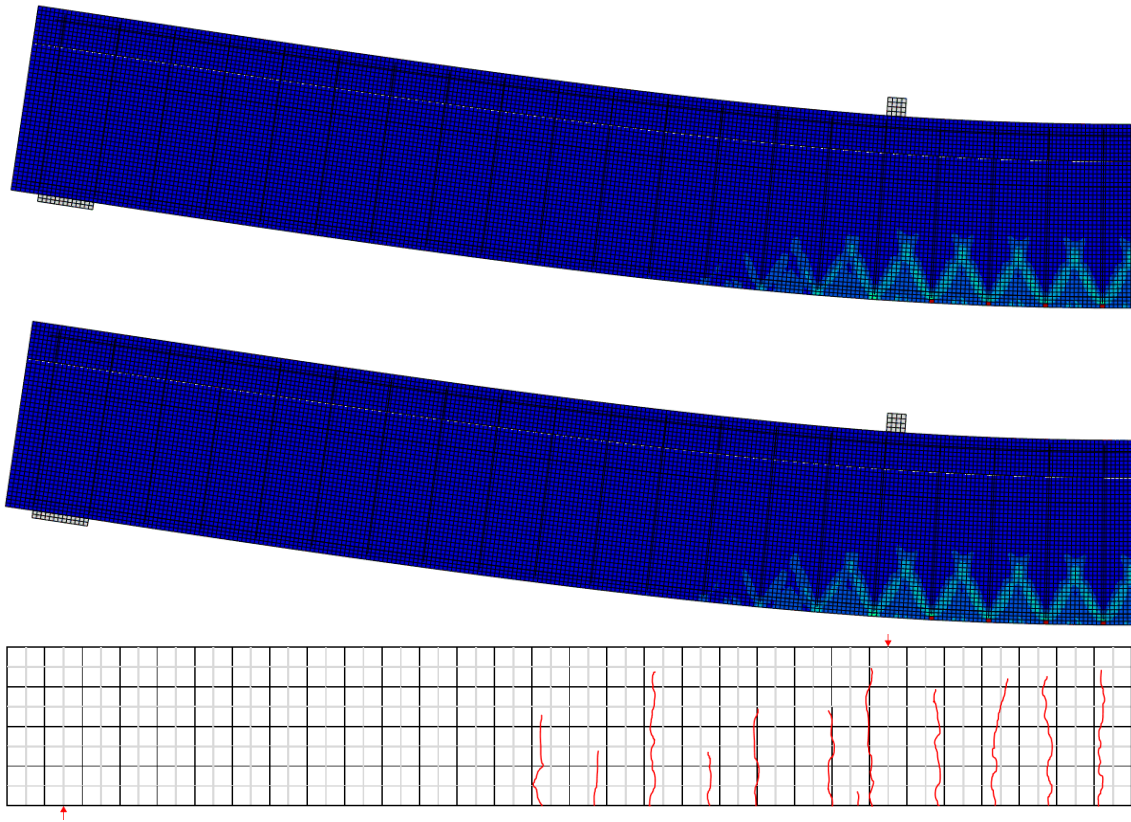


**Figure A.22:** B1: Crack Patterns at 60 kN in ABAQUS. From top to bottom: Damage model 1 and 2, and result from Lab

### A.1.5.3 ABAQUS, Crack Pattern at 90 kN

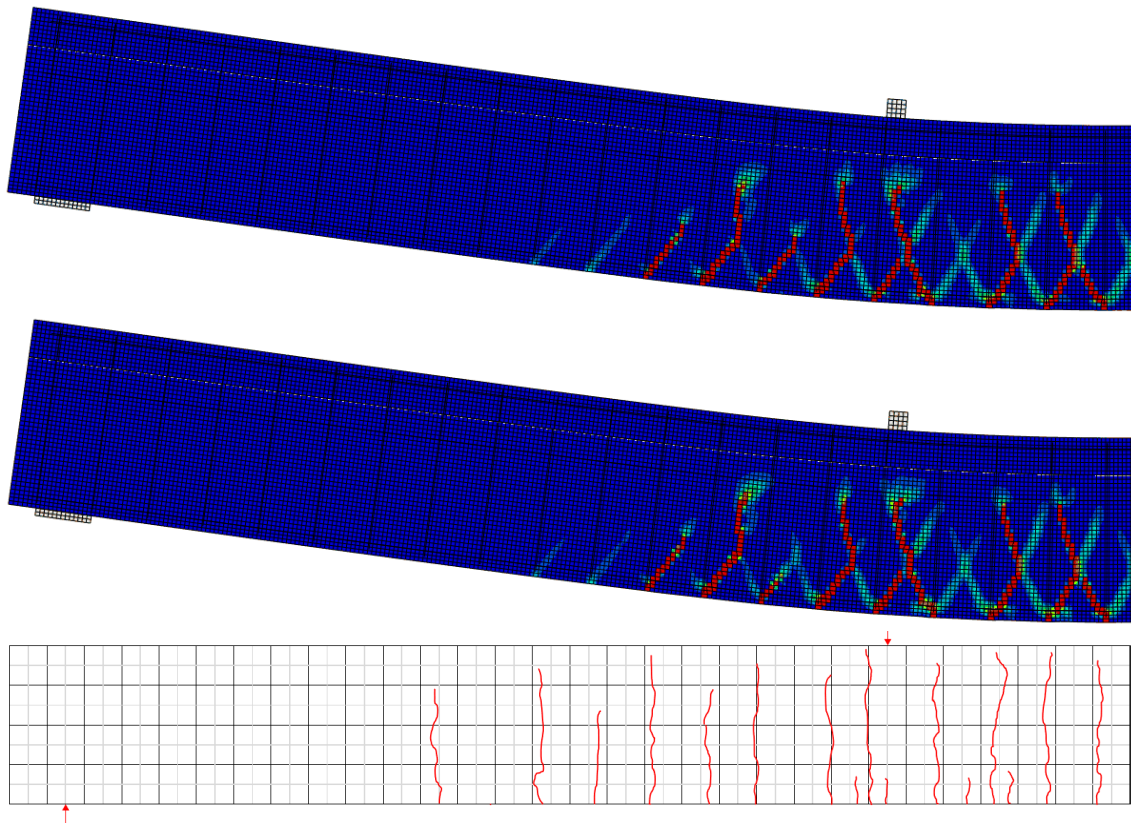


**Figure A.23:** B1: Crack Patterns at 90 kN in ABAQUS. From top to bottom: Damage model 1 and 2, and result from Lab

## A.1.5.4 ABAQUS, Crack Pattern at 120 kN

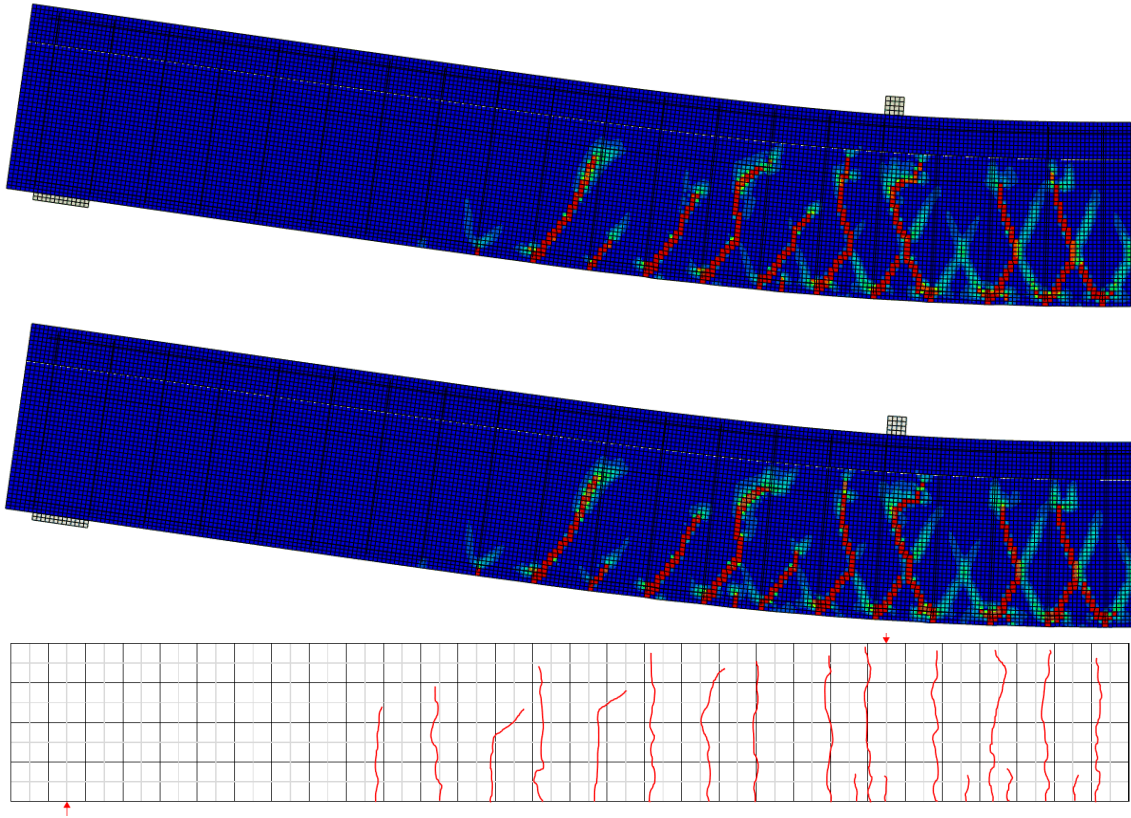


**Figure A.24:** B1: Crack Patterns at 120 kN in ABAQUS. From top to bottom: Damage model 1 and 2, and result from Lab